July 1996 • NREL/TP-442-7815

Effects of Grit Roughness and Pitch Oscillations on the NACA 4415 Airfoil

Airfoil Performance Report, Revised (12/99)

M. J. Hoffmann
R. Reuss Ramsay
G.M. Gregorek
The Ohio State University
Columbus, Ohio

National Renewable Energy Laboratory
1617 Cole Boulevard
Golden, Colorado 80401-3393
A national laboratory of the U.S. Department of Energy
Managed by Midwest Research Institute
for the U.S. Department of Energy
under contract No. DE-AC36-83CH10093

Foreword

Airfoils for wind turbines have been selected by comparing data from different wind tunnels, tested under different conditions, making it difficult to make accurate comparisons. Most wind tunnel data sets do not contain airfoil performance in stall commonly experienced by turbines operating in the field. Wind turbines commonly experience extreme roughness for which there is very little data. Finally, recent tests have shown that dynamic stall is a common occurrence for most wind turbines operating in yawed, stall or turbulent conditions. Very little dynamic stall data exists for the airfoils of interest to a wind turbine designer. In summary, very little airfoil performance data exists which is appropriate for wind turbine design.

Recognizing the need for a wind turbine airfoil performance data base, the National Renewable Energy Laboratory (NREL), funded by the U.S. Department of Energy, awarded a contract to Ohio State University (OSU) to conduct a wind tunnel test program. Under this program, OSU tested a series of popular wind turbine airfoils. A standard test matrix was developed to assure that each airfoil was tested under the same conditions. The test matrix was developed in partnership with industry and is intended to include all of the operating conditions experienced by wind turbines. These conditions include airfoil performance at high angles of attack, rough leading edge (bug simulation), steady and unsteady angles of attack.

Special care has been taken to report as much of the test conditions and raw data as practical so that designers can make their own comparisons and focus on details of the data relevant to their design goals. Some of the airfoil coordinates are proprietary to NREL or an industry partner. To protect the information which defines the exact shape of the airfoil, the coordinates have not been included in the report. Instructions on how to obtain these coordinates may be obtained by contacting C.P. (Sandy) Butterfield at NREL.

C. P. (Sandy) Butterfield
Wind Technology Division
National Renewable Energy Laboratory
1617 Cole Blvd.
Golden, Colorado, 80401 USA
Internet Address: Sandy_Butterfield@NREL.GOV
Phone 303-384-6902
FAX 303-384-6901

Preface

The Ohio State University Aeronautical and Astronautical Research Laboratory is conducting a series of steady state and unsteady wind tunnel tests on a set of airfoils that have been or will be used for horizontal axis wind turbines. The purpose of these tests is to investigate the effect of pitch oscillations and leading edge grit roughness (LEGR) on airfoil performance. The study of pitch oscillation effects can help to understand the behavior of horizontal-axis wind turbines in yaw. The results of these tests will aid in the development of new airfoil performance codes that account for unsteady behavior and also aid in the design of new airfoils for wind turbines. The application of LEGR simulates surface irregularities that occur on wind turbines. These irregularities on the blades are caused by the accumulation of insect debris, ice, and the aging process and can significantly reduce the output of horizontal-axis wind turbines. The experimental results from the application of LEGR will help the development of airfoils that are less sensitive to roughness.

This work was made possible by the efforts and financial support of the National Renewable Energy Laboratory which provided major funding and technical monitoring, the U.S. Department of Energy is credited for its funding of this document through the National Renewable Energy Laboratory under contract number DE-AC36-83CH10093 and KENETECH, Windpower Inc. provided technical assistance and funding for the test model. The staff of The Ohio State University Aeronautical and Astronautical Research Laboratory appreciate the contributions made by personnel from both organizations. In addition, the authors would like to recognize the efforts of the following graduate and undergraduate research assistants: Jolanta M. Janiszewska, Fernando Falasca and Monica Angelats i Coll.

Summary

A NACA 4415 airfoil model was tested in The Ohio State University Aeronautical and Astronautical Research Laboratory 3x5 subsonic wind tunnel under steady state and unsteady conditions. The test defined baseline conditions for steady state angles of attack from -10° to +40° and examined unsteady behavior by oscillating the model about its pitch axis for three mean angles, three frequencies, and two amplitudes. For all cases, Reynolds numbers of 0.75, 1, 1.25, and 1.5 million were used. In addition, these were repeated after the application of leading edge grit roughness (LEGR) to determine contamination effects on the airfoil performance.

Steady state results of the NACA 4415 testing at Reynolds number of 1.00 million showed a baseline maximum lift coefficient of 1.35 at 14.3° angle of attack. The application of LEGR reduced the maximum lift coefficient by 16% and increased the 0.0076 minimum drag coefficient value by 67%. The zero lift pitching moment of -0.0967 showed a 13% reduction in magnitude to -0.0842 with LEGR applied.

Data were also obtained for two pitch oscillation amplitudes: ±5.5° and ±10°. The larger amplitude consistently gave a higher maximum lift coefficient than the smaller amplitude, and both unsteady maximum lift coefficients were greater than the steady state values. Stall was delayed on the airfoil while the angle of attack was increasing, thereby causing an increase in maximum lift coefficient. A hysteresis behavior was exhibited for all the unsteady test cases. The hysteresis loops were larger for the higher reduced frequencies and for the larger amplitude oscillations. As in the steady case, the effect of LEGR in the unsteady case was to reduce the lift coefficient at high angles of attack. In addition, with LEGR, the hysteresis behavior persisted into lower angles of attack than for the clean case.

In general, the unsteady maximum lift coefficient was 10% to 55% higher than the steady state maximum lift coefficient, and variation in the quarter chord pitching moment coefficient magnitude was from -30% to +45% relative to steady state values at high angles of attack. These findings indicate the importance of considering the unsteady flow behavior occurring in wind turbine operation to obtain accurate load estimates.

Contents Page

List of Figures Page

List of Tables Page

List of Symbols

AOA	Angle of attack
A/C, a.c.	Alternating current
c	Model chord length
C_d	Drag coefficient
C_{dmin}	Minimum drag coefficient
C_{dp}	Pressure drag coefficient
C_{dw}	Wake drag coefficient
C_{du}	Uncorrected drag coefficient
C_l	Lift coefficient
C_{lmax}	Maximum lift coefficient
$C_{l\ dec}$	Lift coefficient at angle of maximum lift, but with angle of attack decreasing
C_{lu}	Uncorrected lift coefficient
C_m, $C_{m¼}$	Pitching moment coefficient about the quarter chord
$C_{m\ dec}$	Pitching moment coefficient at angle of maximum lift, but with angle of attack decreasing
$C_{m\ inc}$	Pitching moment coefficient at angle of maximum lift, but with angle of attack increasing
C_{mo}	Pitching moment coefficient about the quarter chord, at zero lift
$C_{m¼u}$	Uncorrected pitching moment coefficient about the quarter chord
C_p	Pressure coefficient, $(p- p_\infty)/q_\infty$
C_{pmin}	Minimum pressure coefficient
f	Frequency
h	Wind tunnel test section height
hp, Hp, HP	Horsepower
Hz	Hertz
k	Grit particle size
k/c	Grit particle size divided by airfoil model chord length
p	Pressure
q	Dynamic pressure
q_u	Uncorrected dynamic pressure
q_w	Dynamic pressure through the model wake
q_∞	Free stream dynamic pressure
Re	Reynolds number
Re_u	Uncorrected Reynolds number
t	Time
U_∞	Corrected free stream velocity
V	Velocity
V_u	Uncorrected velocity
x	Axis parallel to model reference line
y	Axis perpendicular to model reference line

α	Angle of attack
α_{dec}	Decreasing angle of attack
α_{inc}	Increasing angle of attack
α_m	Median angle of attack
α_{mean}	Mean angle of attack
α_u	Uncorrected angle of attack
ϵ	Tunnel solid wall correction scalar
ϵ_{sb}	Solid blockage correction scalar
ϵ_{wb}	Wake blockage correction scalar
Λ	Body-shape factor
π	3.1416
σ	Tunnel solid wall correction parameter
ω_{red}, $\omega_{reduced}$	Reduced frequency, $\pi fc/U_\infty$

Introduction

Horizontal-axis wind turbine rotors experience unsteady aerodynamics due to wind shear when the rotor is yawed, when rotor blades pass through the support tower wake, and when the wind is gusting. An understanding of this unsteady behavior is necessary to assist in the calculation of rotor performance and loads. The rotors also experience performance degradation due to surface roughness. These surface irregularities are caused by the accumulation of insect debris, ice, and the aging process. Wind tunnel studies that examine both the steady and unsteady behavior of airfoils can help define pertinent flow phenomena, and the resultant data can be used to validate analytical computer codes.

A NACA 4415 airfoil model was tested in The Ohio State University Aeronautical and Astronautical Research Laboratory (OSU/AARL) 3x5 subsonic wind tunnel (3x5) under steady flow and stationary model conditions, as well as with the model undergoing pitch oscillations. To study the possible extent of performance loss due to surface roughness, a standard grit pattern (LEGR) was used to simulate leading edge contamination. After baseline cases were completed, the LEGR was applied for both steady state and model pitch oscillation cases. The Reynolds numbers used for steady state conditions were 0.75, 1, 1.25 and 1.5 million, while the angle of attack ranged from -10° to +40°. With the model undergoing pitch oscillations, data were acquired at Reynolds numbers of 0.75, 1, 1.25, and 1.5 million, at frequencies of 0.6, 1.2, and 1.8 Hz. Two sine wave forcing functions were used, ±5.5° and ±10°, at mean angles of attack of 8°, 14°, and 20°. For purposes herein, any reference to unsteady conditions means the airfoil model was in pitch oscillation about the quarter chord.

Experimental Facility

Wind Tunnel

The OSU/AARL 3×5 was used to conduct tests on the NACA 4415 airfoil section. Schematics of the top and side views of the tunnel are shown in figures 1 and 2, respectively. This open circuit tunnel has a velocity range of 0 - 55-m/s (180-ft/s) produced by a 2.4-m (8-ft) diameter, six-bladed fan. The fan is belt driven by a 93.2-kw (125-hp) three phase a.c. motor connected to a variable frequency motor controller. Nominal test section dimensions are 1.0-m (39-in) high by 1.4-m (55-in) wide by 2.4-m (96-in) long. The 457-mm (18-in) chord airfoil model was mounted vertically in the test section. A steel tube through the quarter chord of the model attached the model to the tunnel during testing. An angle of attack potentiometer was fastened to the model at the top of the tunnel as shown in figure 2. The steady state angle of attack was adjusted with a worm gear drive attached to the model strut below the tunnel floor.

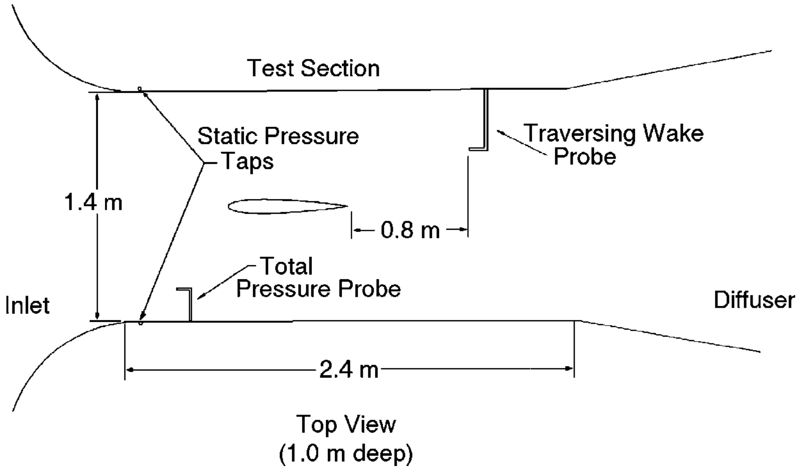

Figure 1. 3x5 subsonic wind tunnel, top view.

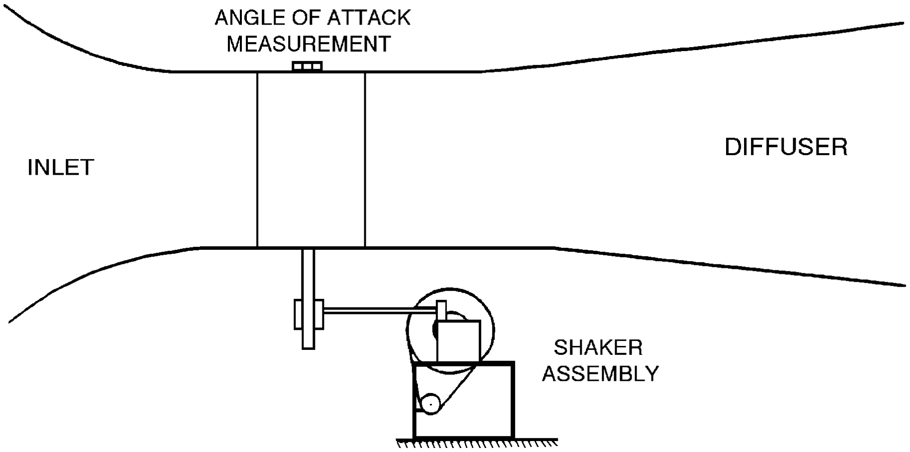

Figure 2. 3x5 subsonic wind tunnel, side view.

Oscillation System

Portions of the airfoil model testing required the use of a reliable pitch oscillation system. The OSU/AARL 'shaker' system incorporated a face cam and follower arm attached to the model support tube below the wind tunnel floor, as shown in figure 3. The choice of cam governed the type and amplitude of the wave form produced. Sine wave forms with amplitudes of ±5.5° and ±10° were used for these tests. The wave form is defined by the equation

$$\alpha = \alpha_m + A\sin(2\pi f t)$$

where A is the respective amplitude. The shaker system was powered by a 5-hp AC motor with variable line frequency controller. The useable oscillating frequency range was 0.1 - 2.0 Hz, with three frequencies used for this test: 0.6, 1.2, and 1.8 Hz.

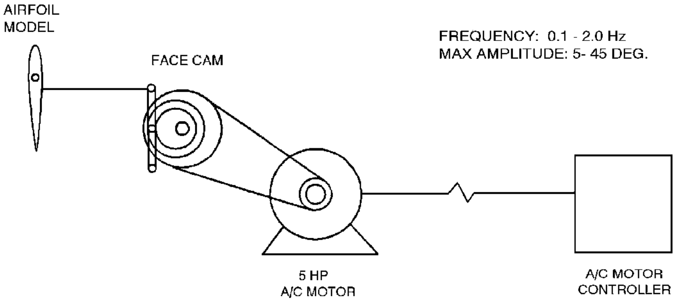

Figure 3. 3x5 wind tunnel oscillation system.

Model Details

A 457-mm (18-in) constant chord NACA 4415 airfoil model was designed by OSU/AARL personnel and manufactured by others. Figure 4 shows the airfoil section; the model measured coordinates are given in Appendix A. The model was made of a carbon composite skin over ribs and foam. The main load bearing member was a 38-mm (1.5-in) diameter steel tube which passed through the model quarter chord station.

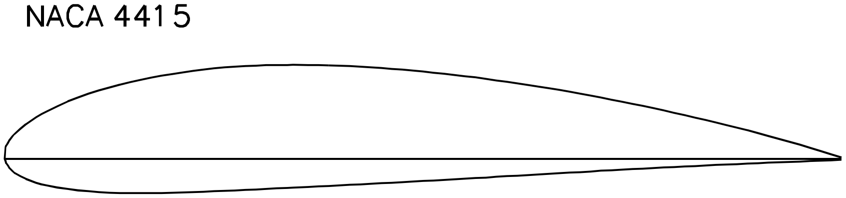

Figure 4. NACA 4415 airfoil section.

Ribs and end plates were used to transfer loads from the composite skin to the steel tube. The final surface was hand finished using templates to attain given coordinates within a tolerance of ±0.25-mm (±0.01-in). The completed model was measured by others using a contact type coordinate measurement machine. Measurements were made in English units and later converted to metric. Figure 5 shows the results of comparing measured-to-desired coordinates by calculating differences normal to the profiled surface at the mid-span station of the model. The spikes apparent near the trailing edge are due to the numerical methods used and are not real.

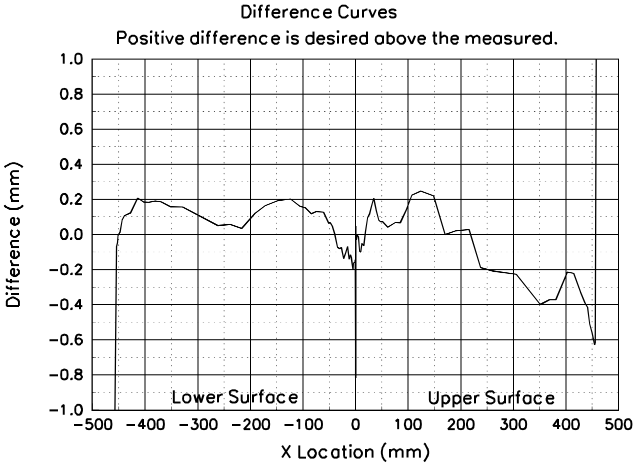

Figure 5. Measured-to-desired model coordinates difference curves.

To minimize pressure response times, which is important for the unsteady testing, the surface pressure tap lead-out lines had to be as short as possible. Consequently, a compartment was built into the model so pressure scanning modules could be installed inside the model. This compartment was accessed through a panel door fitted flush with the model contour on the lower (pressure) surface.

For test cases involving roughness, a standard, repeatable pattern with grit as roughness elements was desired. A roughness pattern was jointly developed by OSU/AARL and KENETECH Windpower personnel from a molded insect pattern taken from a wind turbine in the field by personnel at the University of Texas Permian Basin. The particle density was 5 particles per cm^2 (32 particles per square inch) in the middle of the pattern, thinning to 1.25 particles per cm^2 (8 particles per square inch) at the edge of the pattern. Figure 6 shows the pattern. To make a usable template, the pattern was repeatedly cut into a steel sheet 102-mm

(4-in) wide and 91-cm (3-ft) long with holes just large enough for one piece of grit. Based on average particle size from the field specimen, standard #40 lapidary grit was chosen for the roughness elements, giving k/c=0.0019 for a 457-mm (18-in) chord model.

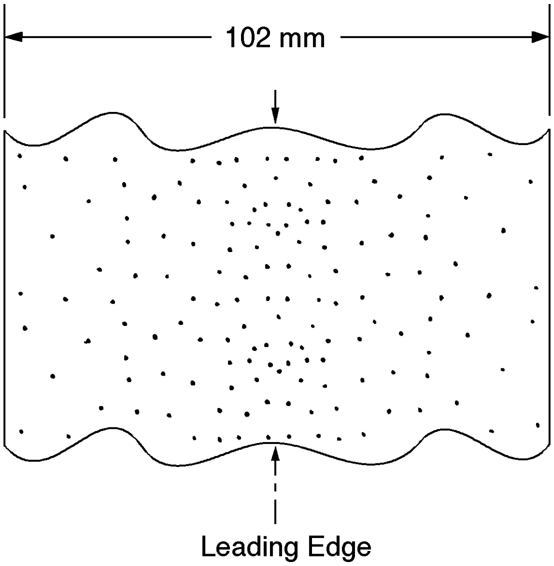

Figure 6. Roughness pattern.

To use the template, 102-mm (4-in) wide double-tack tape was applied to one side of the template and grit was poured and brushed from the opposite side. The tape was then removed from the template and transferred to the model. This method allowed the same roughness pattern to be replicated for any test.

Test Equipment and Procedures

Data Acquisition

Data were acquired and processed from 60 surface pressure taps, four individual tunnel pressure transducers, an angle of attack potentiometer, a wake probe position potentiometer, and a tunnel thermocouple. The data acquisition system included an IBM PC compatible 80486-based computer connected to a Pressure Systems Incorporated (PSI) data scanning system. The PSI system included a 780B Data Acquisition and Control Unit (DACU), 780B Pressure Calibration Unit (PCU), 81-IFC scanning module interface, two 2.5-psid pressure scanning modules (ESPs), one 20-in water column range pressure scanning module, and a 30-channel Remotely Addressed Millivolt Module (RAMM-30). Figure 7 is a schematic the data acquisition system.

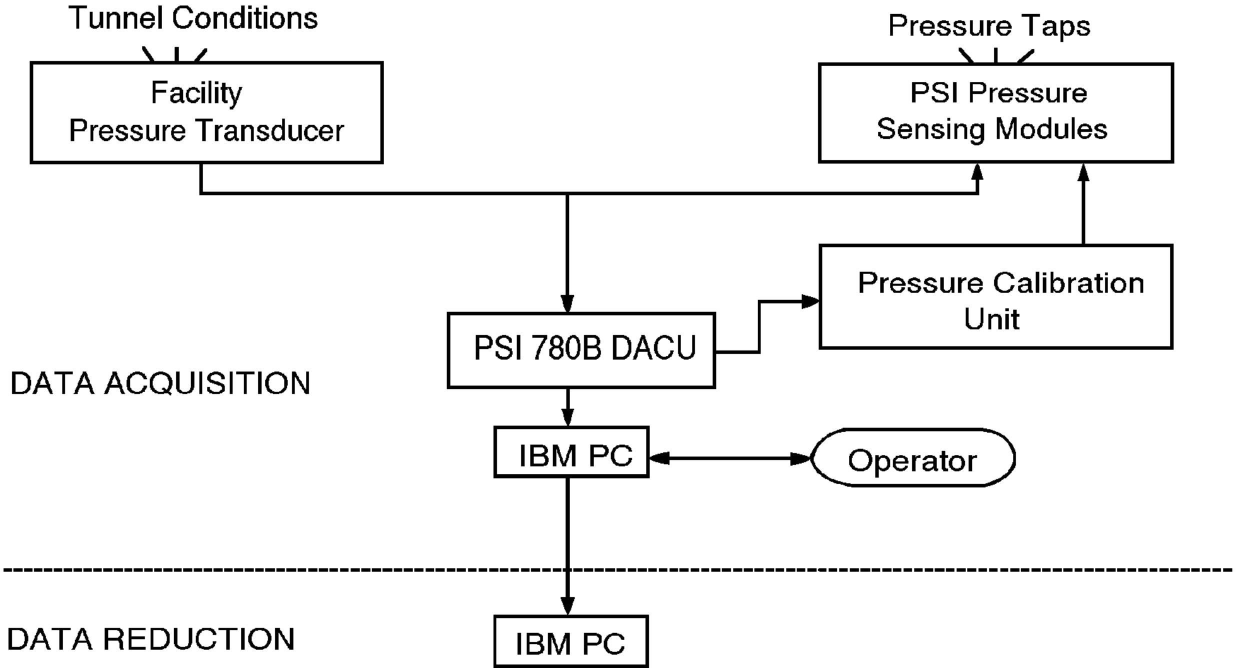

Figure 7. Data acquisition schematic.

Four individual pressure transducers read tunnel total pressure, tunnel north static pressure, tunnel south static pressure, and wake dynamic pressure. Before the test began, these transducers were bench calibrated using a water manometer to determine their sensitivities and offsets. Related values were entered into the data acquisition and reduction program so the transducers could be shunt resistor calibrated before each series of wind tunnel runs.

The rotary angle of attack potentiometer of 0.5% linearity was regularly calibrated during the tunnel pressure transducers shunt calibration. The angle of attack calibration was accomplished by taking voltage readings at known values of set angle of attack. This calibration method gave angle of attack readings within ±0.25° over the entire angle range. The wake probe position potentiometer was a linear potentiometer, and it was also regularly calibrated during the shunt calibration of the tunnel pressure transducers.

Calibration of the three ESPs was done simultaneously using the DACU and PCU. At operator request, the DACU commanded the PCU to apply known regulated pressures to the ESPs and read the output voltages from each integrated pressure sensor. From these values, the DACU calculated the calibration coefficients and stored them internally until the coefficients were requested by the controlling computer. This calibration was done several times during a run set because the ESPs were installed inside the model and their outputs tended to drift with temperature changes during a test sequence. Frequent on-line calibrations minimized the effect.

For steady state cases, the model would be set to angle of attack and the tunnel conditions were adjusted. At operator request, pressure measurements from the airfoil surface taps and all other channels of information were acquired and stored by the DACU and subsequently passed to the controlling computer for final processing. The angles of attack were always set in the same progression, from negative to positive values.

For model oscillating cases, the tunnel conditions were set while the model was stationary at the desired mean angle of attack. The 'shaker' would be started, and after approximately 10 seconds the model surface pressure and tunnel condition data were acquired. Generally, 120 data scans were acquired over three model oscillation cycles. Since surface pressures were scanned sequentially, the data rate was set so the model rotated through less than 0.50° during any data burst. Finally, due to the unsteady and complex nature of the pitch oscillation cases, model wake surveys (for drag) were not conducted.

Data Reduction

The data reduction routine was included as a section of the data acquisition program. This combination of data acquisition and reduction routines allowed data to be reduced on line during a test. By quickly reducing selected runs, integrity checks could be made to ensure the equipment was working properly and to allow timely decisions about the test matrix.

The ambient pressure was manually input into the computer and was updated regularly. This value, along with the measurements from the tunnel pressure transducers and the tunnel thermocouple, were used to calculate tunnel airspeed. As a continuous check of readings, the tunnel total and static pressures were read by both the tunnel individual pressure transducers and the 20-inch water column ESP.

A typical steady state datum point was derived by acquiring 10 data scans of all channels over a 10 second window at each angle of attack and tunnel condition. The reduction portion of the program processed each data scan to coefficients (C_p, C_l, $C_{m¼}$, and C_{dp}) using the measured surface pressure voltages, calibration coefficients, tap locations and wind tunnel conditions. All scan sets for a given condition were then ensemble averaged to provide one data set, and that data set was corrected for the effects of solid tunnel walls. All data were saved in electronic form.

Corrections due to solid tunnel sidewalls were applied to the wind tunnel data. As described by Pope and Harper (1966), tunnel conditions are represented by the following equations:

$$q = q_u(1+2\epsilon)$$

$$V = V_u(1+\epsilon)$$

$$R_e = R_{e_u}(1+\epsilon)$$

Airfoil aerodynamic characteristics are then corrected by:

$$\alpha = \alpha_u + \frac{57.3\sigma}{2\pi}\left(C_{l_u} + 4C_{m\frac{1}{4}_u}\right)$$

$$C_l = C_{l_u}(1-\sigma-2\epsilon)$$

$$C_{m_{\frac{1}{4}}} = C_{m_{\frac{1}{4}_u}} (1 - 2\epsilon) + \frac{\sigma C_l}{4}$$

$$C_d = C_{d_u} (1 - 3\epsilon_{sb} - 2\epsilon_{wb})$$

where

$$\sigma = \frac{\pi^2}{48} \left(\frac{c}{h}\right)^2$$

$$\epsilon = \epsilon_{sb} + \epsilon_{wb}$$

$$\epsilon_{sb} = \Lambda \sigma$$

$$\epsilon_{wb} = \frac{c}{h4} C_{d_u}$$

Model wake data were taken for steady state cases when the wake could be completely traversed. Pressures were acquired from a pitot-static probe that was connected to measure incompressible dynamic pressure through the wake. These pressure measurements were used to calculate drag coefficient using a form of the Jones equation derived from Schlichting (1979):

$$C_{dw} = \frac{2}{c} \int \sqrt{\frac{q_w}{q_\infty}} \left(1 - \sqrt{\frac{q_w}{q_\infty}} \right) dy$$

This equation assumes that static pressure at the measurement site is the free-stream value. The integration was done automatically except the computer operator chose the end points of the integration from a plot of the wake survey displayed on the computer screen.

For pitch oscillation cases, model surface pressures were reduced to pressure coefficient form with subsequent integrations and angle of attack considerations giving lift, moment, and pressure drag coefficients. The wind tunnel was not calibrated for unsteady model pitch conditions; therefore, the unsteady pressure data were not corrected for any possible effects due to time dependent pitching or solid tunnel walls. Also, for these cases, the wind tunnel contraction pressures (used for steady state cases) could not be used to calculate instantaneous freesteam conditions due to slow response. The tunnel conditions were obtained from a total pressure probe and the average of opposing static taps in the test section entrance. This gave nearly instantaneous flow pressure conditions for the pitching frequencies used.

Test Matrix

The test was designed to study steady state and unsteady pitch oscillation data. Steady state data were acquired at Reynolds numbers of 0.75, 1, 1.25, and 1.5 million with and without LEGR. Refer to the tabular data in Appendix B for the actual Reynolds number for each angle of attack for the steady state data. The angle of attack increment was two degrees when $-10° < \alpha < +10°$ or $+20° < \alpha < +40°$ and one degree when $+10° < \alpha < +20°$. Wake surveys were conducted to find total airfoil drag over an approximate angle of attack range of -10° to +10°. Unsteady data were taken for Reynolds numbers of 0.75, 1, 1.25, and 1.5 million. Sine wave cams with amplitudes ±5.5° and ±10° were used for pitch oscillations, and the mean angles for both these amplitudes were 8°, 14°, and 20°. For all these conditions, the frequencies were varied to 0.6, 1.2, and 1.8 Hz. All data points for the unsteady cases were acquired for both clean and LEGR cases.

Results and Discussion

The NACA 4415 airfoil model was tested under steady state and pitch oscillation conditions. A brief discussion of the results follows, beginning with a comparison of experimental data and computational predictions.

Comparison with Theory

The wind tunnel steady state data collected in this study were compared with computed predictions made using the North Carolina State Airfoil Analysis Code. This analysis code has proven to be accurate for moderate angles of attack. The analysis was made with specifications set to allow free transition from laminar to turbulent flow, and the pressure distribution comparisons were matched to the same angle of attack as the wind tunnel cases.

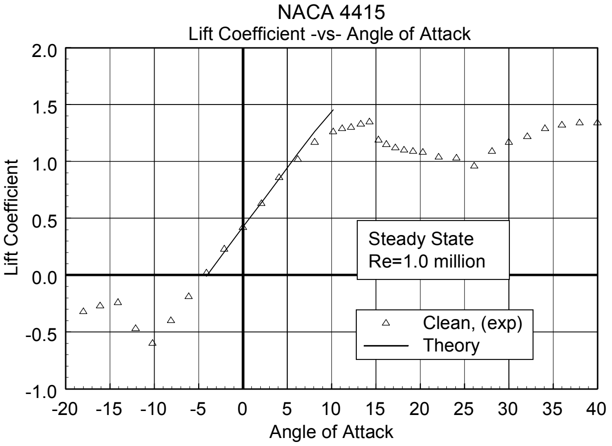

Figure 8. Comparison with theory, C_l vs α.

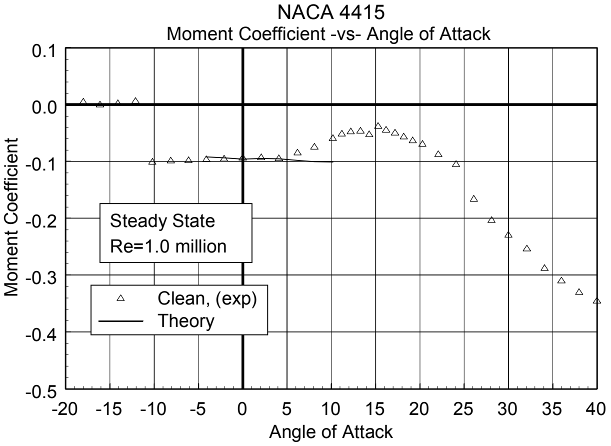

Figure 9. Comparison with theory, C_m vs α.

Figure 8 shows the lift coefficient versus angle of attack for the 1 million Reynolds number case. For moderate angles of attack, where the analysis code is valid, the comparison showed good agreement. The pitching moment about the quarter chord, figure 9, also showed good agreement for angles of attack from -5° to 5°. The pressure distributions shown in figures 10 and 11 are for angles of attack of 0° and 6°, respectively, and include clean and LEGR wind tunnel data as compared to computed free transition pressure

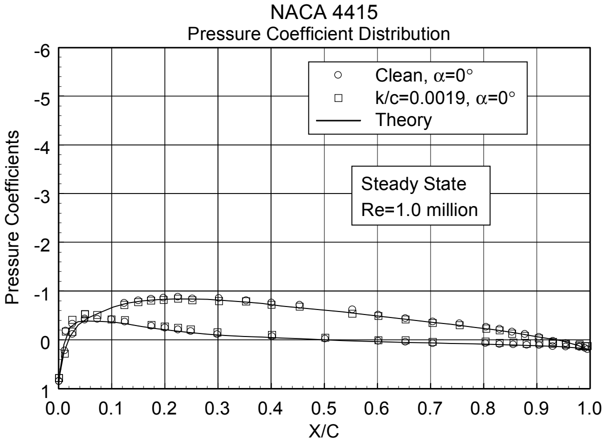

Figure 10. Comparison with theory,
C_p vs x/c, α=0°.

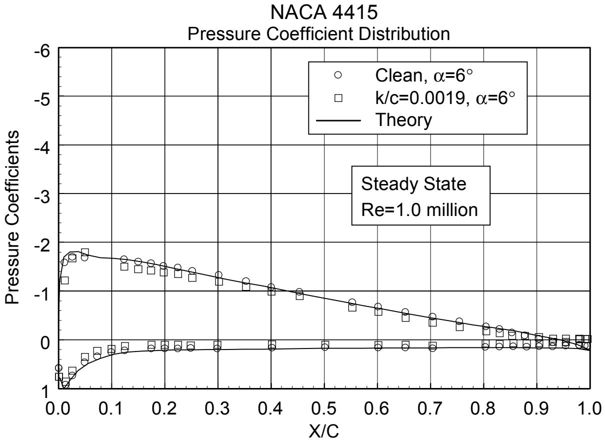

Figure 11. Comparison with theory,
C_p vs x/c, α=6°.

distributions. For both angles of attack, there was excellent correlation between the experimental and predicted values.

Steady State Data

The NACA 4415 airfoil model was tested at four Reynolds numbers at nominal angles of attack from -10° to +40°. Figures 12 and 13 show lift coefficients for all the test Reynolds numbers for a clean model and with LEGR applied, respectively. The maximum positive lift coefficient for the clean cases was about 1.38 and about 1.11 for the LEGR cases, a 20% reduction. The stall characteristic was similar for both clean and LEGR cases, with indications of stall occurring at lower angles of attack in the higher Reynolds number cases. This was an unexpected result that is not yet understood. For the clean cases, surface pressure taps may have locally affected the boundary layer, resulting in greater energy losses at the higher Reynolds numbers. Fixed grit roughness size and thinning boundary layer with increasing Reynolds number may explain the effect for LEGR cases. Finally, the average lift curve slope for clean data was about 0.104; it was slightly lower for the LEGR case at 0.095. The associated average lift coefficients at zero angle of attack are 0.42 for the clean case and 0.36 for the LEGR case.

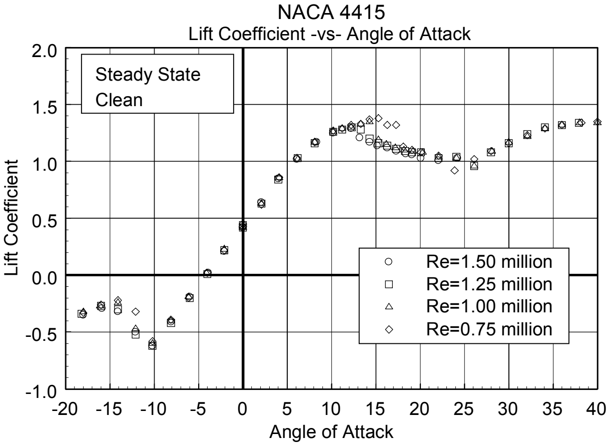

Figure 12. C_l vs α, clean.

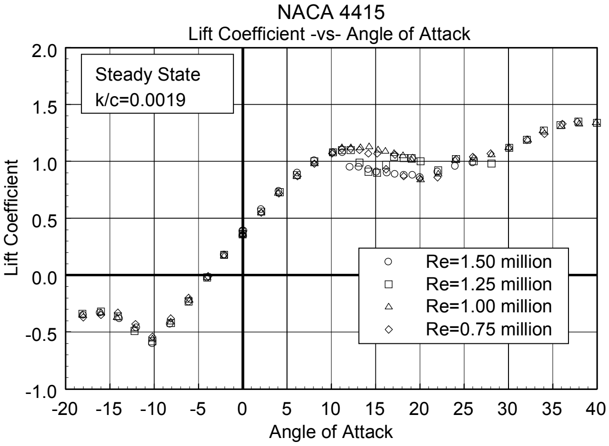

Figure 13. C_l vs α, LEGR, k/c=0.0019.

Figure 14 shows the pitching moment about the quarter chord for the clean cases, and figure 15 shows the same for the LEGR cases. The LEGR data had slightly more positive pitching moment at low angles of attack. The moment coefficient about the quarter chord for the 1 million Reynolds number, was -0.0967 for the clean case and -0.0842 for the LEGR case.

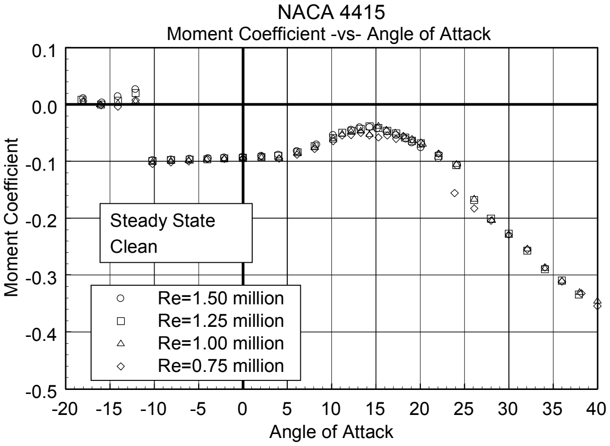

Figure 14. C_m vs α, clean.

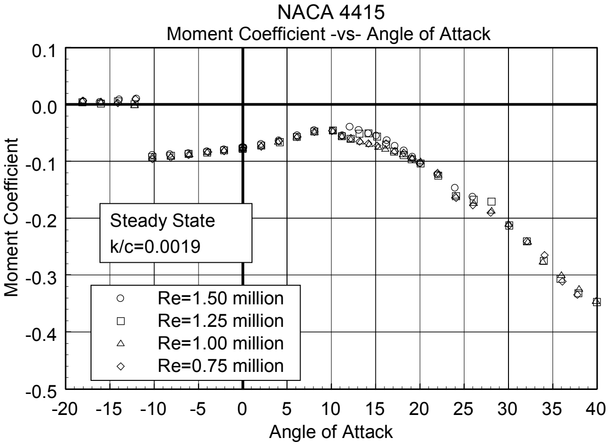

Figure 15. C_m vs α, LEGR, k/c=0.0019.

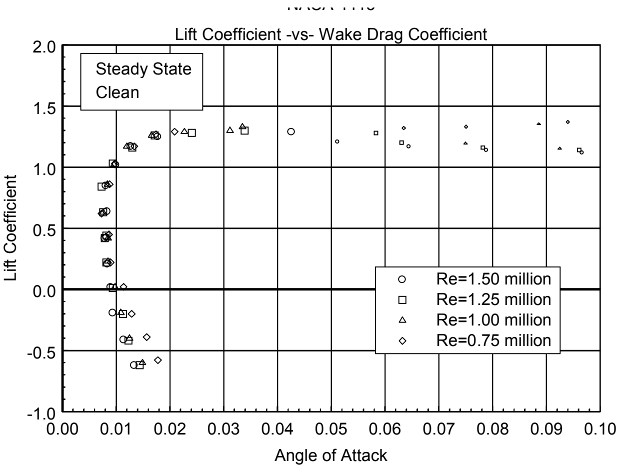

Figure 16. Clean, drag polar.

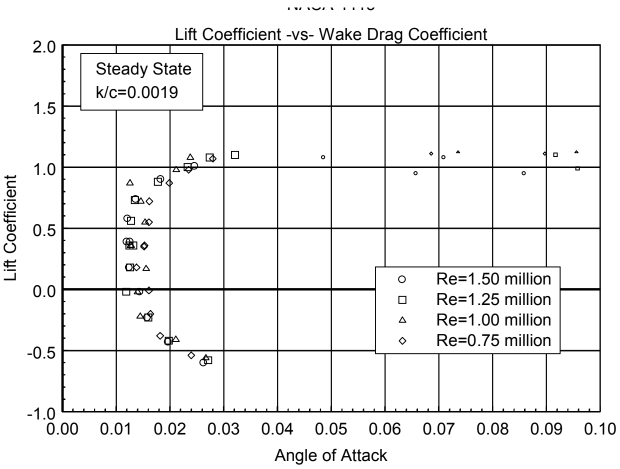

Figure 17. LEGR, drag polar.

Total wake drag data were obtained for both the clean and LEGR cases over a nominal angle of attack range of -10° to 10°. A pitot-static probe was used to describe the wake profile. This method is reliable when there is relatively low turbulence in the wake flow; therefore, only moderate angles of attack have reliable total drag coefficient data. At angles of attack other than those where a wake survey was taken, surface pressure data were integrated to give C_{dp} and are shown in the drag polars as small symbols. The model clean drag data are shown in figure 16, and the LEGR case is shown in figure 17. At 1 million Reynolds number, minimum drag coefficient for the clean cases was measured as 0.0076, and 0.0127 for LEGR, a 67% increase. The general effect of LEGR is to increase drag consistently through most angles of attack.

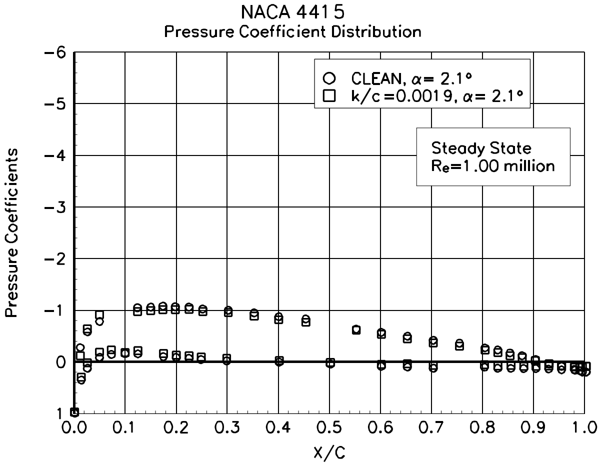

Figure 18. Pressure distribution, α=2.1°.

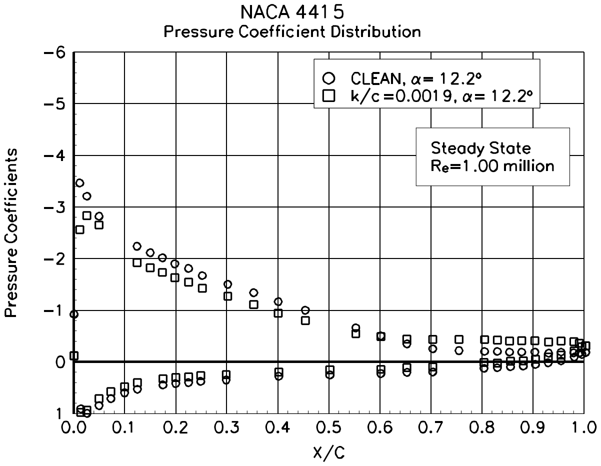

Figure 19. Pressure distribution, α=12.2°.

Two examples of the surface pressure distributions are shown in figures 18 and 19 for 2.1° and 12.2°, respectively, for 1 million Reynolds number. At the angles of attack close to zero degrees, the effect of LEGR did not appear to significantly affect the pressure distribution compared to the clean case distribution. However, there was an effect apparent in the lift coefficient with values of 0.55 for the LEGR case and 0.63 for the clean case. For the higher angle of attack case, figure 19, the effect of LEGR was to reduce the magnitude of the pressure peak from -3.5 to -2.9 and generally bring all surface pressures closer to freestream. Also, flow separation occured earlier in the LEGR case. The net effect was a reduction in lift coefficient from 1.35 to 1.13, a 16% decrease.

Unsteady Data

Unsteady experimental data were obtained for the NACA 4415 airfoil model undergoing sinusoidal pitch oscillations. As mentioned earlier, no attempt was made to calibrate the wind tunnel for the unsteady oscillating model conditions; the steady state tunnel calibration was used to set the flow conditions while the model was stationary at its mean angle of attack. The use of the unsteady data should be limited to comparisons with other models tested in this same facility and can be used to detect possible trends. A comprehensive set of test conditions was used to describe unsteady behavior of an airfoil, including two angle of attack amplitudes, ±5.5° and ±10°; four Reynolds numbers, 0.75, 1, 1.25, and 1.5 million; three pitch oscillation frequencies, 0.6, 1.2, and 1.8; and three mean angles of attack, 8°, 14°, and 20°.

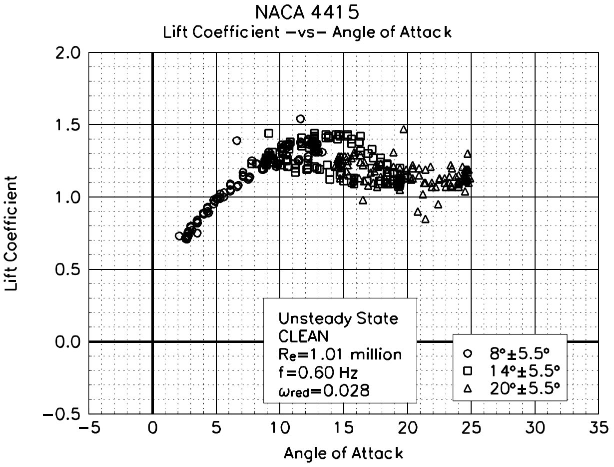

Figure 20. Clean, C_l vs α, ω_{red}=0.028, ±5.5°.

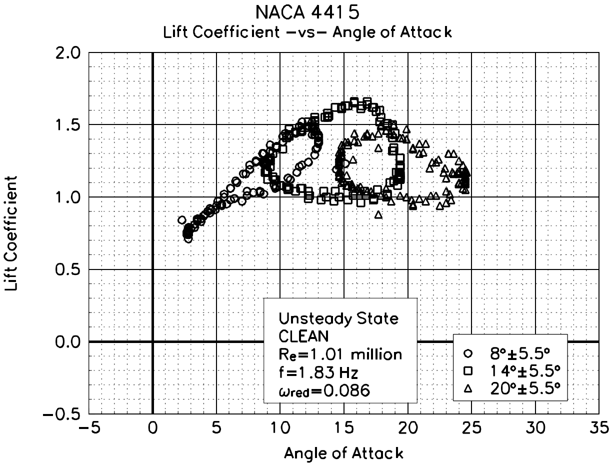

Figure 21. Clean, C_l vs α, ω_{red}=0.086, ±5.5°.

Figure 20 shows the lift coefficient versus angle of attack for the ±5.5° amplitude, model clean case, at reduced frequency of 0.028 and 1 million Reynolds number. Note that all three mean angles of attack are plotted on the same figure. The maximum pre-stall lift coefficient for this case was near 1.44 and occured when the airfoil was traveling with the angle of attack increasing. In contrast, when the model was traveling through decreasing angles of attack, the stall recovery was delayed and a hysteresis behavior was exhibited in the lift coefficient that can be seen throughout all the unsteady data. To obtain some measure of this hysteresis behavior, the lift coefficient on the "return" portion of the curve, at the angle of attack where maximum lift coefficient occurs, can be used. For the case discussed here the hysteresis lift coefficient was 1.21, a 16% decrease from the 1.44 unsteady maximum value. By comparison, the steady state maximum lift coefficient was 1.35. At higher reduced frequency of 0.086, the hysteresis behavior was more pronounced, as seen in figure 21. In addition to greater hysteresis, the maximum lift coefficient was increased to about 1.66, a 23% increase over the steady state value. The corresponding hysteresis lift coefficient was 1.08. This significant difference between steady state behavior and unsteady hysteresis behavior is a main reason that unsteady testing should be required for airfoils used in wind turbine applications.

The pitching moment shown in figures 22 and 23 corresponds to the same conditions as the two lift coefficient plots previously discussed. Hysteresis behavior was indicated but it was not as apparent as in the lift coefficient plots. However, the higher reduced frequency case did show more hysteresis than the lower reduced frequency case. For reference, the steady state maximum lift occured near 14° angle of attack, and the steady state pitching moment at this maximum lift point is -0.0526. In comparison, when the airfoil was undergoing pitch oscillation for the lower frequency, pitching moment varied from -0.0593 to -0.0310 (at the angle of attack where maximum lift occurs); a 13% increase to a 41% decrease in magnitude from the steady

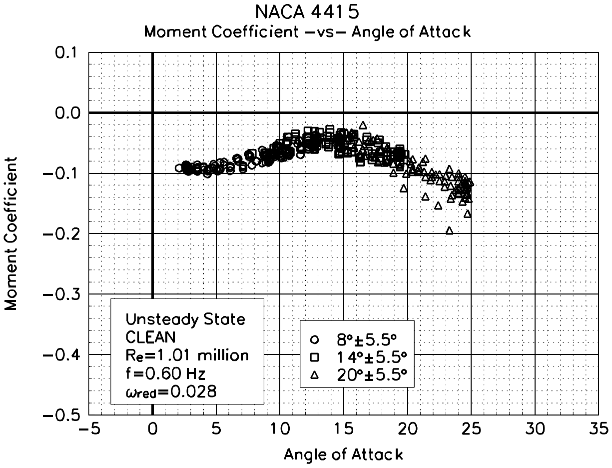

Figure 22. Clean, C_m vs α, ω_{red}=0.028, ±5.5°.

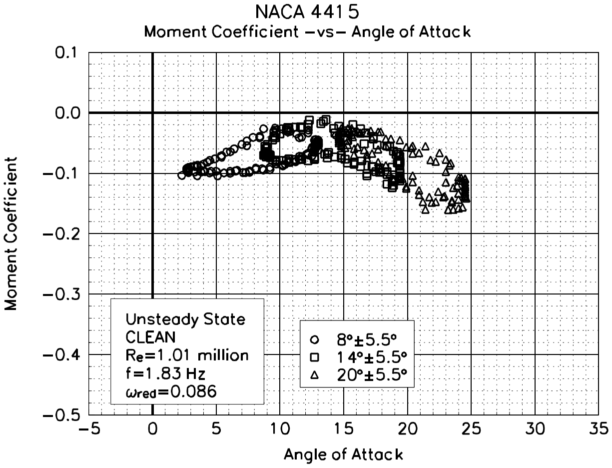

Figure 23. Clean, C_m vs α, ω_{red}=0.086, ±5.5°.

state value. Note the angle of attack where the maximum lift coefficient occured does not necessarily show the greatest hysteresis behavior but does give a relative indication of the effect.

Compared to the clean data, the application of LEGR reduces the maximum lift coefficient in the pitch oscillation cases. Lift coefficient versus angle of attack with LEGR applied is shown in figure 24 for the 0.028 reduced frequency case. The 0.087 reduced frequency case is shown in figure 25. Both correspond to the same run conditions that were described earlier for the clean cases. For the lower reduced frequency, the maximum unsteady lift coefficient was reduced to 1.17 from the corresponding clean case of 1.44, a 19% decrease. Hysteresis behavior was apparent at this frequency and was of similar order to the clean case; the corresponding hysteresis lift coefficient was 0.88 when LEGR is applied. In contrast, the higher frequency LEGR case had a maximum lift coefficient of 1.39 while the model was increasing in angle of attack, and the corresponding decreasing angle of attack lift coefficient was 0.72. In this case, the application of LEGR gave a greater hysteresis loop behavior than the clean case at the same run conditions.

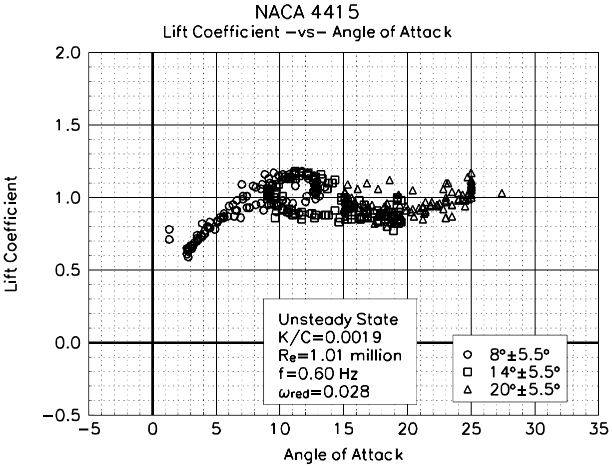

Figure 24. LEGR, C_l vs α, ω_{red}=0.028, ±5.5°.

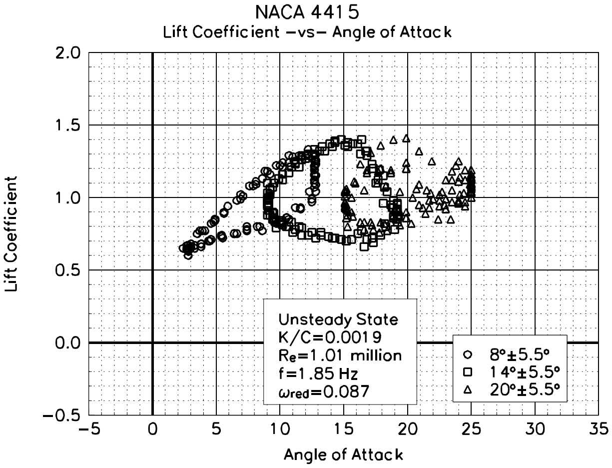

Figure 25. LEGR, C_l vs α, ω_{red}=0.087, ±5.5°.

The pitching moment coefficient shown in figure 26 is for 0.028 reduced frequency with LEGR applied. At the angle of unsteady maximum lift, the pitching moment ranged from -0.0508 to -0.0267, while the steady state LEGR pitching moment was -0.0617 at the steady state stall angle of attack (12.2°). The higher reduced frequency of 0.087 with LEGR applied is shown in figure 27. As was seen with the lift coefficient, pitching moment hysteresis was more apparent at the higher reduced frequency than in the corresponding clean case

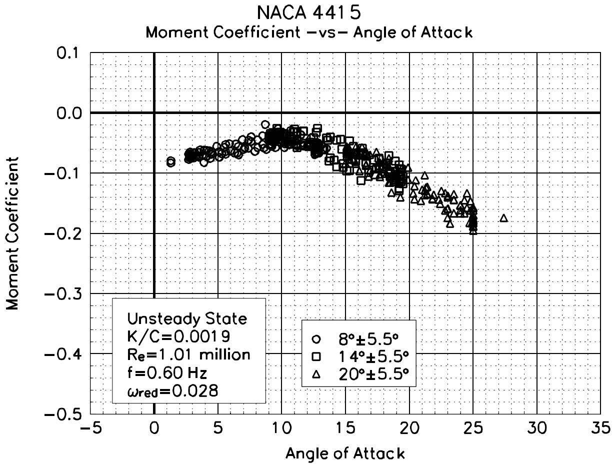

Figure 26. **LEGR, C_m vs α, ω_{red}=0.028, ±5.5°.**

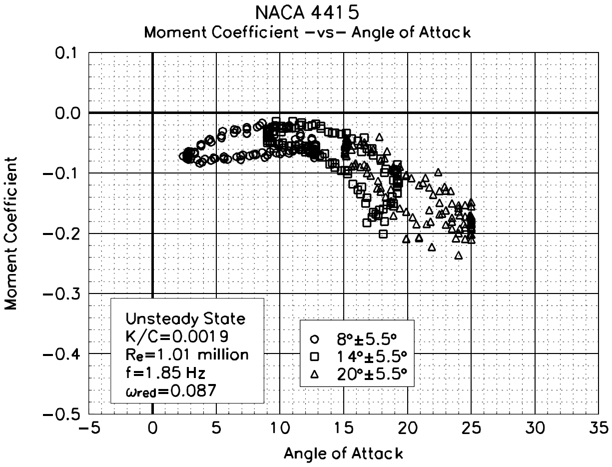

Figure 27. **LEGR, C_m vs α, ω_{red}=0.087, ±5.5°.**

(shown in figure 23). Unsteady maximum lift angle of attack for this reduced frequency occured at 14.3°, and the pitching moment ranged from -0.0841 to -0.0341 at that angle. Throughout the higher angle of attack range, the magnitude of the unsteady pitching moment can be much different than that resulting from steady state clean conditions (steady state pitching moment at maximum lift was -0.0526). It seems these differences can have an impact on the fatigue life predictions of a wind turbine system.

In addition to the ±5.5° unsteady experimental data, ±10° unsteady data were obtained with and without LEGR. The data were taken at 1 million Reynolds number using the same mean angles and frequencies as the 5.5° amplitude cases. Figures 28 and 29 show the ±10°, unsteady, clean, lift coefficient for the reduced frequencies of 0.029 and 0.089, respectively. The maximum lift coefficient for the lower frequency was 1.55 and occured, as expected, when the airfoil was traveling through increasing angles of attack. The hysteresis lift coefficient (at 14.9°) was 1.07. At the higher reduced frequency, the maximum lift coefficient occured at a higher angle of attack, 19.4°, and was 1.95. The corresponding hysteresis lift coefficient was 0.92. The difference between the maximum lift coefficient and the hysteresis lift coefficient indicates a much greater hysteresis response than experienced for the lower reduced frequency. The steady state, clean, maximum lift coefficient was 1.35; therefore, the unsteady behavior created lift coefficients up to 44% higher than the steady state conditions.

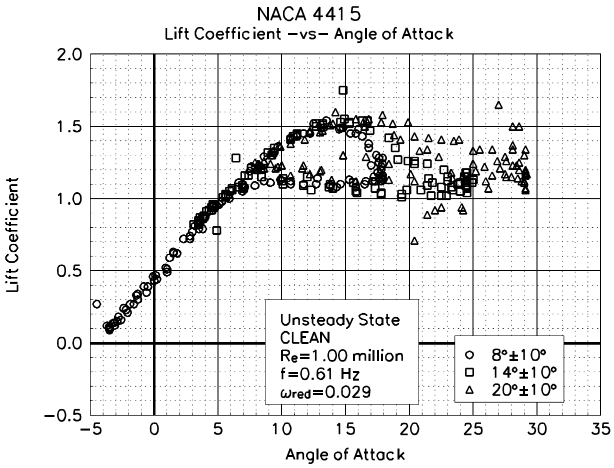

Figure 28. **Clean, C_l vs α, ω_{red}=0.029, ±10°.**

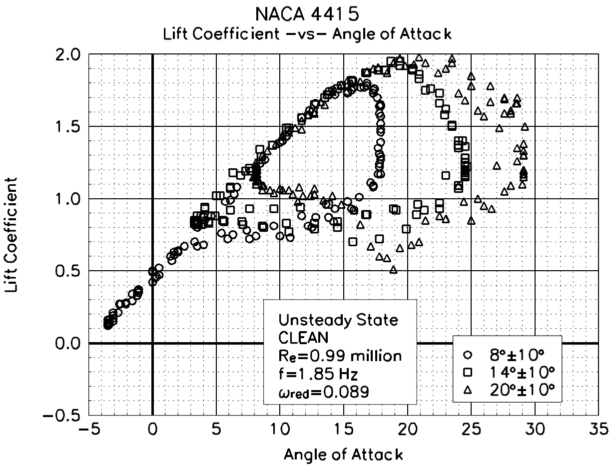

Figure 29. **Clean, C_l vs α, ω_{red}=0.089, ±10°.**

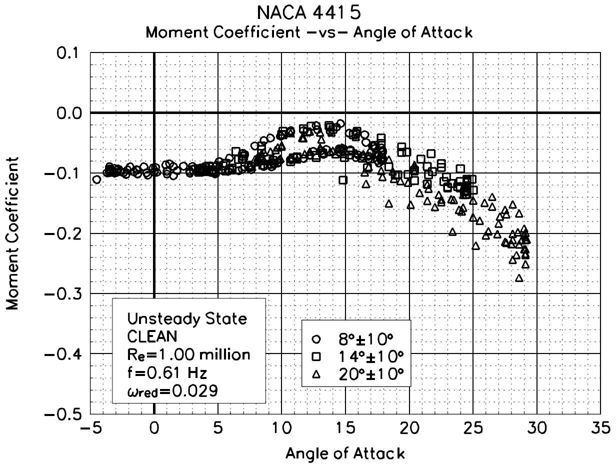

Figure 30. Clean, C_m vs α, ω_{red}=0.029, ±10°.

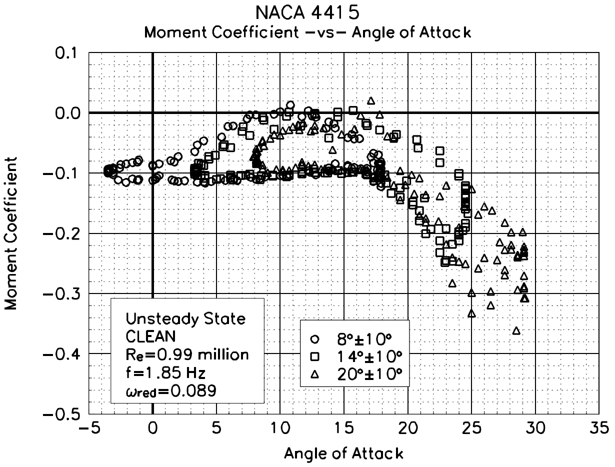

Figure 31. Clean, C_m vs α, ω_{red}=0.089, ±10°.

The quarter chord pitching moments with the same reduced frequencies as the lift coefficient cases are shown in figures 30 and 31. The hysteresis behavior observed in the lift coefficient plots is also reflected in this pitching moment data. Near the maximum lift angle, 14.9° for the lower frequency, the pitching moment coefficient ranged from -0.0743 to -0.0276; the 0.089 reduced frequency case had maximum lift near 19.4° and pitching moment ranged from -0.1399 to -0.0358. The higher reduced frequency again showed large hysteresis loops for all three mean angles of attack. In comparison, the steady state pitching moment was -0.0526 near the steady state maximum lift coefficient angle of attack of 14°.

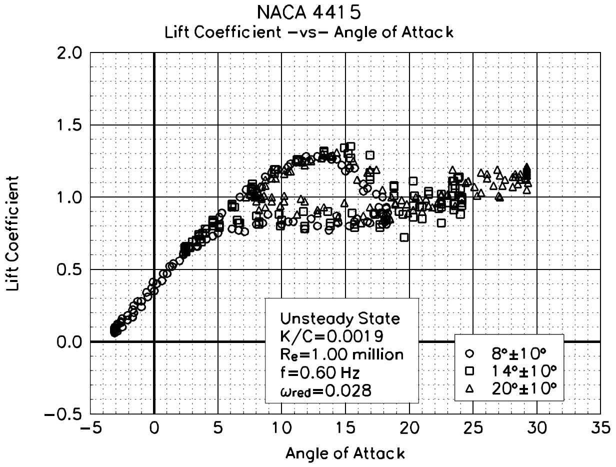

Figure 32. LEGR, C_l vs α, ω_{red}=0.028, ±10°.

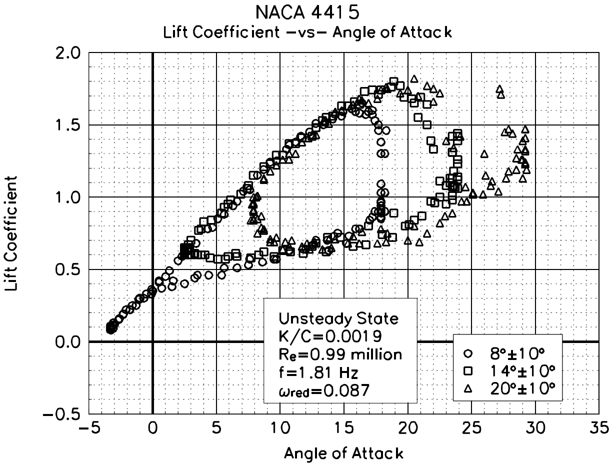

Figure 33. LEGR, C_l vs α, ω_{red}=0.087, ±10°.

The application of LEGR degraded the lift performance of the airfoil, as would be expected from the results discussed previously. The LEGR lift coefficient data for reduced frequencies of 0.028 and 0.087 are shown in figures 32 and 33, respectively. The maximum lift coefficient was reduced to 1.34 from 1.55 for the low frequency clean case. Although there was a reduction, this value was still significantly higher than the LEGR steady state case, which had a maximum lift coefficient of 1.13 at 14.3° angle of attack. The higher reduced frequency had a maximum lift coefficient of 1.80, which occured near 19° angle of attack. The corresponding lift coefficient at 19° for the airfoil traveling with decreasing angle of attack was 0.71, a 60% reduction from the maximum.

Figures 34 and 35 show the corresponding pitching moment coefficients for the reduced frequencies of 0.028 and 0.087. For the 0.028 reduced frequency case, the pitching moment varied from -0.1119 to -0.0488 at 14.9° (where the maximum lift occured). The hysteresis behavior was more pronounced for the higher reduced frequency case, where the range of pitching moments at the maximum lift angle of 18.9° was from -0.2082 to -0.0625. These values can then be compared to the steady state LEGR value of -0.0617.

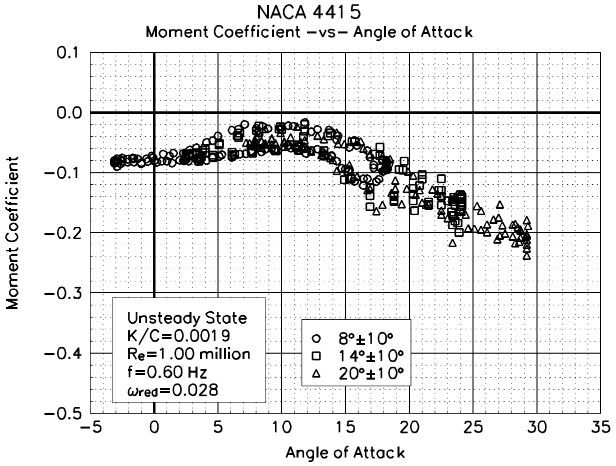

Figure 34. LEGR, C_m vs α, ω_{red}=0.028, ±10°.

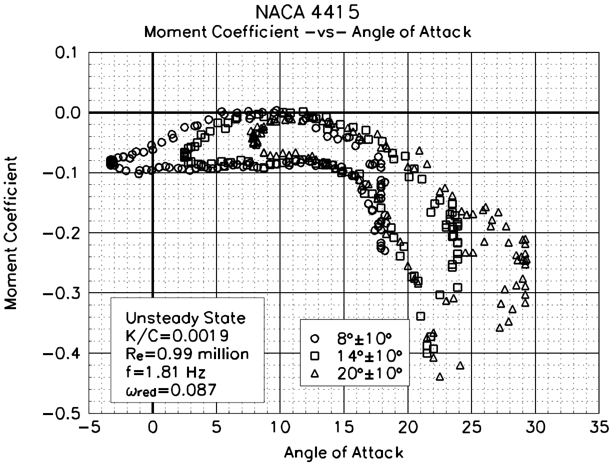

Figure 35. LEGR, C_m vs α, ω_{red}=.087,±10°

Although all the unsteady data have not been discussed here, the previous discussion included typical examples of the wind tunnel data. The remaining cases of the ±5.5° and ±10° oscillation data for all the Reynolds numbers are included in Appendix C.

The following four unsteady pressure distributions show examples of the data used to calculate the lift, pressure drag, and pitching moment coefficients. Figure 36 shows the distribution for a clean model with a reduced frequency of 0.028, mean angle of attack of 8°, and ±10° pitch oscillation. For plotting clarity, the model pressures were 'unwrapped' about the trailing edge. The upper surface pressures are depicted on the right side of the surface plot; lower surface values are on the left. The trailing edge is at the midpoint of the x-axis with the leading edge at each extreme. The time scale corresponds to angle of attack. For this case, the separated flow area is defined by the irregular, rough areas of the upper surface portion of the plot. The lower surface stayed attached through all airfoil oscillations. Figure 37 shows the LEGR case for the same test conditions as the previous figure. In this case, the pressure peaks were not as high as for the clean

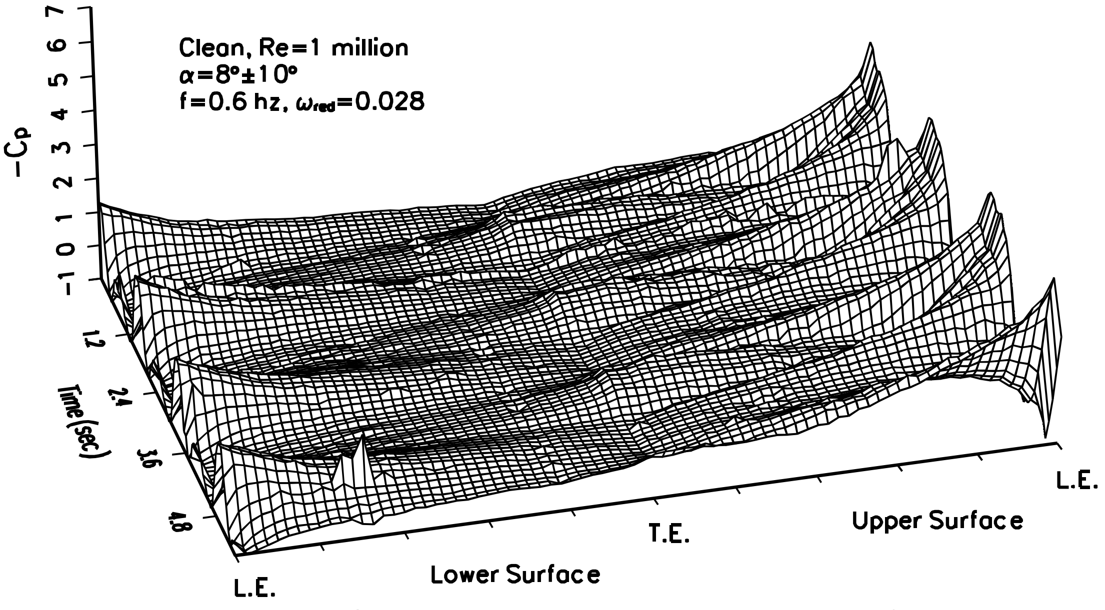

Figure 36. Clean, unsteady pressure distribution, ±10°.

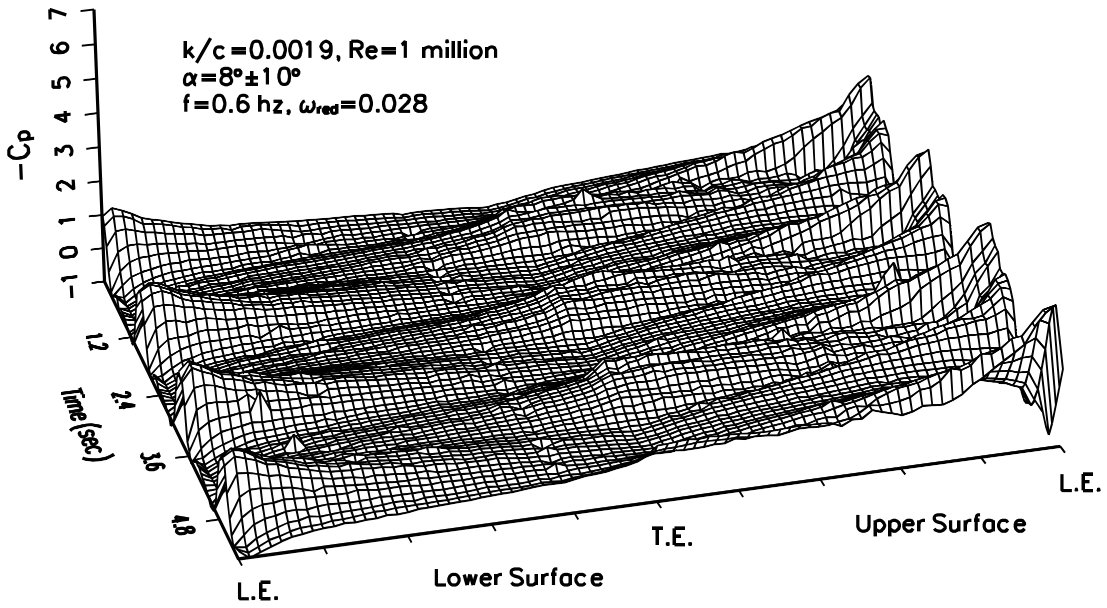

Figure 37. LEGR, unsteady pressure distribution, ±10°.

case, and the stall behavior was more pronounced. Also, each case showed the effect of a bad tap on the lower surface near the trailing edge; it is indicated by the line of pressure irregularity. This lower response tap did not significantly affect the integrated results and remained in the reduction process.

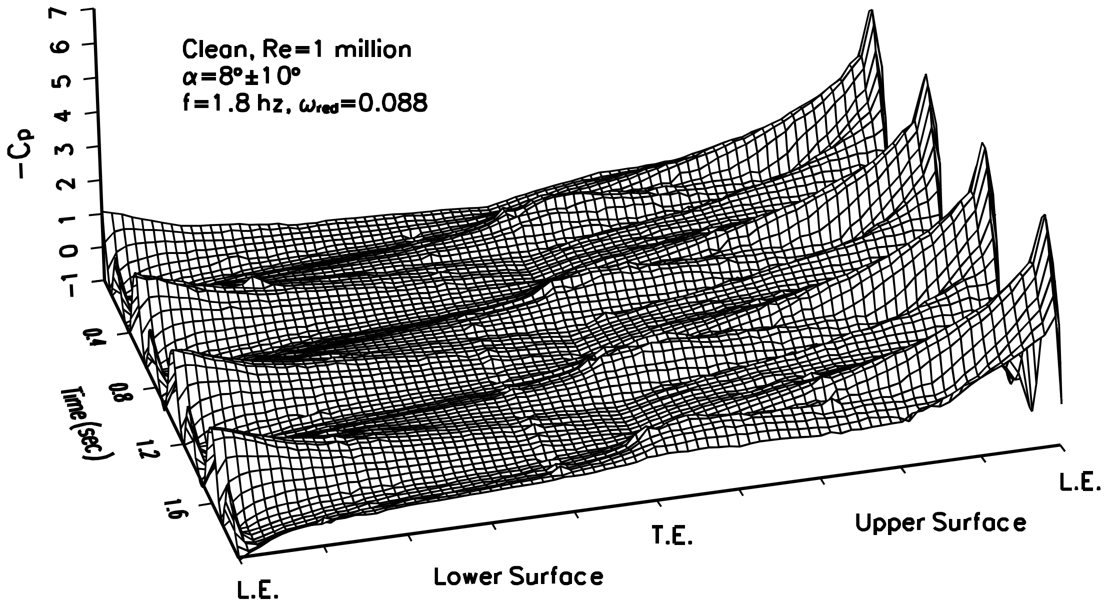

Figure 38. Clean, unsteady pressure distribution, ±10°.

Figure 38 shows the same clean run conditions at a higher frequency of pitch oscillation. At this higher frequency, the character of the flow was similar to the previous clean case. Noticeably different, however, are the larger magnitude pressure peaks. This was reflected in the maximum lift coefficient results, with values of 1.95 for this case and only 1.52 for the lower frequency case.

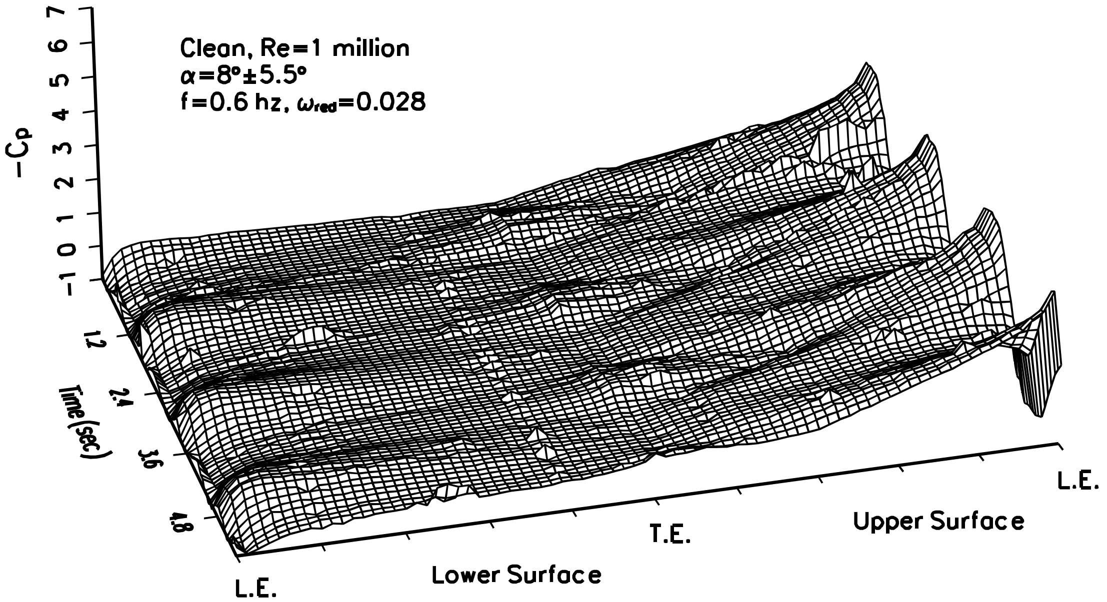

Figure 39. Clean, unsteady pressure distribution, ±5.5°.

Figure 39 shows the smaller mean angle for the clean case at the same conditions indicated above. The structure is different from the previous figure because less of the upper surface flow is separated, the consequence of lower angles of attack.

Summary of Results

A NACA 4415 airfoil model was tested under steady state and pitch oscillation conditions. Baseline tests were made while the model was clean, and then corresponding tests were conducted with LEGR applied.

A summary of the steady state aerodynamic parameters is shown in table 1. As observed, the application of LEGR reduced the maximum lift of the airfoil up to 19%, and the minimum drag coefficient increased more than 50%. LEGR also affected the zero lift pitching moment coefficient by reducing the magnitude by an average of 13%.

Table 1. NACA 4415, Steady State Parameters Summary.

Grit Pattern	Re x 10^{-6}	C_{lmax}	C_{dmin}	C_{mo}
Clean	0.75	1.38 @ 15.3°	0.0073	-0.0962
k/c=0.0019	0.75	1.11 @ 11.2°	0.0138	-0.0835
Clean	1.00	1.35 @ 14.3°	0.0076	-0.0967
k/c=0.0019	1.00	1.13 @ 14.3°	0.0127	-0.0842
Clean	1.25	1.30 @ 12.3°	0.0073	-0.0962
k/c=0.0019	1.25	1.10 @ 11.2°	0.0119	-0.0844
Clean	1.50	1.29 @ 12.2°	0.0079	-0.0947
k/c=0.0019	1.50	1.08 @ 10.2°	0.0120	-0.0827

Table 2. NACA 4415, Unsteady, Clean, ±5.5°.

ω_{red}	Re x 10^{-6}	f	C_{lmax}	α_{max}	$C_{l\ dec}$	$C_{m\ inc}$	$C_{m\ dec}$
0.037	0.75	0.59	1.52	16.8	1.11	-0.0941	-0.0338
0.076	0.75	1.21	1.65	16.5	1.00	-0.0744	-0.0202
0.116	0.75	1.85	1.75	15.7	1.05	-0.0899	-0.0301
0.028	1.01	0.60	1.44	12.7	1.21	-0.0593	-0.0310
0.056	1.01	1.21	1.57	16.3	1.05	-0.0897	-0.0381
0.086	1.01	1.83	1.66	15.8	1.08	-0.0833	-0.0459
0.022	1.26	0.61	1.45	12.7	1.22	-0.0632	-0.0402
0.044	1.26	1.18	1.54	14.8	1.09	-0.0748	-0.0341
0.069	1.26	1.85	1.61	16.3	1.05	-0.0942	-0.0395
0.019	1.51	0.60	1.43	14.3	1.13	-0.0645	-0.0338
0.037	1.50	1.19	1.50	14.3	1.14	-0.0610	-0.0370
0.056	1.51	1.81	1.57	14.8	1.03	-0.0705	-0.0321

The pitch oscillation data can be divided into two groups, the ±5.5° amplitude and ±10° amplitude oscillations, which show similar trends. For both ±5.5° and ±10°, the unsteady test conditions and the maximum lift coefficients are listed in tables 2, 3, 4, and 5. As the reduced frequency, which takes oscillation and tunnel speed into account, was increased, the maximum lift coefficient also increased. In addition, the hysteresis behavior became increasingly apparent with increased reduced frequency.

Table 3. NACA 4415, Unsteady, LEGR, ±5.5°.

ω_{red}	Re x 10^{-6}	f	C_{lmax}	α_{max}	$C_{l\ dec}$	$C_{m\ inc}$	$C_{m\ dec}$
0.038	0.76	0.61	1.23	14.3	0.83	-0.0991	-0.0400
0.073	0.76	1.17	1.37	14.3	0.72	-0.0971	-0.0334
0.116	0.76	1.85	1.50	16.2	0.80	-0.1274	-0.0556
0.028	1.01	0.61	1.17	11.1	0.88	-0.0508	-0.0267
0.056	1.01	1.19	1.26	13.7	0.81	-0.0793	-0.0340
0.087	1.01	1.85	1.39	14.3	0.72	-0.0841	-0.0341
0.023	1.26	0.61	1.21	11.7	0.97	-0.0700	-0.0403
0.046	1.25	1.21	1.30	13.8	0.87	-0.0907	-0.0388
0.068	1.25	1.83	1.39	13.8	0.82	-0.0899	-0.0212
0.019	1.51	0.61	1.18	11.8	0.98	-0.0705	-0.0350
0.038	1.50	1.21	1.21	13.3	0.86	-0.0764	-0.0258
0.057	1.50	1.83	1.25	13.2	0.76	-0.0766	-0.0307

Table 4. NACA 4415, Unsteady, Clean, ±10°.

ω_{red}	Re x 10^{-6}	f	C_{lmax}	α_{max}	$C_{l\ dec}$	$C_{m\ inc}$	$C_{m\ dec}$
0.039	0.74	0.61	1.66	15.4	1.18	-0.0812	-0.0679
0.076	0.74	1.18	1.91	17.9	0.54	-0.1018	-0.0692
0.118	0.74	1.83	2.05	18.4	0.73	-0.1168	-0.0899
0.029	1.00	0.61	1.55	14.9	1.07	-0.0743	-0.0276
0.057	0.99	1.18	1.77	16.6	0.88	-0.0831	-0.0495
0.089	0.99	1.85	1.95	19.4	0.92	-0.1399	-0.0358
0.023	1.24	0.61	1.51	14.5	1.09	-0.0747	-0.0257
0.046	1.24	1.21	1.67	16.8	0.95	-0.0893	-0.0241
0.070	1.23	1.83	1.88	17.9	0.97	-0.1064	-0.0265
0.019	1.49	0.60	1.51	14.8	1.06	-0.0709	-0.0364
0.038	1.49	1.21	1.65	17.0	1.01	-0.0895	-0.0348
0.058	1.49	1.83	1.77	18.4	0.96	-0.1129	-0.0448

As expected, the application of LEGR reduced the aerodynamic performance of the airfoil. The maximum lift coefficient was reduced by 15% - 20% for the ±5.5° case and 10% - 15% for the ±10° case. In addition to following the same trends as the clean, unsteady data discussed previously, the LEGR caused the hysteresis behavior to persist into lower angles of attack than in the clean cases. Overall, the unsteady wind tunnel data show hysteresis behavior that became more apparent with increased reduced frequency. The maximum unsteady lift coefficient could be up to 25% higher for the ±5.5° amplitude and up to 50% higher for the ±10° amplitude than the steady state maximum lift coefficient. Variation in the quarter chord pitching moment coefficient could be 40% greater than that indicated by steady state results. These findings indicate that it is important to consider the unsteady loading that will occur in wind turbine operation because steady state results can greatly underestimate the forces.

Table 5. NACA 4415, Unsteady, LEGR, ±10°.

ω_{red}	Re x 10^{-6}	ω	C_{lmax}	α_{max}	$C_{l\ dec}$	$C_{m\ inc}$	$C_{m\ dec}$
0.038	0.75	0.60	1.44	14.3	0.86	-0.0903	-0.0360
0.076	0.75	1.19	1.72	17.1	0.76	-0.1634	-0.0615
0.119	0.74	1.85	1.92	18.4	0.87	-0.1829	-0.0851
0.028	1.00	0.60	1.34	14.9	0.79	-0.1119	-0.0488
0.058	0.99	1.21	1.52	16.9	0.81	-0.1468	-0.0464
0.087	0.99	1.81	1.80	18.9	0.71	-0.2082	-0.0625
0.023	1.25	0.61	1.30	13.1	0.85	-0.0784	-0.0340
0.046	1.24	1.19	1.48	15.1	0.73	-0.1061	-0.0276
0.070	1.24	1.83	1.63	17.8	0.77	-0.1713	-0.0469
0.019	1.50	0.60	1.27	12.8	0.97	-0.0717	-0.0313
0.037	1.49	1.18	1.39	12.8	0.81	-0.0674	-0.0190
0.058	1.49	1.85	1.58	15.9	0.66	-0.1151	-0.0394

References

Pope, A., Harper, J.J. 1966. *Low Speed Wind Tunnel Testing*. New York, NY: John Wiley & Sons, Inc.

Schlichting, H. 1979. *Boundary Layer Theory*. New York, NY: McGraw-Hill Inc.

Smetana, F., Summey, D., et-al. 1975. *Light Aircraft Lift, Drag, Moment Prediction - a Review and Analysis.* North Carolina State University. NASA-CR2523.

Appendix A: Model and Surface Pressure Tap Coordinates

List of Tables Page

Table A1. NACA 4415 Measured Model Coordinates, 18 inch desired chord

Chord Station (in)	Upper Ordinate (in)		Chord Station (in)	Lower Ordinate (in)
-0.002	0.091		-0.002	0.091
0.000	0.138		0.000	0.039
0.002	0.151		0.002	0.028
0.005	0.174		0.004	0.012
0.009	0.196		0.009	-0.008
0.018	0.234		0.016	-0.035
0.050	0.320		0.045	-0.108
0.077	0.369		0.070	-0.155
0.135	0.450		0.131	-0.232
0.214	0.541		0.205	-0.297
0.315	0.641		0.304	-0.364
0.390	0.705		0.378	-0.405
0.478	0.772		0.466	-0.447
0.613	0.864		0.600	-0.499
0.746	0.945		0.731	-0.540
0.901	1.030		0.886	-0.580
1.052	1.103		1.035	-0.612
1.169	1.158		1.152	-0.633
1.363	1.240		1.345	-0.664
1.574	1.325		1.555	-0.693
1.740	1.386		1.721	-0.711
1.904	1.442		1.887	-0.725
2.037	1.486		2.018	-0.734
2.417	1.600		2.398	-0.752
2.969	1.725		2.950	-0.759
3.349	1.799		3.330	-0.757
3.808	1.872		3.789	-0.747
4.213	1.924		4.196	-0.734
4.891	1.987		4.876	-0.707

Table A1. NACA 4415 Measured Model Coordinates, 18 inch desired chord

Chord Station (in)	Upper Ordinate (in)	Chord Station (in)	Lower Ordinate (in)
5.836	2.031	5.821	-0.662
6.724	2.035	6.711	-0.616
7.503	2.010	7.492	-0.575
8.515	1.944	8.505	-0.520
9.368	1.863	9.360	-0.471
10.299	1.752	10.293	-0.417
12.066	1.479	12.937	-0.266
13.845	1.138	13.844	-0.219
14.531	0.984	14.535	-0.186
14.997	0.874	14.999	-0.164
15.863	0.653	15.503	-0.141
16.335	0.526	15.867	-0.124
16.828	0.391	16.308	-0.106
17.172	0.296	16.835	-0.081
17.384	0.235	17.302	-0.061
17.526	0.190	17.462	-0.053
17.694	0.147	17.620	-0.044
17.896	0.087	17.703	-0.041
17.946	0.071	17.782	-0.037
18.052	0.039	17.834	-0.033
		17.905	-0.030
		18.052	-0.019

End of Table A1

Table A2. NACA 4415, Surface Pressure Taps, Non-Dimensional Coordinates

Tap Number	Chord Station	Ordinate
1	1.0035	-0.0001
2	0.9958	-0.0015
3	0.9807	-0.0032
4	0.9549	-0.0044
5	0.9298	-0.0056
6	0.9047	-0.0067
7	0.8809	-0.0077
8	0.8559	-0.0087
9	0.8296	-0.0099
10	0.8039	-0.0109
11	0.7537	-0.0132
12	0.7041	-0.0159
13	0.6533	-0.0188
14	0.6024	-0.0217
15	0.5545	-0.0244
16	0.5021	-0.0274
17	0.4024	-0.0327
18	0.2989	-0.0379
19	0.2490	-0.0400
20	0.2250	-0.0408
21	0.2000	-0.0413
22	0.1755	-0.0418
23	0.1493	-0.0417
24	0.1252	-0.0411
25	0.1001	-0.0395
26	0.0735	-0.0363
27	0.0496	-0.0319
28	0.0256	-0.0243

Table A2. NACA 4415, Surface Pressure Taps, Non-Dimensional Coordinates

Tap Number	Chord Station	Ordinate
29	0.0138	-0.0178
30	0.0010	0.0001
31	0.0119	0.0306
32	0.0257	0.0423
33	0.0498	0.0572
34	0.0749	0.0689
35	0.1010	0.0787
36	0.1242	0.0859
37	0.1502	0.0926
38	0.1741	0.0977
39	0.1981	0.1021
40	0.2254	0.1057
41	0.2523	0.1086
42	0.3016	0.1119
43	0.3528	0.1130
44	0.4007	0.1122
45	0.4538	0.1091
46	0.5027	0.1049
47	0.5534	0.0993
48	0.6016	0.0927
49	0.6533	0.0844
50	0.7040	0.0755
51	0.7548	0.0655
52	0.8046	0.0546
53	0.8299	0.0486
54	0.8538	0.0426
55	0.8783	0.0363
56	0.9041	0.0294
57	0.9309	0.0219

Table A2. NACA 4415, Surface Pressure Taps, Non-Dimensional Coordinates		
Tap Number	Chord Station	Ordinate
58	0.9551	0.0152
59	0.9800	0.0081
60	0.9908	0.0043
End of Table A2		

Appendix B: Steady-State Data

Integrated Coefficients and Pressure Distributions

List of Tables Page

List of Figures Page

Pressure Distributions, Steady State, Re = 1.5 million B-50

Table B1. NACA 4415, Clean, Re = 0.75 x 10^6

RUN	AOA	C_l	C_{dp}	$C_{m¼}$	Re x10^{-6}	C_{dw}
76	-20.1	-0.39	0.2599	0.0130	0.77	--
77	-18.0	-0.33	0.2208	0.0062	0.77	--
78	-16.0	-0.26	0.1840	-0.0015	0.77	--
79	-14.1	-0.22	0.1563	-0.0038	0.76	--
80	-12.1	-0.32	0.1501	0.0080	0.77	--
81	-10.2	-0.58	-0.0121	-0.1048	0.76	0.0178
82	-8.1	-0.39	-0.0133	-0.1015	0.76	0.0157
83	-6.1	-0.20	-0.0118	-0.1000	0.76	0.0129
84	-4.0	0.02	-0.0085	-0.0962	0.76	0.0114
85	-2.1	0.22	-0.0059	-0.0958	0.76	0.0090
86	0.0	0.43	-0.0012	-0.0958	0.75	0.0081
87	2.1	0.62	0.0055	-0.0912	0.76	0.0073
88	4.1	0.86	0.0122	-0.0951	0.76	0.0088
89	6.1	1.03	0.0192	-0.0882	0.76	0.0098
90	8.1	1.17	0.0283	-0.0780	0.76	0.0134
91	10.2	1.27	0.0412	-0.0645	0.75	0.0174
92	11.2	1.29	0.0455	-0.0545	0.76	0.0209
93	12.2	1.32	0.0635	-0.0538	0.75	--
94	13.3	1.33	0.0751	-0.0497	0.75	--
95	14.3	1.37	0.0940	-0.0544	0.77	--
96	15.3	1.38	0.1138	-0.0579	0.76	--
97	16.3	1.32	0.1184	-0.0545	0.77	--
98	17.3	1.32	0.1395	-0.0605	0.77	--
99	18.1	1.13	0.1249	-0.0555	0.76	--
100	19.1	1.10	0.1433	-0.0614	0.76	--
101	20.1	1.08	0.1638	-0.0677	0.76	--
102	22.1	1.05	0.2138	-0.0863	0.76	--
103	23.9	0.92	0.4504	-0.1558	0.74	--

Table B1. NACA 4415, Clean, Re = 0.75 x 10^6

RUN	AOA	C_l	C_{dp}	$C_{m¼}$	Re x10^{-6}	C_{dw}
104	26.1	1.02	0.5403	-0.1826	0.80	--
105	28.0	1.09	0.6147	-0.2041	0.79	--
106	30.0	1.16	0.7034	-0.2288	0.81	--
107	32.1	1.23	0.7973	-0.2546	0.81	--
108	34.1	1.29	0.9007	-0.2862	0.82	--
109	36.0	1.32	0.9928	-0.3112	0.83	--
110	38.2	1.34	1.0844	-0.3323	0.85	--
111	40.0	1.35	1.1643	-0.3542	0.86	--

End of Table B1

Table B2. NACA 4415, Clean, Re = 1.0 x 10^6

RUN	AOA	C_l	C_{dp}	$C_{m¼}$	Re x10^{-6}	C_{dw}
38	-20.1	-0.38	0.2555	0.0118	1.03	--
39	-18.0	-0.32	0.2181	0.0047	1.03	--
40	-16.1	-0.27	0.1854	-0.0002	1.02	--
41	-14.1	-0.24	0.1613	0.0021	1.02	--
42	-12.1	-0.47	0.1541	0.0058	1.02	--
43	-10.2	-0.60	-0.0141	-0.1014	1.01	0.0149
44	-8.1	-0.40	-0.0139	-0.0990	1.01	0.0125
45	-6.1	-0.19	-0.0123	-0.0981	1.01	0.0109
46	-4.1	0.02	-0.0088	-0.0967	1.01	0.0098
47	-2.1	0.23	-0.0061	-0.0954	1.00	0.0085
48	0.0	0.42	-0.0005	-0.0939	1.01	0.0085
49	2.1	0.63	0.0049	-0.0931	1.00	0.0076
50	4.1	0.86	0.0126	-0.0947	1.01	0.0084
51	6.2	1.02	0.0197	-0.0846	1.01	0.0096
52	8.1	1.17	0.0257	-0.0745	1.01	0.0120
53	10.2	1.26	0.0360	-0.0598	1.01	0.0166
54	11.2	1.29	0.0432	-0.0519	1.01	0.0227
55	12.2	1.30	0.0554	-0.0477	1.00	0.0312
56	13.3	1.33	0.0682	-0.0467	1.01	0.0335
57	14.3	1.35	0.0886	-0.0526	1.01	--
58	15.3	1.19	0.0750	-0.0378	1.02	--
59	16.2	1.15	0.0925	-0.0447	1.02	--
60	17.2	1.12	0.1095	-0.0497	1.02	--
61	18.2	1.10	0.1264	-0.0568	1.02	--
62	19.2	1.09	0.1469	-0.0634	1.02	--
63	20.3	1.08	0.1675	-0.0695	1.02	--
64	22.1	1.04	0.2161	-0.0877	1.03	--
65	24.1	1.03	0.2705	-0.1050	1.03	--

Table B2. NACA 4415, Clean, Re = 1.0 x 10^6

RUN	AOA	C_l	C_{dp}	$C_{m¼}$	Re $x10^{-6}$	C_{dw}
66	26.1	0.96	0.5087	-0.1663	1.05	--
67	28.1	1.09	0.6176	-0.2039	1.07	--
68	30.0	1.17	0.7070	-0.2294	1.07	--
69	32.1	1.22	0.7936	-0.2536	1.09	--
70	34.1	1.29	0.9035	-0.2882	1.10	--
71	36.0	1.32	0.9890	-0.3101	1.10	--
72	38.0	1.34	1.0748	-0.3303	1.12	--
73	40.0	1.34	1.1520	-0.3456	1.13	--

End of Table B2

Table B3. NACA 4415, Clean, Re = 1.25 x 10^6

RUN	AOA	C_l	C_{dp}	$C_{m¼}$	Re $x10^{-6}$	C_{dw}
2	-20.1	-0.39	0.2608	0.0157	1.29	--
3	-18.2	-0.34	0.2247	0.0085	1.28	--
4	-16.0	-0.27	0.1852	0.0000	1.28	--
5	-14.1	-0.30	0.1696	0.0065	1.28	--
6	-12.1	-0.52	0.1608	0.0201	1.28	--
7	-10.2	-0.62	-0.0145	-0.0994	1.26	0.0144
8	-8.1	-0.42	-0.0132	-0.0974	1.26	0.0123
9	-6.0	-0.20	-0.0117	-0.0967	1.27	0.0113
10	-4.0	0.01	-0.0090	-0.0962	1.25	0.0094
11	-2.1	0.22	-0.0053	-0.0948	1.25	0.0082
1	0.0	0.44	-0.0019	-0.0935	1.26	0.0082
12	0.0	0.42	-0.0001	-0.0939	1.26	0.0079
13	2.1	0.63	0.0052	-0.0926	1.26	0.0076
14	4.0	0.84	0.0105	-0.0904	1.26	0.0073
15	6.2	1.03	0.0187	-0.0840	1.26	0.0094
16	8.1	1.16	0.0261	-0.0731	1.26	0.0130
17	10.2	1.26	0.0377	-0.0595	1.26	0.0172
18	11.2	1.28	0.0412	-0.0494	1.26	0.0241
19	12.3	1.30	0.0520	-0.0464	1.26	0.0339
20	13.3	1.28	0.0583	-0.0428	1.27	--
21	14.3	1.20	0.0631	-0.0383	1.27	--
22	15.3	1.16	0.0782	-0.0409	1.26	--
23	16.3	1.14	0.0961	-0.0463	1.27	--
24	17.3	1.11	0.1117	-0.0510	1.27	--
25	18.3	1.09	0.1306	-0.0580	1.27	--
26	19.1	1.08	0.1469	-0.0640	1.27	--
27	20.1	1.08	0.1660	-0.0685	1.28	--
28	22.1	1.03	0.2203	-0.0900	1.28	--

Table B3. NACA 4415, Clean, Re = 1.25 x 10^6						
RUN	AOA	C_l	C_{dp}	$C_{m¼}$	Re x10^{-6}	C_{dw}
29	24.1	1.04	0.2732	-0.1064	1.29	--
30	26.1	0.96	0.5119	-0.1679	1.32	--
31	28.0	1.08	0.6108	-0.2004	1.32	--
32	30.0	1.16	0.7014	-0.2271	1.35	--
33	32.1	1.24	0.8035	-0.2569	1.35	--
34	34.1	1.30	0.9090	-0.2893	1.36	--
35	36.0	1.32	0.9899	-0.3094	1.38	--
36	37.9	1.34	1.0797	-0.3341	1.41	--
37	40.1	1.34	1.1659	-0.3549	1.41	--
End of Table B3						

Table B4. NACA 4415, Clean, Re = 1.25 x 10^6, Repeat runs						
RUN	AOA	C_l	C_{dp}	$C_{m¼}$	Re x10^{-6}	C_{dw}
113	-6.0	-0.19	-0.0114	-0.0968	1.26	0.0105
114	-4.0	0.03	-0.0089	-0.0958	1.26	0.0091
115	-2.1	0.21	-0.0057	-0.0956	1.26	0.0077
112	0.0	0.43	-0.0010	-0.0955	0.75	0.0074
116	0.0	0.42	-0.0009	-0.0932	1.26	0.0085
117	2.1	0.64	0.0043	-0.0923	1.25	0.0072
118	4.1	0.86	0.0110	-0.0917	1.25	0.0077
119	6.1	1.03	0.0170	-0.0847	1.27	0.0092
120	8.1	1.17	0.0235	-0.0717	1.27	0.0112
121	10.2	1.26	0.0380	-0.0596	1.26	0.0155
122	11.2	1.29	0.0440	-0.0511	1.25	0.0218
123	12.3	1.30	0.0524	-0.0462	1.26	0.0495
124	13.3	1.28	0.0585	-0.0430	1.27	--
125	14.3	1.19	0.0633	-0.0383	1.28	--
126	15.3	1.17	0.0789	-0.0407	1.27	--
127	16.1	1.14	0.0905	-0.0455	1.27	--
128	17.3	1.12	0.1137	-0.0521	1.27	--
129	18.1	1.10	0.1293	-0.0587	1.27	--
130	19.1	1.08	0.1477	-0.0644	1.30	--
131	20.1	1.06	0.1694	-0.0720	1.30	--
End of Table B4						

Table B5. NACA 4415, Clean, Re = 1.5 x 10^6

RUN	AOA	C_l	C_{dp}	$C_{m¼}$	Re x10^{-6}	C_{dw}
132	-20.1	-0.39	0.2596	0.0136	1.55	--
133	-18.0	-0.35	0.2269	0.0104	1.53	--
134	-15.9	-0.29	0.1895	0.0034	1.55	--
135	-14.1	-0.32	0.1767	0.0140	1.54	--
136	-12.1	-0.50	0.1702	0.0265	1.53	--
137	-10.2	-0.62	-0.0142	-0.0981	1.52	0.0134
138	-8.1	-0.41	-0.0137	-0.0968	1.52	0.0114
139	-6.0	-0.19	-0.0106	-0.0958	1.52	0.0094
140	-3.9	0.02	-0.0086	-0.0947	1.51	0.0090
141	-2.1	0.21	-0.0056	-0.0938	1.52	0.0084
142	0.0	0.42	-0.0008	-0.0927	1.52	0.0079
143	2.1	0.64	0.0039	-0.0908	1.52	0.0083
144	4.0	0.85	0.0089	-0.0886	1.52	0.0081
145	6.1	1.02	0.0165	-0.0823	1.52	0.0099
146	8.3	1.17	0.0270	-0.0704	1.53	0.0127
147	10.2	1.25	0.0319	-0.0541	1.52	0.0177
148	12.2	1.29	0.0470	-0.0446	1.52	0.0426
149	13.2	1.21	0.0511	-0.0404	1.52	--
150	14.3	1.17	0.0644	-0.0399	1.53	--
151	15.2	1.14	0.0788	-0.0431	1.52	--
152	16.3	1.12	0.0966	-0.0480	1.52	--
153	17.3	1.09	0.1162	-0.0544	1.53	--
154	18.4	1.07	0.1342	-0.0600	1.53	--
155	19.1	1.06	0.1508	-0.0677	1.53	--
156	20.1	1.03	0.1751	-0.0758	1.54	--
157	22.1	1.01	0.2280	-0.0950	1.55	--
158	24.2	1.03	0.2784	-0.1070	1.54	--

End of Table B5

Table B6. NACA 4415, Clean, Re = 1.5 x 10^6, Repeat runs						
RUN	AOA	C_l	C_{dp}	$C_{m¼}$	Re x10^{-6}	C_{dw}
169	-17.0	-0.36	0.2181	0.0190	1.53	--
168	-16.0	-0.36	0.2091	0.0216	1.54	--
167	-15.1	-0.42	0.2136	0.0387	1.54	--
166	-14.1	-0.40	0.1939	0.0306	1.53	--
165	-13.3	-0.91	-0.0089	-0.0990	1.51	--
164	-12.3	-0.81	-0.0106	-0.0993	1.51	--
163	-11.2	-0.71	-0.0124	-0.0990	1.50	--
162	-10.2	-0.62	-0.0136	-0.0986	1.51	--
161	-8.1	-0.40	-0.0131	-0.0972	1.50	--
160	-3.9	0.03	-0.0087	-0.0950	1.51	--
159	0.0	0.44	-0.0024	-0.0926	1.51	--
End of Table B6						

Table B7. NACA 4415, k/c=0.0019, Re = 0.75 x 10^6

RUN	AOA	C_l	C_{dp}	$C_{m1/4}$	Re x10^{-6}	C_{dw}
180	-20.1	-0.40	0.2352	0.0131	0.77	--
179	-18.0	-0.37	0.1939	0.0065	0.77	--
178	-16.0	-0.35	0.1594	0.0047	0.76	--
177	-14.1	-0.33	0.1300	0.0025	0.76	--
176	-12.1	-0.43	0.1100	0.0093	0.76	--
175	-10.2	-0.54	-0.0132	-0.0960	0.76	0.0240
174	-8.1	-0.38	-0.0175	-0.0930	0.76	0.0182
173	-6.1	-0.20	-0.0161	-0.0889	0.76	0.0164
172	-3.9	-0.01	-0.0113	-0.0835	0.76	0.0161
171	-2.1	0.18	-0.0083	-0.0817	0.76	0.0138
170	0.0	0.36	-0.0031	-0.0785	0.76	0.0153
181	0.0	0.35	-0.0029	-0.0780	0.75	0.0152
182	2.1	0.55	0.0002	-0.0738	0.75	0.0161
183	4.1	0.72	0.0063	-0.0644	0.76	0.0162
184	6.2	0.87	0.0152	-0.0572	0.75	0.0199
185	8.1	0.98	0.0264	-0.0480	0.75	0.0235
186	10.1	1.07	0.0485	-0.0465	0.76	0.0280
187	11.2	1.11	0.0686	-0.0556	0.75	--
188	12.2	1.11	0.0897	-0.0592	0.75	--
189	13.2	1.10	0.1101	-0.0650	0.77	--
190	14.2	1.07	0.1283	-0.0685	0.77	--
191	15.2	1.07	0.1499	-0.0723	0.76	--
192	16.2	0.93	0.1547	-0.0689	0.77	--
193	17.2	1.06	0.1966	-0.0821	0.77	--
194	18.2	0.87	0.2075	-0.0849	0.77	--
195	19.2	1.03	0.2461	-0.0958	0.78	--
196	20.0	0.85	0.2647	-0.1034	0.79	--
197	22.0	0.86	0.3285	-0.1204	0.76	--

Table B7. NACA 4415, k/c=0.0019, Re = 0.75 x 10^6

RUN	AOA	C_l	C_{dp}	$C_{m¼}$	Re x10^{-6}	C_{dw}
198	24.1	1.02	0.4381	-0.1639	0.78	--
199	26.0	1.04	0.4994	-0.1770	0.79	--
200	28.0	1.07	0.5644	-0.1902	0.80	--
201	30.1	1.12	0.6523	-0.2121	0.80	--
202	32.1	1.19	0.7493	-0.2404	0.82	--
203	34.1	1.24	0.8410	-0.2647	0.83	--
204	36.1	1.33	0.9734	-0.3110	0.83	--
205	37.8	1.35	1.0589	-0.3344	0.84	--
206	40.1	1.33	1.1206	-0.3408	0.85	--

End of Table B7

Table B8. NACA 4415, k/c=0.0019, Re = 1.0 x 10^6						
RUN	AOA	C_l	C_{dp}	$C_{m¼}$	Re x10^{-6}	C_{dw}
217	-20.1	-0.39	0.2349	0.0109	1.03	--
216	-18.1	-0.35	0.1999	0.0067	1.02	--
215	-16.0	-0.33	0.1651	0.0028	1.02	--
214	-14.2	-0.37	0.1333	0.0027	1.02	--
213	-12.2	-0.47	0.1017	-0.0019	1.02	--
212	-10.2	-0.56	-0.0135	-0.0922	1.01	0.0267
211	-8.1	-0.41	-0.0184	-0.0916	1.00	0.0211
210	-6.0	-0.22	-0.0167	-0.0883	1.01	0.0145
209	-4.0	-0.02	-0.0123	-0.0842	1.01	0.0140
208	-2.1	0.17	-0.0087	-0.0811	1.01	0.0156
207	0.0	0.36	-0.0049	-0.0779	1.01	0.0127
218	0.0	0.36	-0.0051	-0.0773	1.01	0.0128
219	2.1	0.55	0.0008	-0.0730	1.02	0.0154
220	4.0	0.72	0.0055	-0.0661	1.01	0.0146
221	6.1	0.87	0.0131	-0.0572	1.02	0.0126
222	8.1	0.98	0.0284	-0.0491	1.02	0.0212
223	10.2	1.08	0.0507	-0.0473	1.01	0.0238
224	11.2	1.12	0.0736	-0.0567	1.02	--
225	12.2	1.12	0.0956	-0.0617	1.02	--
226	13.3	1.12	0.1152	-0.0656	1.02	--
227	14.3	1.13	0.1379	-0.0703	1.00	--
228	15.3	1.10	0.1589	-0.0753	1.04	--
229	16.1	1.09	0.1774	-0.0786	1.03	--
230	17.1	1.07	0.1978	-0.0825	1.02	--
231	18.1	1.05	0.2207	-0.0881	1.03	--
232	19.1	1.01	0.2417	-0.0943	1.04	--
233	20.1	0.84	0.2658	-0.1009	1.04	--
234	22.1	0.89	0.3395	-0.1240	1.06	--

Table B8. NACA 4415, k/c=0.0019, Re = 1.0 x 10^6						
RUN	AOA	C_l	C_{dp}	$C_{m¼}$	Re x10^{-6}	C_{dw}
235	24.0	1.01	0.4355	-0.1608	1.05	--
236	26.1	1.03	0.4968	-0.1737	1.04	--
237	28.1	1.06	0.5643	-0.1875	1.05	--
238	30.0	1.12	0.6480	-0.2103	1.07	--
239	32.2	1.19	0.7573	-0.2422	1.07	--
240	33.9	1.27	0.8627	-0.2770	1.09	--
241	36.0	1.31	0.9549	-0.3004	1.11	--
242	38.0	1.33	1.0436	-0.3246	1.12	--
243	39.9	1.34	1.1294	-0.3462	1.12	--
End of Table B8						

Table B9. NACA 4415, k/c=0.0019, Re = 1.25 x 10^6

RUN	AOA	C_l	C_{dp}	$C_{m¼}$	Re x10^{-6}	C_{dw}
254	-20.1	-0.40	0.2384	0.0107	1.29	--
253	-18.1	-0.34	0.2006	0.0038	1.27	--
252	-16.0	-0.32	0.1692	0.0014	1.28	--
251	-14.1	-0.36	0.1394	0.0055	1.28	--
250	-12.2	-0.49	0.1060	0.0006	1.26	--
249	-10.2	-0.58	-0.0150	-0.0926	1.26	0.0271
248	-8.1	-0.42	-0.0181	-0.0900	1.27	0.0198
247	-6.1	-0.23	-0.0146	-0.0868	1.27	0.0160
246	-4.0	-0.02	-0.0124	-0.0844	1.28	0.0119
245	-2.1	0.18	-0.0092	-0.0807	1.27	0.0126
244	0.0	0.36	-0.0050	-0.0775	1.28	0.0125
255	0.0	0.36	-0.0050	-0.0773	1.26	0.0132
256	2.1	0.56	0.0001	-0.0723	1.26	0.0128
257	4.2	0.73	0.0071	-0.0662	1.26	0.0135
258	6.1	0.88	0.0143	-0.0569	1.26	0.0178
259	8.1	1.00	0.0257	-0.0473	1.26	0.0233
260	10.2	1.08	0.0479	-0.0458	1.26	0.0274
261	11.2	1.10	0.0708	-0.0559	1.27	0.0321
262	12.2	1.10	0.0917	-0.0604	1.26	--
263	13.2	0.99	0.0958	-0.0515	1.27	--
264	14.2	0.91	0.1063	-0.0506	1.27	--
265	15.2	0.90	0.1272	-0.0567	1.27	--
266	16.2	0.97	0.1630	-0.0704	1.28	--
267	17.1	1.04	0.1952	-0.0828	1.28	--
268	18.2	1.03	0.2234	-0.0891	1.29	--
269	19.1	1.03	0.2469	-0.0964	1.28	--
270	20.1	1.00	0.2720	-0.1040	1.28	--
271	22.1	0.92	0.3406	-0.1251	1.30	--

Table B9. NACA 4415, k/c=0.0019, Re = 1.25 x 10^6						
RUN	AOA	C_l	C_{dp}	$C_{m¼}$	Re $x10^{-6}$	C_{dw}
272	24.1	1.02	0.4383	-0.1610	1.30	--
273	26.1	1.00	0.4885	-0.1674	1.31	--
274	28.1	0.98	0.5311	-0.1708	1.31	--
275	30.1	1.12	0.6563	-0.2126	1.34	--
276	32.1	1.19	0.7546	-0.2403	1.34	--
277	34.0	1.27	0.8638	-0.2746	1.37	--
278	35.9	1.32	0.9664	-0.3065	1.38	--
279	37.9	1.35	1.0583	-0.3315	1.40	--
280	40.0	1.34	1.1341	-0.3471	1.41	--
End of Table B9						

Table B10. NACA 4415, k/c=0.0019, Re = 1.5 x 10^6

RUN	AOA	C_l	C_{dp}	$C_{m\frac{1}{4}}$	Re x10^{-6}	C_{dw}
291	-20.1	-0.39	0.2386	0.0083	1.54	--
290	-18.0	-0.35	0.2035	0.0049	1.53	--
289	-16.1	-0.33	0.1743	0.0037	1.53	--
288	-13.9	-0.38	0.1435	0.0082	1.53	--
287	-12.0	-0.46	0.1145	0.0101	1.52	--
286	-10.2	-0.60	-0.0130	-0.0893	1.52	0.0263
285	-8.2	-0.43	-0.0164	-0.0881	1.52	0.0197
284	-6.1	-0.23	-0.0155	-0.0863	1.52	0.0158
283	-4.0	-0.02	-0.0124	-0.0827	1.53	0.0144
282	-2.1	0.18	-0.0095	-0.0795	1.52	0.0124
292	0.0	0.39	-0.0070	-0.0755	1.51	0.0126
281	0.1	0.39	-0.0065	-0.0752	1.52	0.0120
293	2.1	0.58	-0.0038	-0.0699	1.51	0.0121
294	4.1	0.74	0.0039	-0.0634	1.51	0.0137
295	6.2	0.90	0.0121	-0.0549	1.51	0.0183
296	8.1	1.01	0.0224	-0.0458	1.51	0.0246
297	10.2	1.08	0.0485	-0.0465	1.51	--
298	11.3	1.08	0.0709	-0.0547	1.50	--
299	12.1	0.95	0.0657	-0.0396	1.51	--
300	13.1	0.95	0.0858	-0.0449	1.52	--
301	14.2	0.93	0.1067	-0.0511	1.52	--
302	15.1	0.91	0.1242	-0.0556	1.52	--
303	16.3	0.90	0.1516	-0.0631	1.53	--
304	17.2	0.89	0.1777	-0.0732	1.53	--
305	18.2	0.88	0.2051	-0.0811	1.53	--
306	19.2	0.88	0.2381	-0.0922	1.54	--
307	20.0	0.86	0.2704	-0.1032	1.55	--
308	22.0	0.91	0.3400	-0.1234	1.56	--

Table B10. NACA 4415, k/c=0.0019, Re = 1.5 x 10^6

RUN	AOA	C_l	C_{dp}	$C_{m¼}$	Re $x10^{-6}$	C_{dw}
309	24.0	0.96	0.4137	-0.1473	1.56	--
310	26.0	0.99	0.4775	-0.1627	1.54	--

End of Table B10

NACA 4415

Pressure Distributions, Steady State, Re = 0.75 million

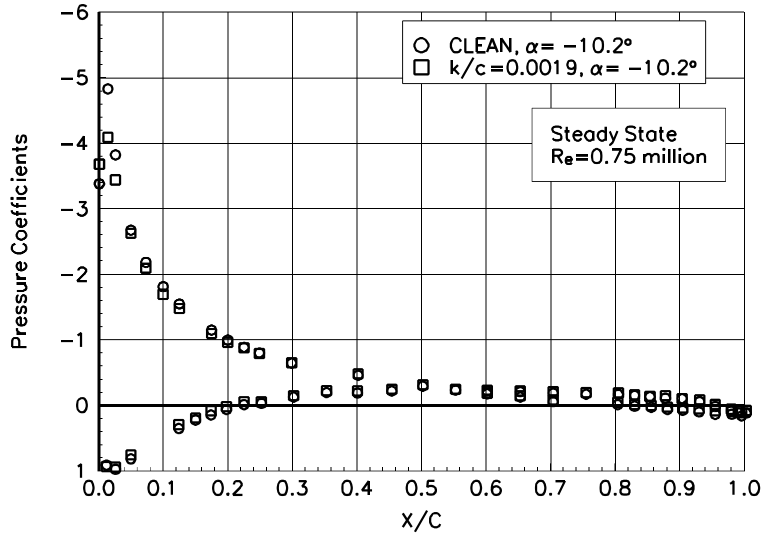

Figure B1. α = -10.2°

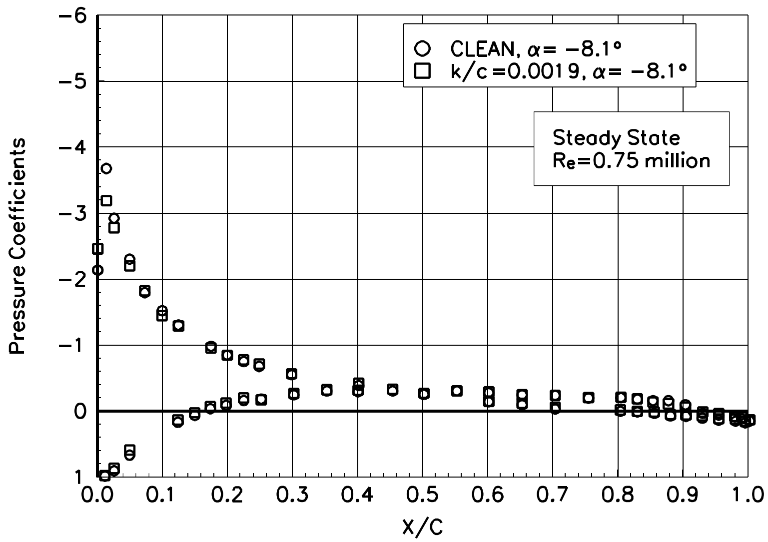

Figure B2. α = -8.1°

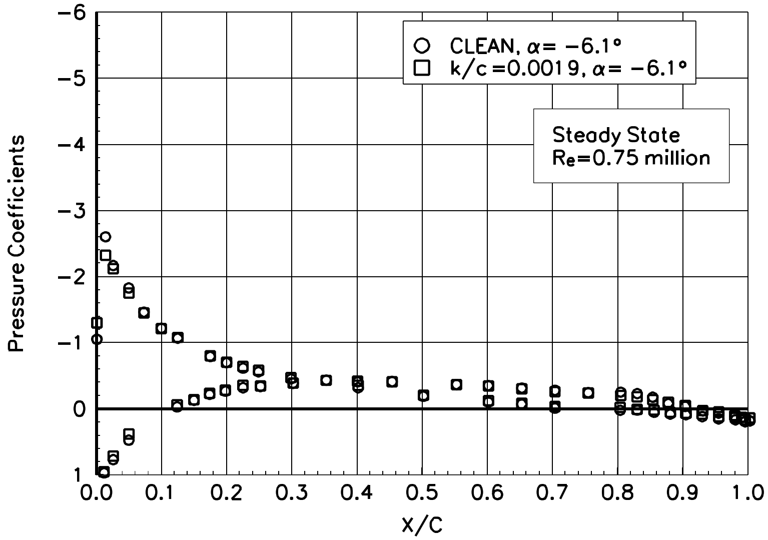

Figure B3. α = -6.1°

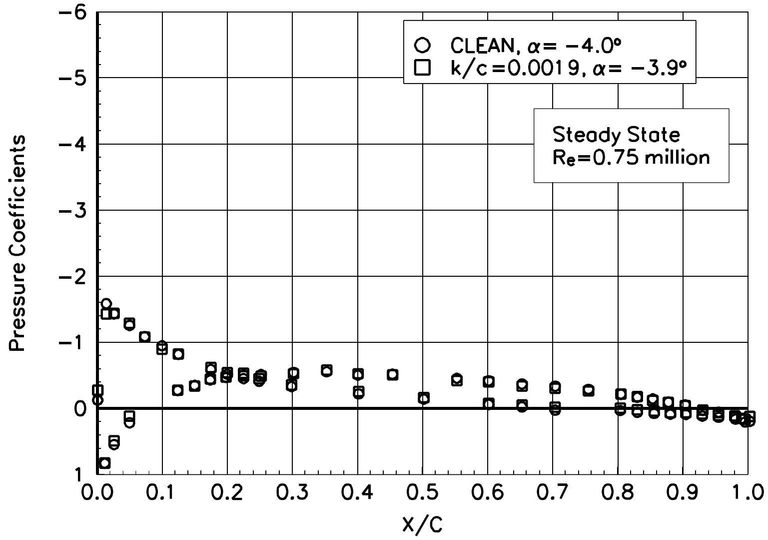

Figure B4. α = -4.0°

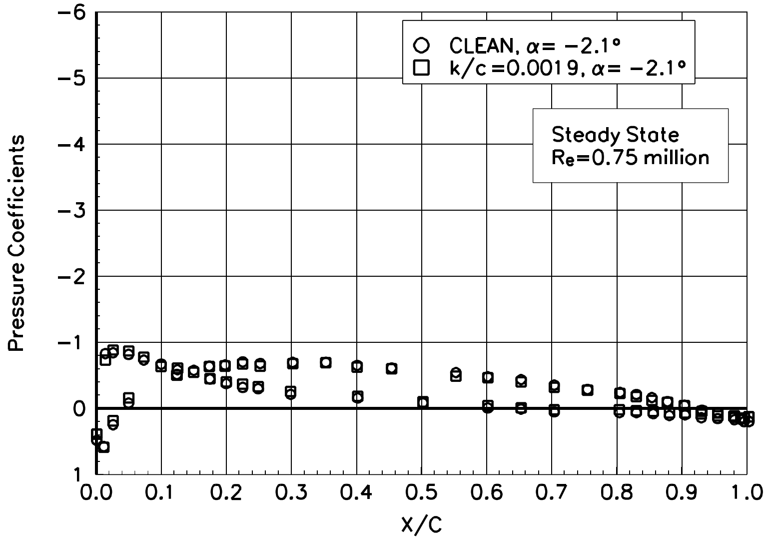

Figure B5. α = -2.1°

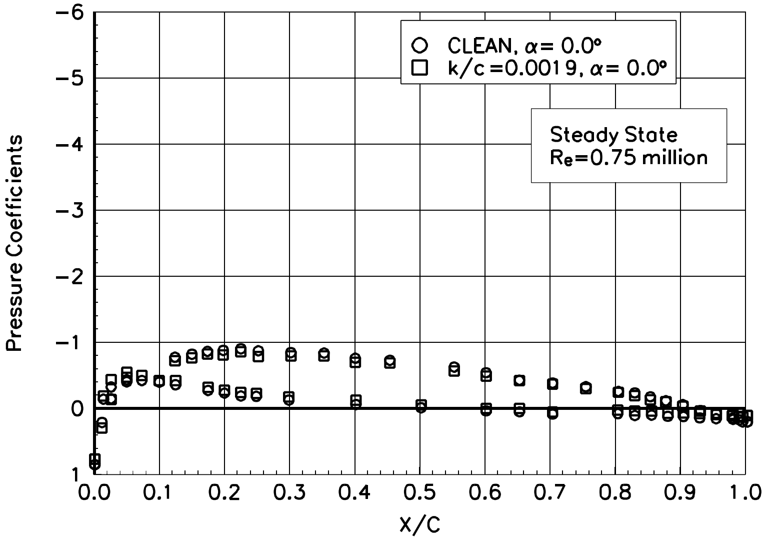

Figure B6. α = 0.0°

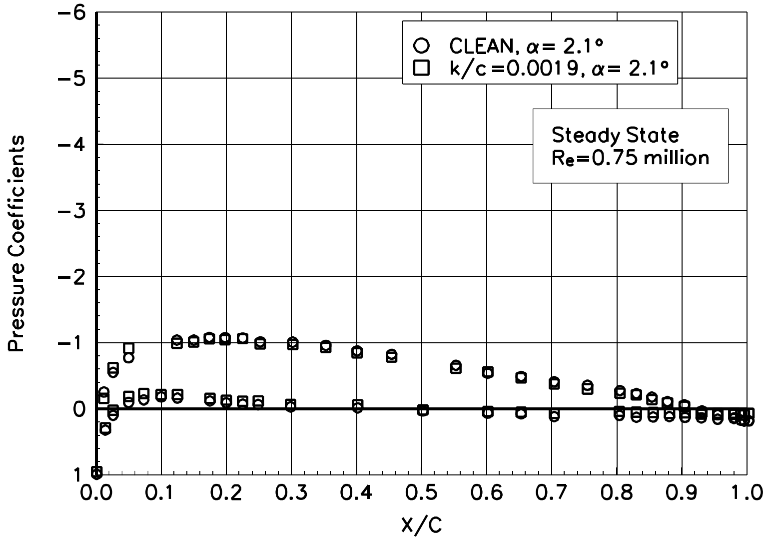

Figure B7. α = 2.1°

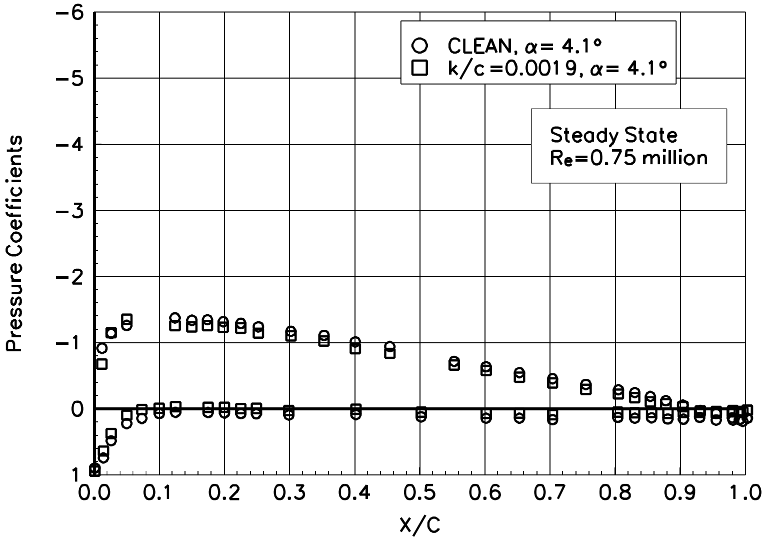

Figure B8. α = 4.1°

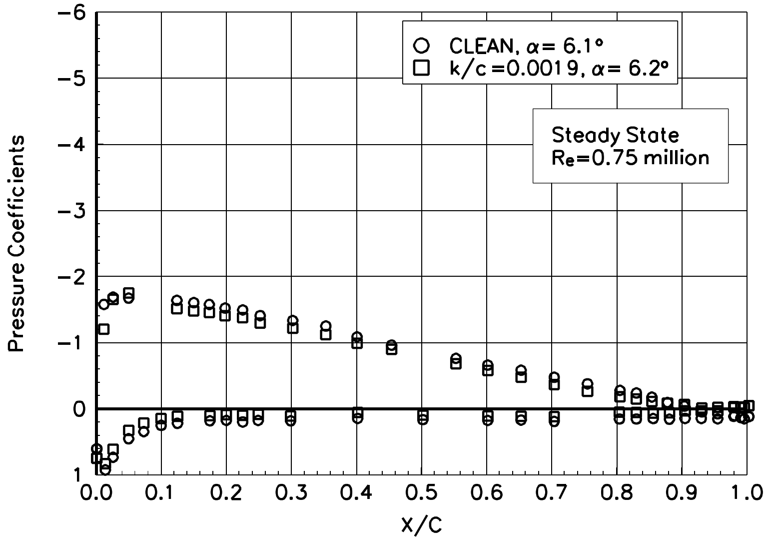

Figure B9. α = 6.1°

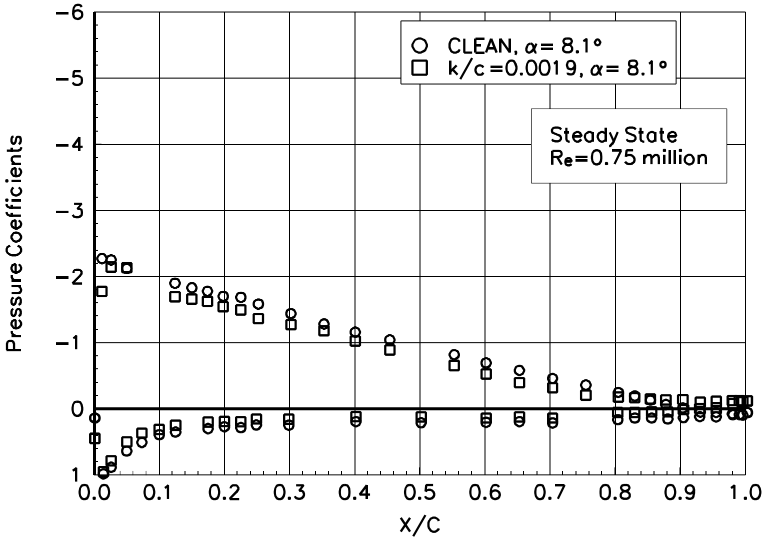

Figure B10. α = 8.1°

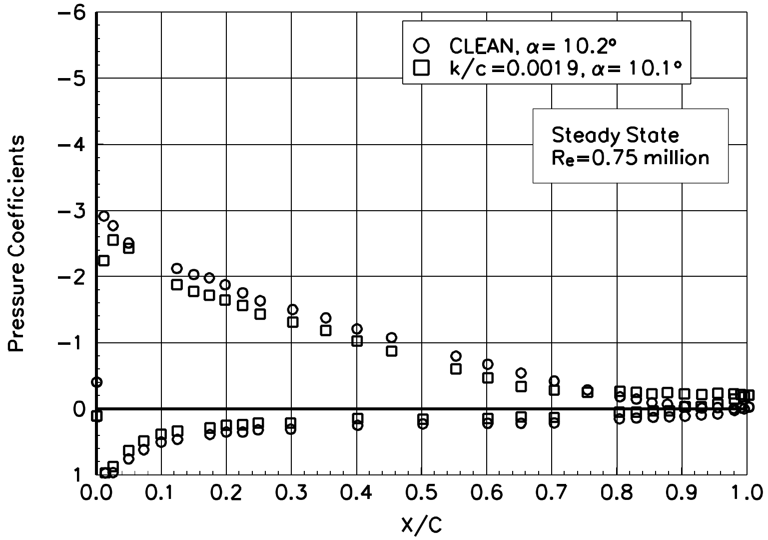

Figure B11. α = 10.2°

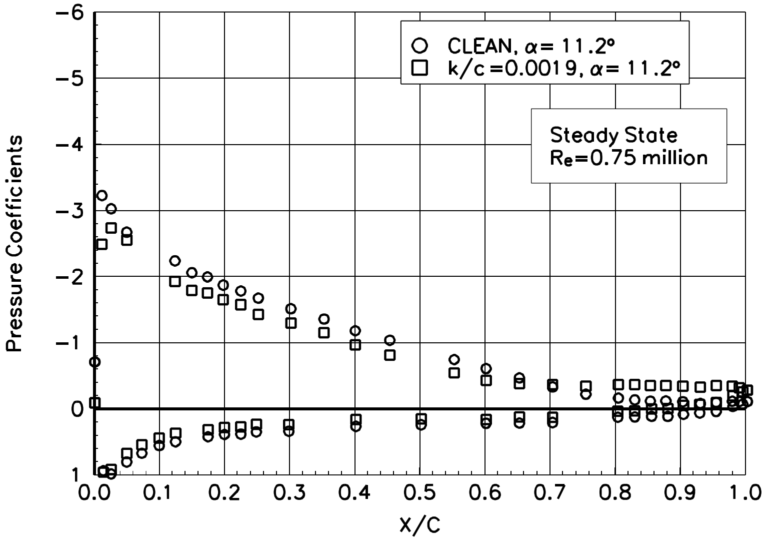

Figure B12. α = 11.2°

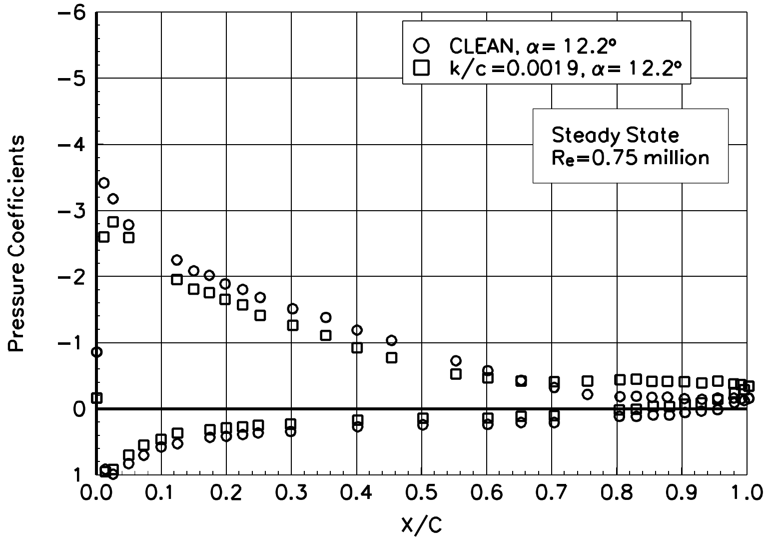

Figure B13. α = 12.2°

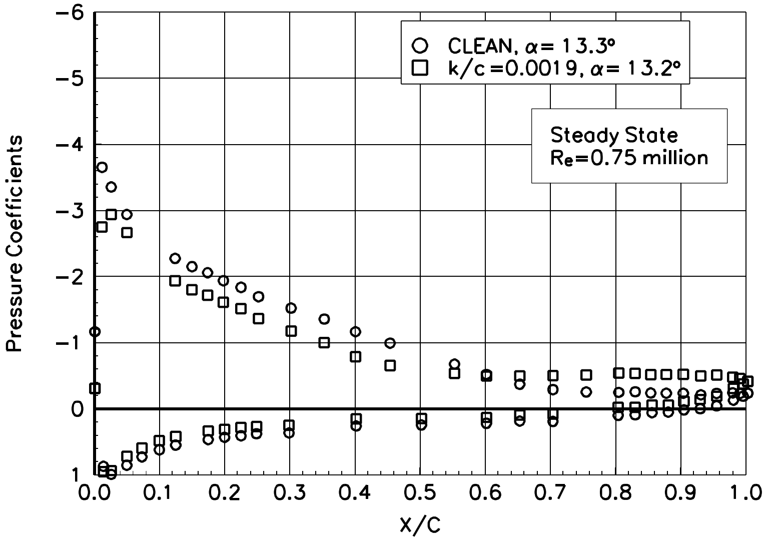

Figure B14. α = 13.3°

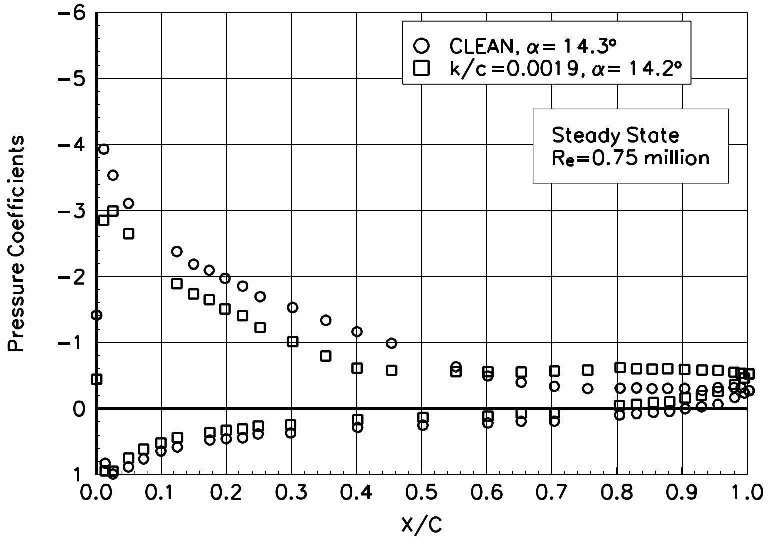

Figure B15. α = 14.3°

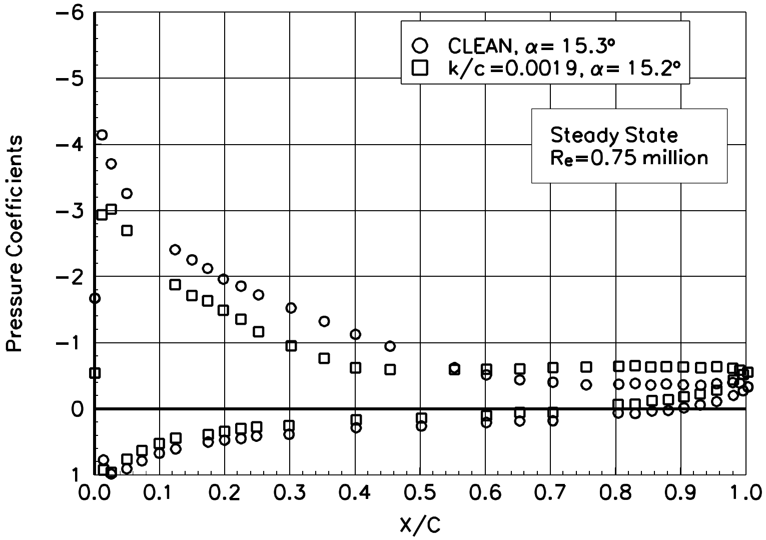

Figure B16. α = 15.3˙

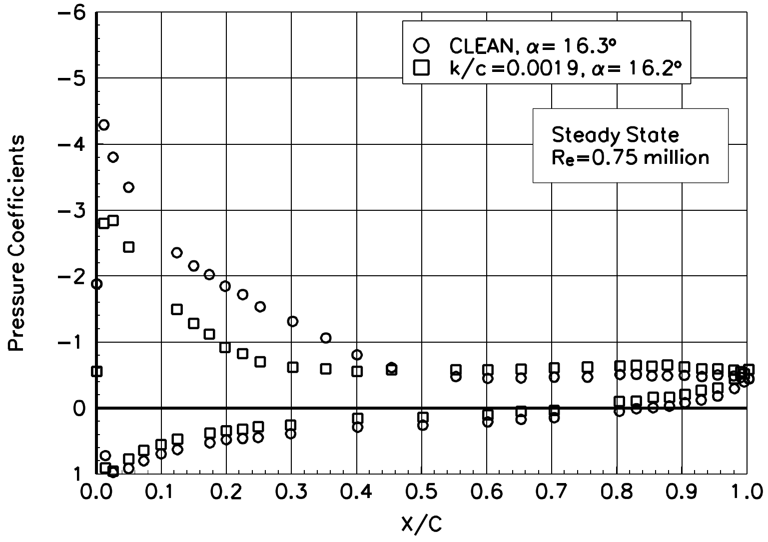

Figure B17. α = 16.3°

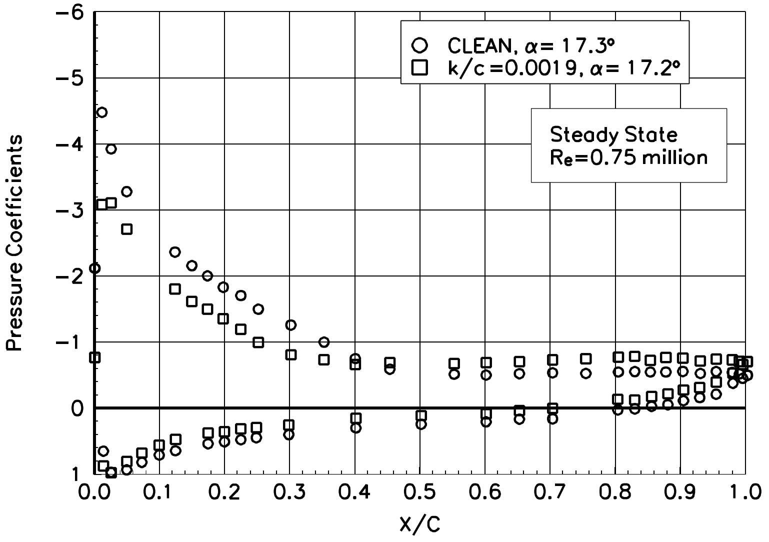

Figure B18. α = 17.3°

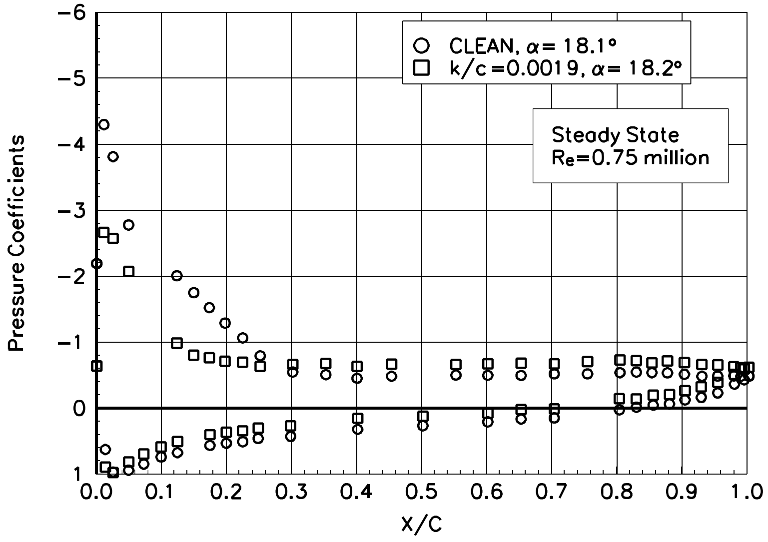

Figure B19. α = 18.1°

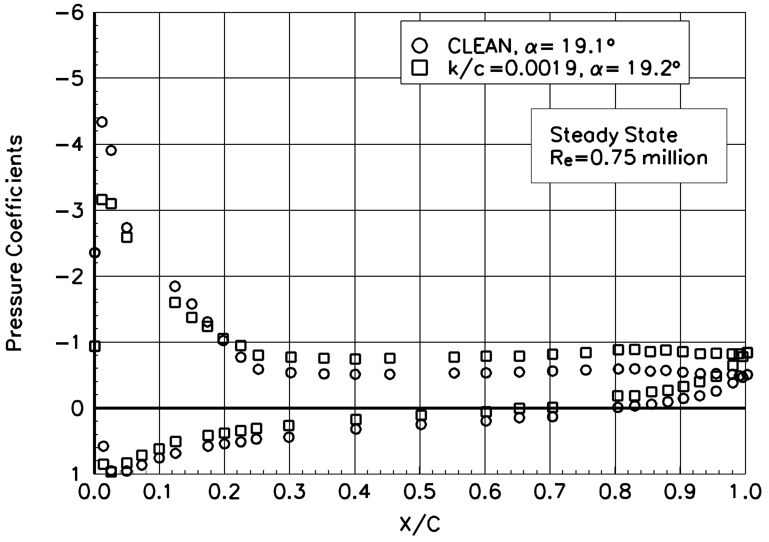

Figure B20. α = 19.1°

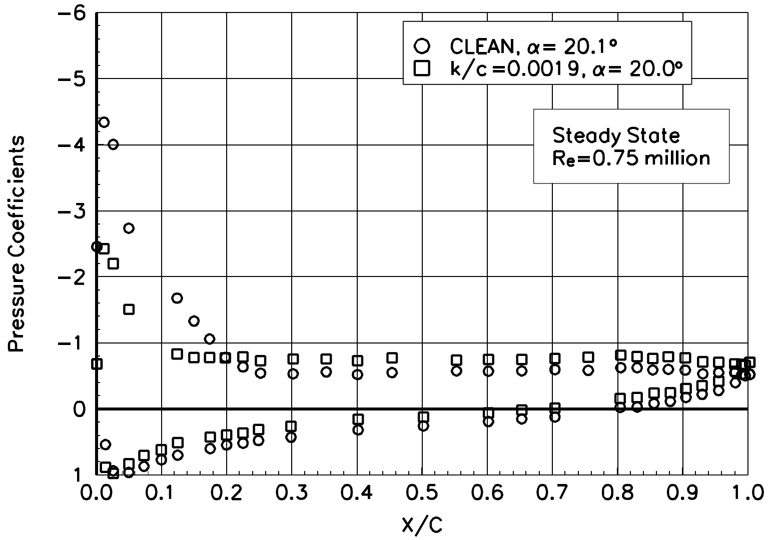

Figure B21. α = 20.1°

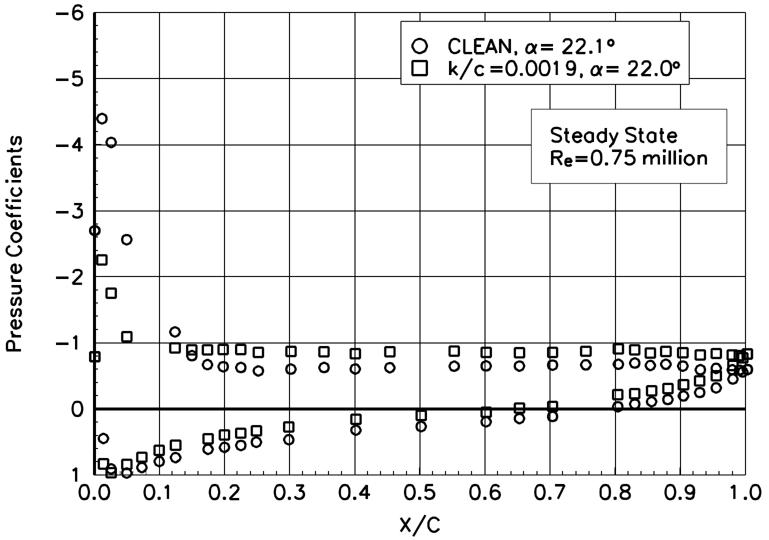

Figure B22. α = 22.1°

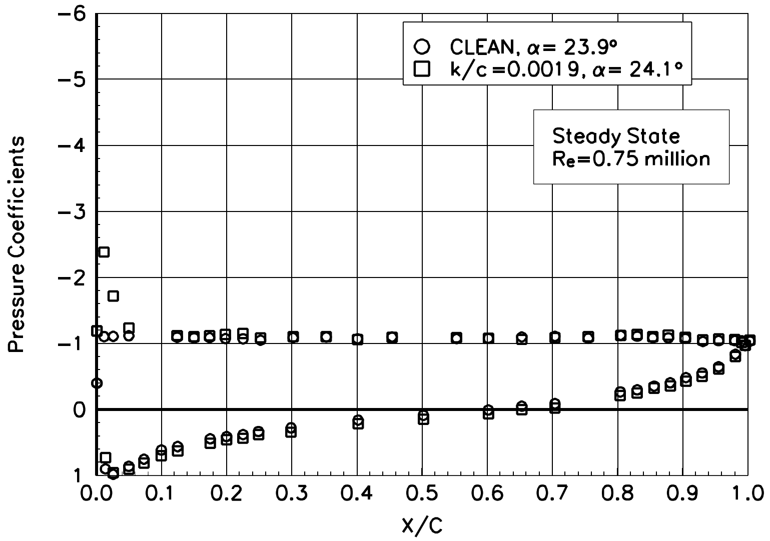

Figure B23. α = 23.9°

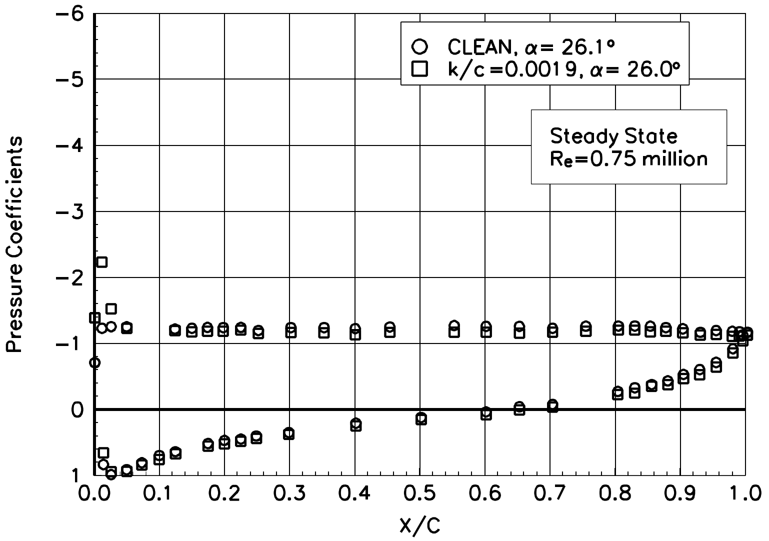

Figure B24. α = 26.1°

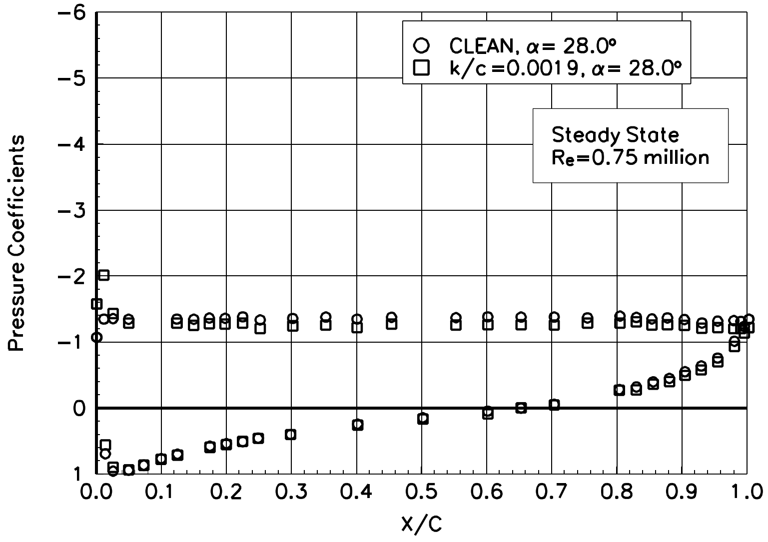

Figure B25. α = 28.0°

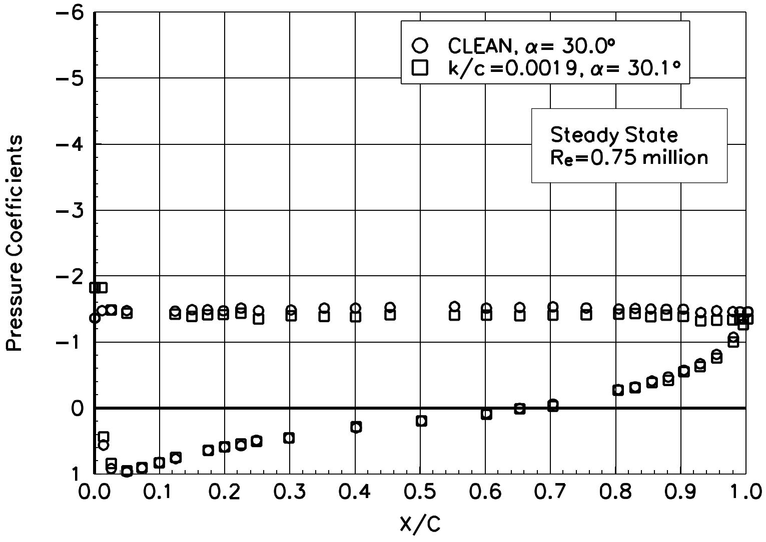

Figure B26. α = 30.0°

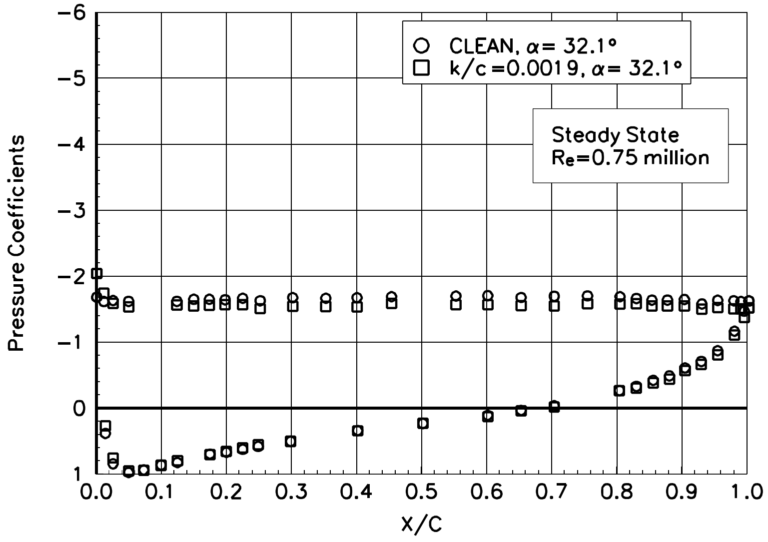

Figure B27. α = 32.1°

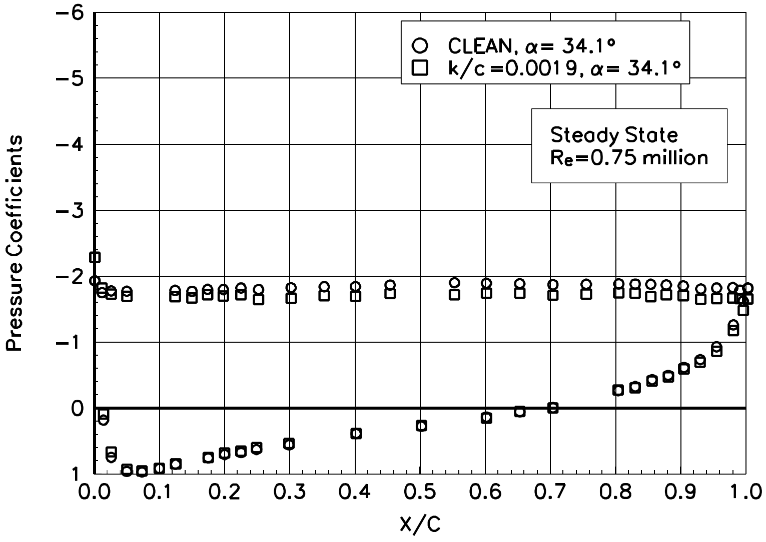

Figure B28. α = 34.1°

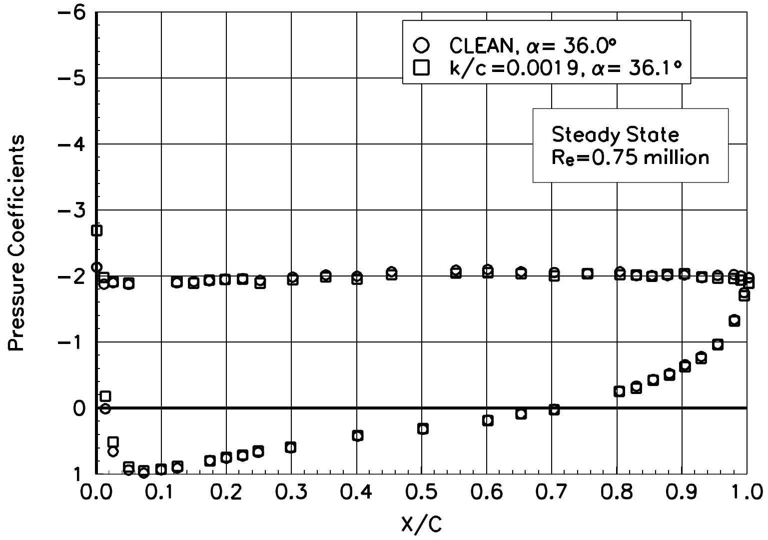

Figure B29. α = 36.0°

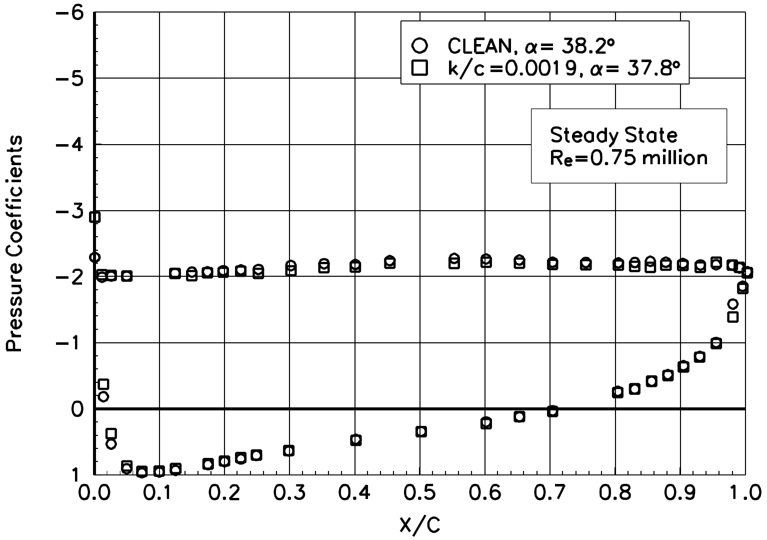

Figure B30. α = 38.2°

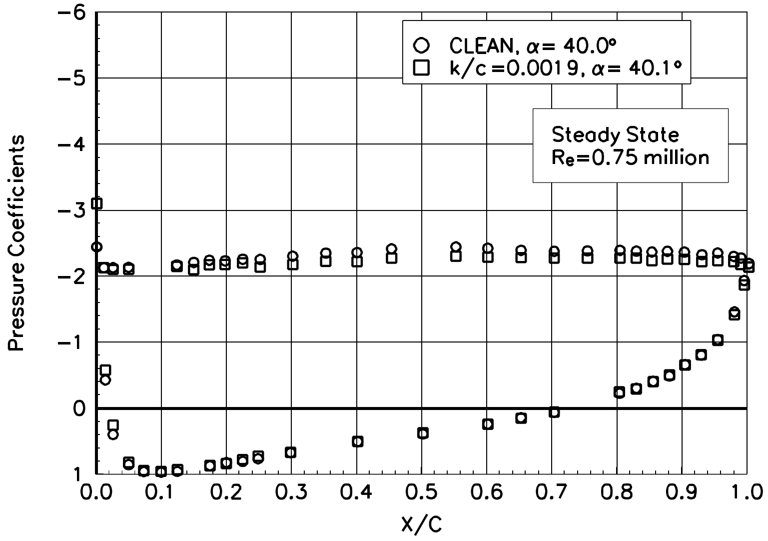

Figure B31. α = 40.0°

NACA 4415

Pressure Distributions, Steady State, Re = 1 million

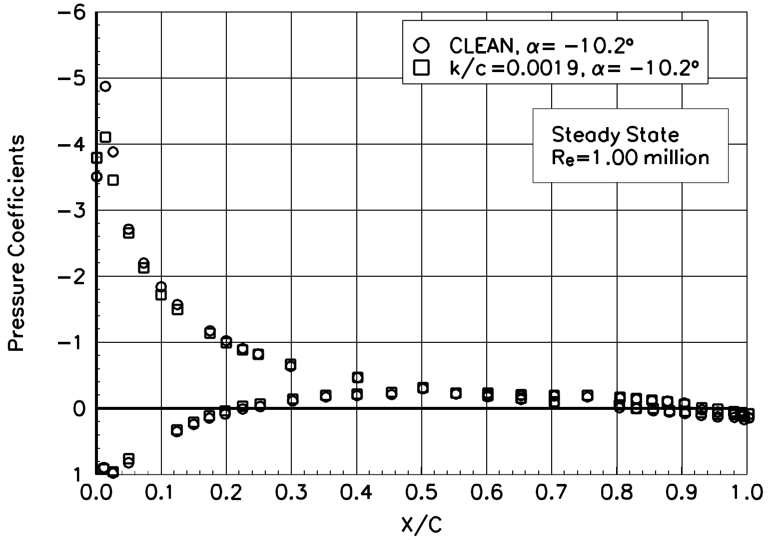

Figure B32. α = -10.2°

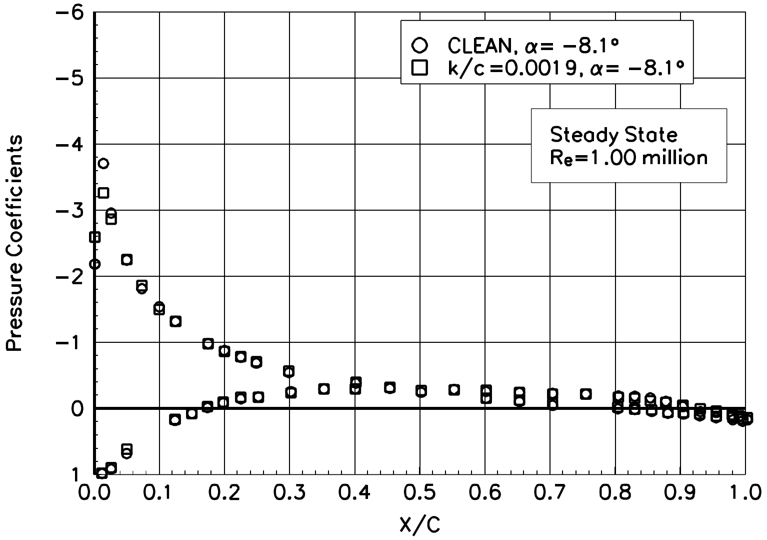

Figure B33. α = -8.1°

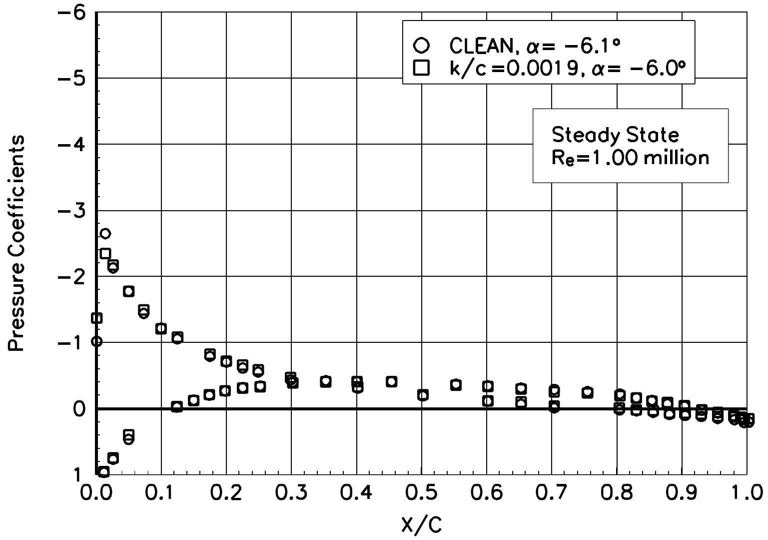

Figure B34. α = -6.1°

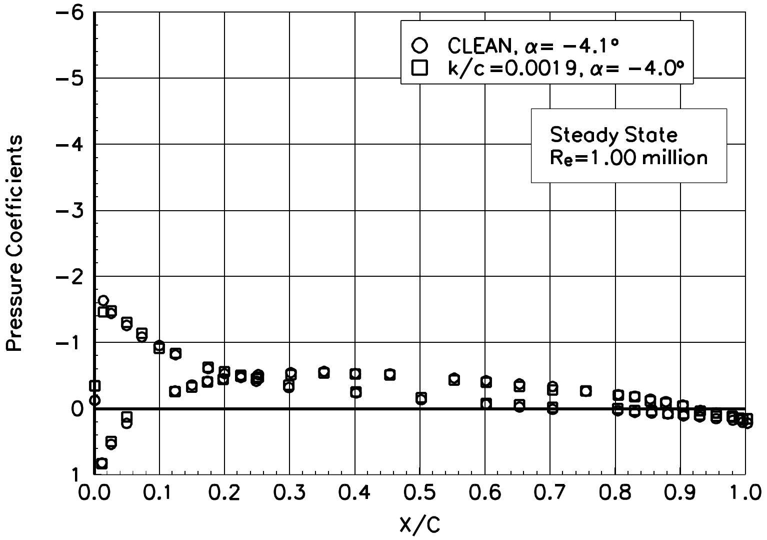

Figure B35. α = -4.1°

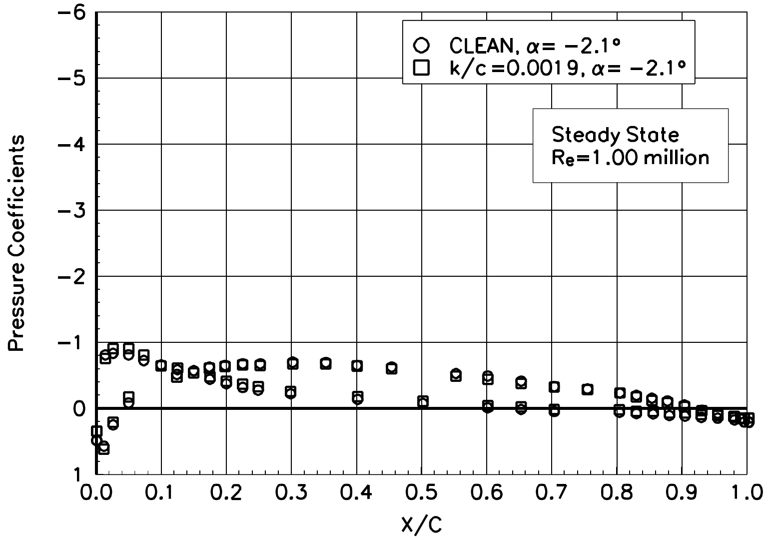

Figure B36. α = -2.1°

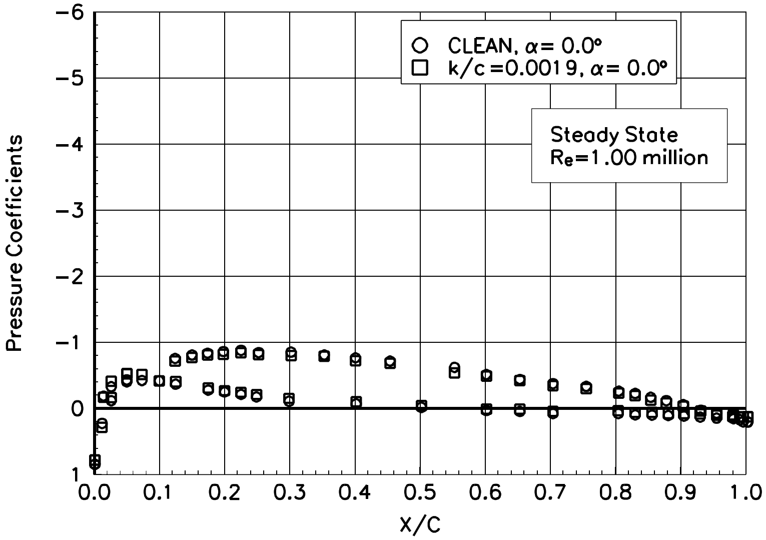

Figure B37. α = 0.0°

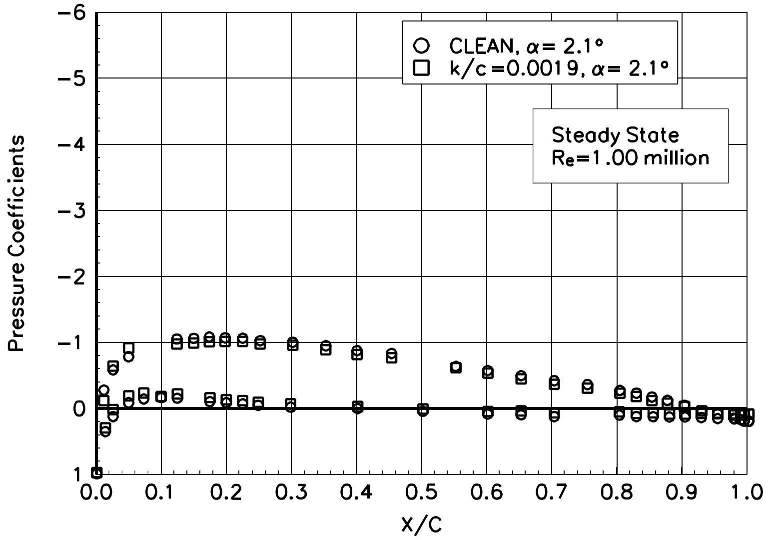

Figure B38. α = 2.1°

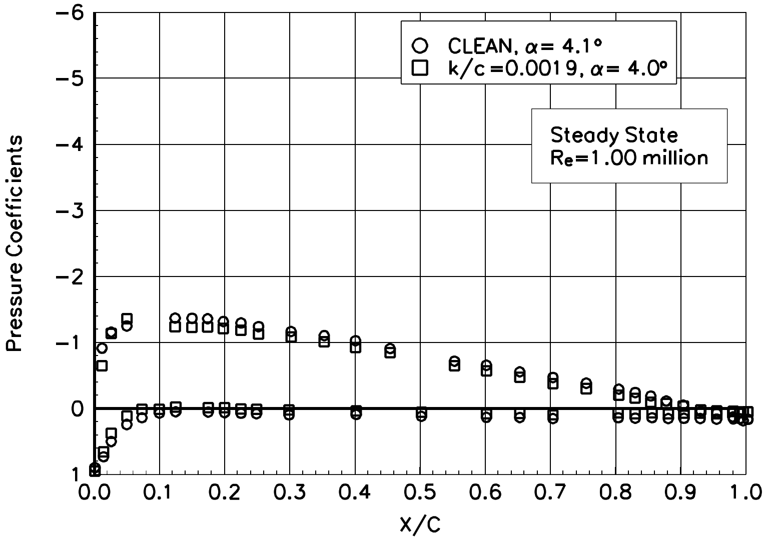

Figure B39. α = 4.1°

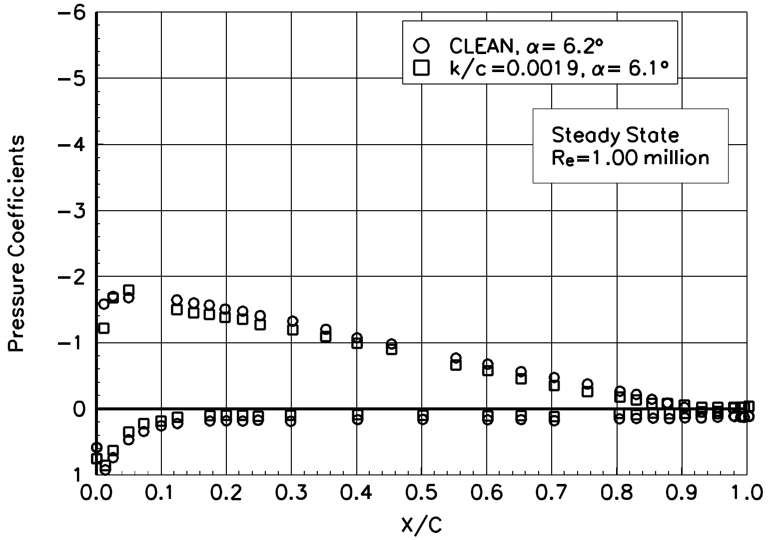

Figure B40. α = 6.2°

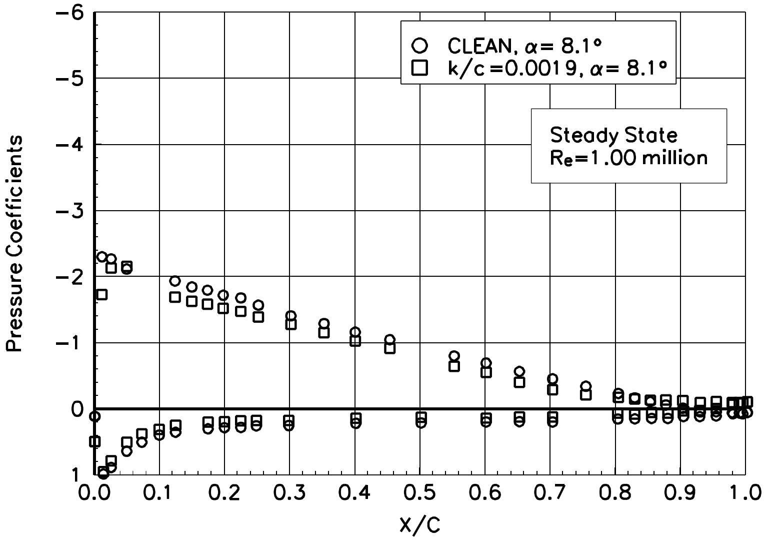

Figure B41. α = 8.1°

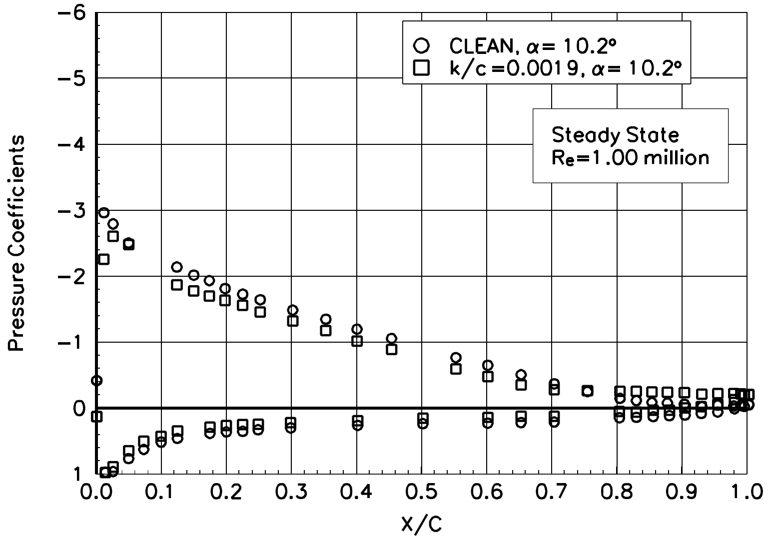

Figure B42. α = 10.2°

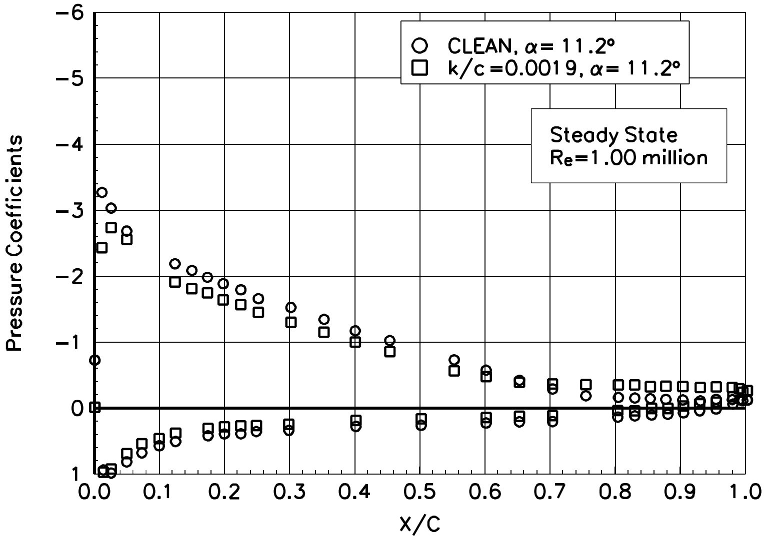

Figure B43. α = 11.2°

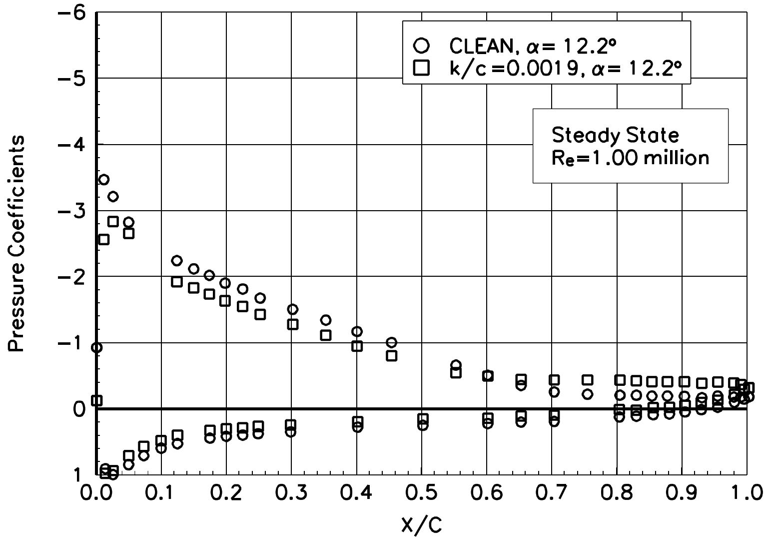

Figure B44. α = 12.2°

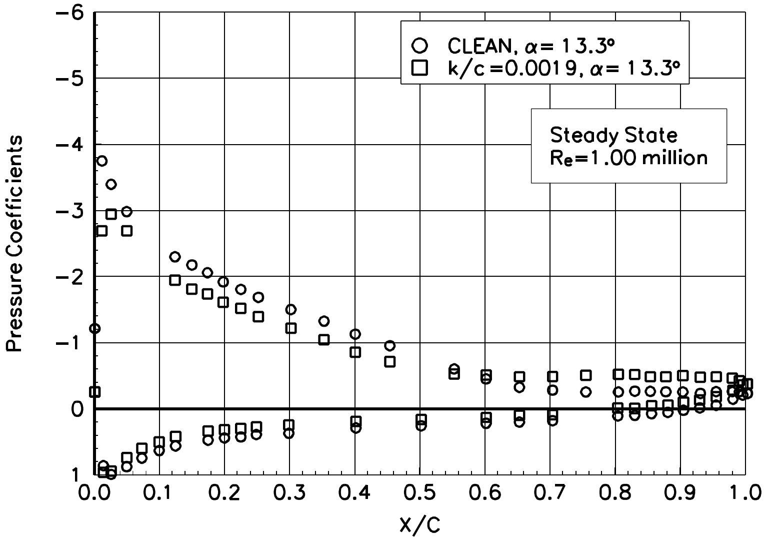

Figure B45. α = 13.3°

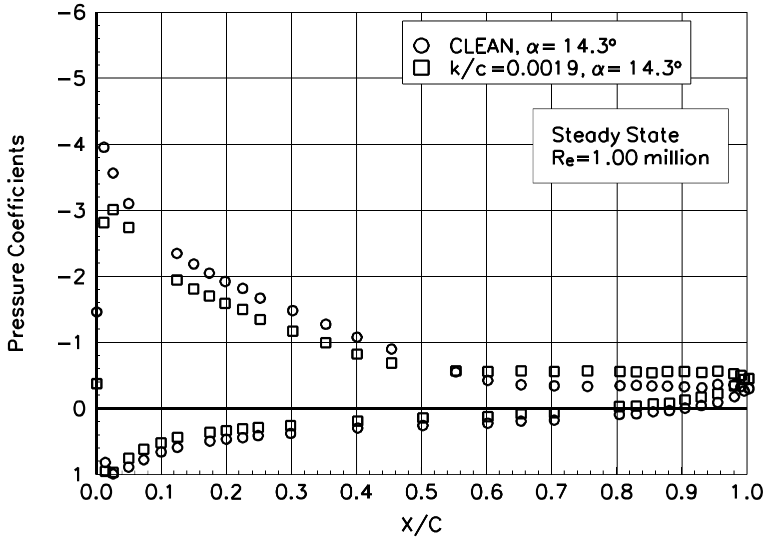

Figure B46. α = 14.3°

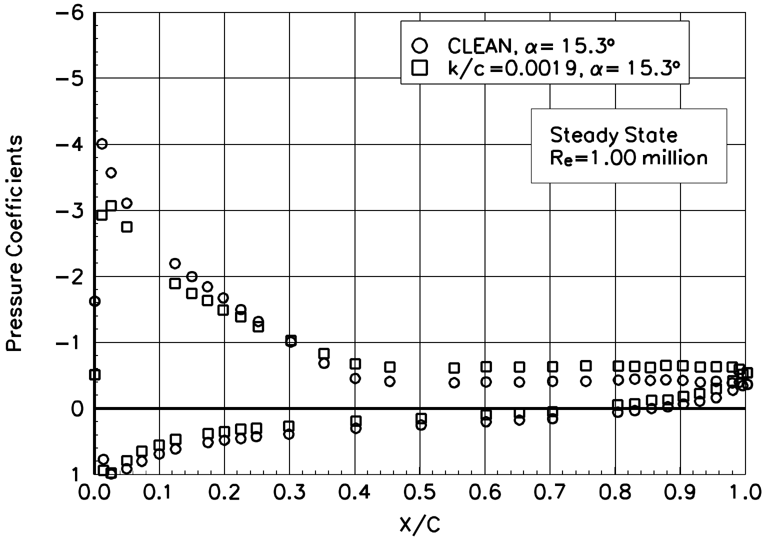

Figure B47. α = 15.3°

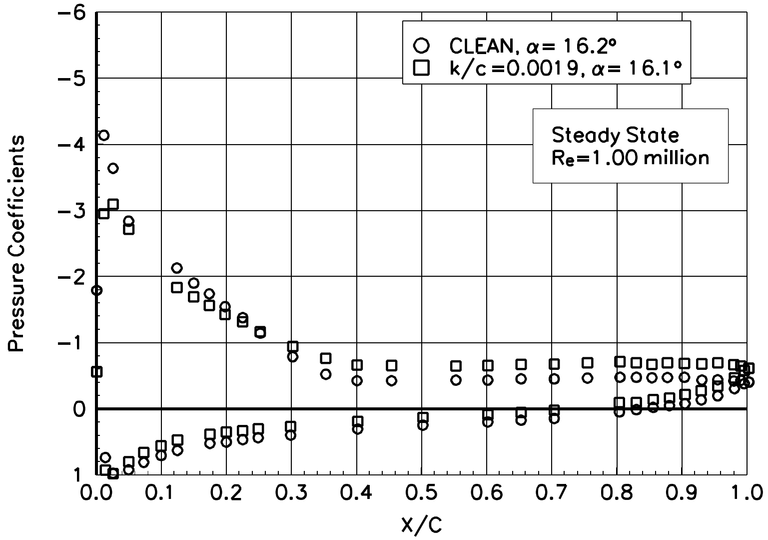

Figure B48. α = 16.2°

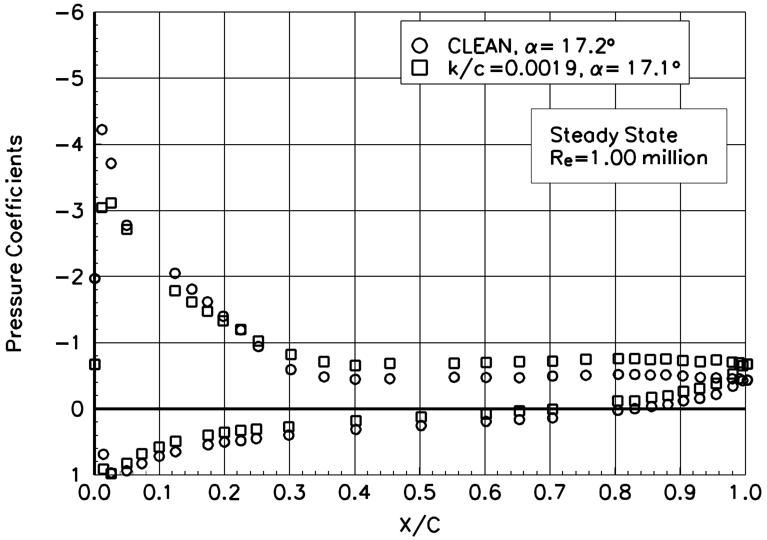

Figure B49. α = 17.2°

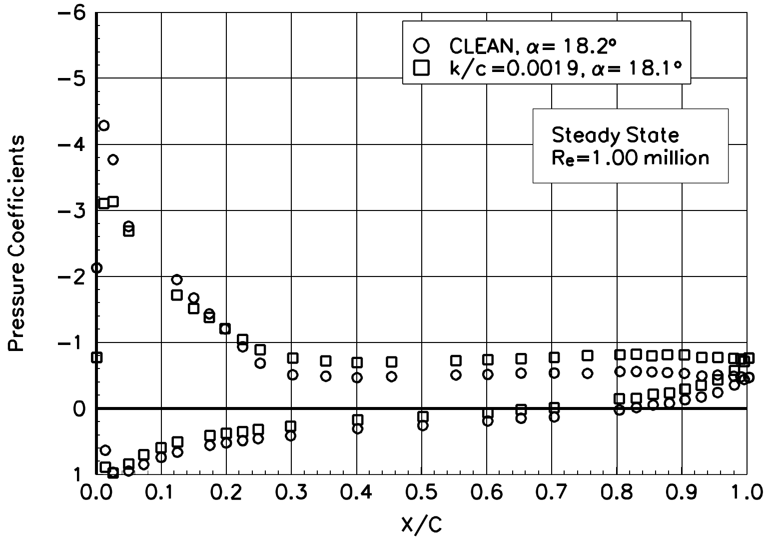

Figure B50. α = 18.2°

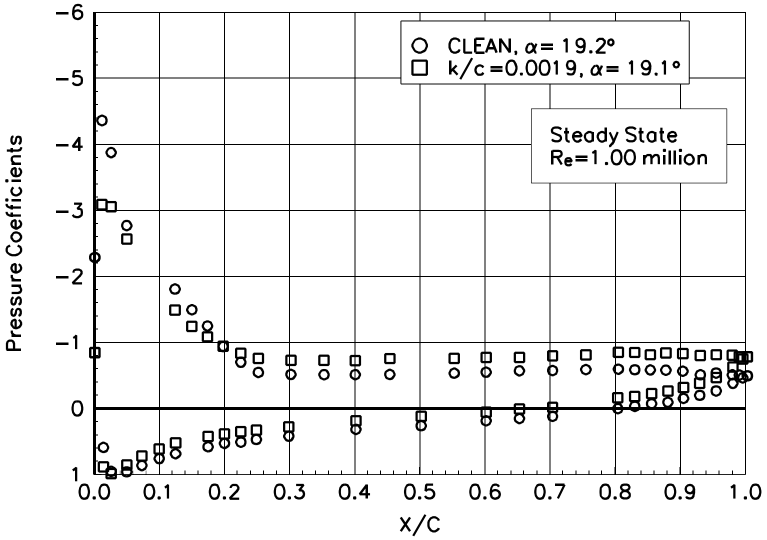

Figure B51. α = 19.2°

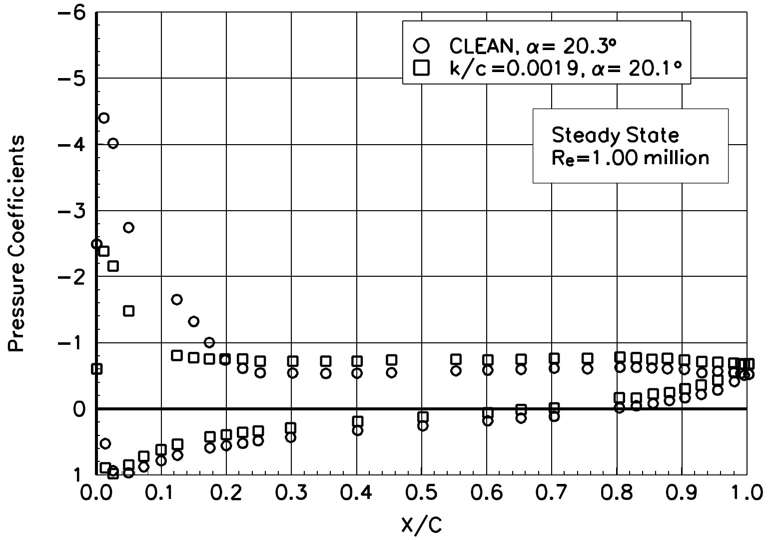

Figure B52. α = 20.3°

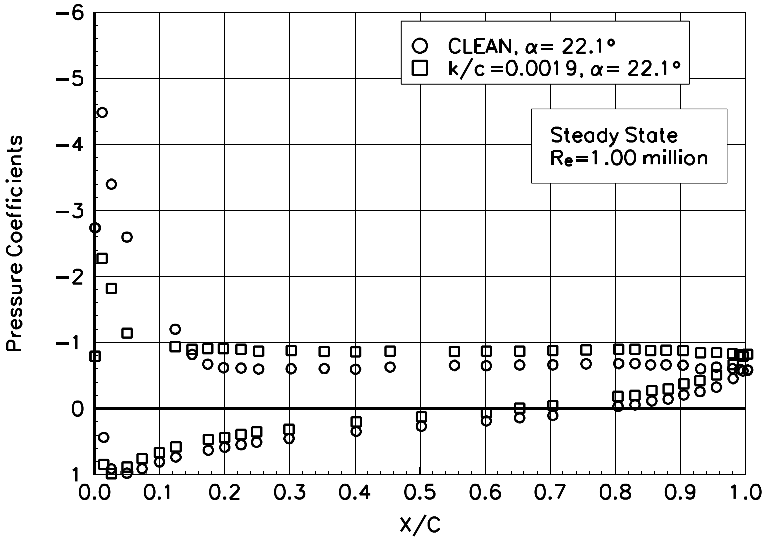

Figure B53. α = 22.1°

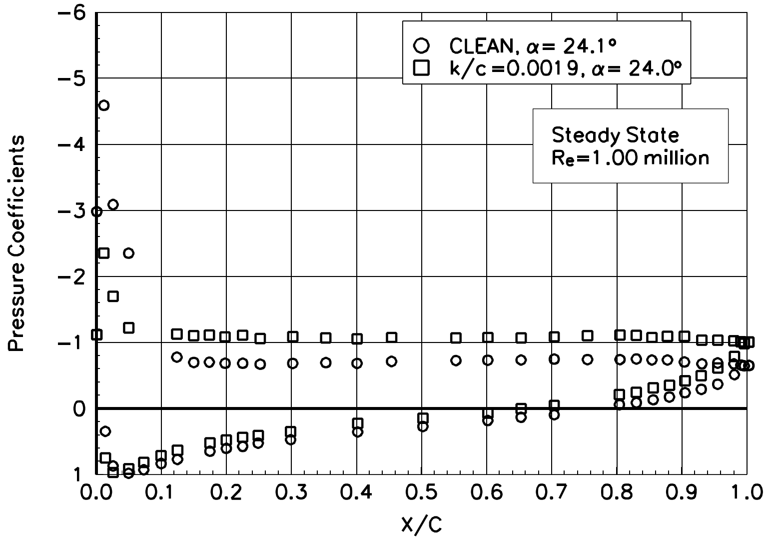

Figure B54. α = 24.1°

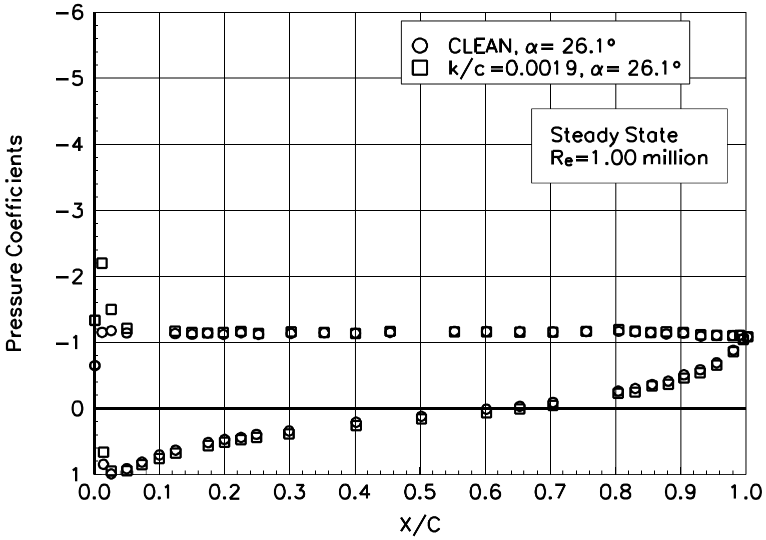

Figure B55. α = 26.1°

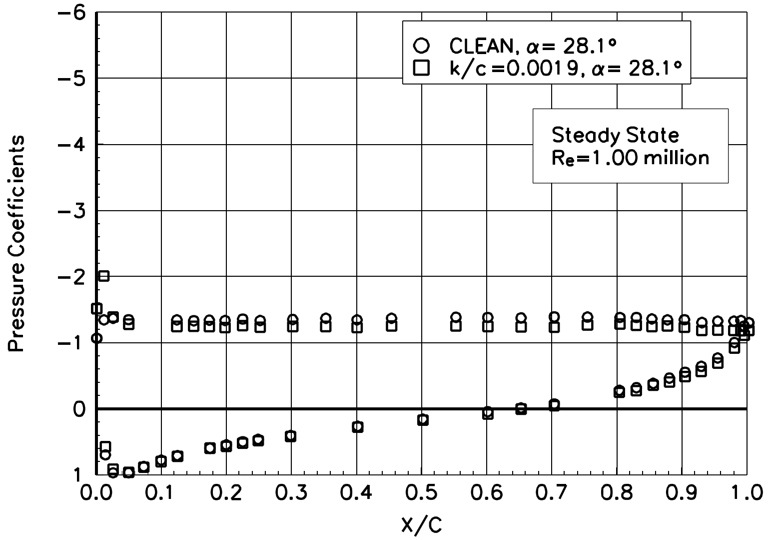

Figure B56. α = 28.1°

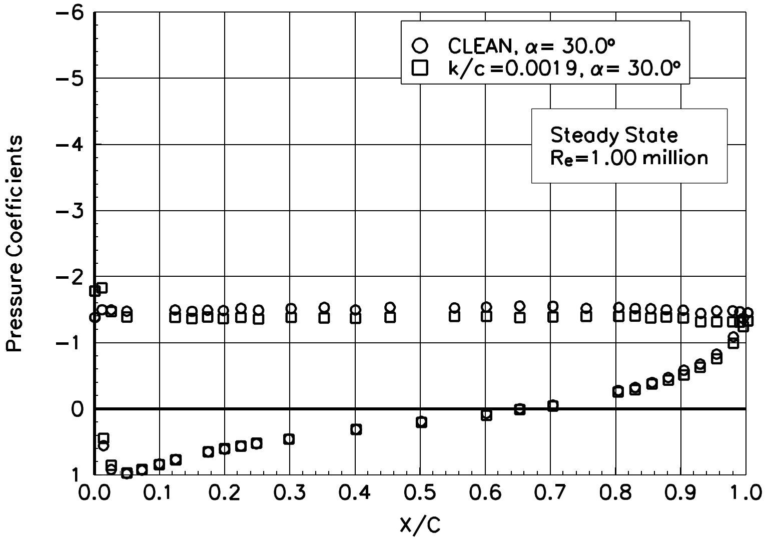

Figure B57. α = 30.0°

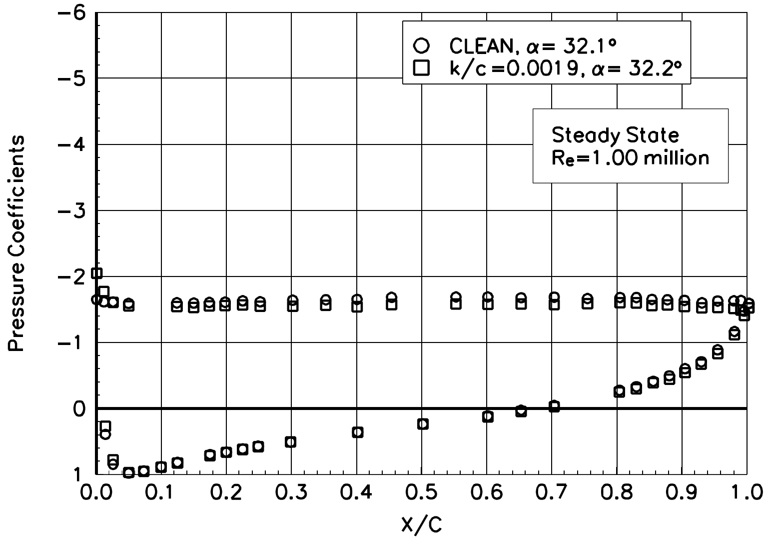

Figure B58. α = 32.1°

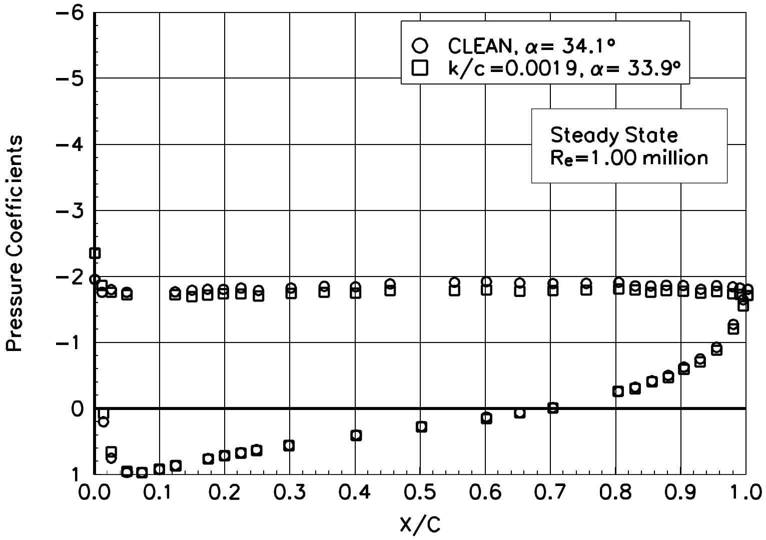

Figure B59. α = 34.1°

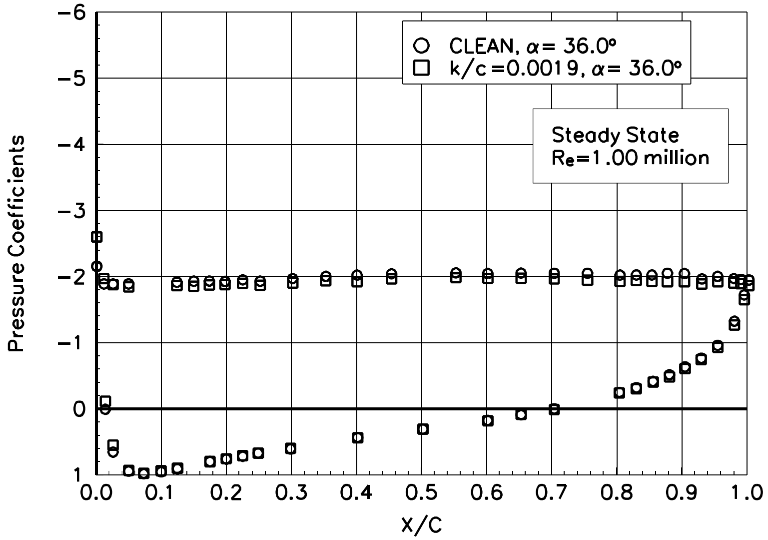

Figure B60. α = 36.0°

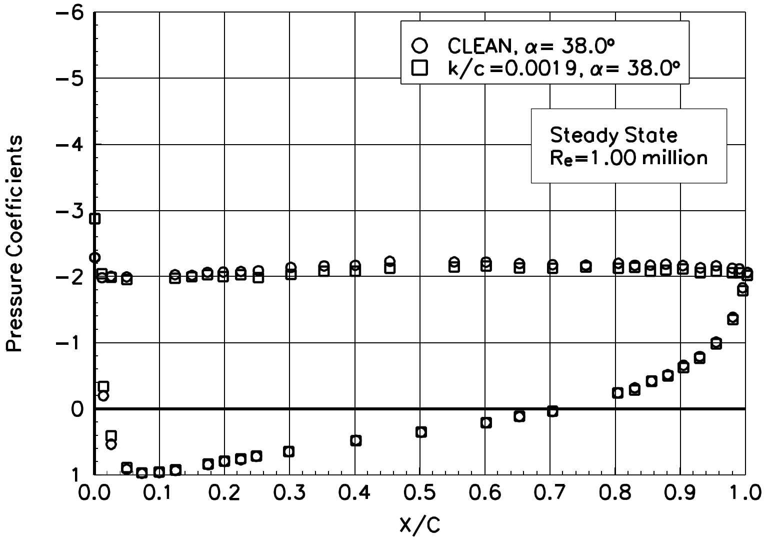

Figure B61. α = 38.0°

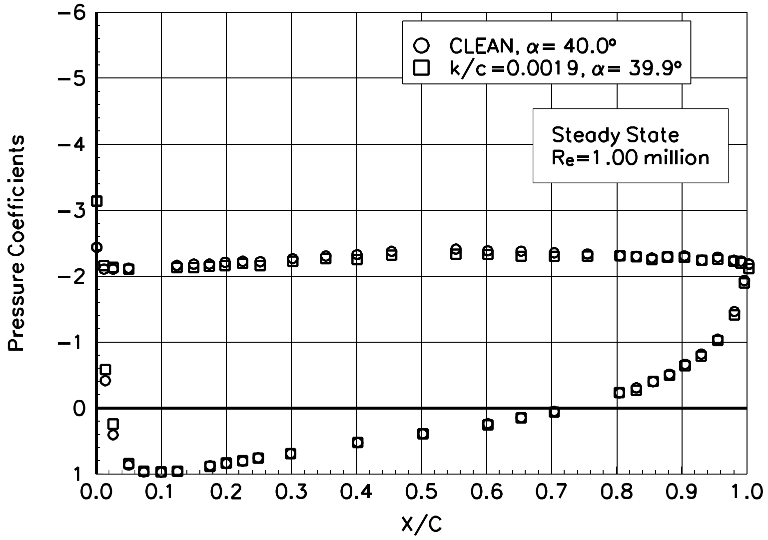

Figure B62. α = 40.0°

NACA 4415

Pressure Distributions, Steady State, Re = 1.25 million

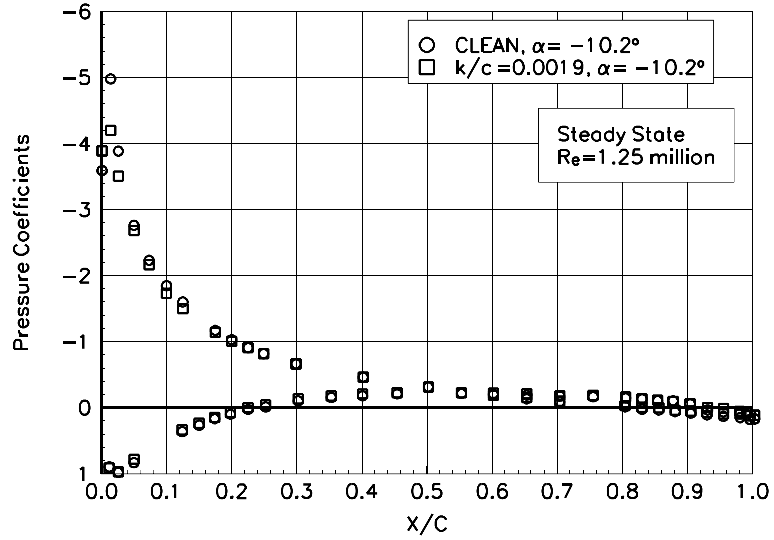

Figure B63. α = -10.2°

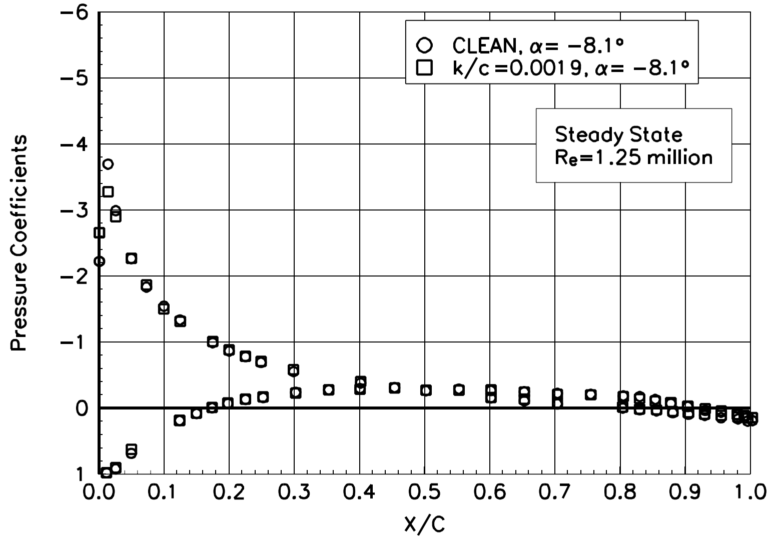

Figure B64. α = -8.1°

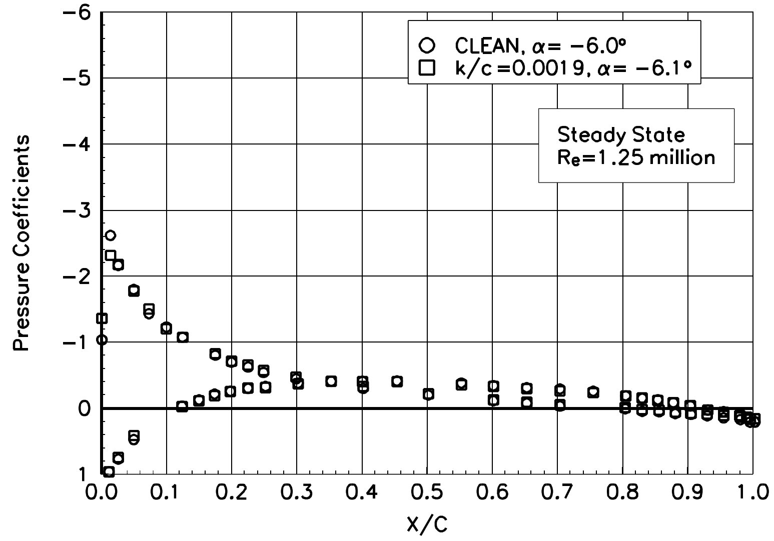

Figure B65. α = -6.0°

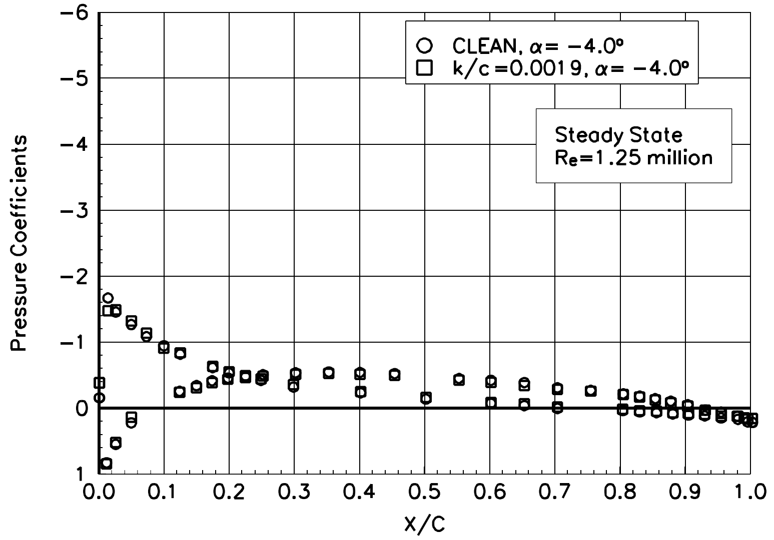

Figure B66. α = -4.0°

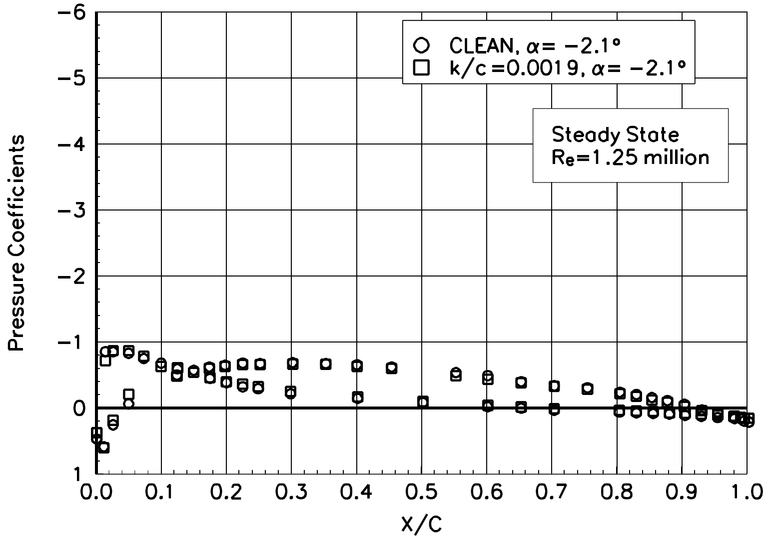

Figure B67. α = -2.1°

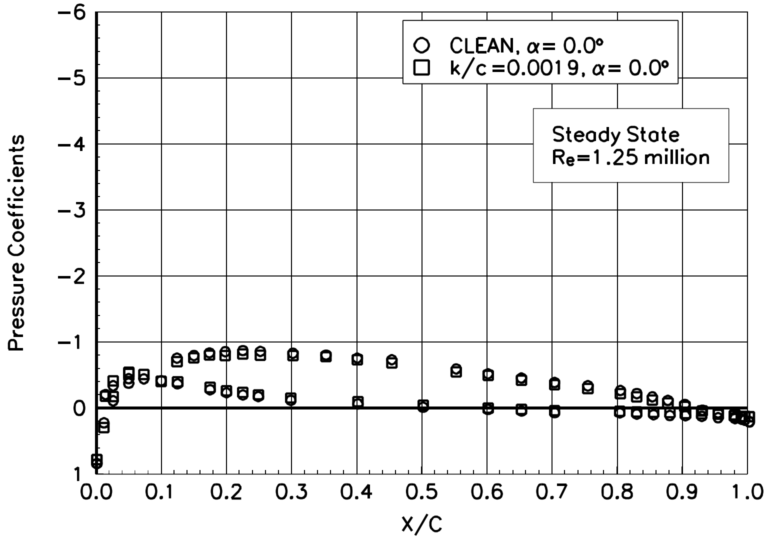

Figure B68. α = 0.0°

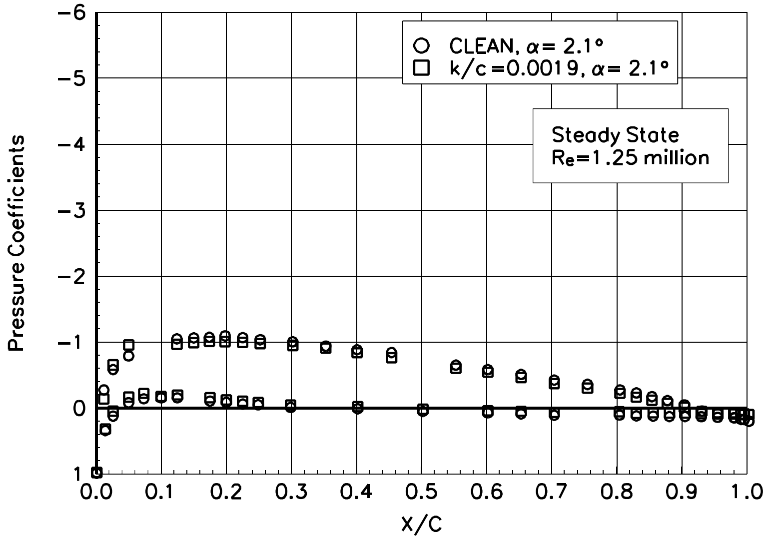

Figure B69. α = 2.1°

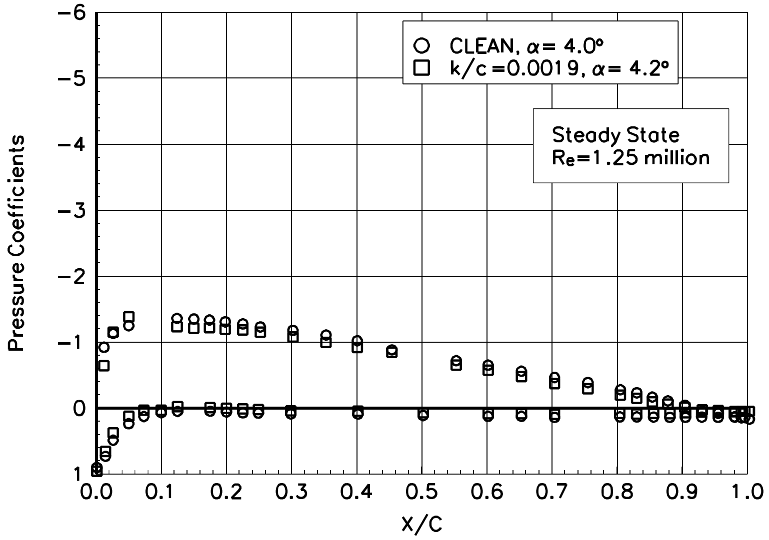

Figure B70. α = 4.0°

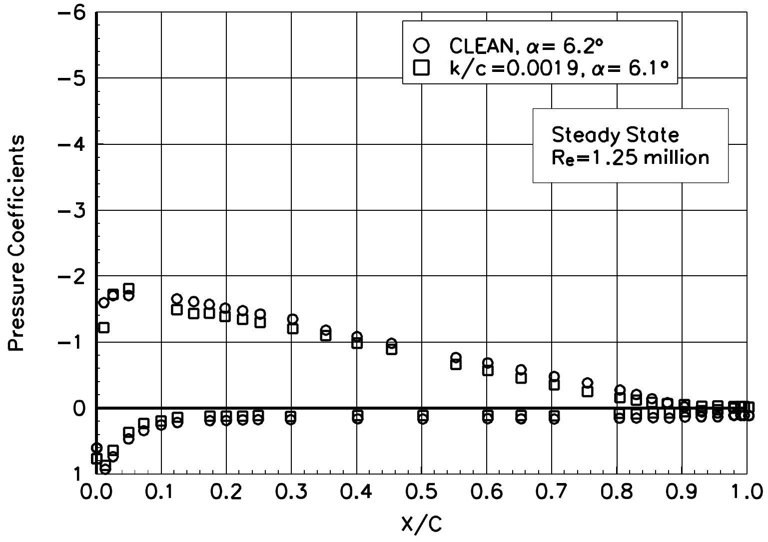

Figure B71. α = 6.2°

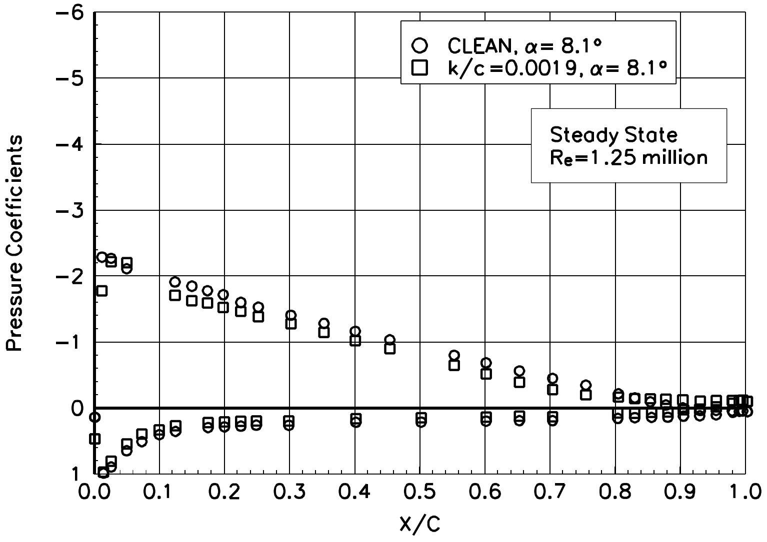

Figure B72. α = 8.1°

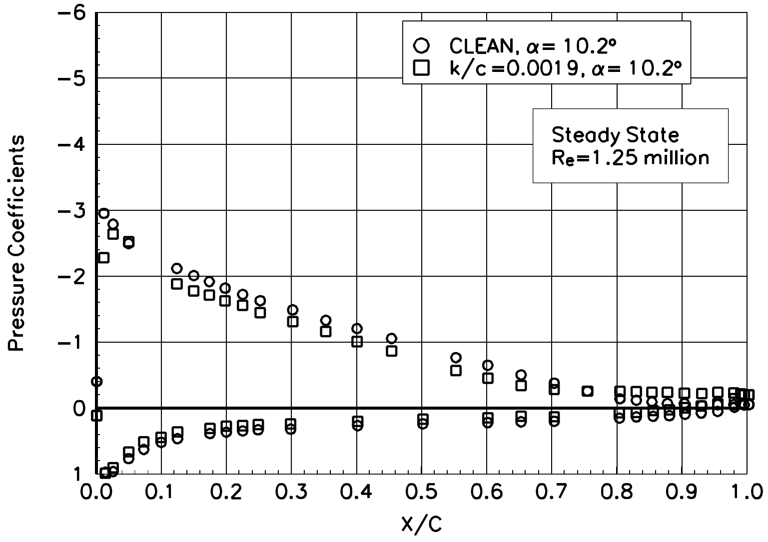

Figure B73. α = 10.2°

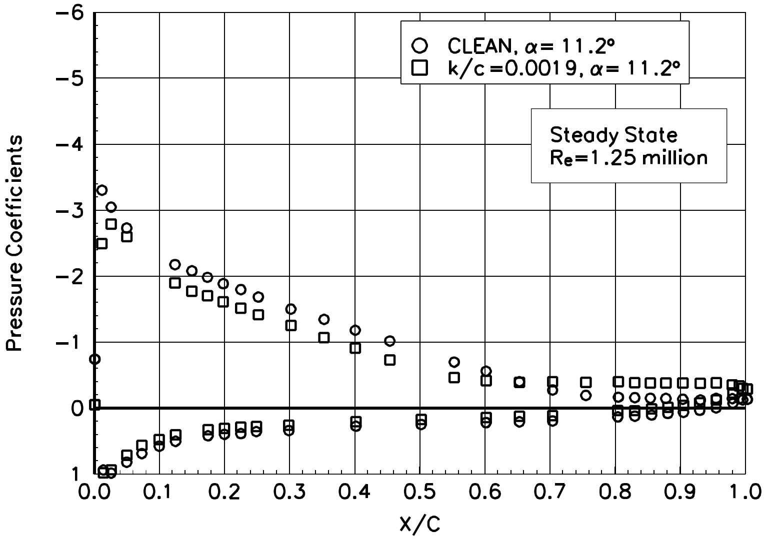

Figure B74. α = 11.2°

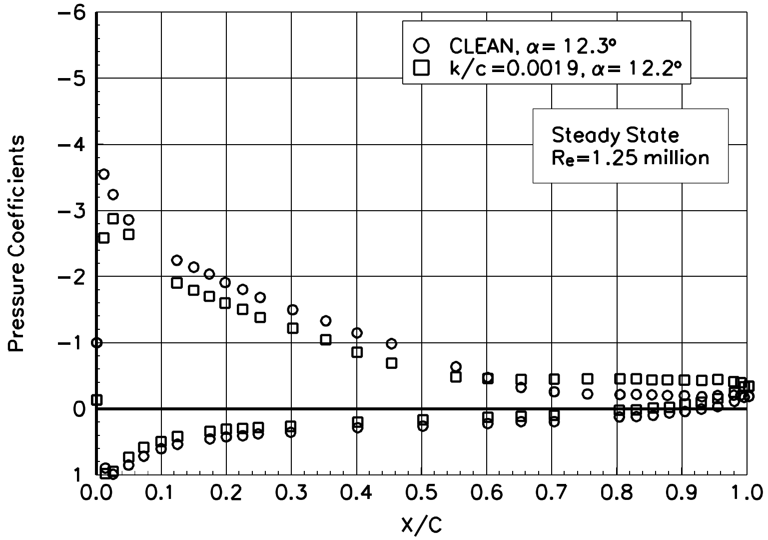

Figure B75. α = 12.3°

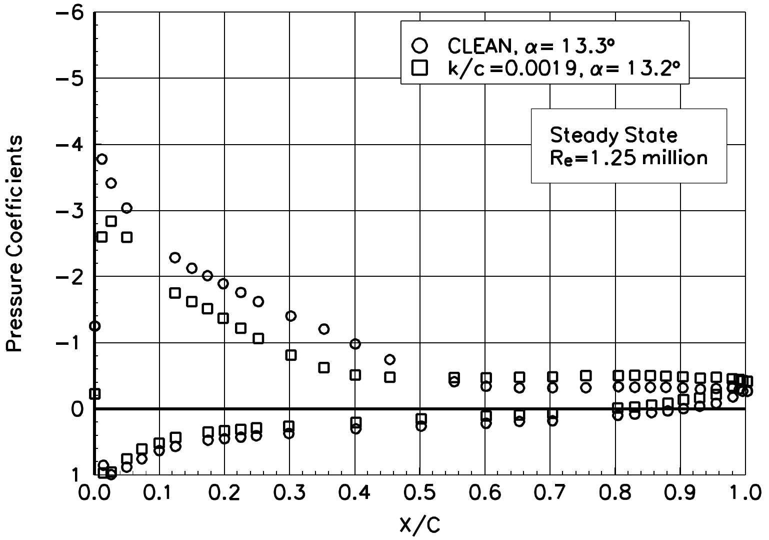

Figure B76. α = 13.3°

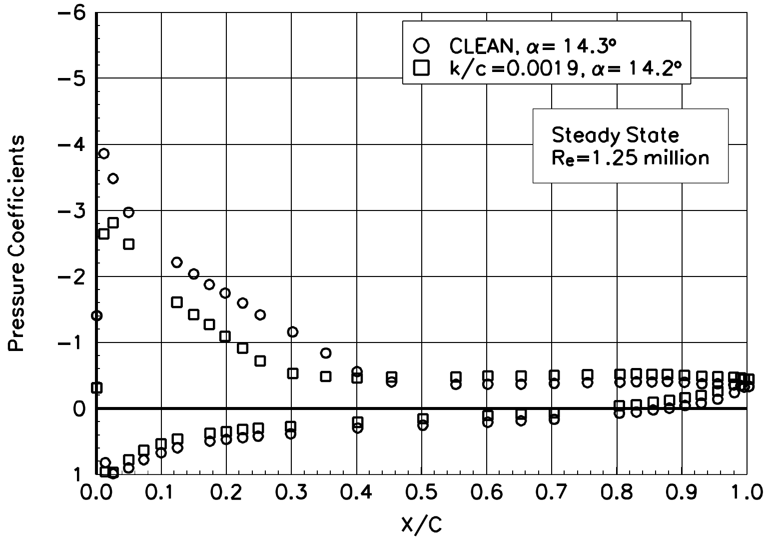

Figure B77. α = 14.3°

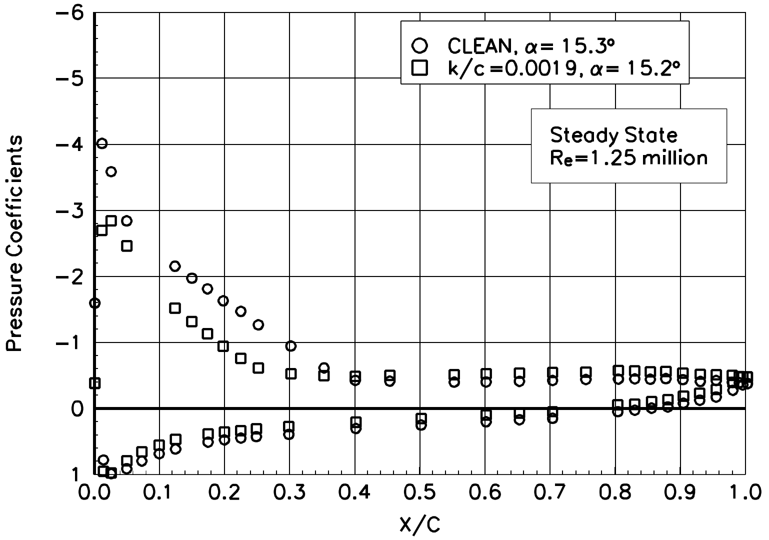

Figure B78. α = 15.3°

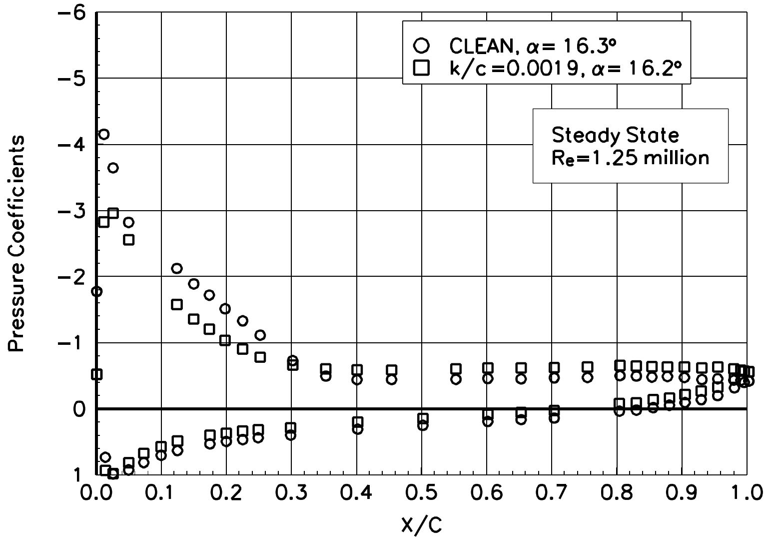

Figure B79. α = 16.3°

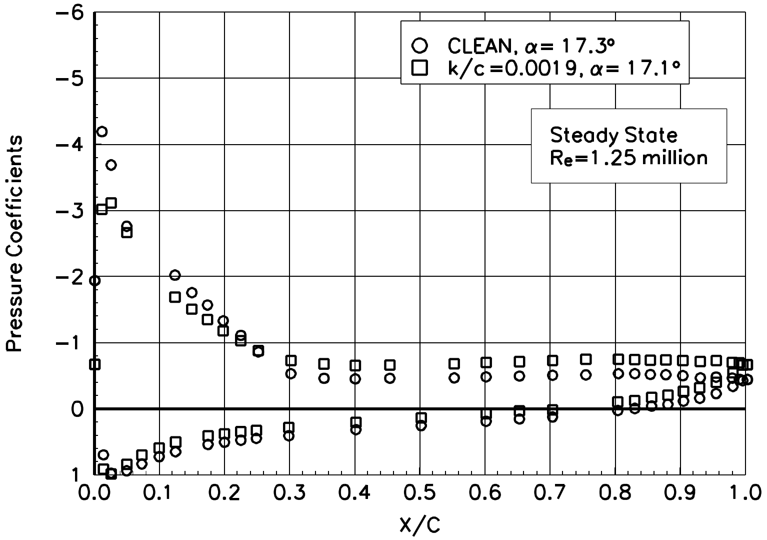

Figure B80. α = 17.3°

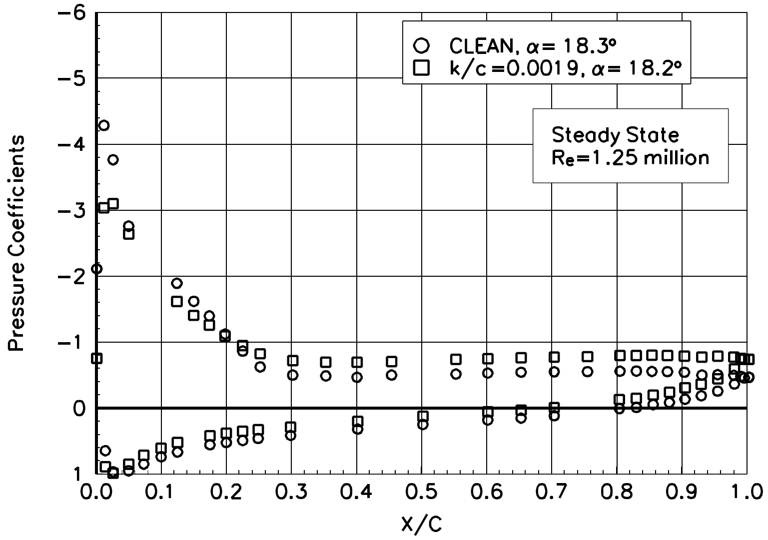

Figure B81. α = 18.3°

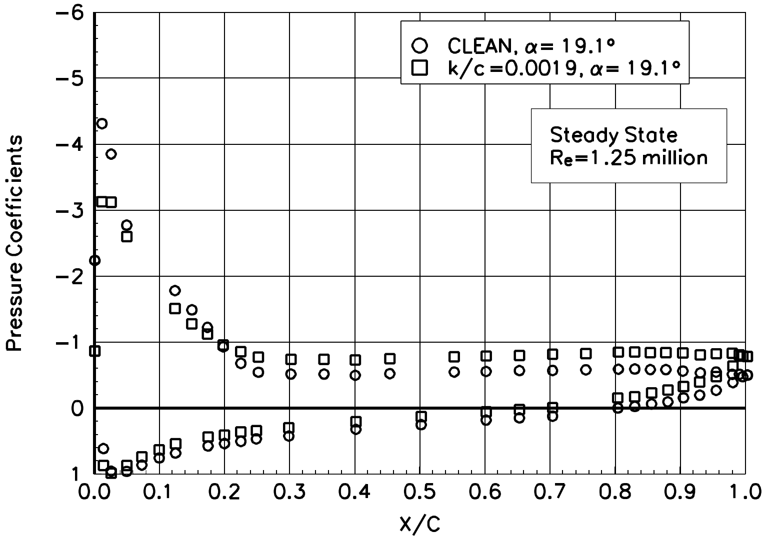

Figure B82. α = 19.1°

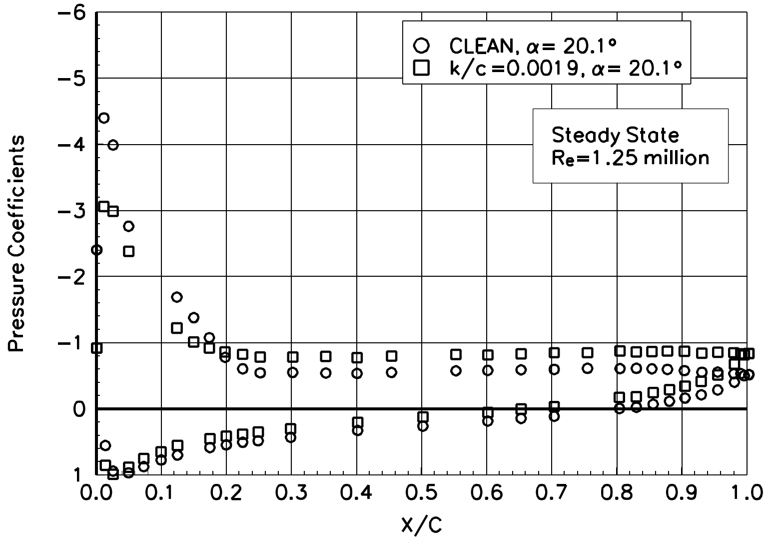

Figure B83. α **= 20.1°**

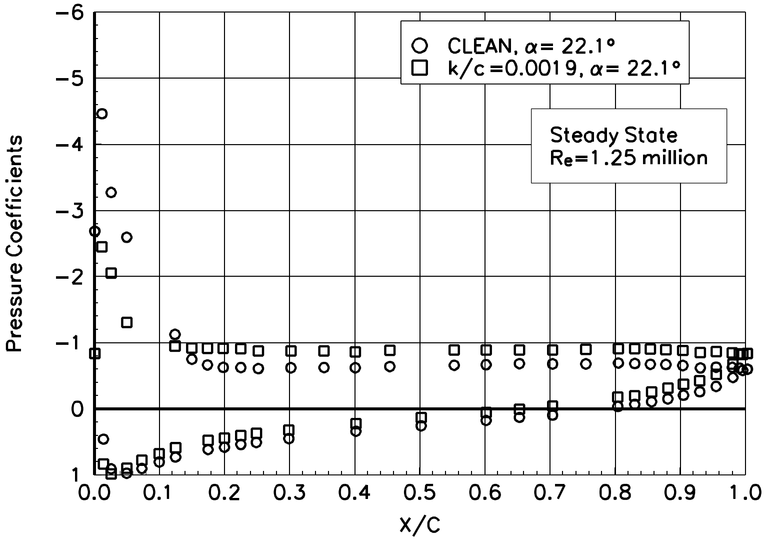

Figure B84. α **= 22.1°**

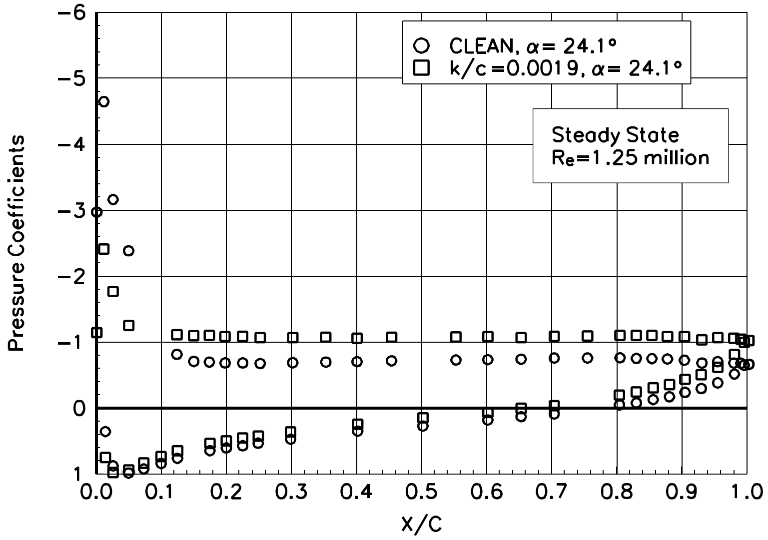

Figure B85. α **= 24.1°**

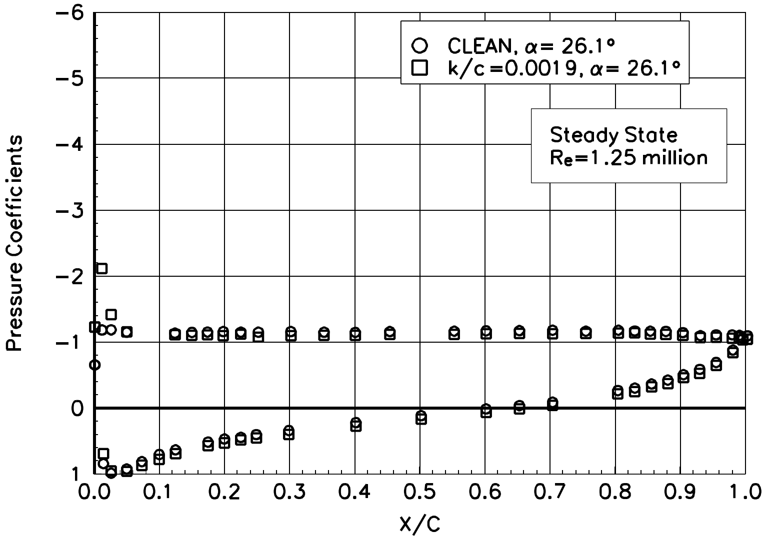

Figure B86. α **= 26.1°**

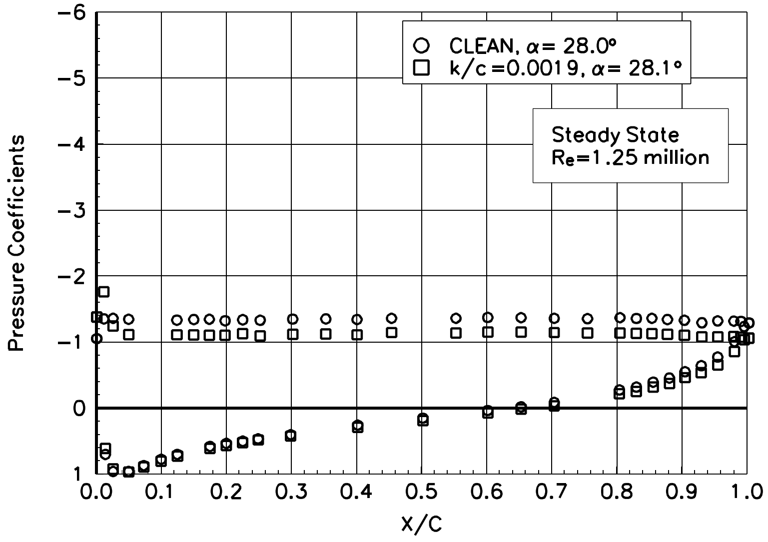

Figure B87. α = 28.0°

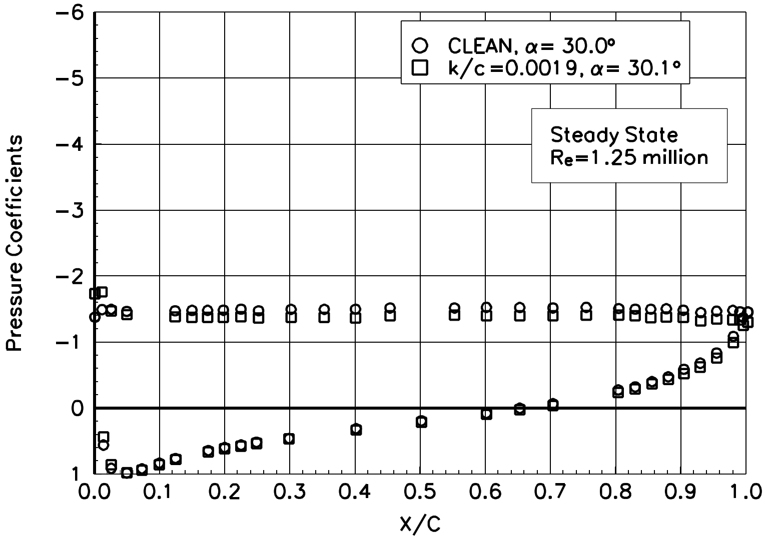

Figure B88. α = 30.0°

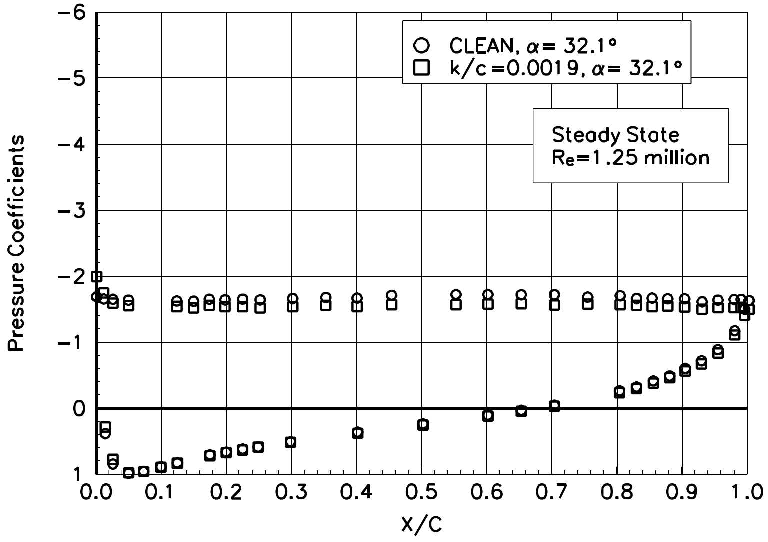

Figure B89. α = 32.1°

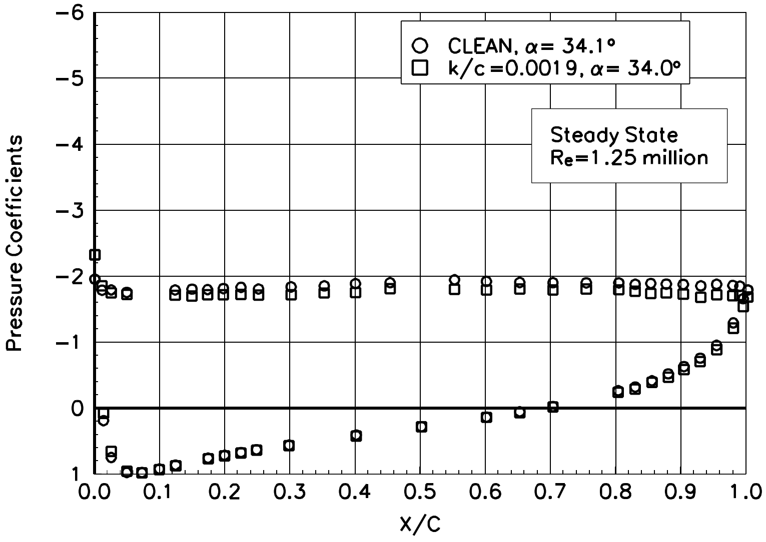

Figure B90. α = 34.1°

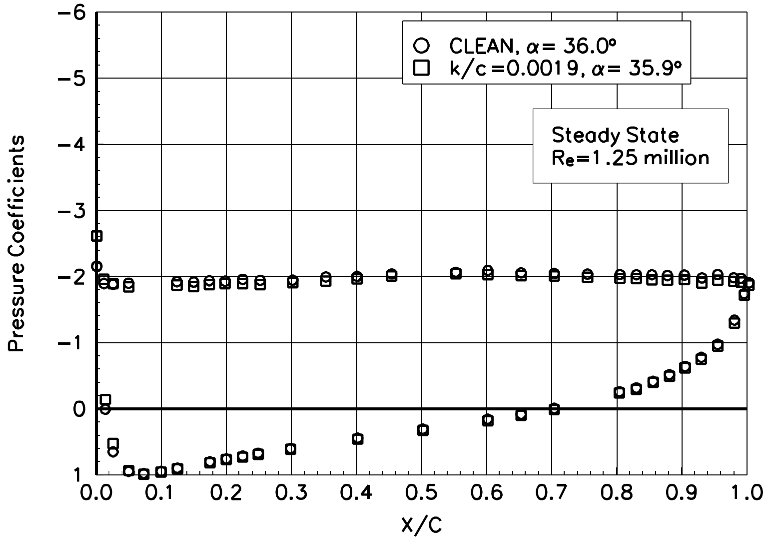

Figure B91. α = 36.0°

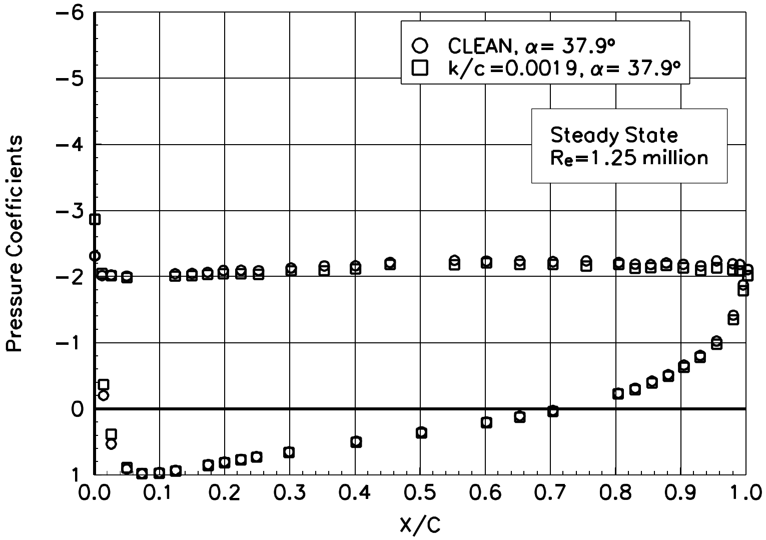

Figure B92. α = 37.9°

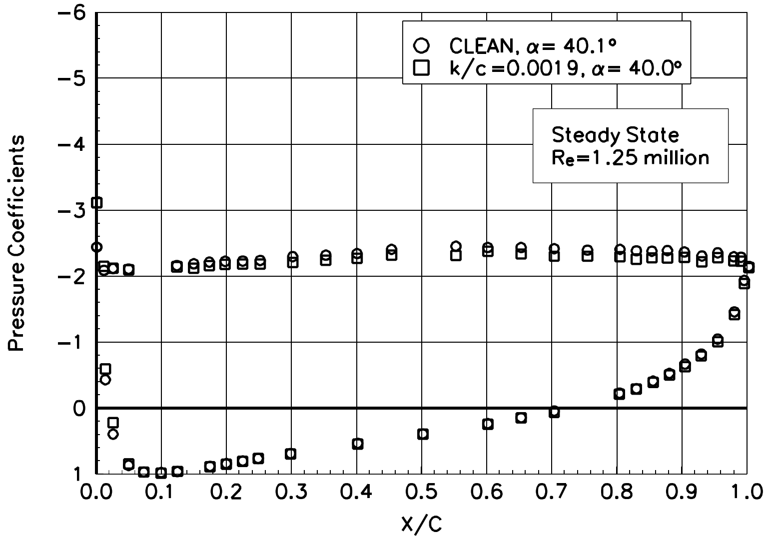

Figure B93. α = 40.1°

NACA 4415

Pressure Distributions, Steady State, Re = 1.5 million

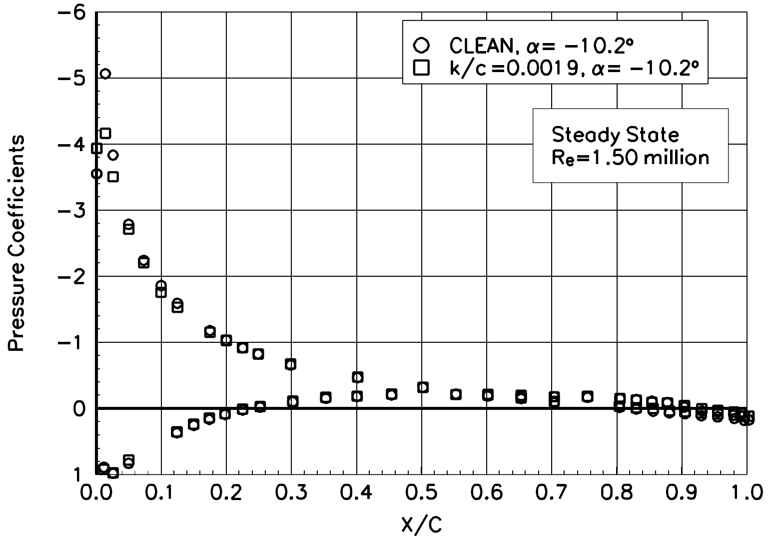

Figure B94. α = -10.2°

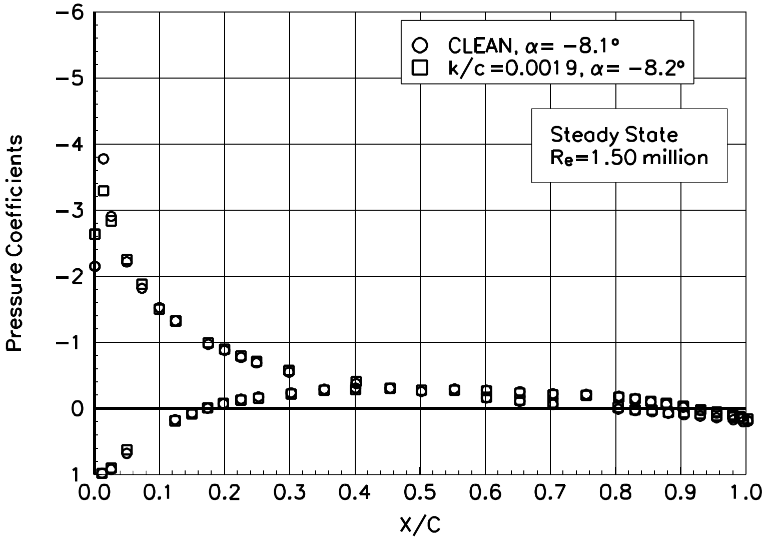

Figure B95. α = -8.1°

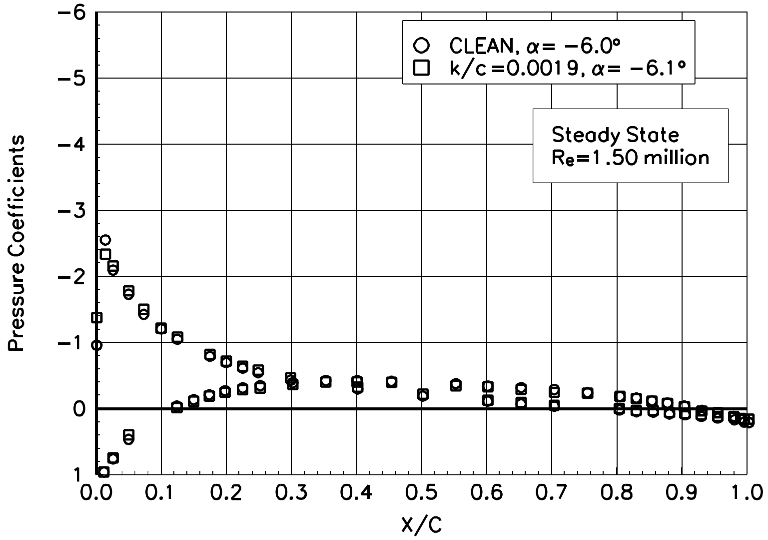

Figure B96. α = -6.0°

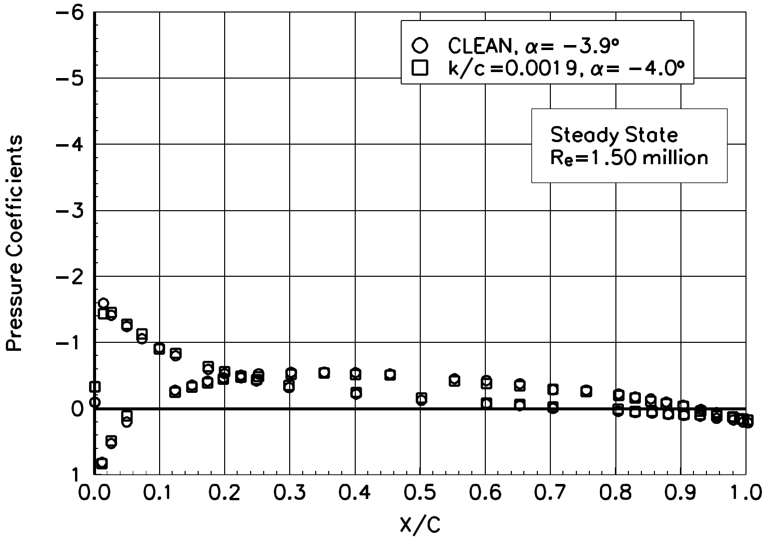

Figure B97. α = -3.9°

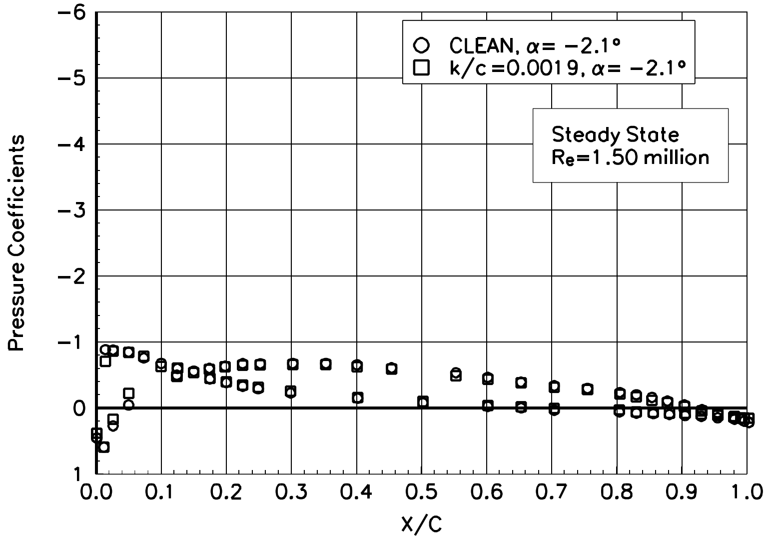

Figure B98. α = -2.1°

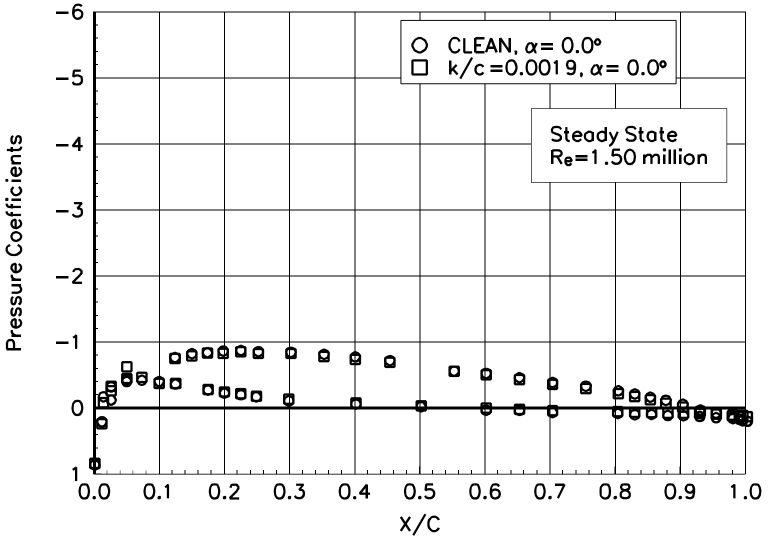

Figure B99. α = 0.0°

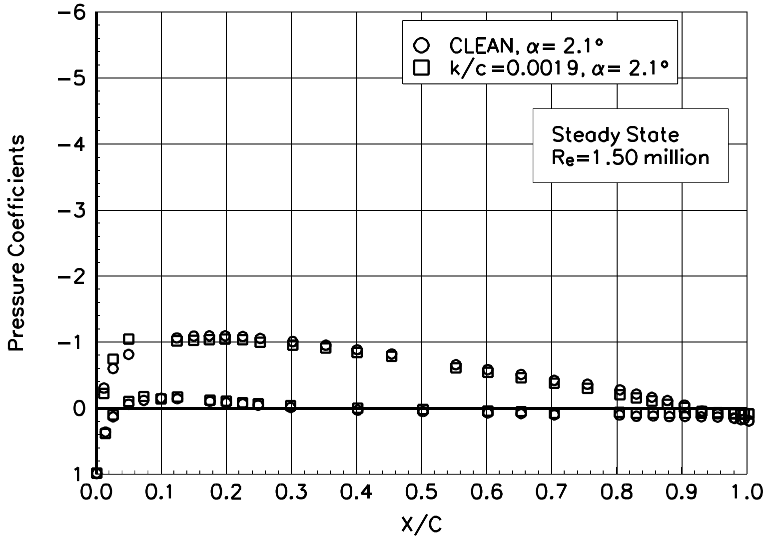

Figure B100. α = 2.1°

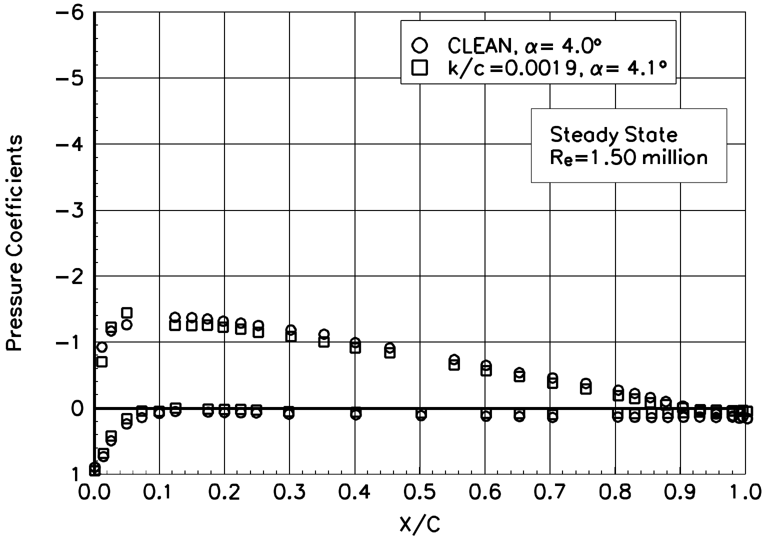

Figure B101. α = 4.0°

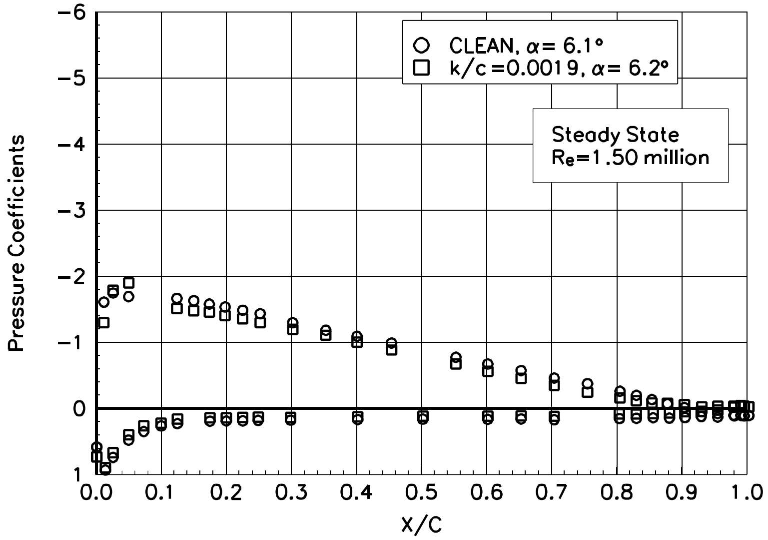

Figure B102. α = 6.1°

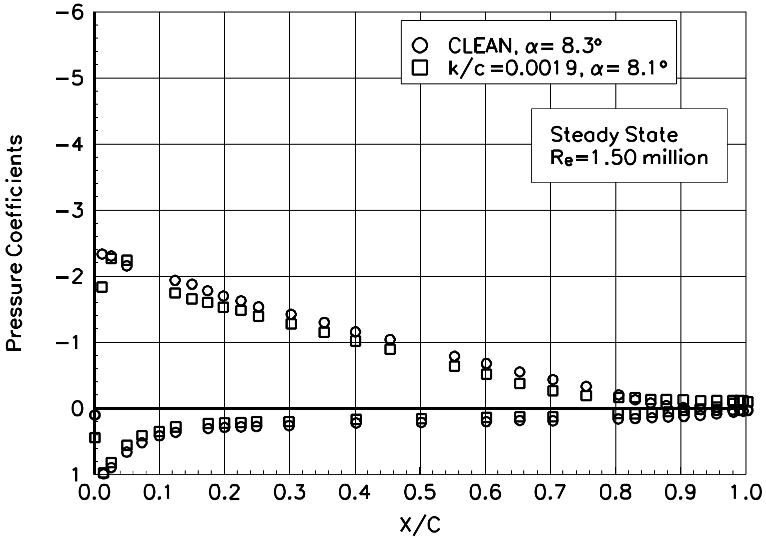

Figure B103. α = 8.3°

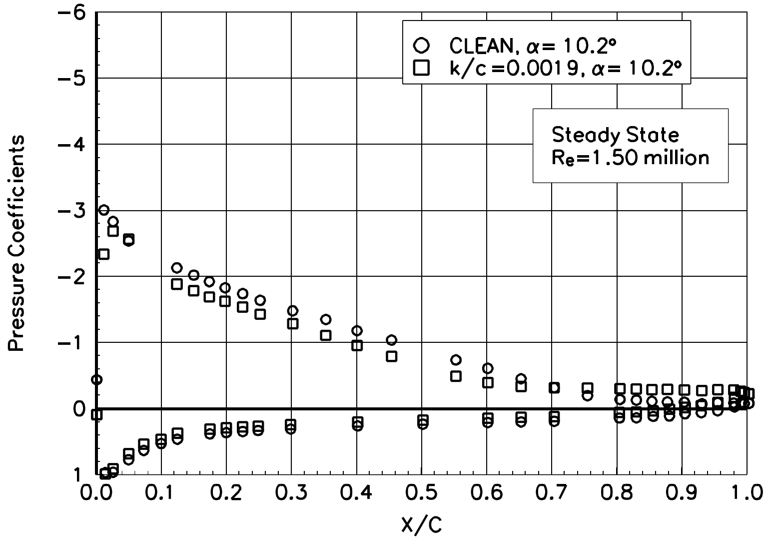

Figure B104. α = 10.2°

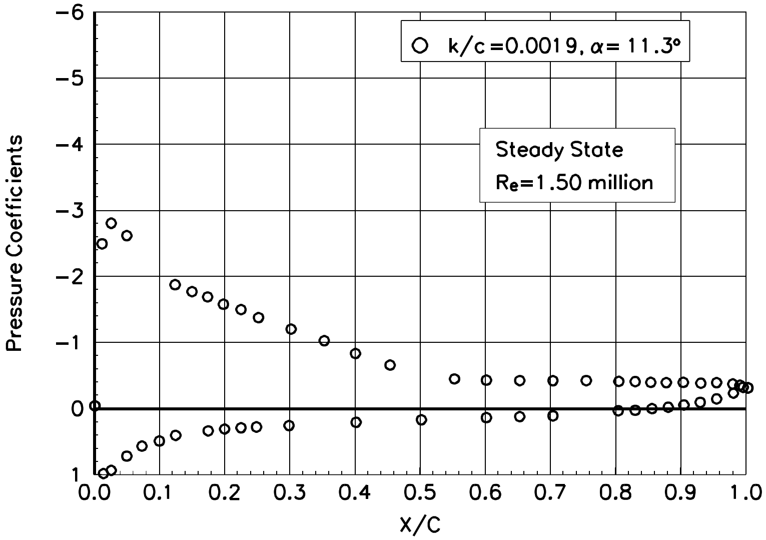

Figure B105. α = 11.3°

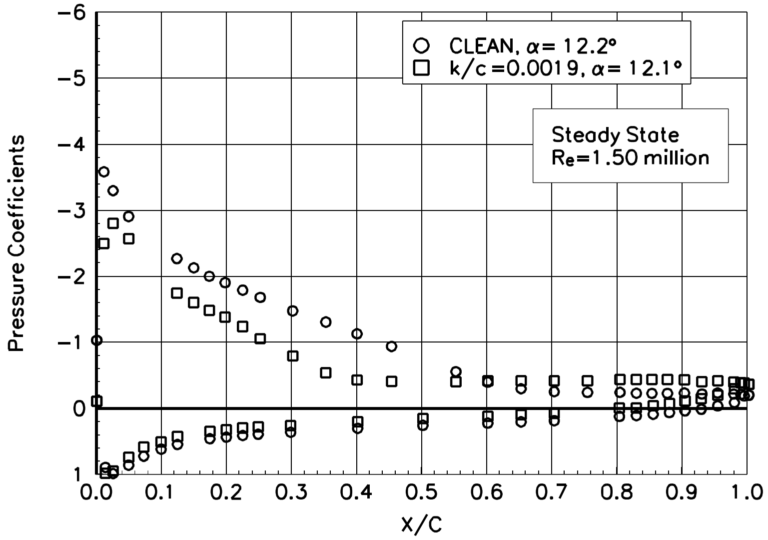

Figure B106. α = 12.2°

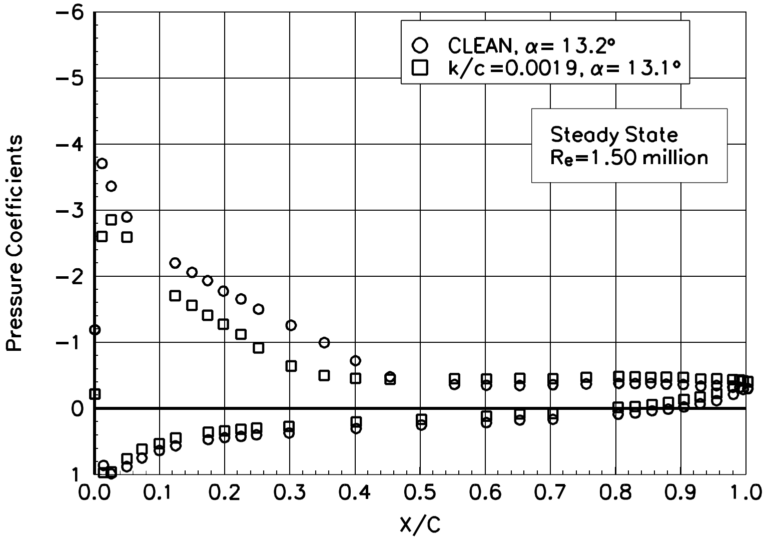

Figure B107. α = 13.2°

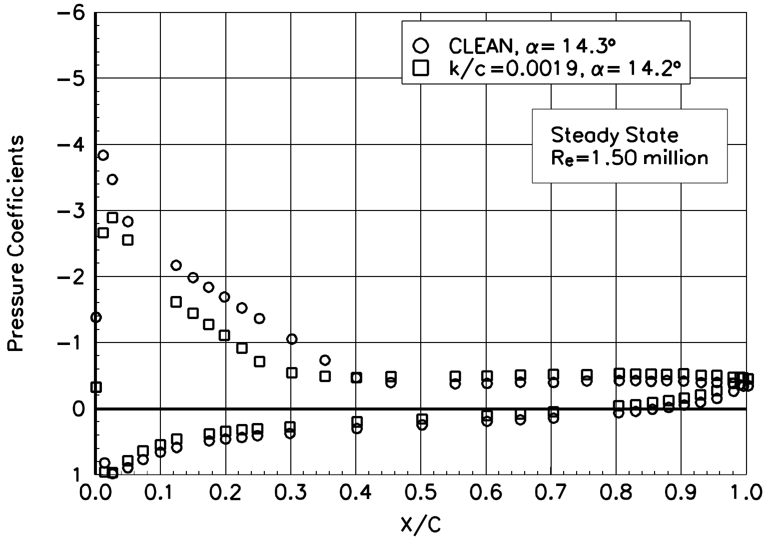

Figure B108. α = 14.3°

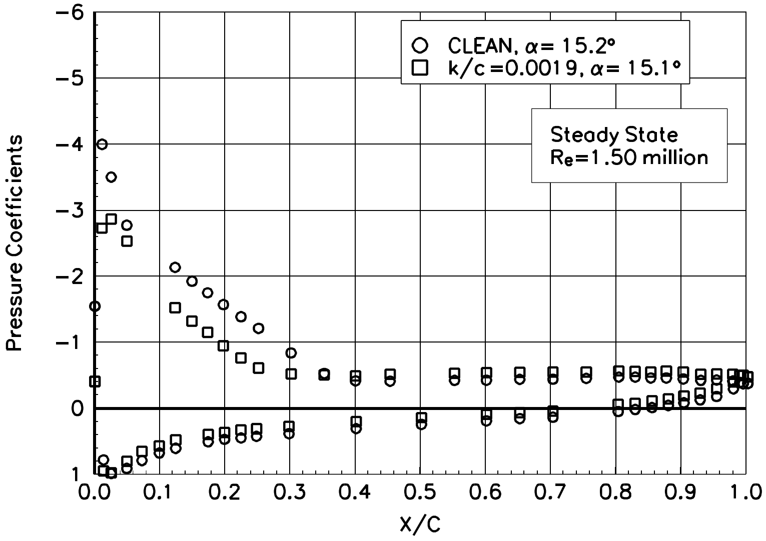

Figure B109. α = 15.2°

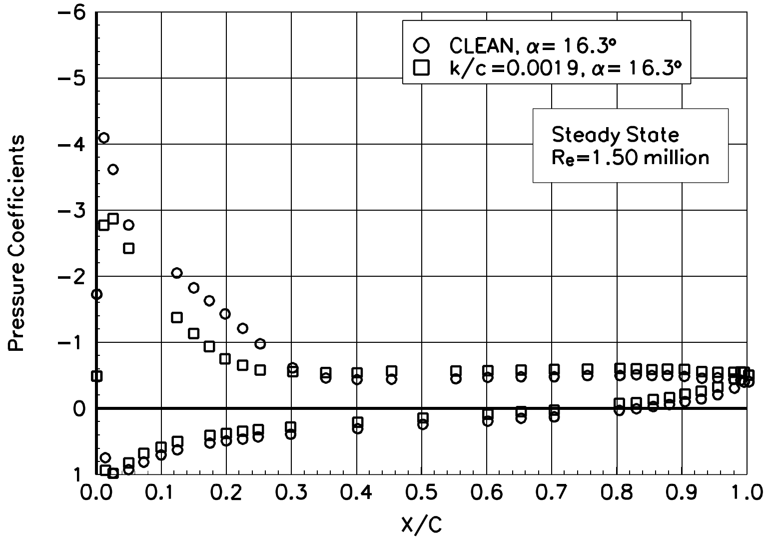

Figure B110. α = 16.3°

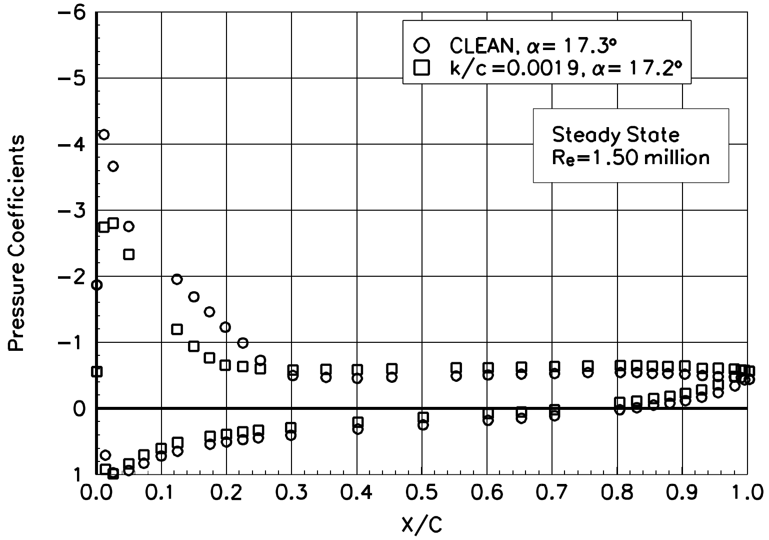

Figure B111. α = 17.3°

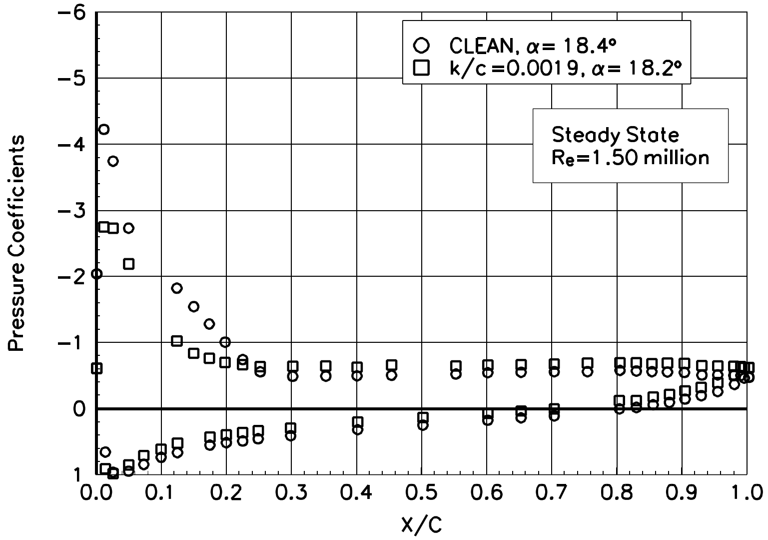

Figure B112. α = 18.4°

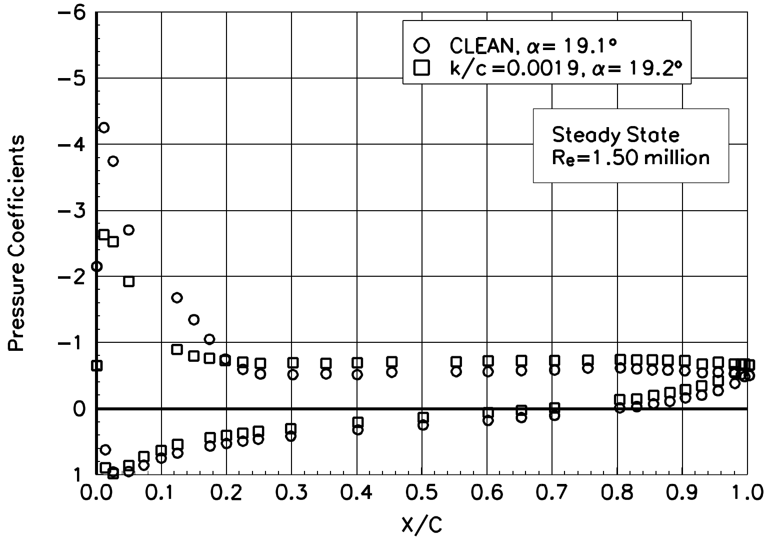

Figure B113. α = 19.1°

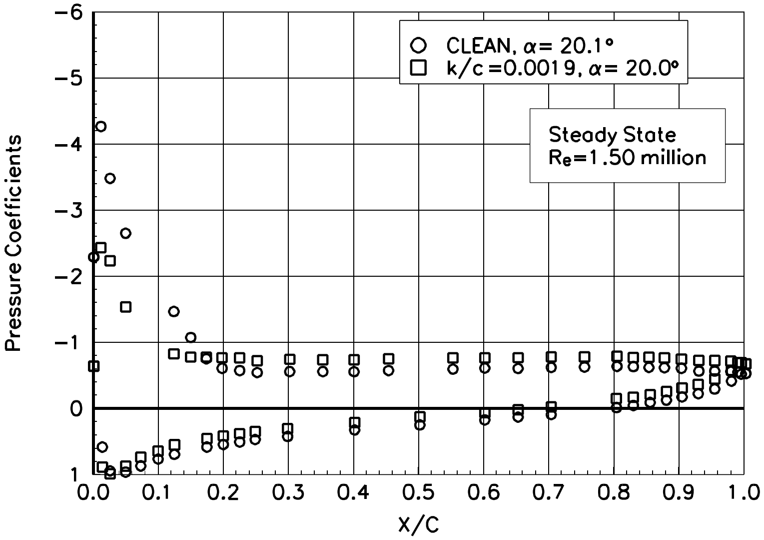

Figure B114. α = 20.1°

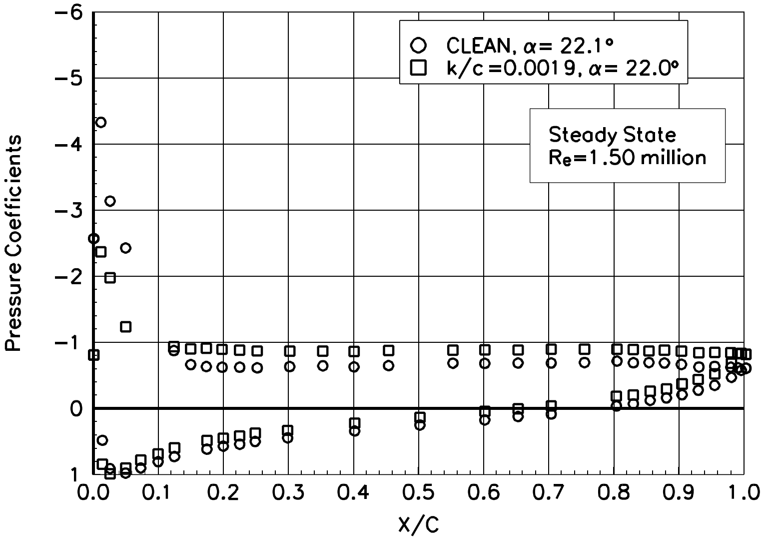

Figure B115. α = 22.1°

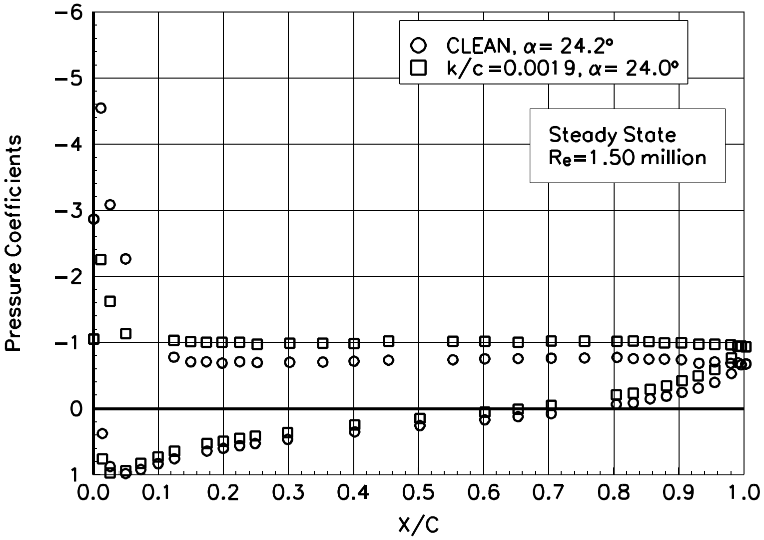

Figure B116. α = 24.2°

Appendix C: Unsteady Integrated Coefficients

List of Figures Page

Unsteady Airfoil Characteristics

±5.5° Sine, Re = 0.75 million

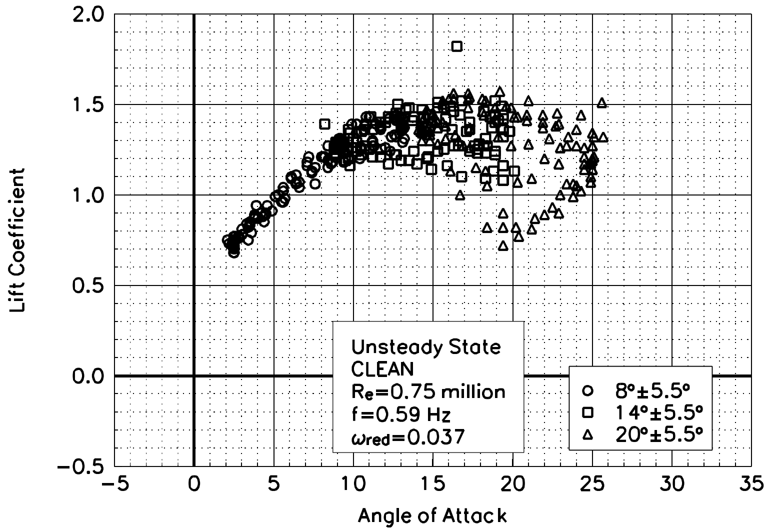

Figure C1. Lift coefficient vs α.

NACA 4415
Clean
Re=0.75 million
$\omega_{reduced}$=0.037

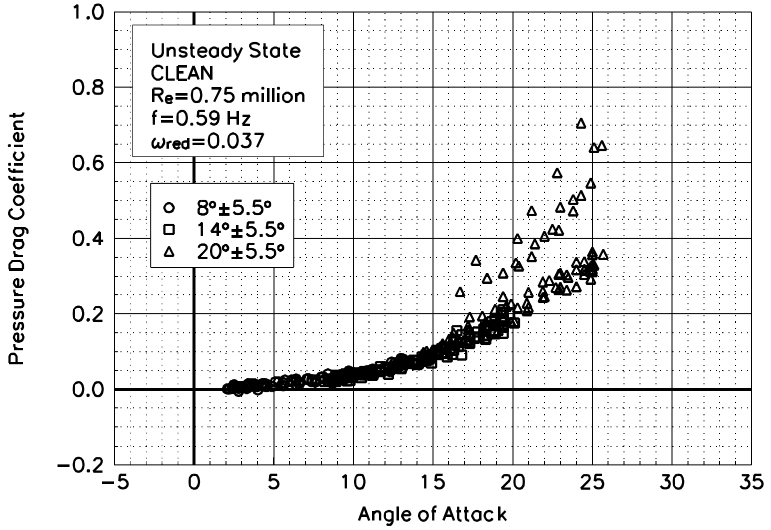

Figure C2. Pressure drag coefficient vs α.

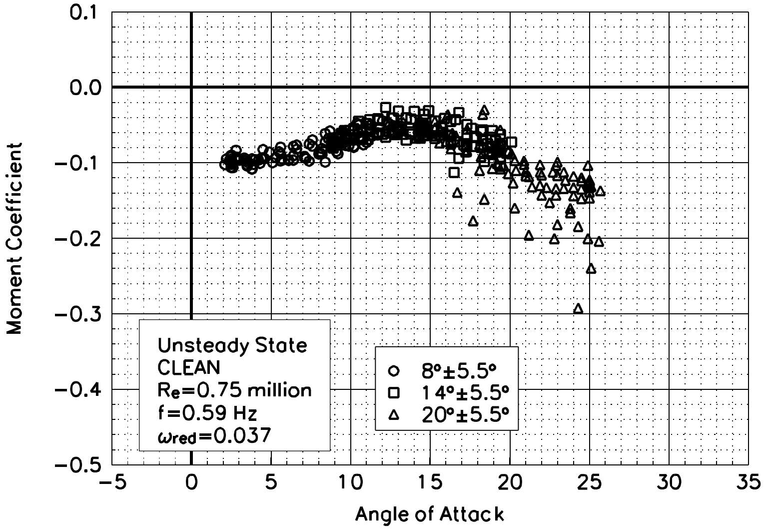

Figure C3. Moment coefficient vs α.

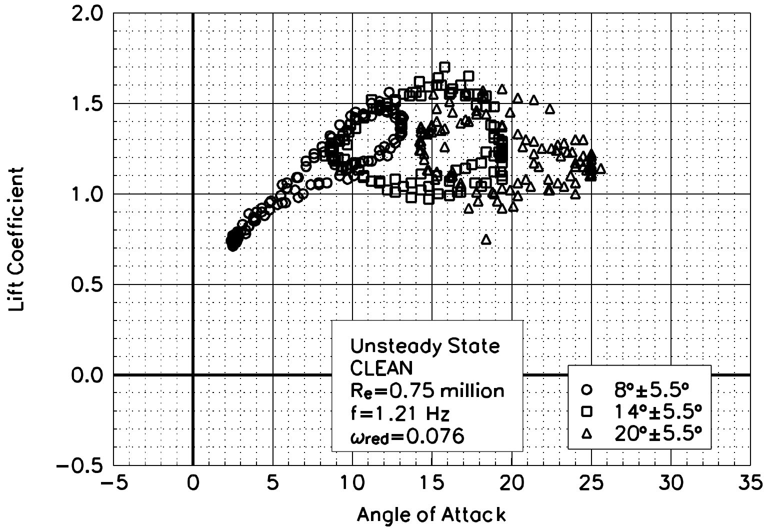

Figure C4. Lift coefficient vs α.

NACA 4415
Clean
Re=0.75 million
$\omega_{reduced}$=0.076

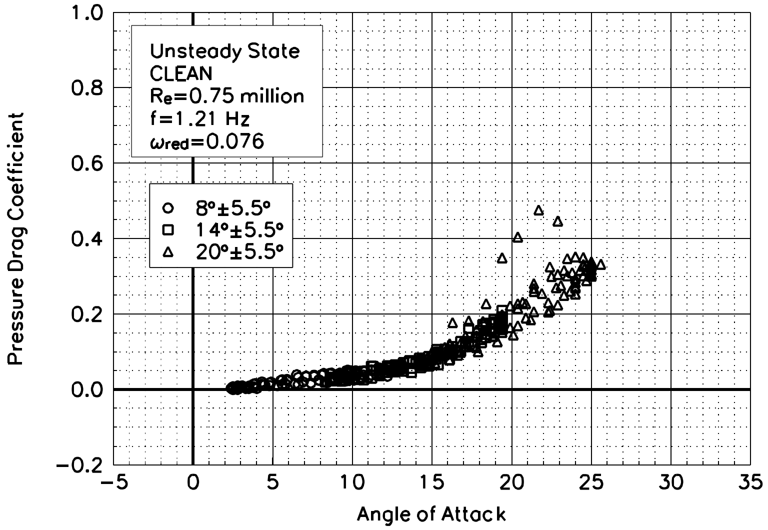

Figure C5. Pressure drag coefficient vs α.

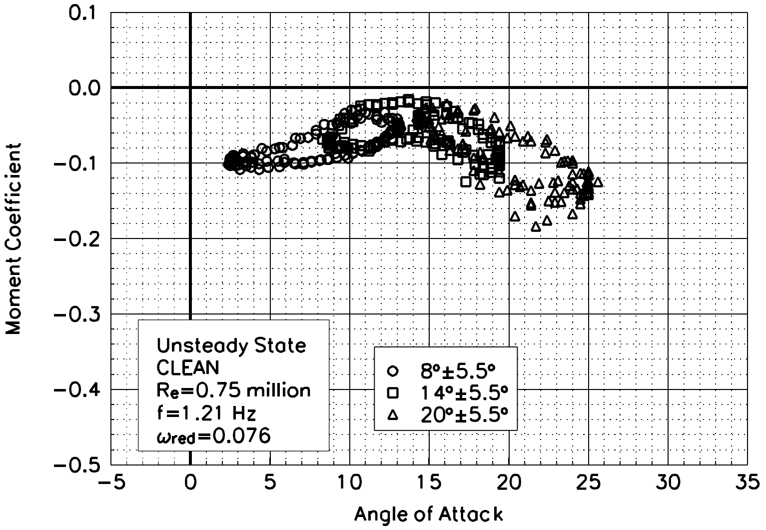

Figure C6. Moment coefficient vs α.

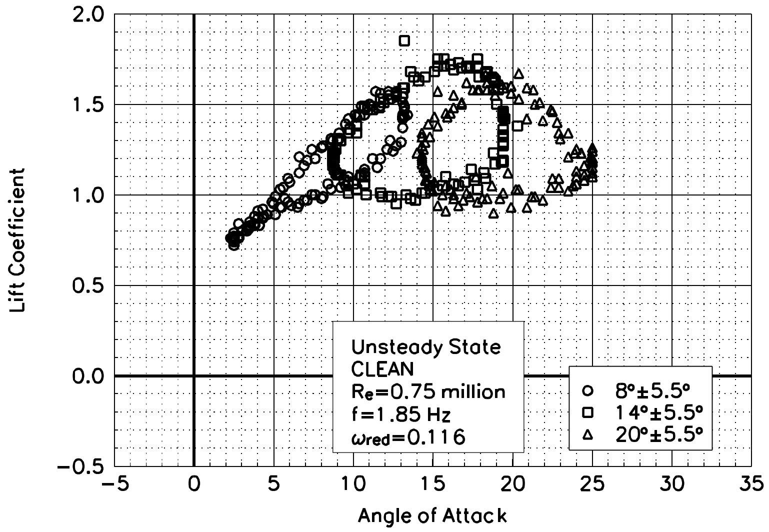

Figure C7. Lift coefficient vs α.

NACA 4415
Clean
Re=0.75 million
$\omega_{reduced}$=0.116

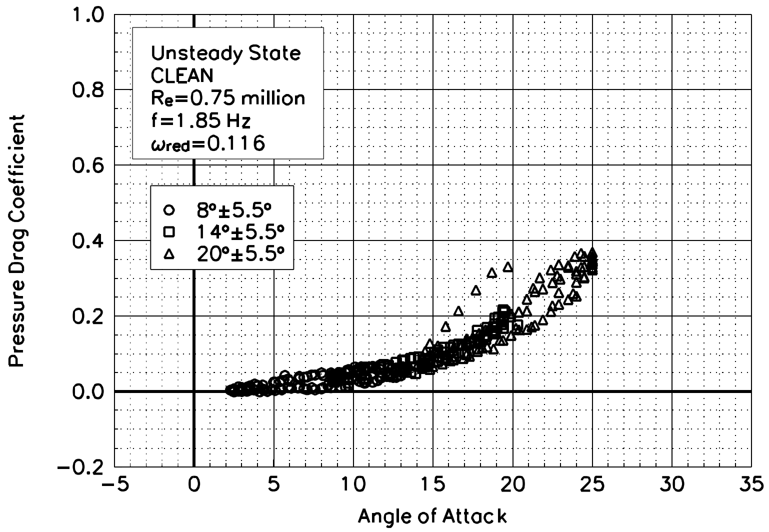

Figure C8. Pressure drag coefficient vs α.

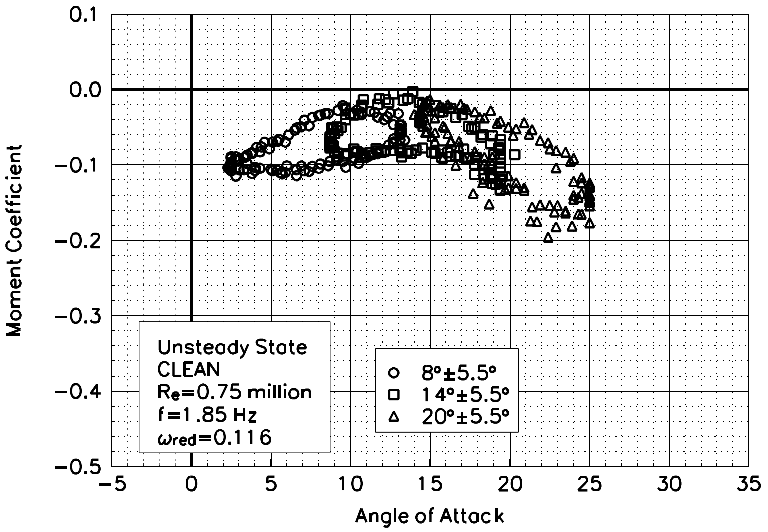

Figure C9. Moment coefficient vs α.

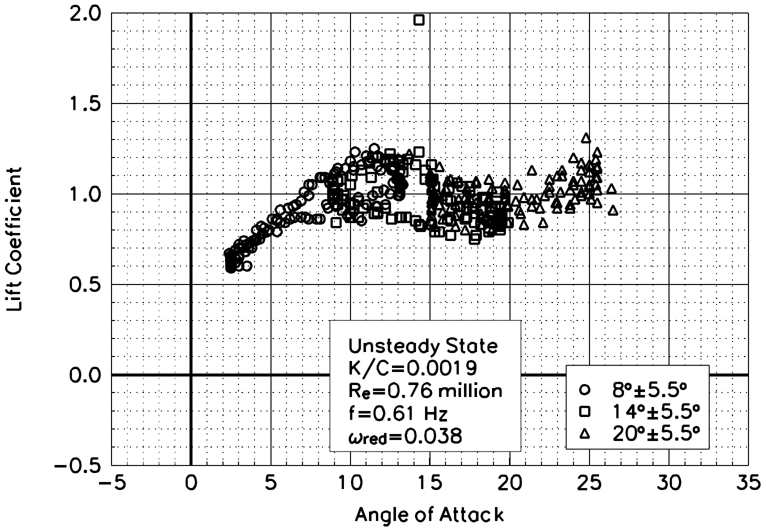

Figure C10. Lift coefficient vs α.

NACA 4415
LEGR
Re=0.76 million
$\omega_{reduced}$=0.038

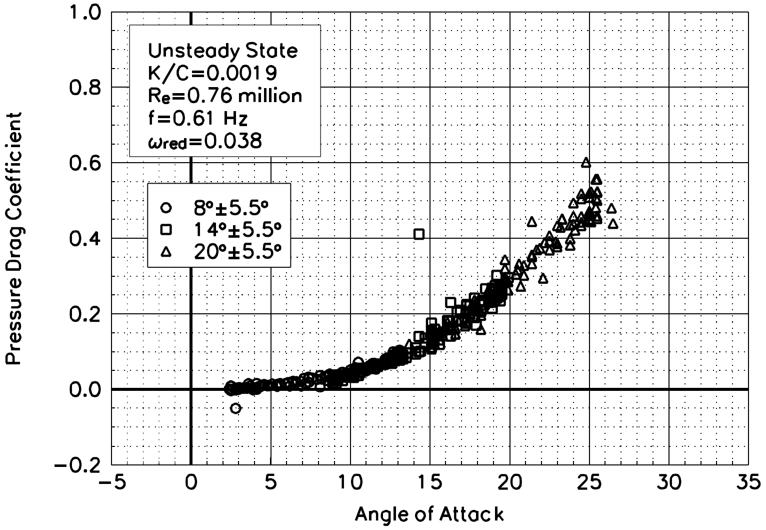

Figure C11. Pressure drag coefficient vs α.

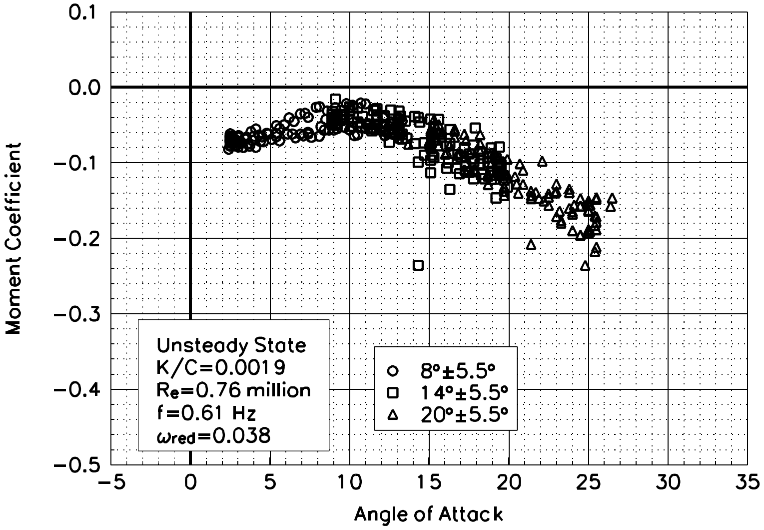

Figure C12. Moment coefficient vs α.

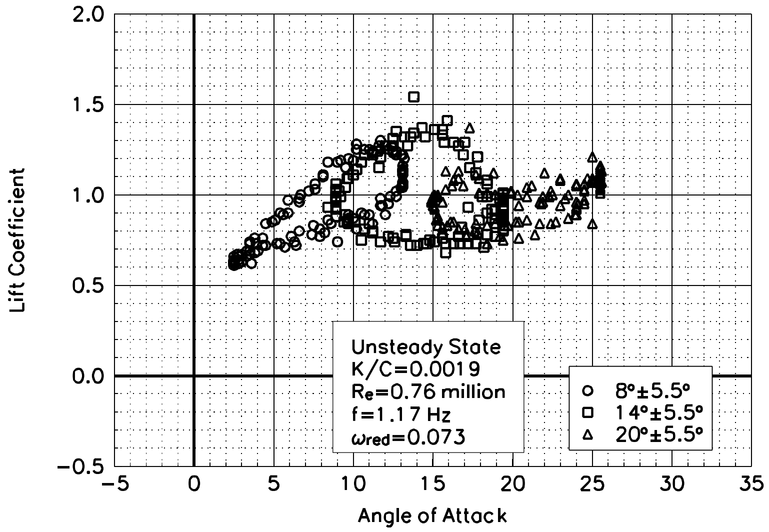

Figure C13. Lift coefficient vs α.

NACA 4415
LEGR
Re=0.76 million
$\omega_{reduced}$=0.073

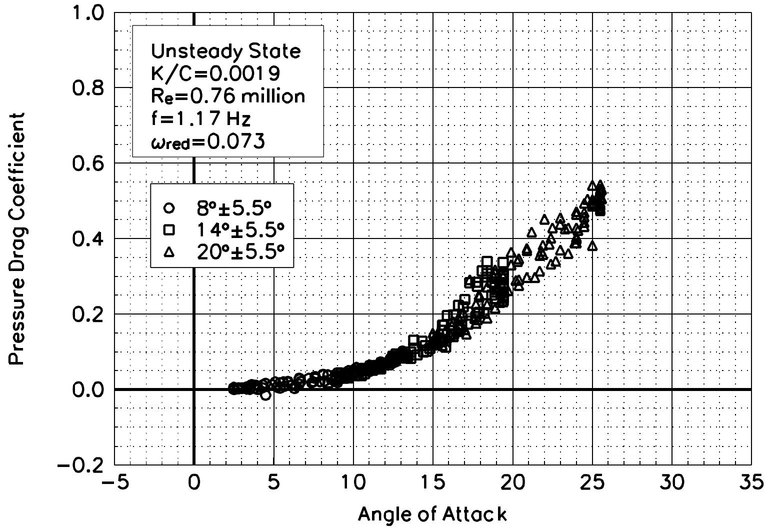

Figure C14. Pressure drag coefficient vs α.

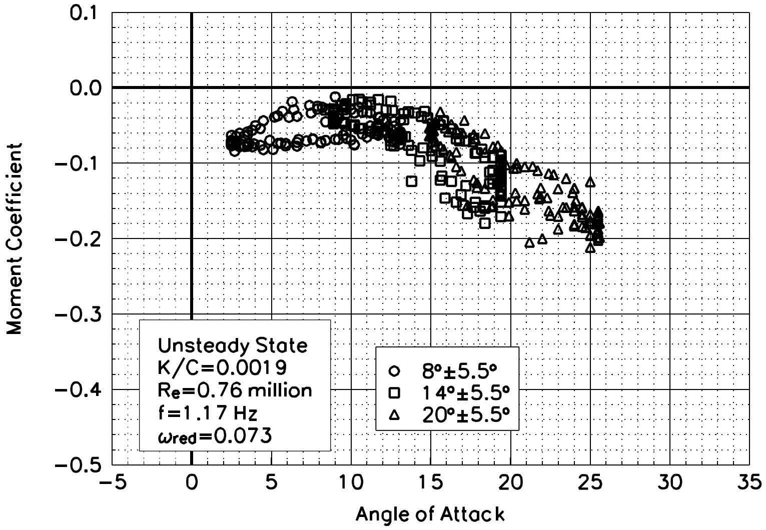

Figure C15. Moment coefficient vs α.

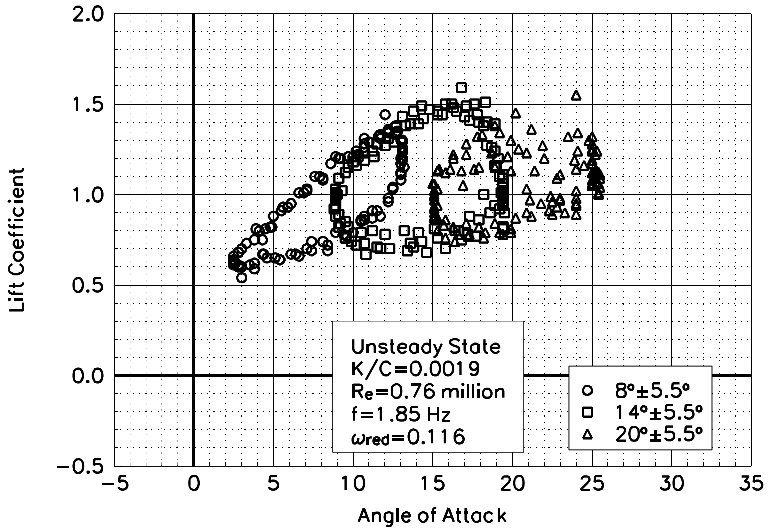

Figure C16. Lift coefficient vs α.

NACA 4415
LEGR
Re=0.76 million
$\omega_{reduced}$=0.116

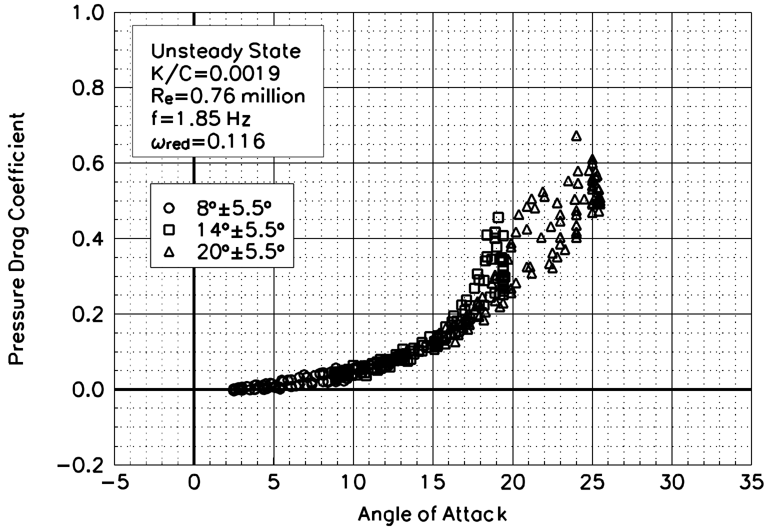

Figure C17. Pressure drag coefficient vs α.

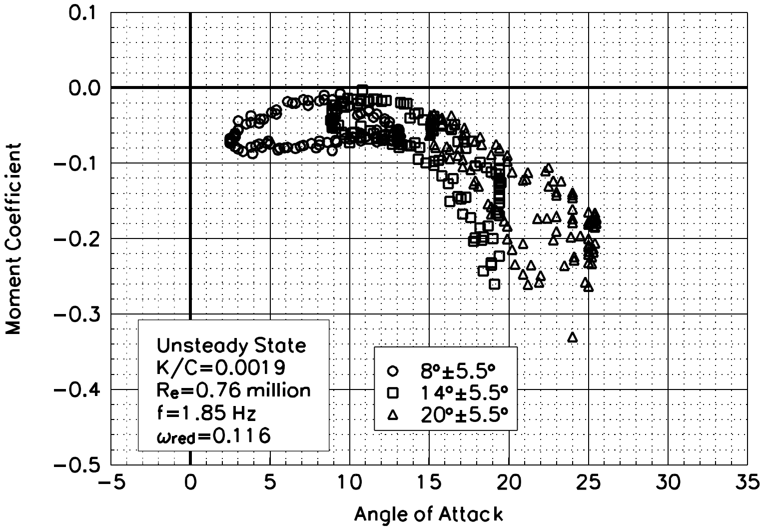

Figure C18. Moment coefficient vs α.

Unsteady Airfoil Characteristics

±5.5° Sine, Re = 1 million

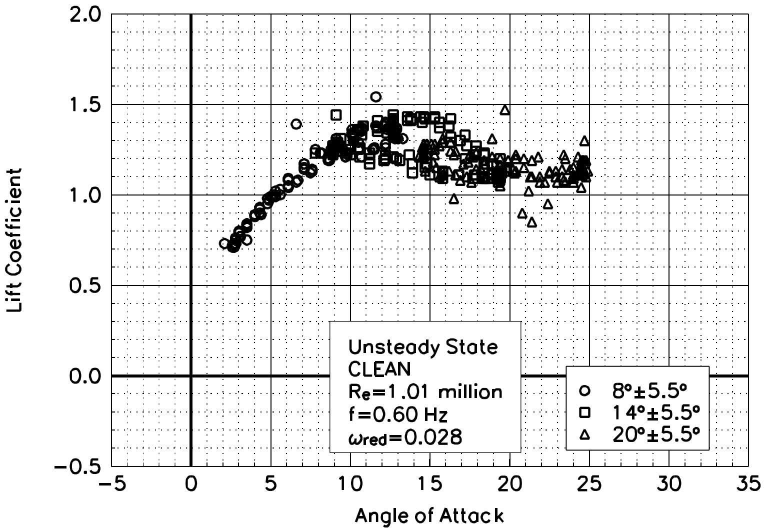

Figure C19. Lift coefficient vs α.

NACA 4415
Clean
Re=1.01 million
$\omega_{reduced}$=0.028

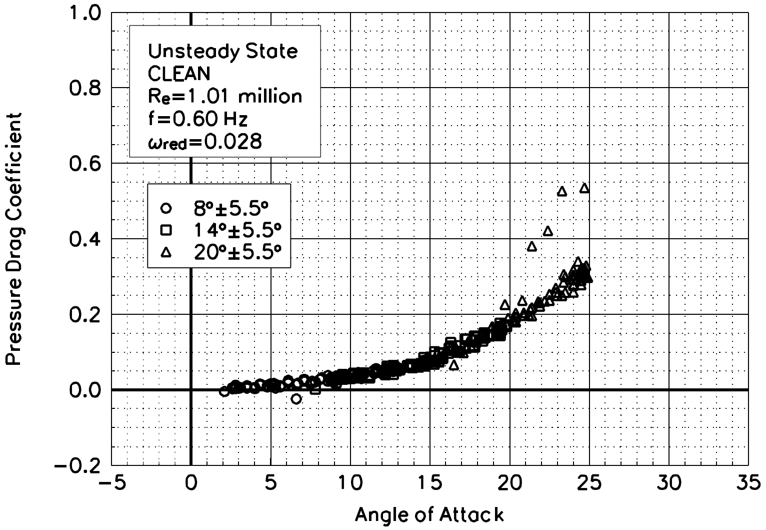

Figure C20. Pressure drag coefficient vs α.

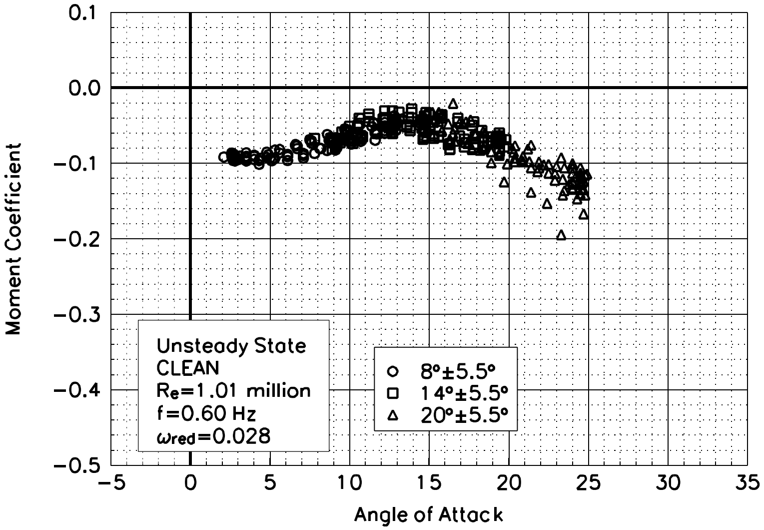

Figure C21. Moment coefficient vs α.

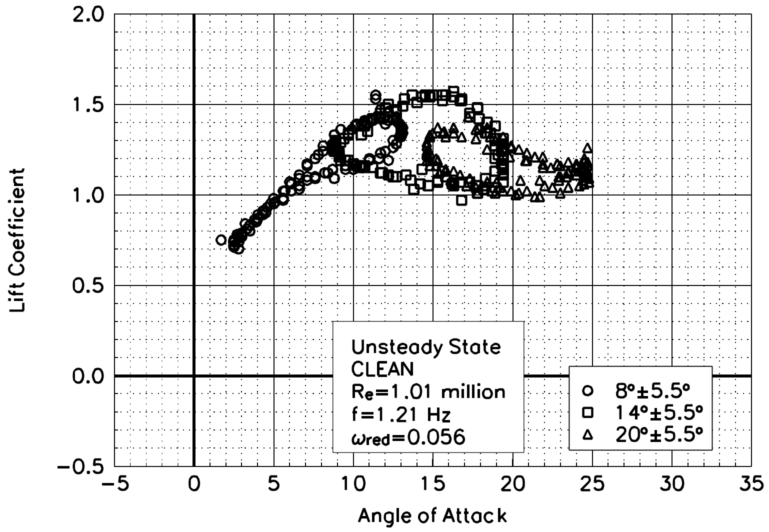

Figure C22. Lift coefficient vs α.

NACA 4415
Clean
Re=1.01 million
$\omega_{reduced}$=0.056

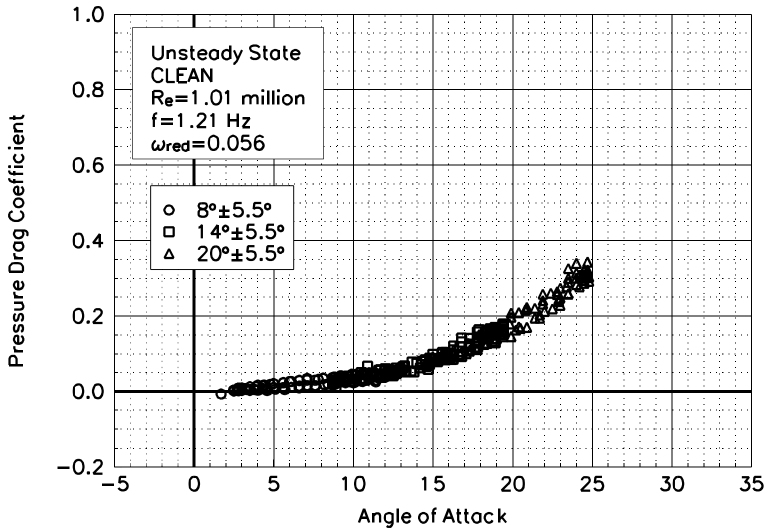

Figure C23. Pressure drag coefficient vs α.

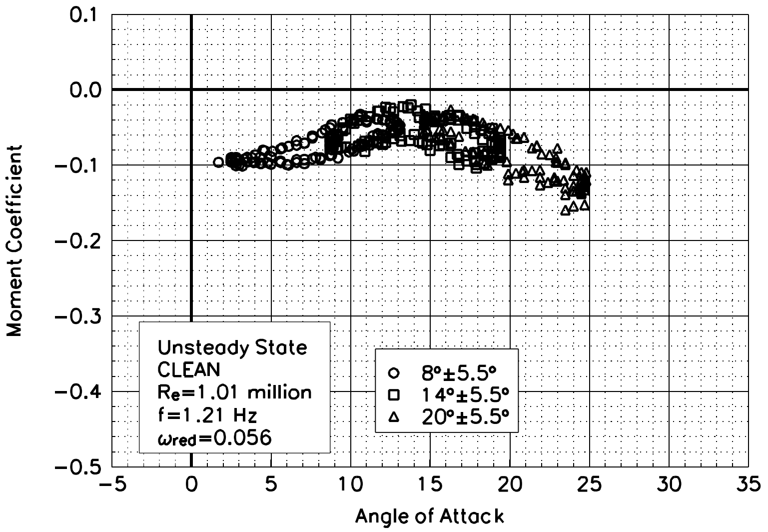

Figure C24. Moment coefficient vs α.

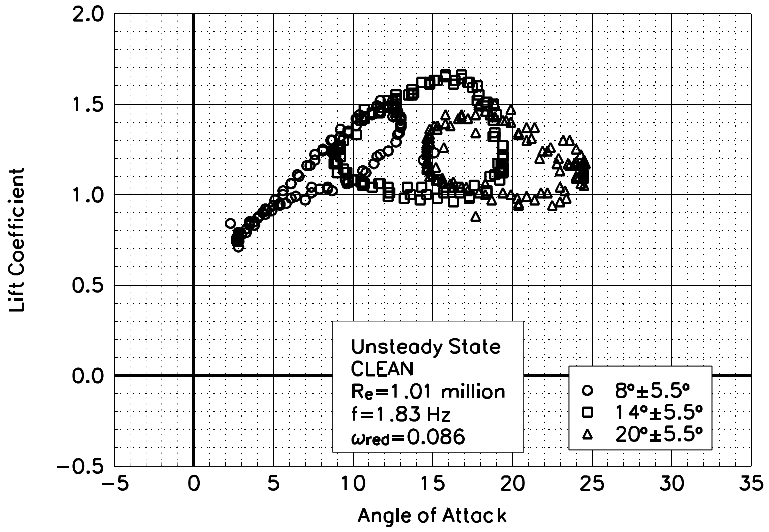

Figure C25. Lift coefficient vs α.

NACA 4415
Clean
Re=1.01 million
$\omega_{reduced}$=0.086

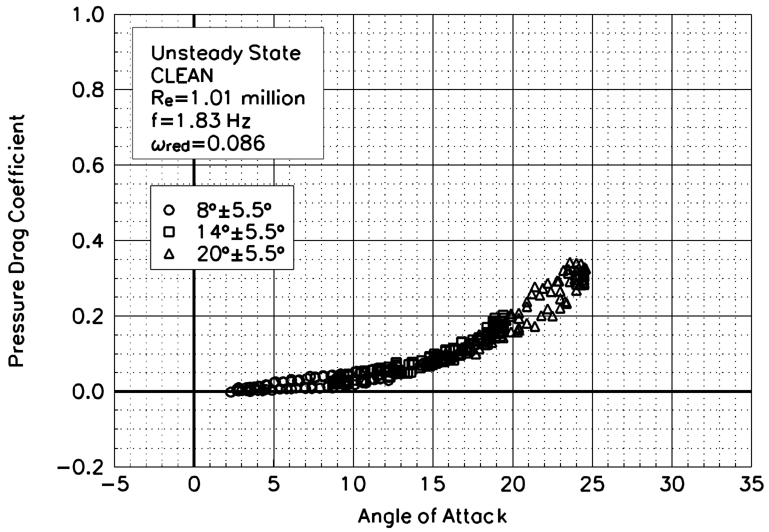

Figure C26. Pressure drag coefficient vs α.

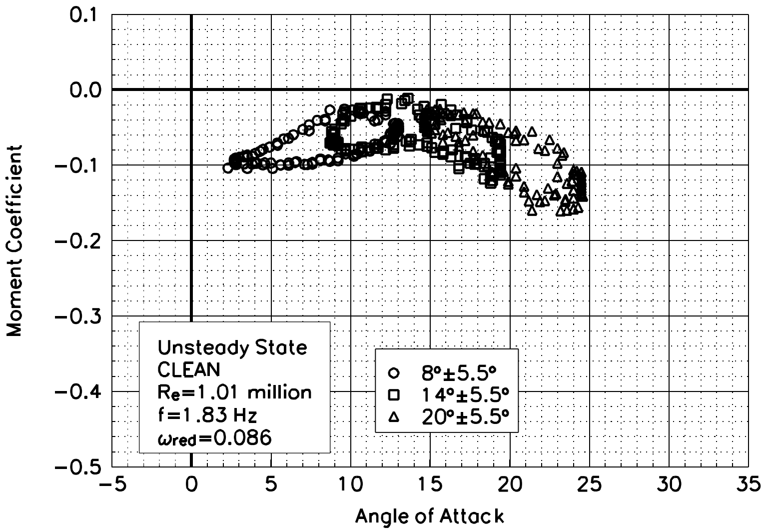

Figure C27. Moment coefficient vs α.

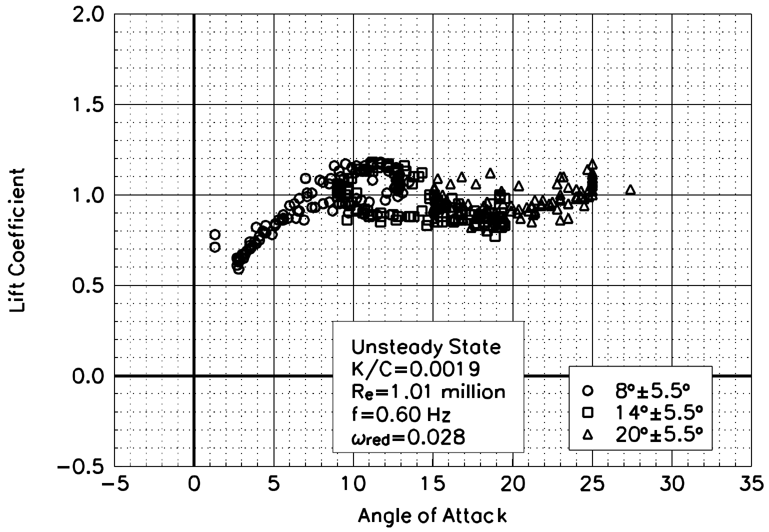

Figure C28. Lift coefficient vs α.

NACA 4415
LEGR
Re=1.01 million
$\omega_{reduced}$=0.028

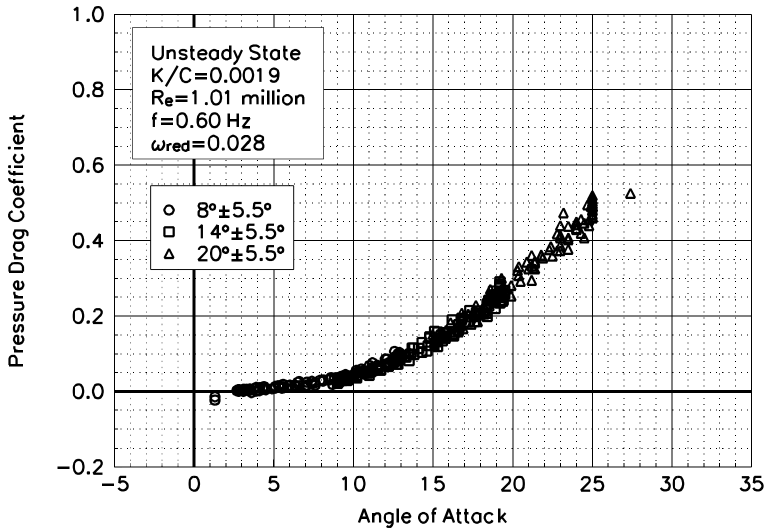

Figure C29. Pressure drag coefficient vs α.

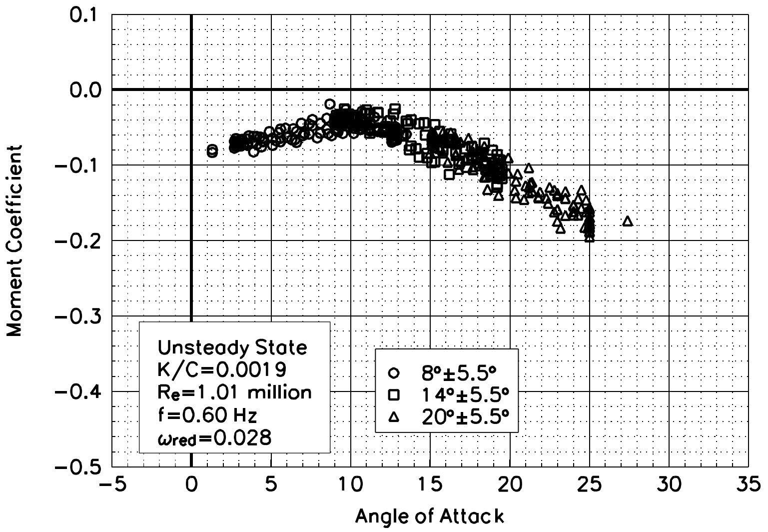

Figure C30. Moment coefficient vs α.

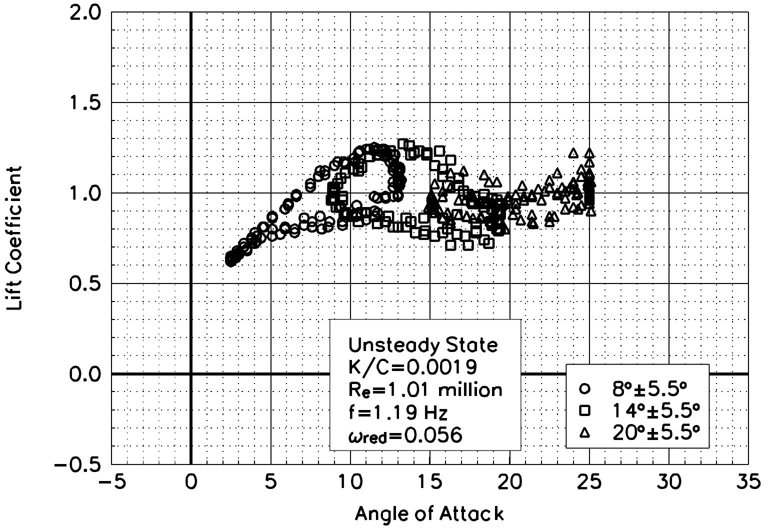

Figure C31. Lift coefficient vs α.

NACA 4415
LEGR
Re=1.01 million
$\omega_{reduced}$=0.056

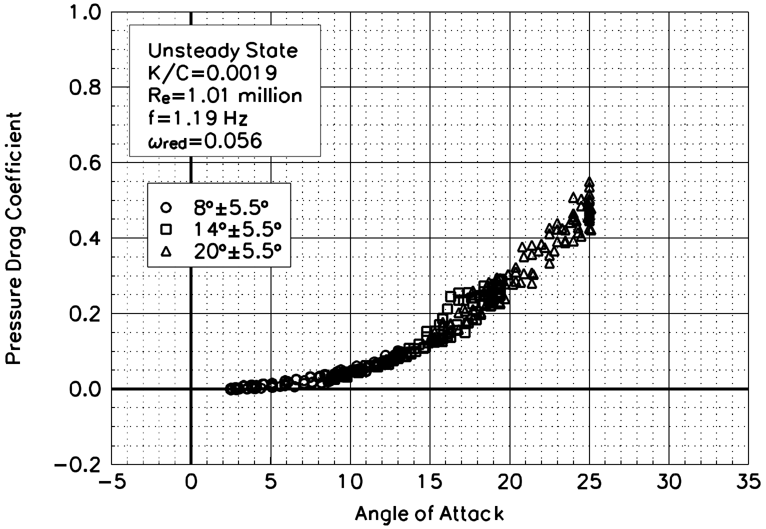

Figure C32. Pressure drag coefficient vs α.

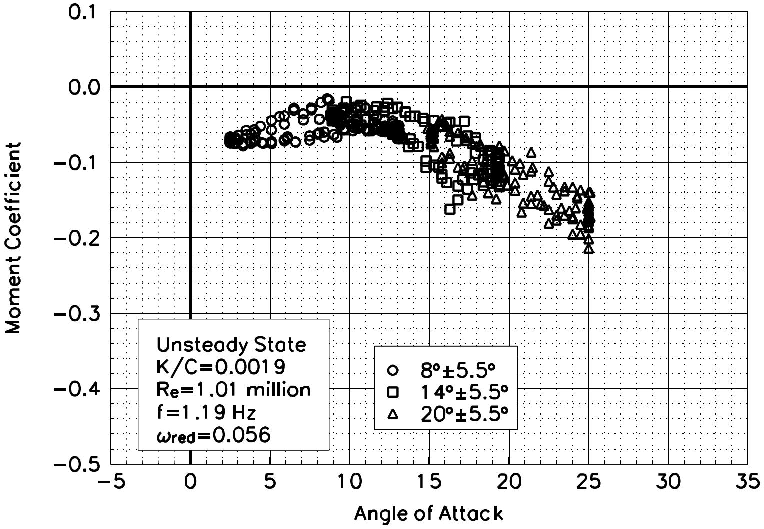

Figure C33. Moment coefficient vs α.

NACA 4415
LEGR
Re=1.01 million
$\omega_{reduced}$=0.087

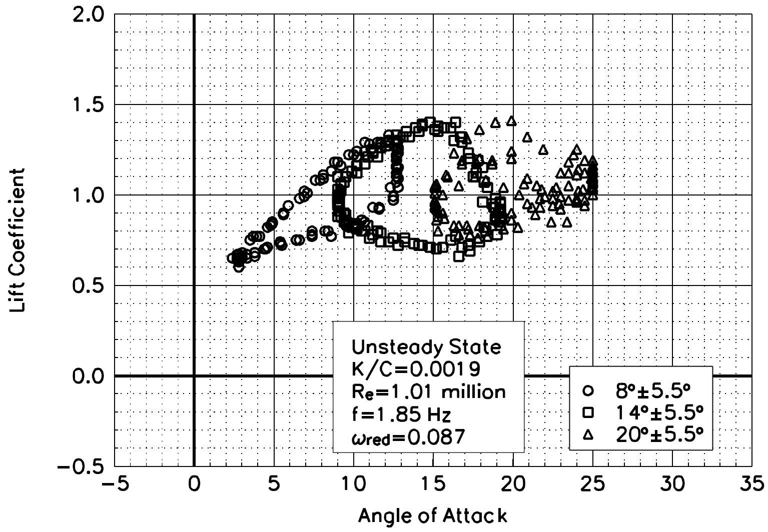

Figure C34. Lift coefficient vs α.

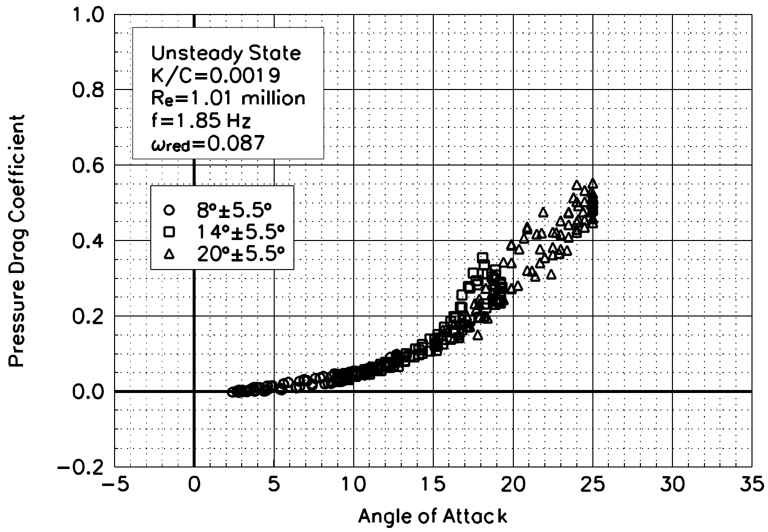

Figure C35. Pressure drag coefficient vs α.

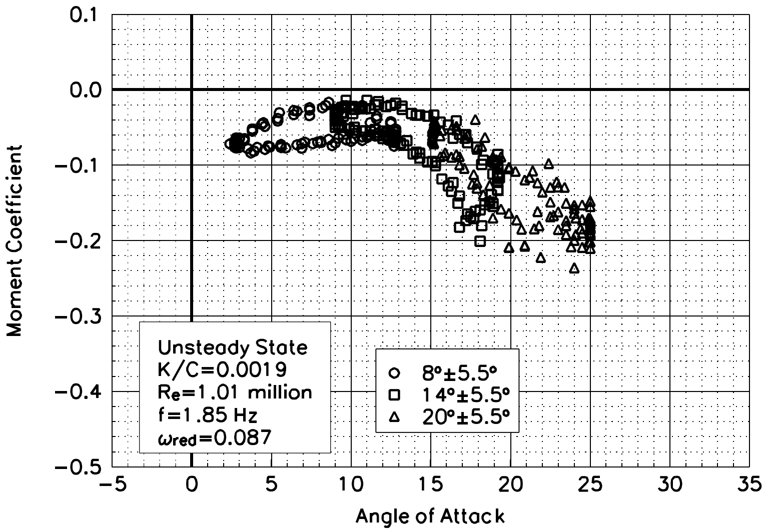

Figure C36. Moment coefficient vs α.

Unsteady Airfoil Characteristics

±5.5° Sine, Re= 1.25 million

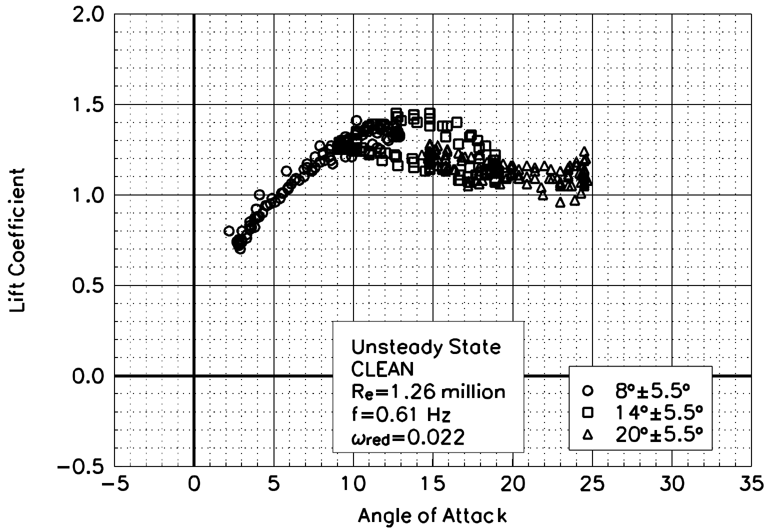

Figure C37. Lift coefficient vs α.

NACA 4415
Clean
Re=1.26 million
$\omega_{reduced}$=0.022

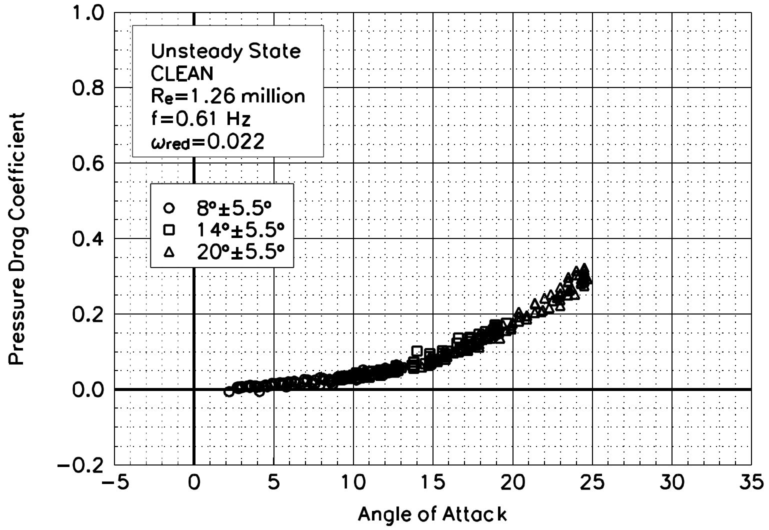

Figure C38. Pressure drag coefficient vs α.

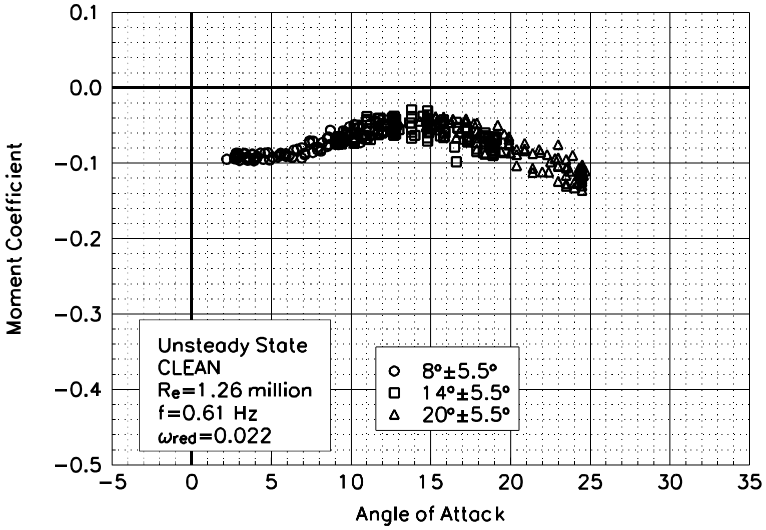

Figure C39. Moment coefficient vs α.

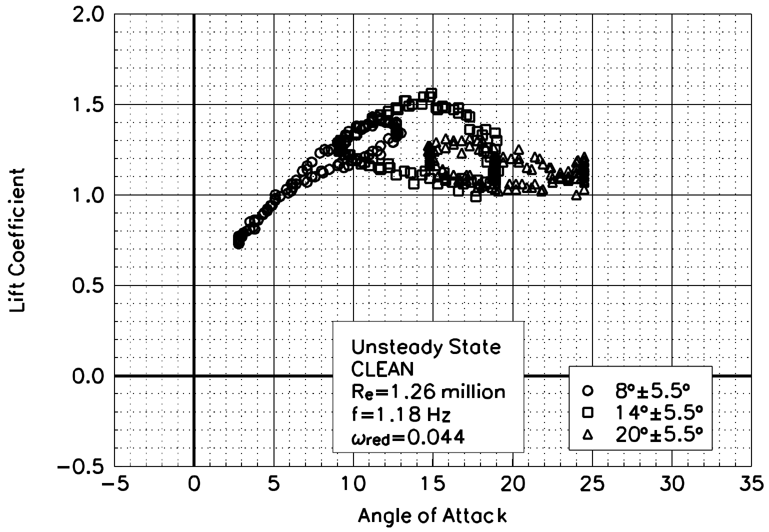

Figure C40. Lift coefficient vs α.

NACA 4415
Clean
Re=1.26 million
$\omega_{reduced}$=0.044

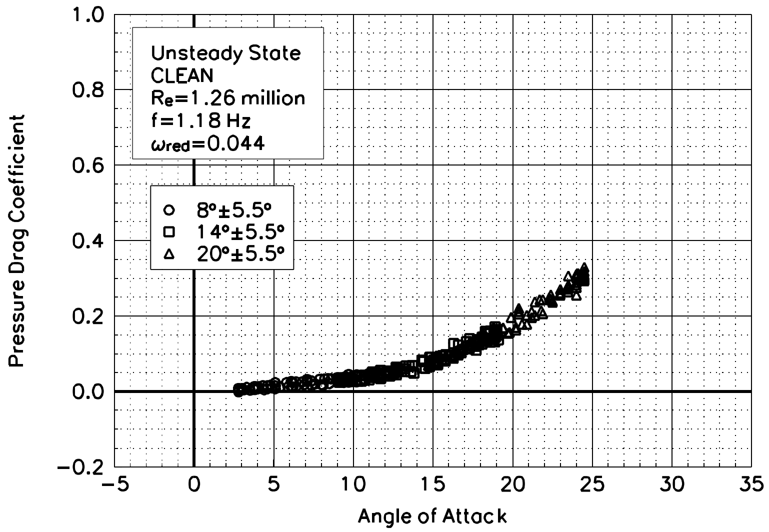

Figure C41. Pressure drag coefficient vs α.

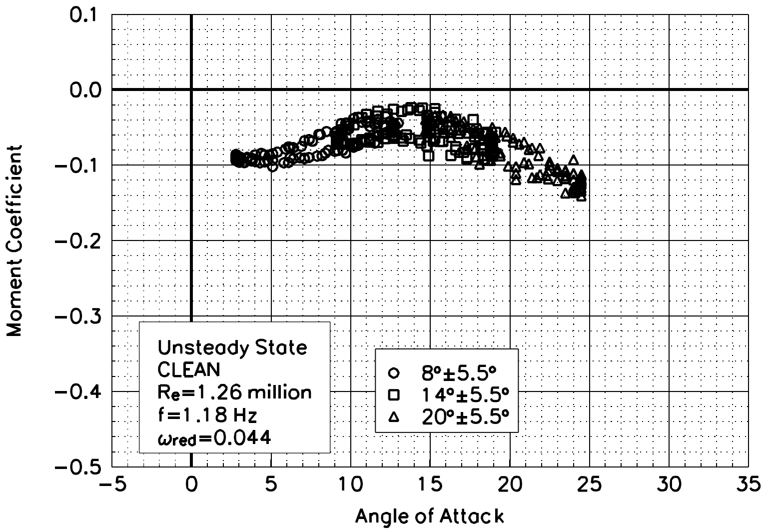

Figure C42. Moment coefficient vs α.

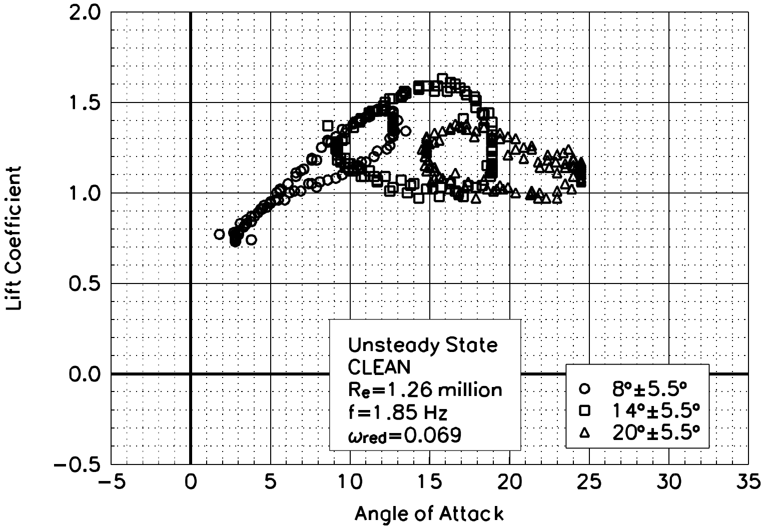

Figure C43. Lift coefficient vs α.

NACA 4415
Clean
Re=1.26 million
$\omega_{reduced}$=0.069

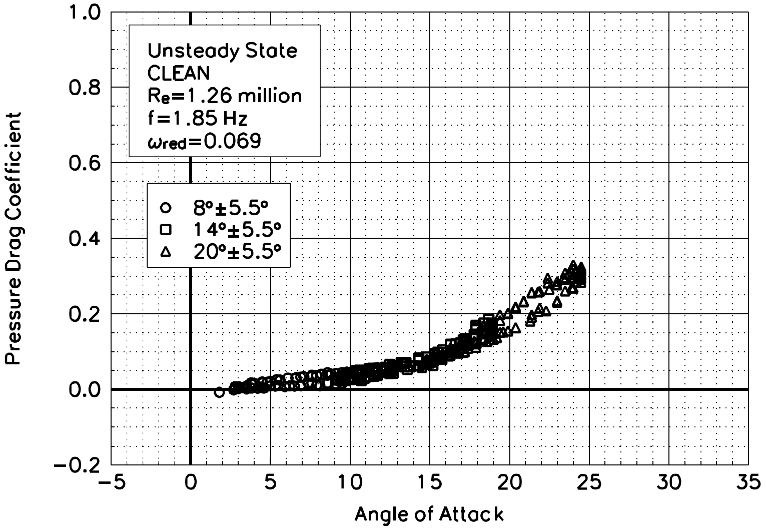

Figure C44. Pressure drag coefficient vs α.

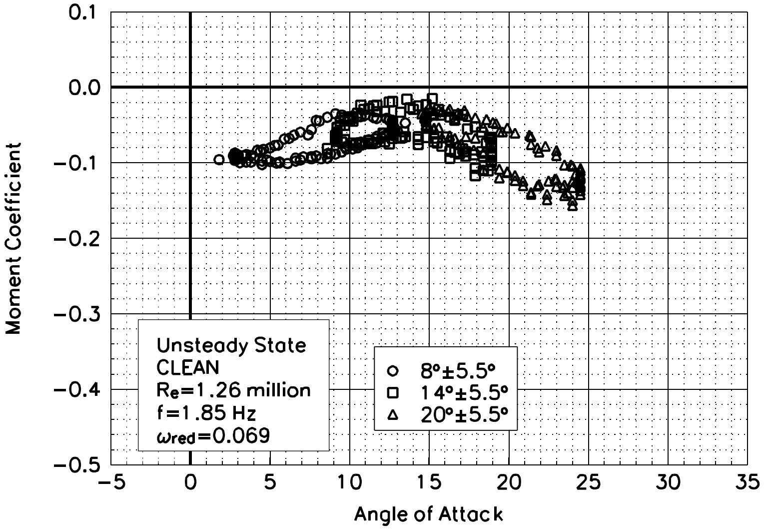

Figure C45. Moment coefficient vs α.

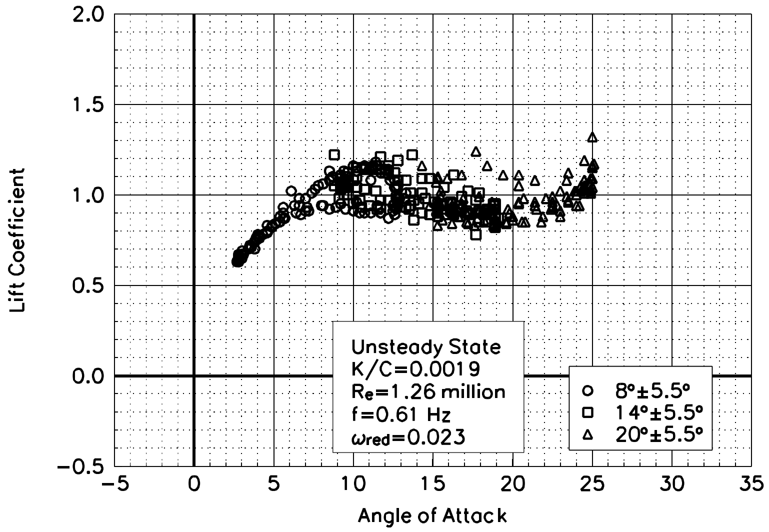

Figure C46. Lift coefficient vs α.

NACA 4415
LEGR
Re=1.26 million
$\omega_{reduced}$=0.023

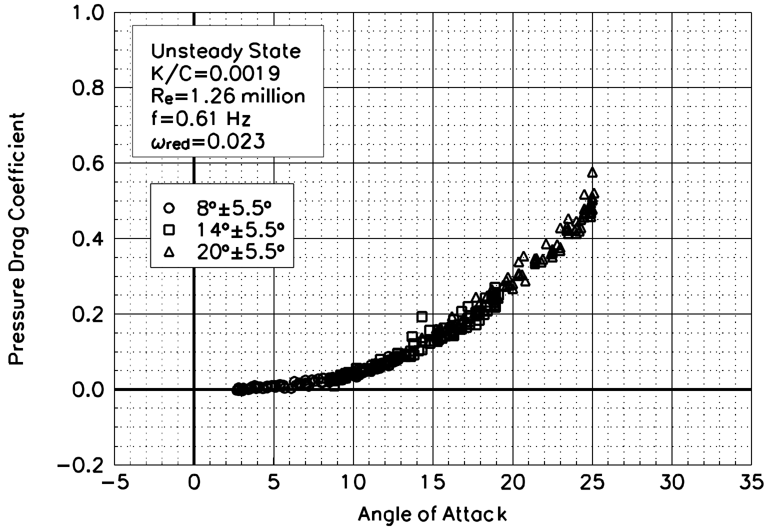

Figure C47. Pressure drag coefficient vs α.

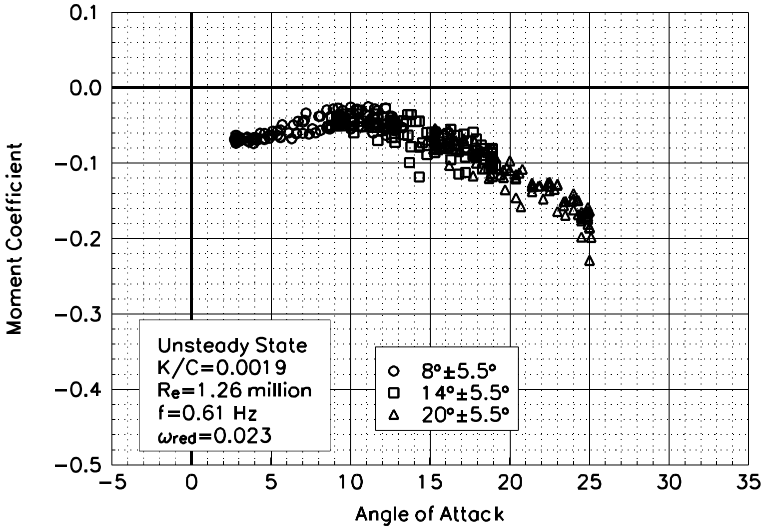

Figure C48. Moment coefficient vs α.

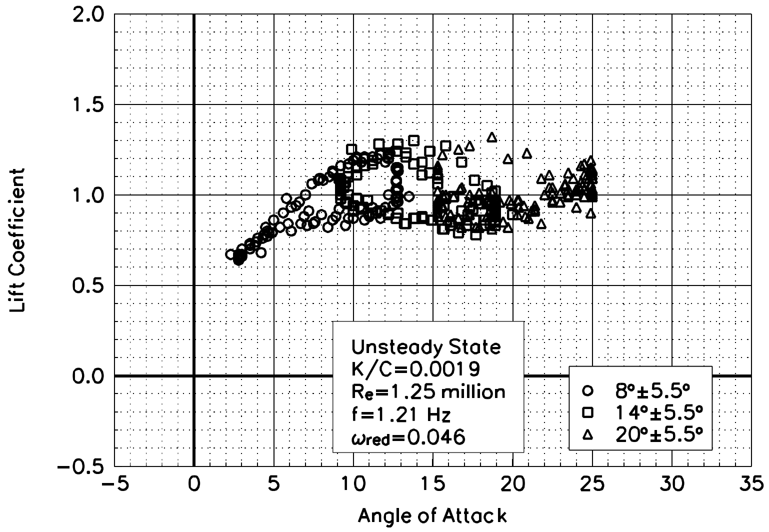

Figure C49. Lift coefficient vs α.

NACA 4415
LEGR
Re=1.25 million
$\omega_{reduced}$=0.046

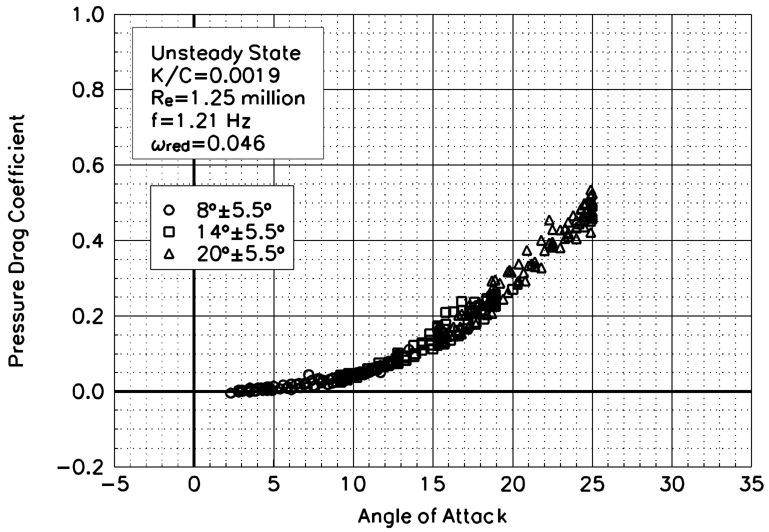

Figure C50. Pressure drag coefficient vs α.

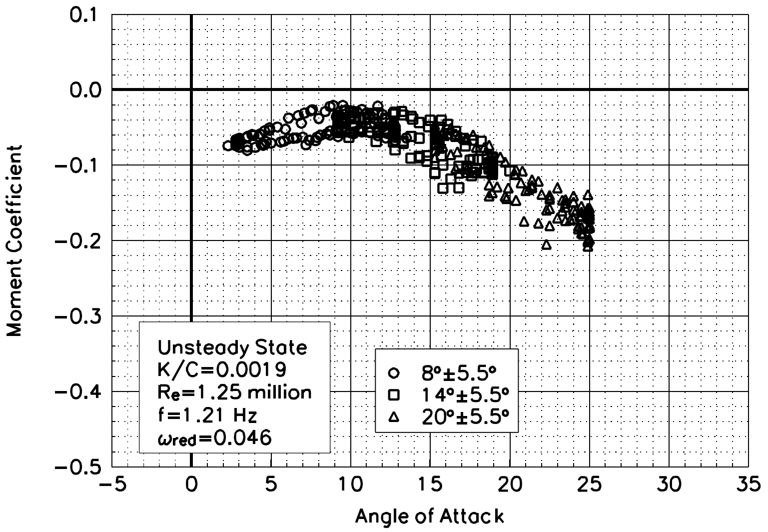

Figure C51. Moment coefficient vs α.

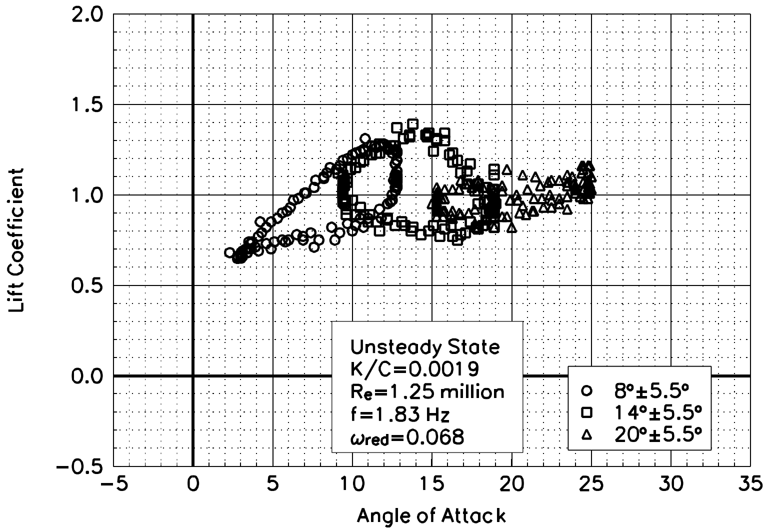

Figure C52. Lift coefficient vs α.

NACA 4415
LEGR
Re=1.25 million
$\omega_{reduced}$=0.068

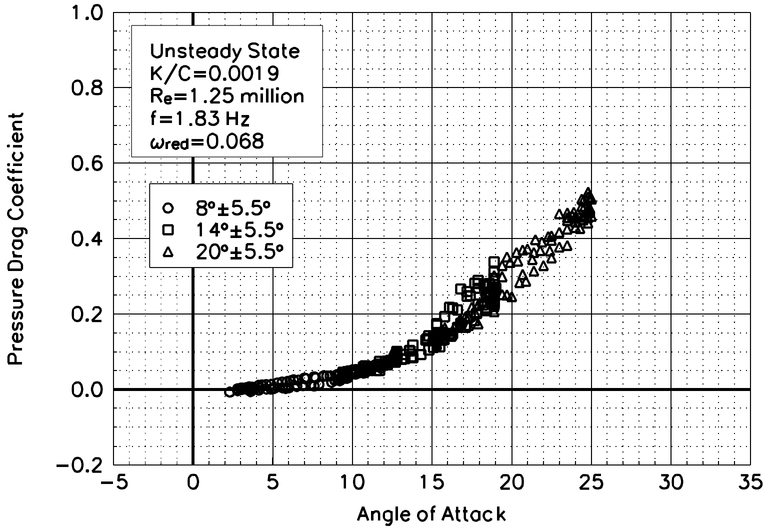

Figure C53. Pressure drag coefficient vs α.

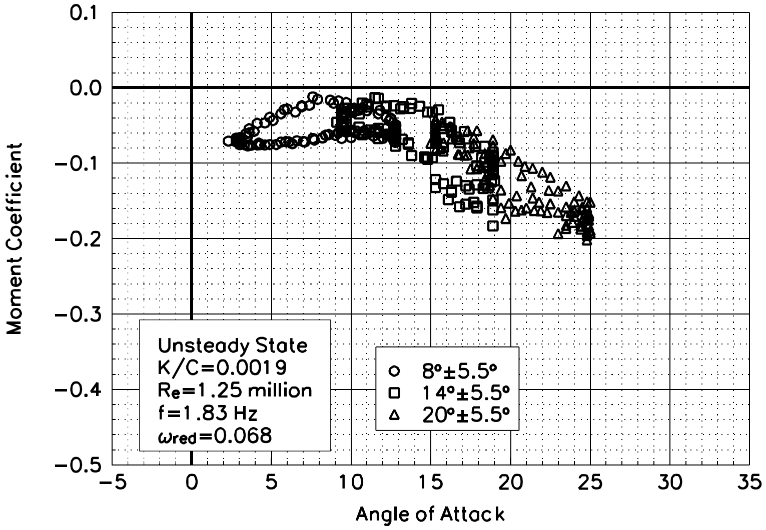

Figure C54. Moment coefficient vs α.

Unsteady Airfoil Characteristics

±5.5° Sine, Re = 1.5 million

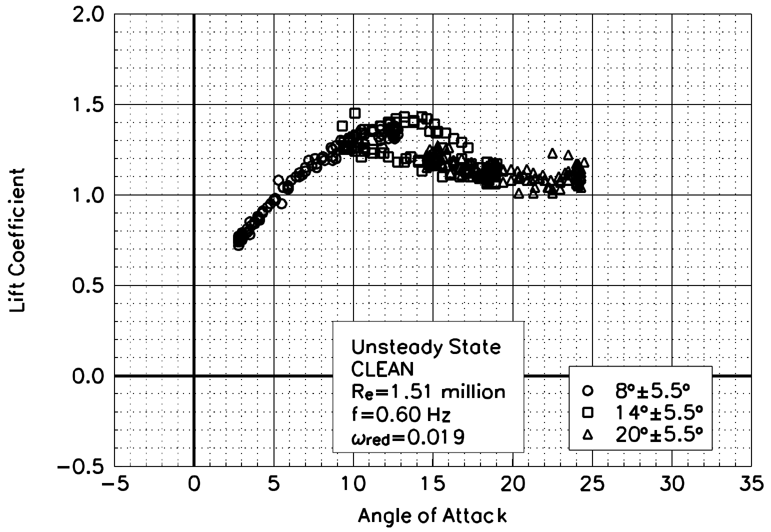

Figure C55. Lift coefficient vs α.

NACA 4415
Clean
Re=1.51 million
$\omega_{reduced}$=0.019

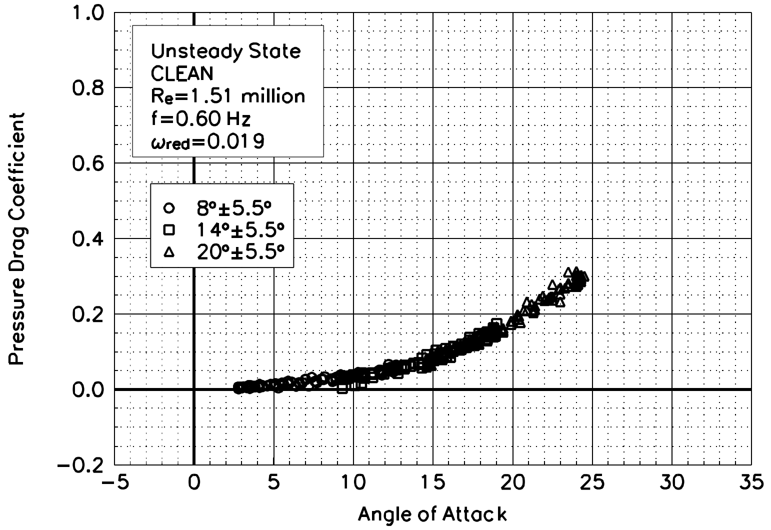

Figure C56. Pressure drag coefficient vs α.

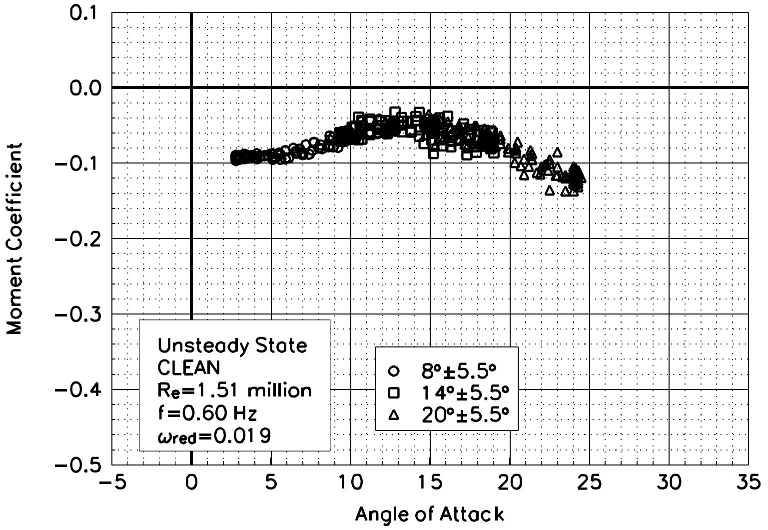

Figure C57. Moment coefficient vs α.

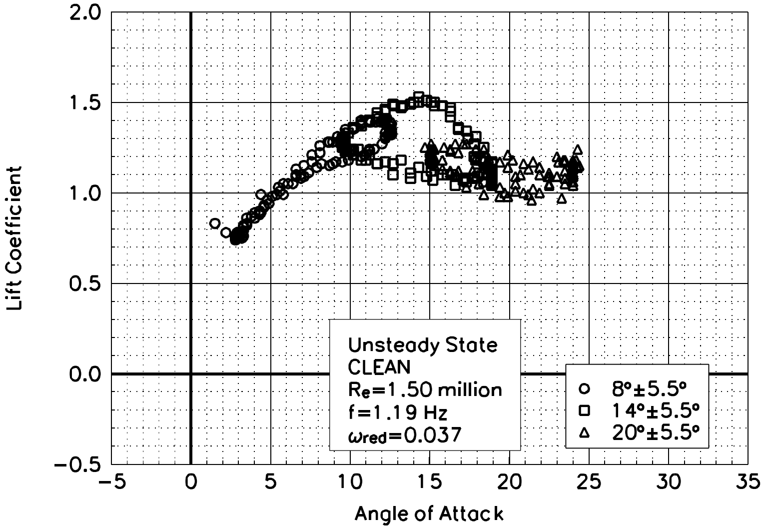

Figure C58. Lift coefficient vs α.

NACA 4415
Clean
Re=1.50 million
$\omega_{reduced}$=0.037

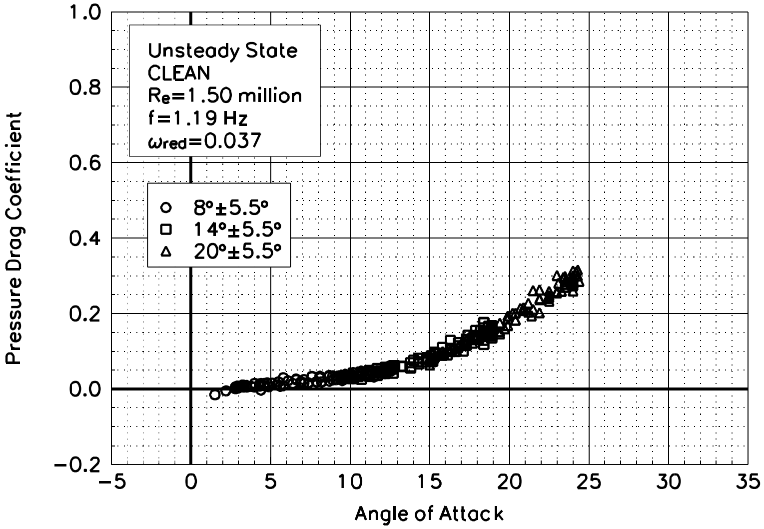

Figure C59. Pressure drag coefficient vs α.

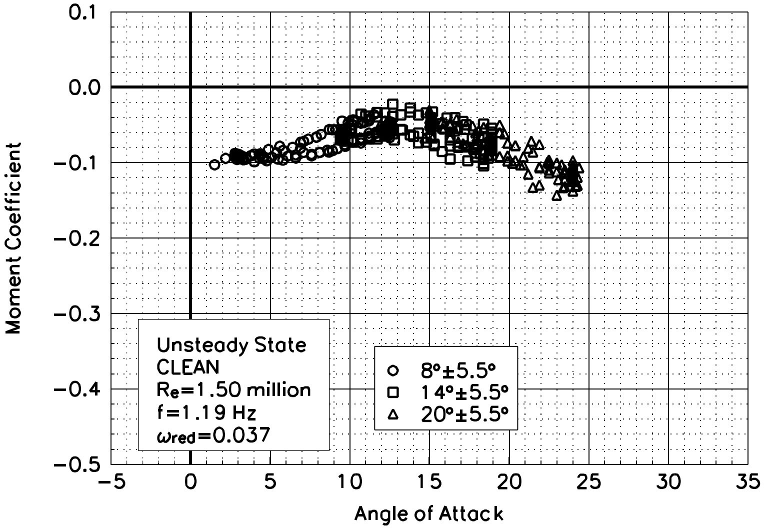

Figure C60. Moment coefficient vs α.

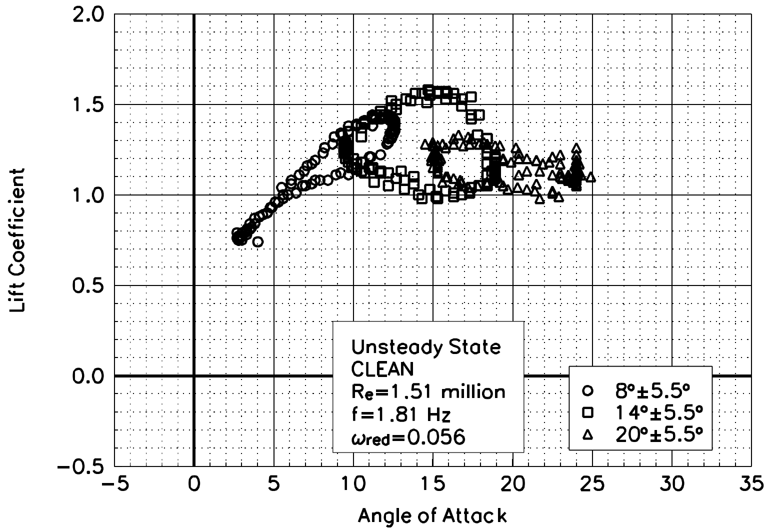

Figure C61. Lift coefficient vs α.

NACA 4415
Clean
Re=1.51 million
$\omega_{reduced}$=0.056

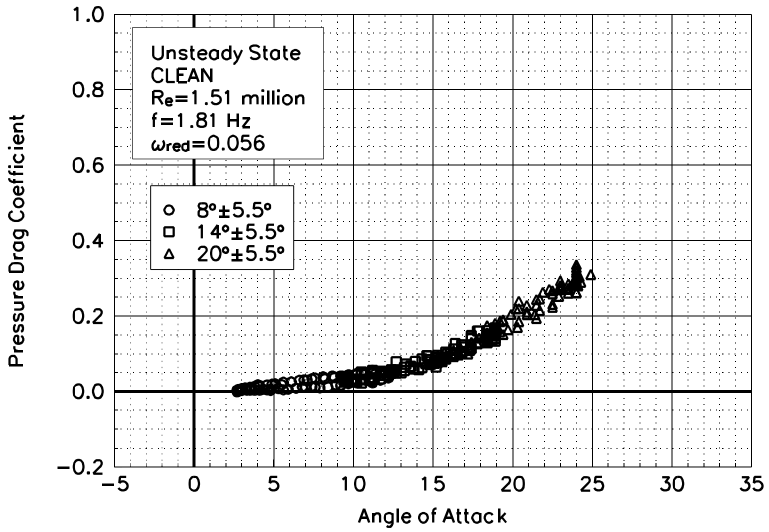

Figure C62. Pressure drag coefficient vs α.

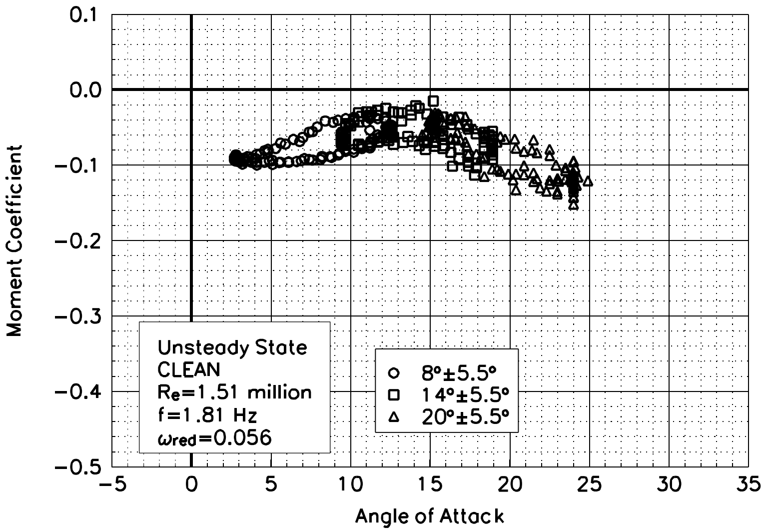

Figure C63. Moment coefficient vs α.

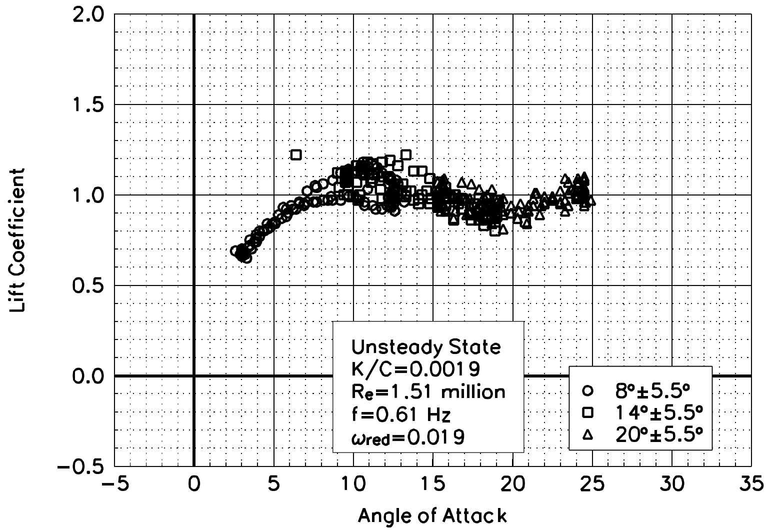

Figure C64. Lift coefficient vs α.

NACA 4415
LEGR
Re=1.51 million
$\omega_{reduced}$=0.019

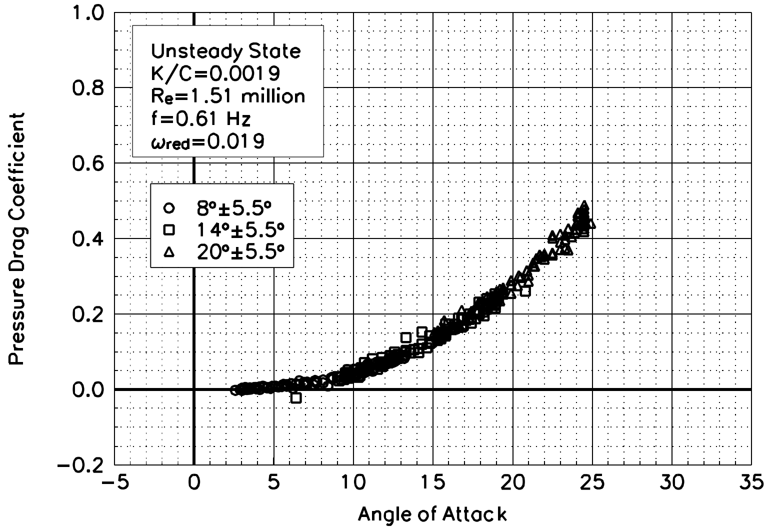

Figure C65. Pressure drag coefficient vs α.

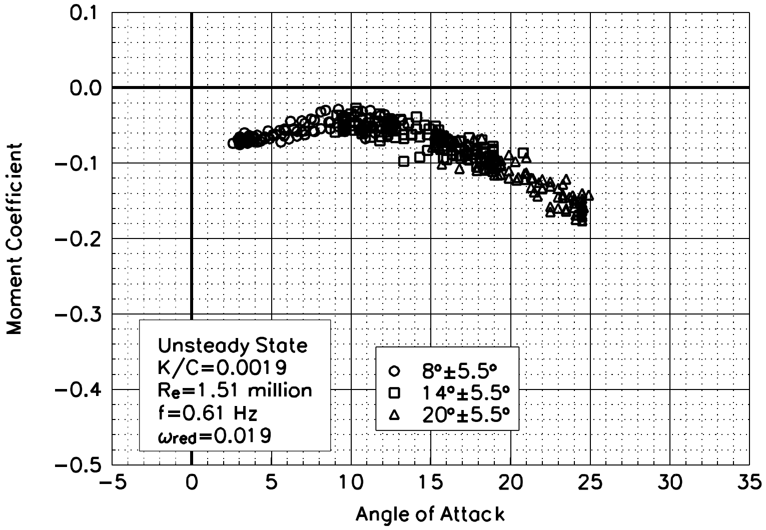

Figure C66. Moment coefficient vs α.

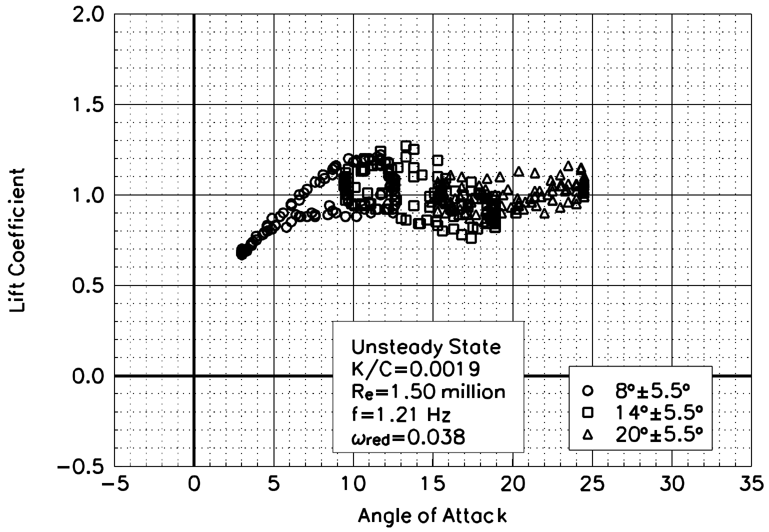

Figure C67. Lift coefficient vs α.

NACA 4415
LEGR
Re=1.50 million
$\omega_{reduced}$=0.038

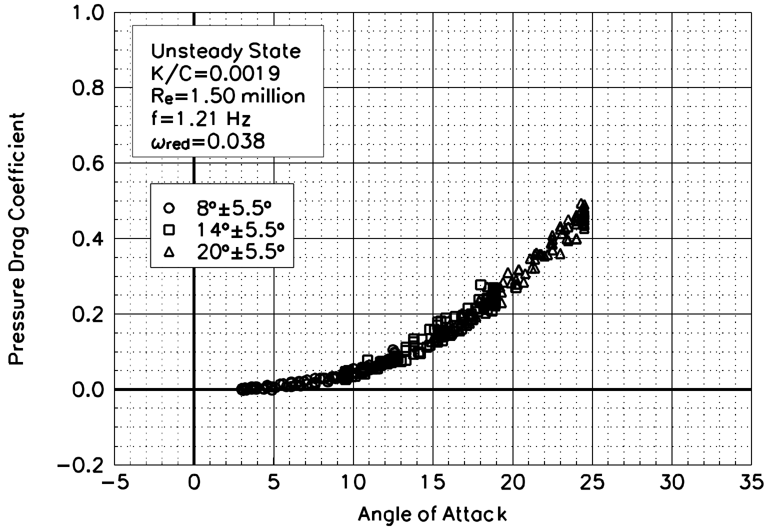

Figure C68. Pressure drag coefficient vs α.

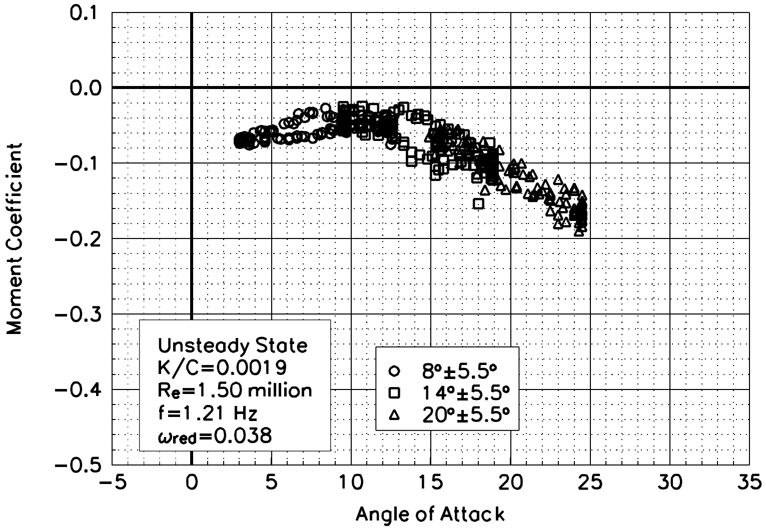

Figure C69. Moment coefficient vs α.

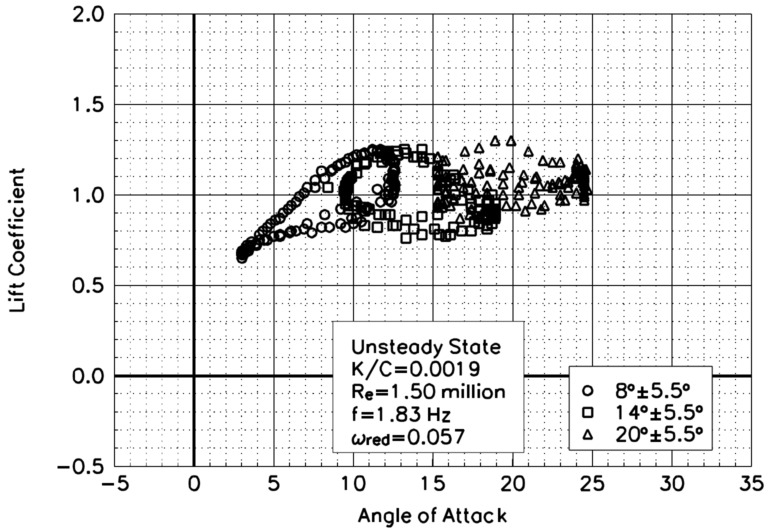

Figure C70. Lift coefficient vs α.

NACA 4415
LEGR
Re=1.50 million
$\omega_{reduced}$=0.057

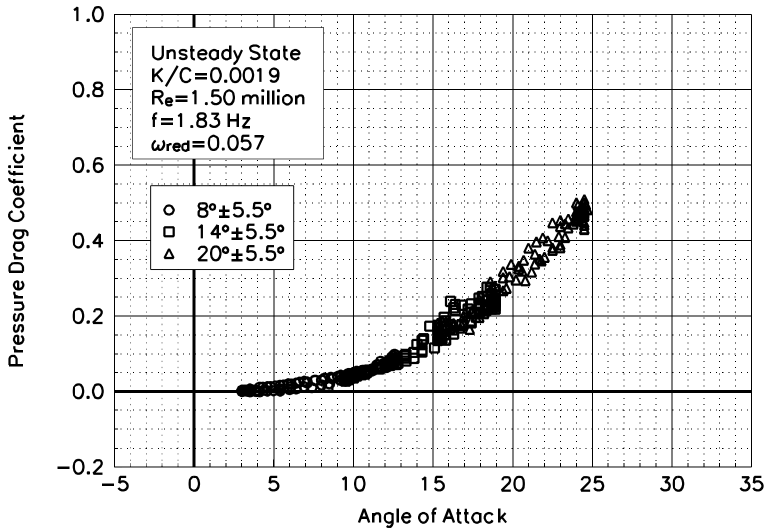

Figure C71. Pressure drag coefficient vs α.

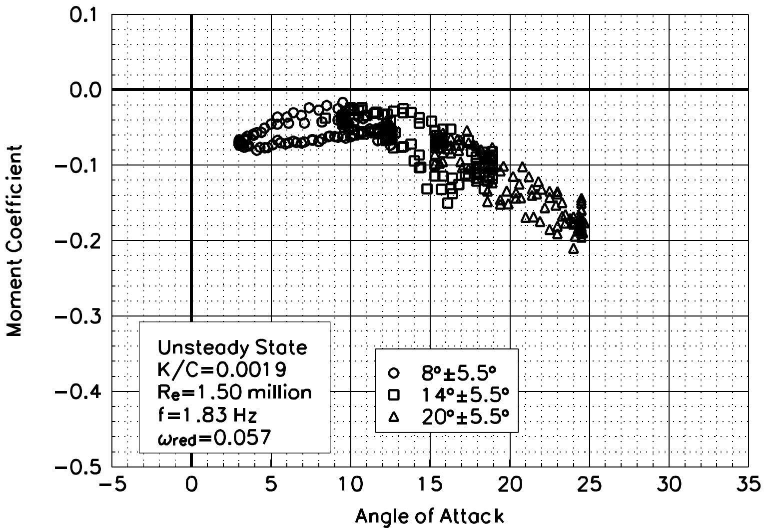

Figure C72. Moment coefficient vs α.

Unsteady Airfoil Characteristics

±10° Sine, Re = 0.75 million

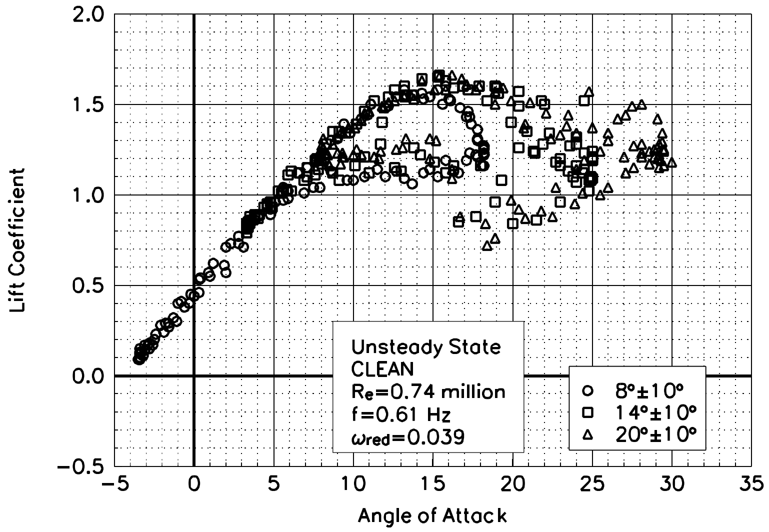

Figure C73. Lift coefficient vs α.

NACA 4415
Clean
Re=0.74 million
$\omega_{reduced}$=0.039

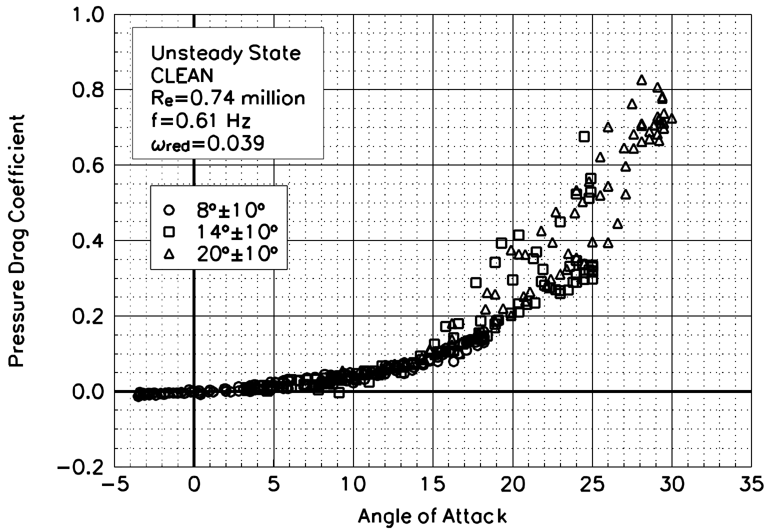

Figure C74. Pressure drag coefficient vs α.

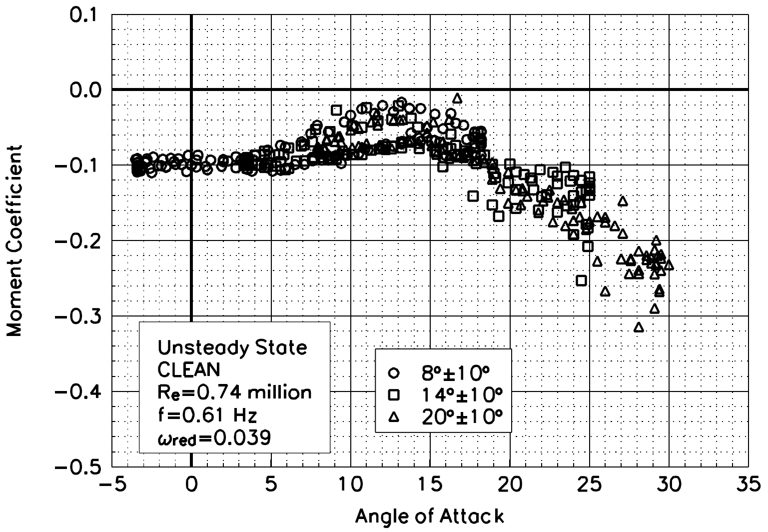

Figure C75. Moment coefficient vs α.

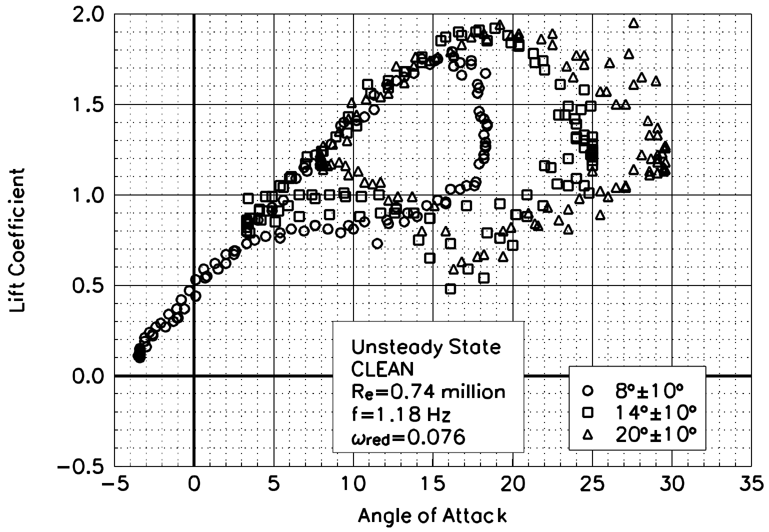

Figure C76. Lift coefficient vs α.

NACA 4415
Clean
Re=0.74 million
$\omega_{reduced}$=0.076

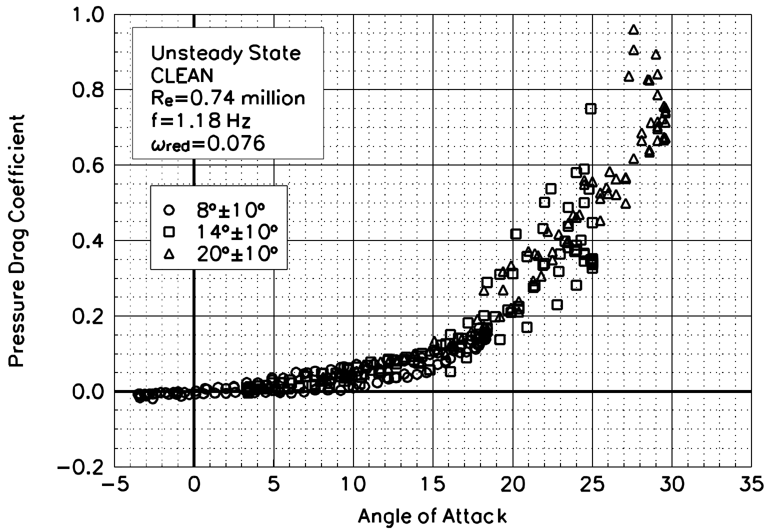

Figure C77. Pressure drag coefficient vs α.

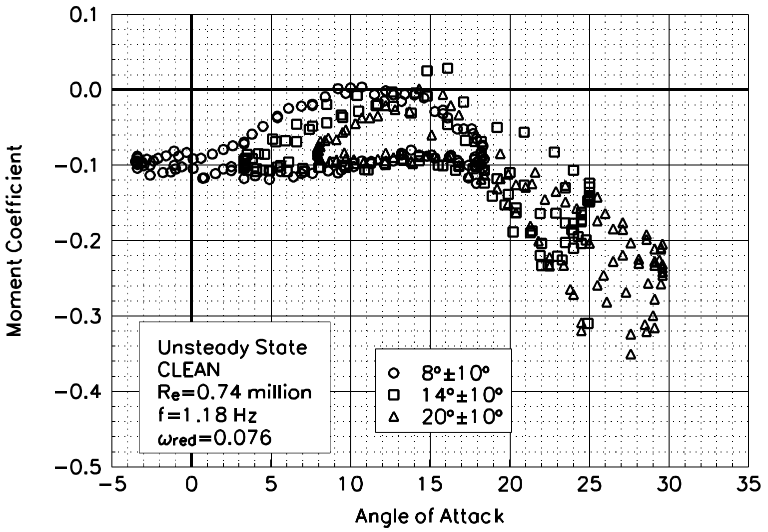

Figure C78. Moment coefficient vs α.

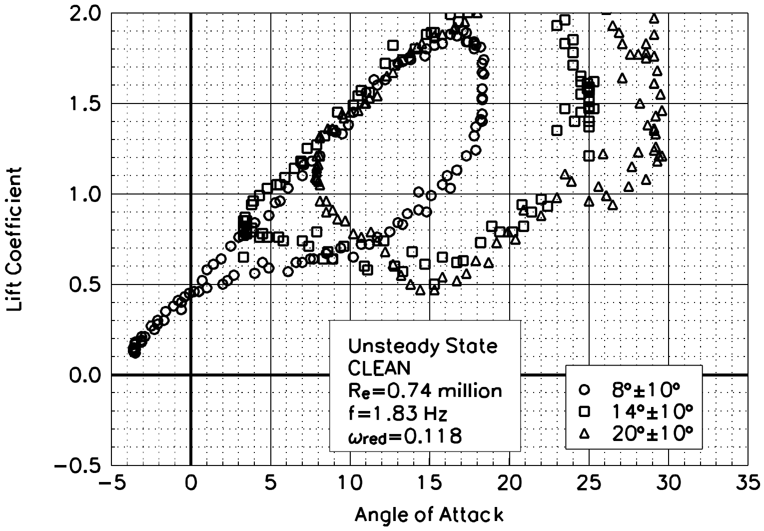

Figure C79. Lift coefficient vs α.

NACA 4415
Clean
Re=0.74 million
$\omega_{reduced}$=0.118

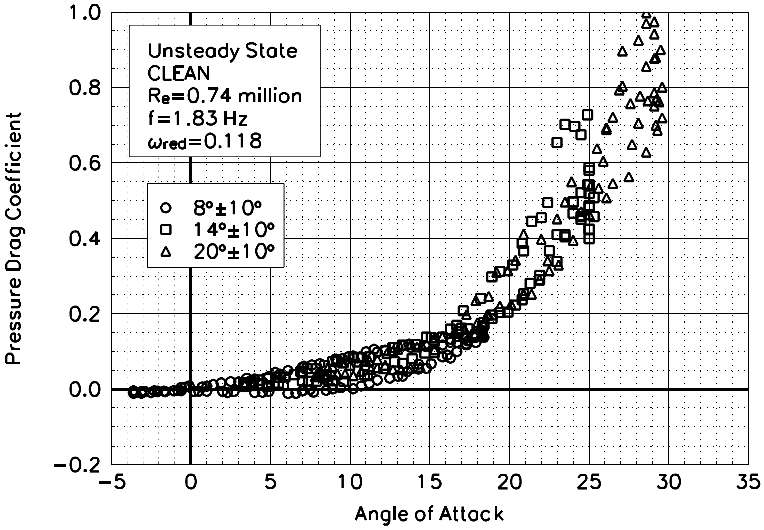

Figure C80. Pressure drag coefficient vs α.

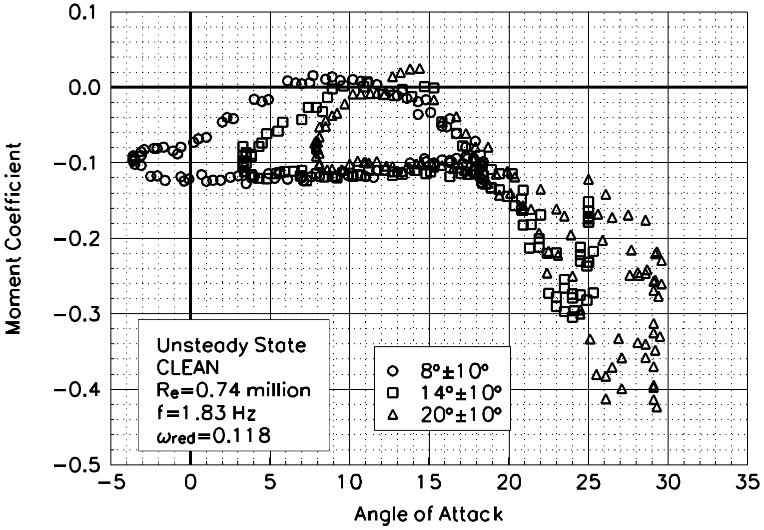

Figure C81. Moment coefficient vs α.

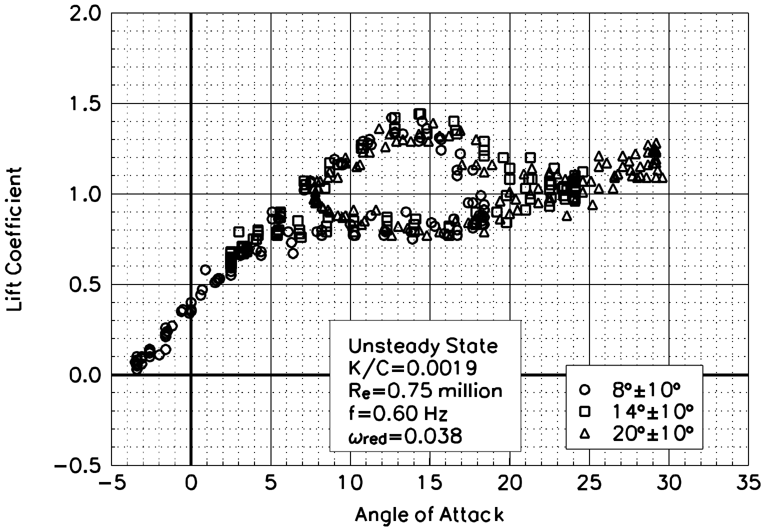

Figure C82. Lift coefficient vs α.

NACA 4415
LEGR
Re=0.75 million
$\omega_{reduced}$=0.038

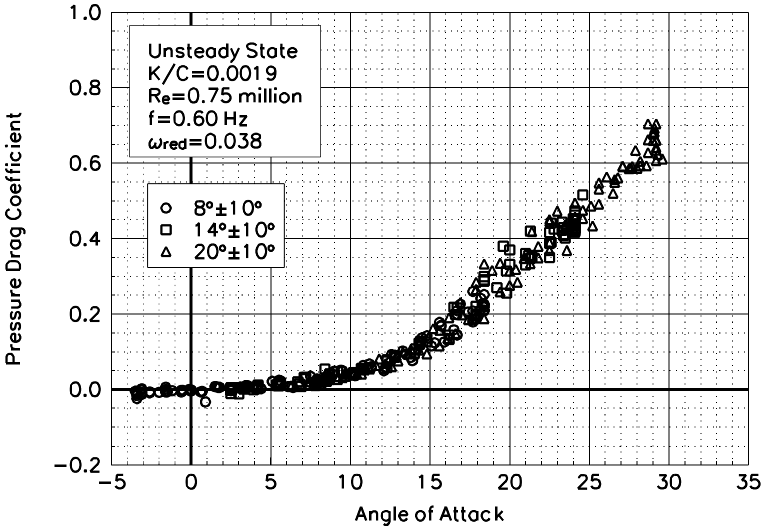

Figure C83. Pressure drag coefficient vs α.

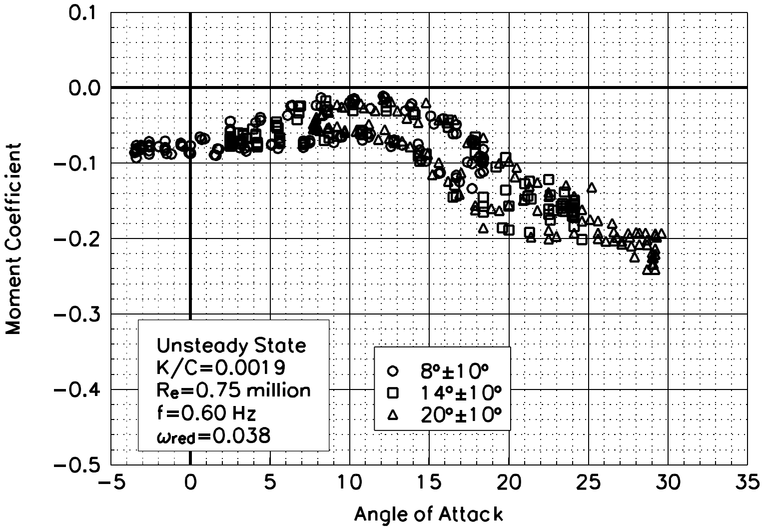

Figure C84. Moment coefficient vs α.

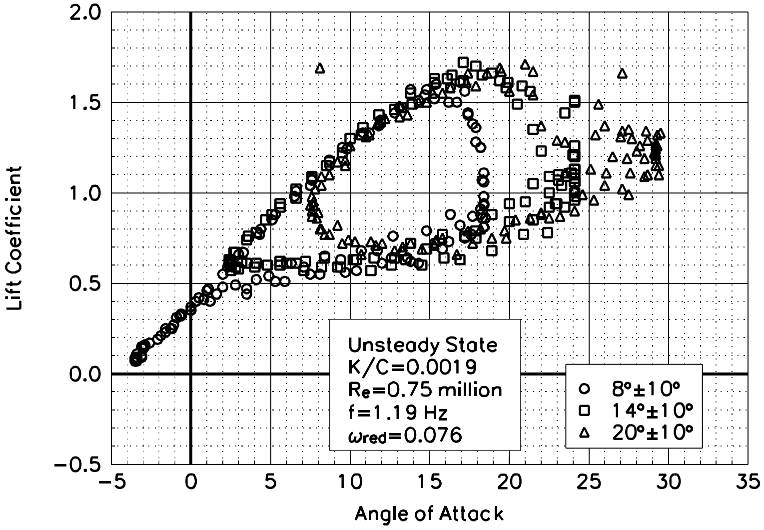

Figure C85. Lift coefficient vs α.

NACA 4415
LEGR
Re=0.75 million
$\omega_{reduced}$=0.076

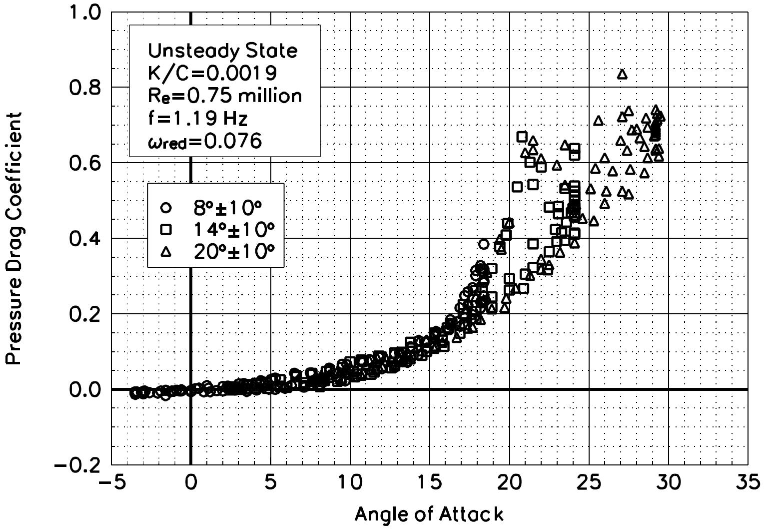

Figure C86. Pressure drag coefficient vs α.

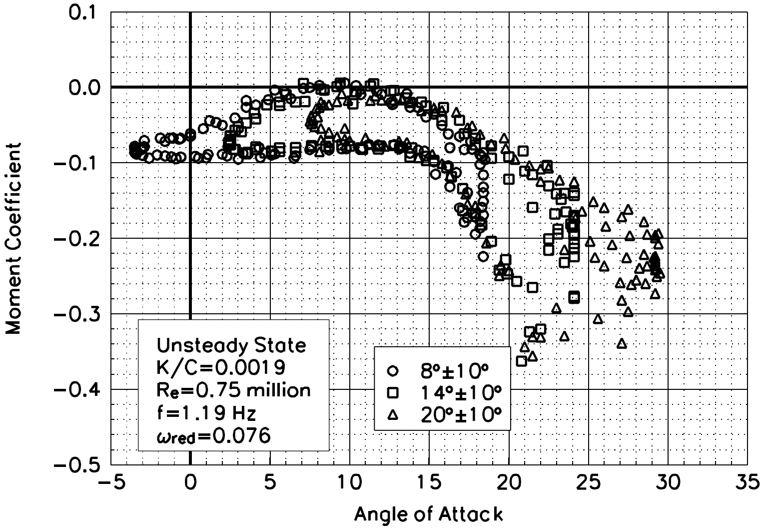

Figure C87. Moment coefficient vs α.

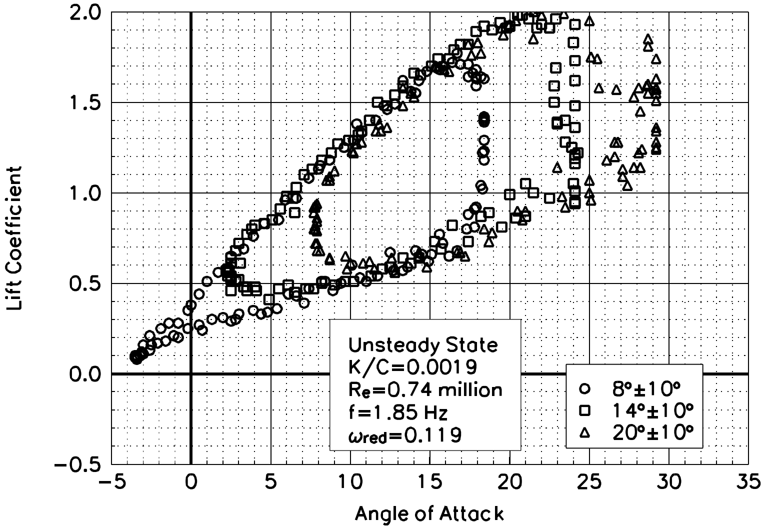

Figure C88. Lift coefficient vs α.

NACA 4415
LEGR
Re=0.74 million
$\omega_{reduced}$=0.119

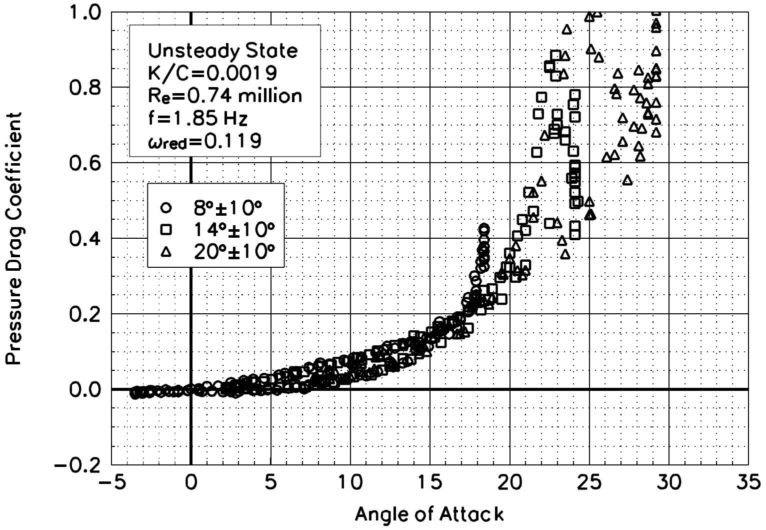

Figure C89. Pressure drag coefficient vs α.

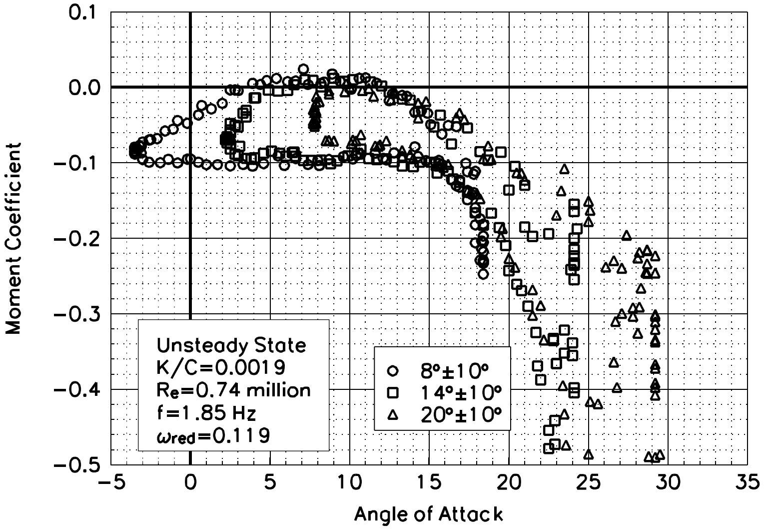

Figure C90. Moment coefficient vs α.

Unsteady Airfoil Characteristics

±10° Sine, Re = 1 million

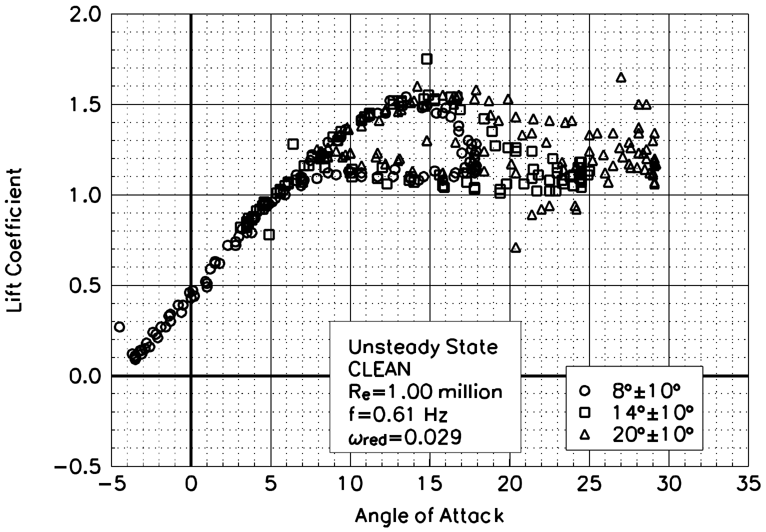

Figure C91. Lift coefficient vs α.

NACA 4415
Clean
Re=1.00 million
$\omega_{reduced}$=0.029

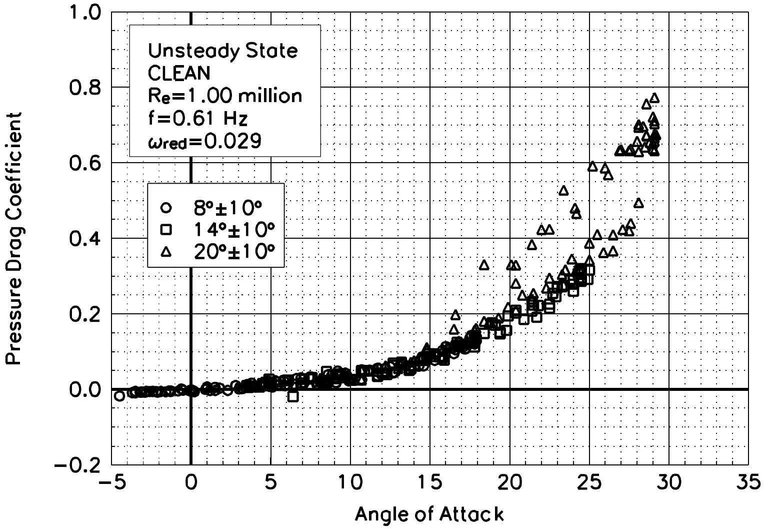

Figure C92. Pressure drag coefficient vs α.

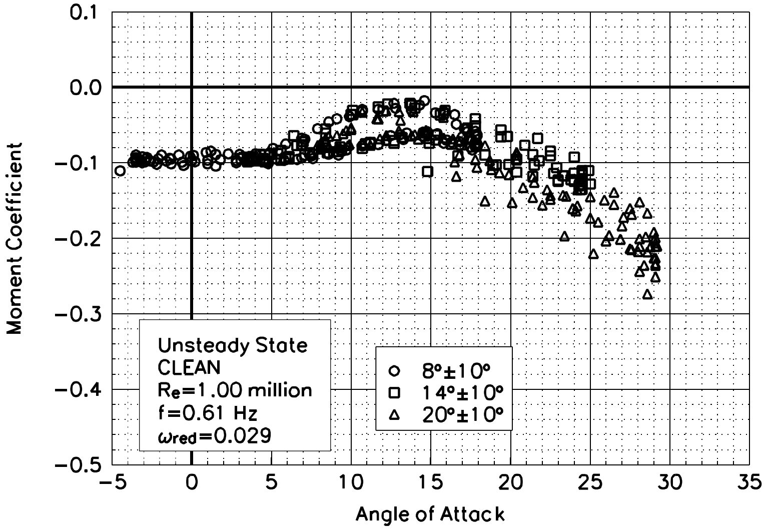

Figure C93. Moment coefficient vs α.

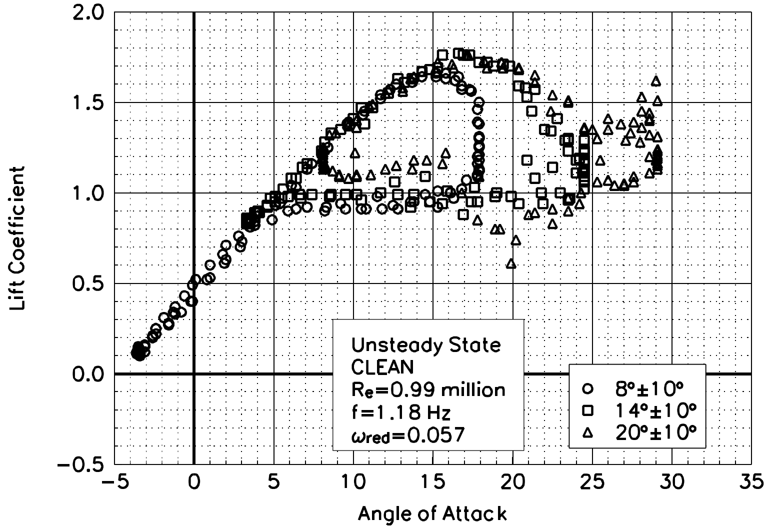

Figure C94. Lift coefficient vs α.

NACA 4415
Clean
Re=0.99 million
$\omega_{reduced}$=0.057

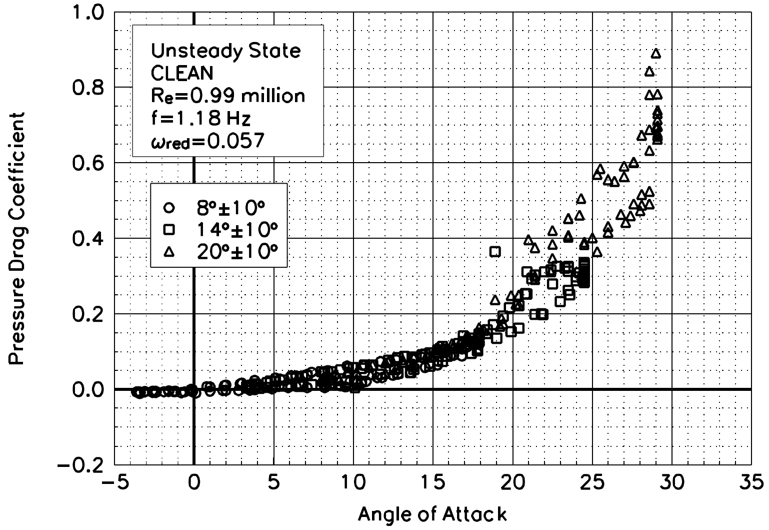

Figure C95. Pressure drag coefficient vs α.

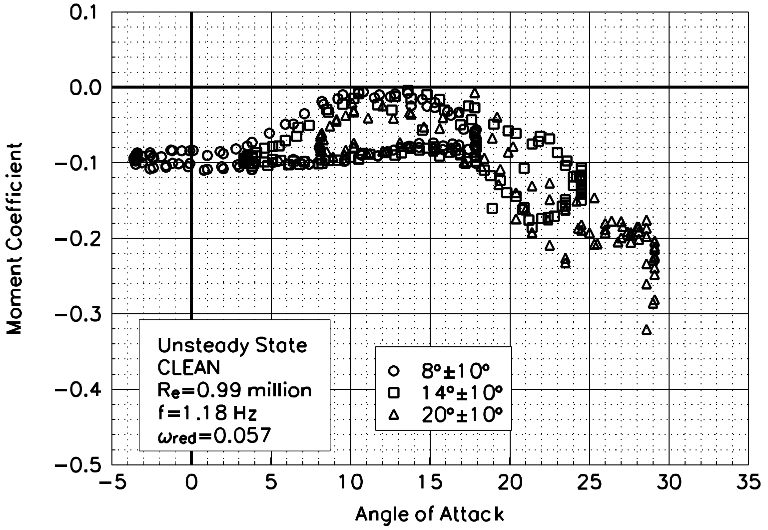

Figure C96. Moment coefficient vs α.

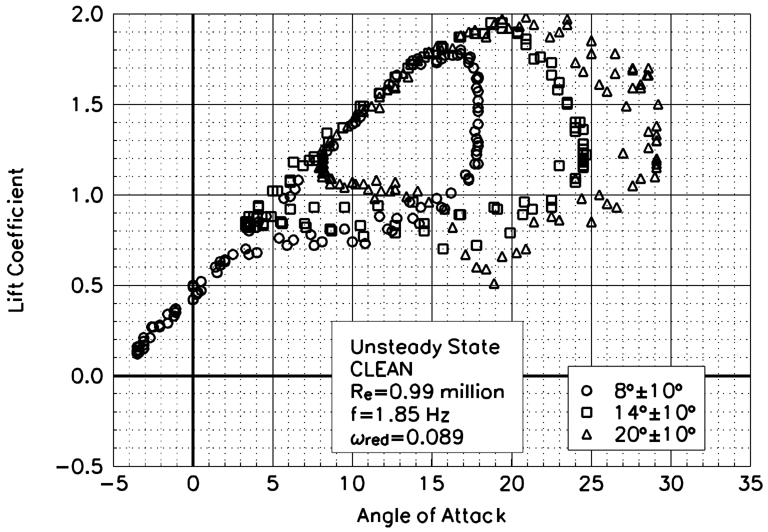

Figure C97. Lift coefficient vs α.

NACA 4415
Clean
Re=0.99 million
$\omega_{reduced}$=0.089

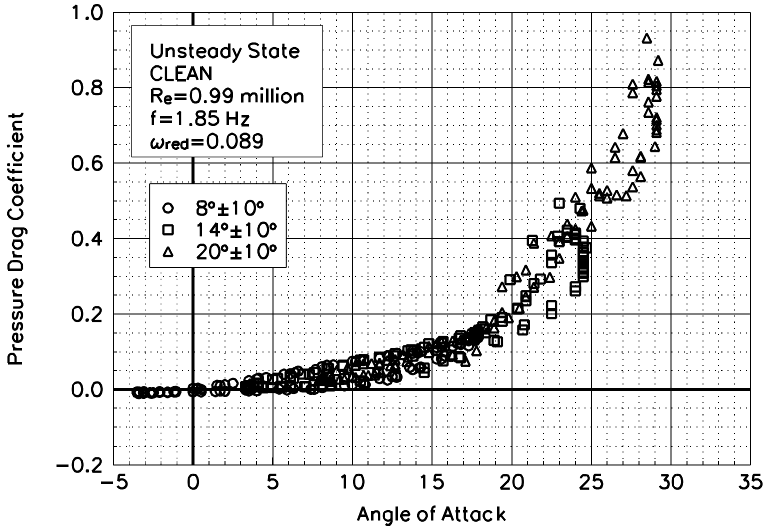

Figure C98. Pressure drag coefficient vs α.

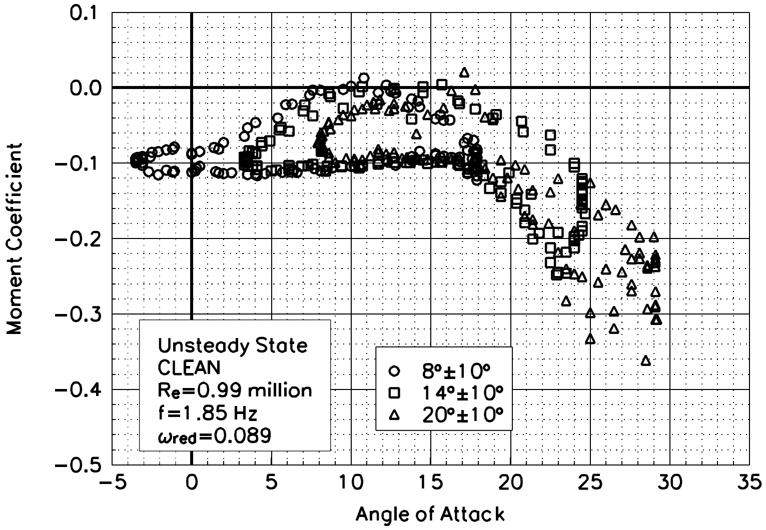

Figure C99. Moment coefficient vs α.

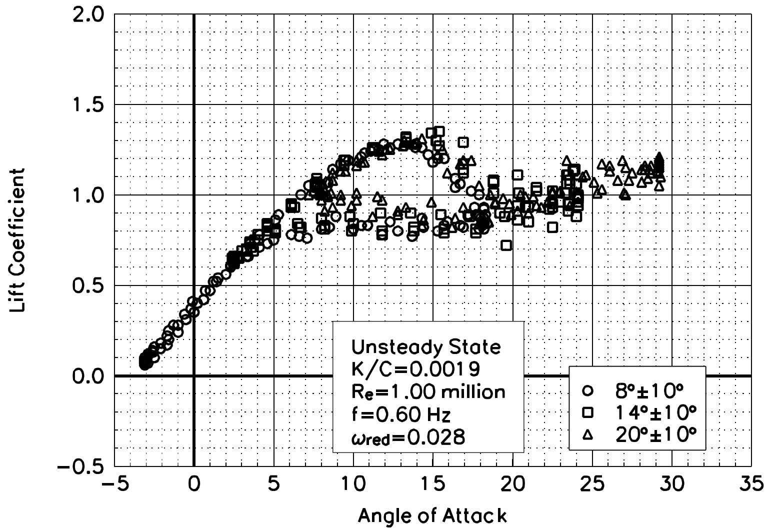

Figure C100. Lift coefficient vs α.

NACA 4415
LEGR
Re=1.00 million
$\omega_{reduced}$=0.028

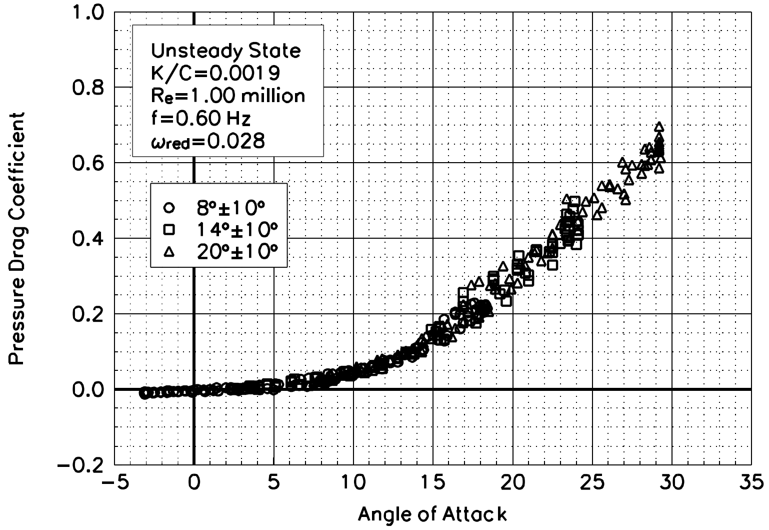

Figure C101. Pressure drag coefficient vs α.

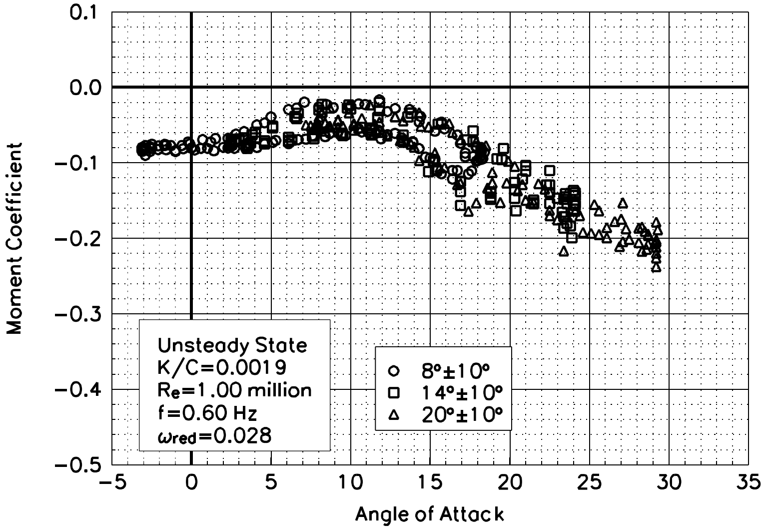

Figure C102. Moment coefficient vs α.

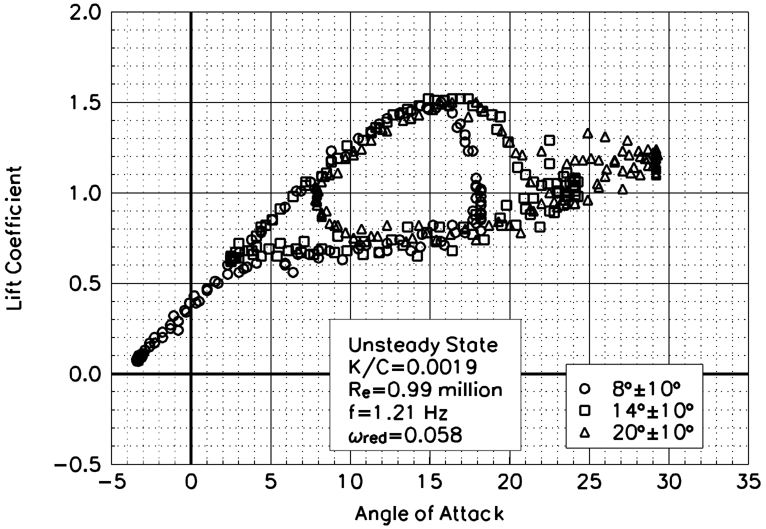

Figure C103. Lift coefficient vs α.

NACA 4415
LEGR
Re=0.99 million
$\omega_{reduced}$=0.058

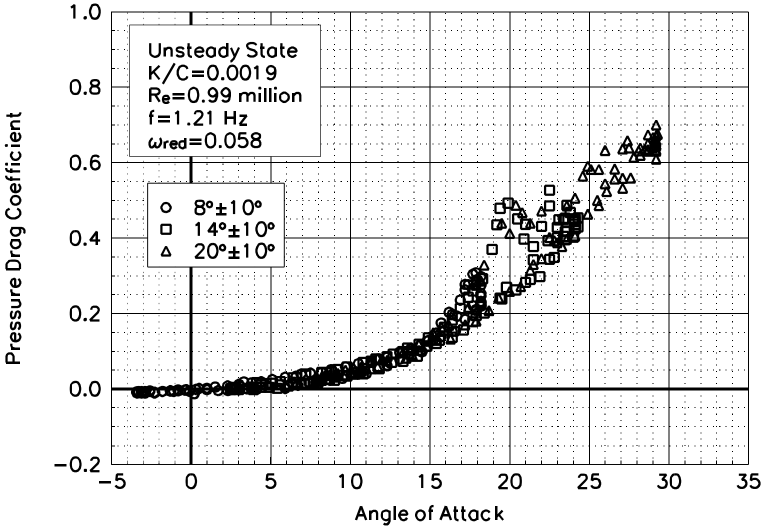

Figure C104. Pressure drag coefficient vs α.

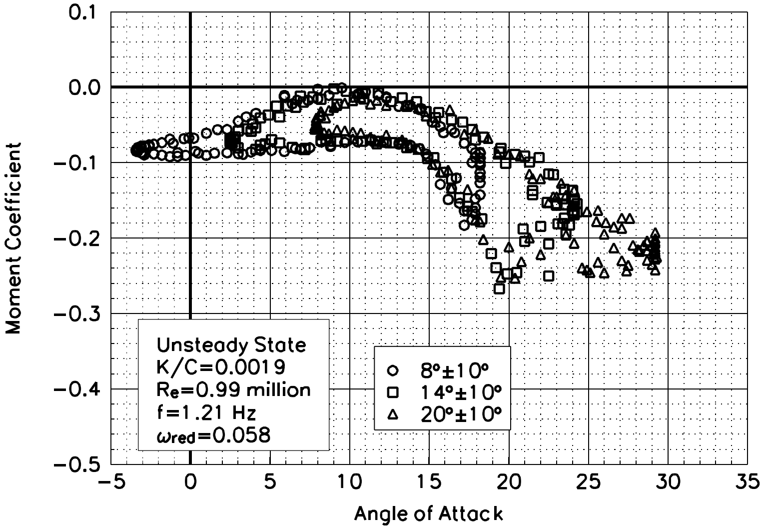

Figure C105. Moment coefficient vs α.

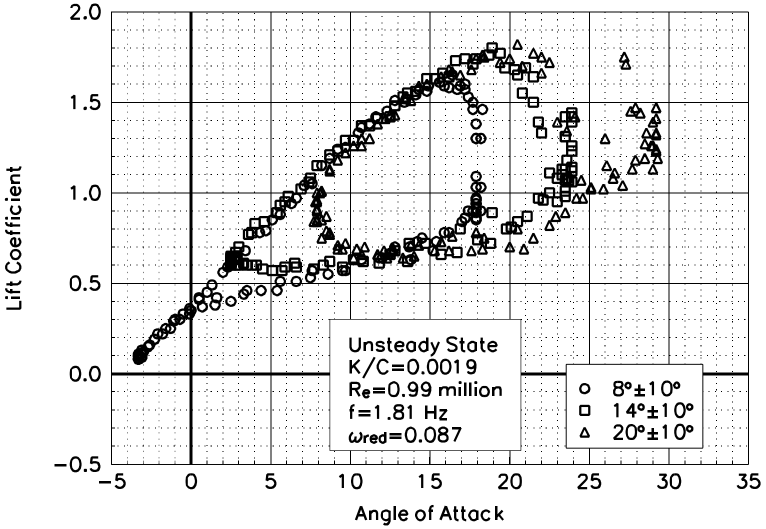

Figure C106. Lift coefficient vs α.

NACA 4415
LEGR
Re=0.99 million
$\omega_{reduced}$=0.087

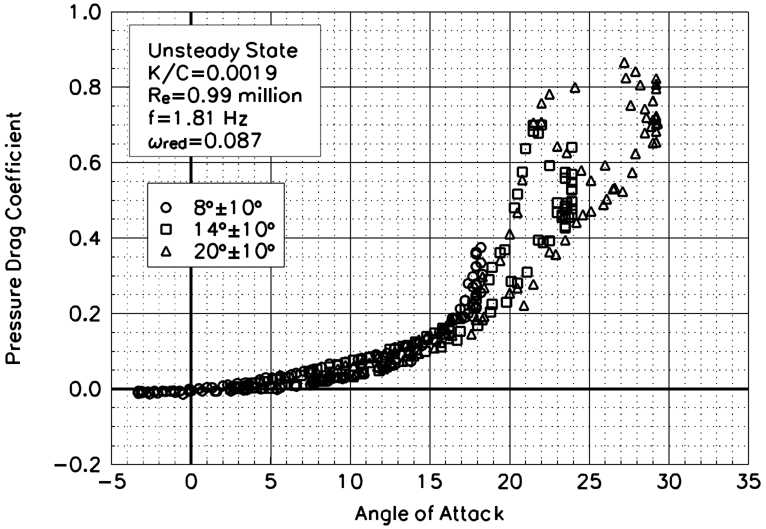

Figure C107. Pressure drag coefficient vs α.

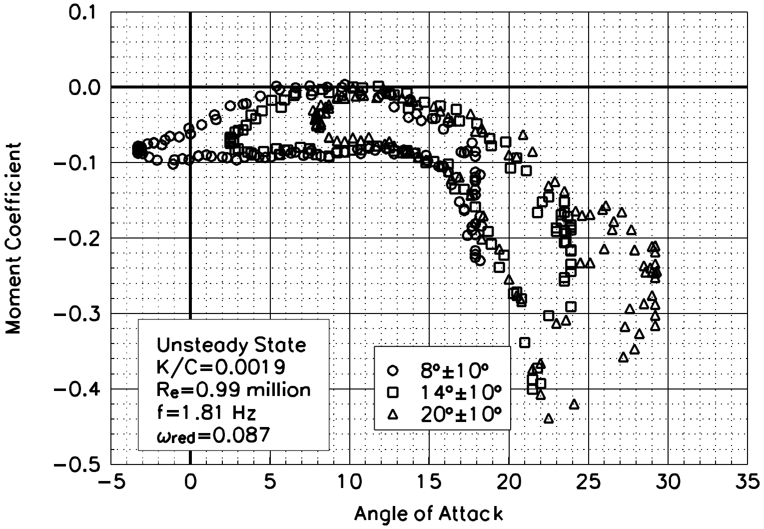

Figure C108. Moment coefficient vs α.

Unsteady Airfoil Characteristics

±10° Sine, Re = 1.25 million

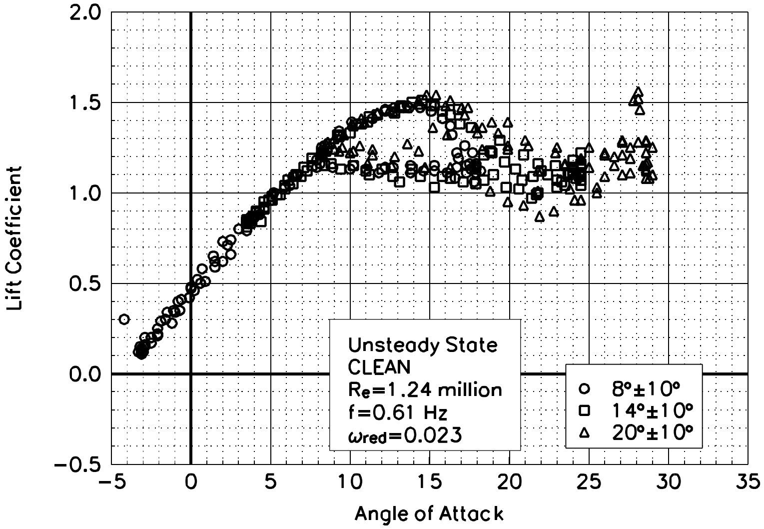

Figure C109. Lift coefficient vs α.

NACA 4415
Clean
Re=1.24 million
$\omega_{reduced}$=0.023

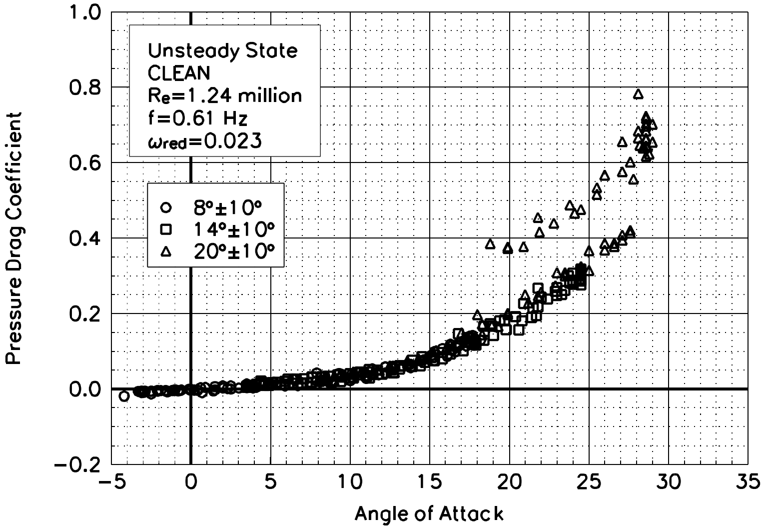

Figure C110. Pressure drag coefficient vs α.

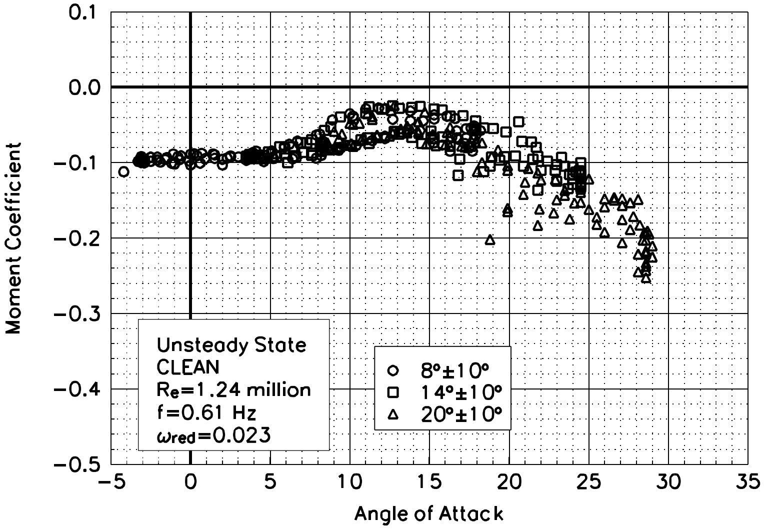

Figure C111. Moment coefficient vs α.

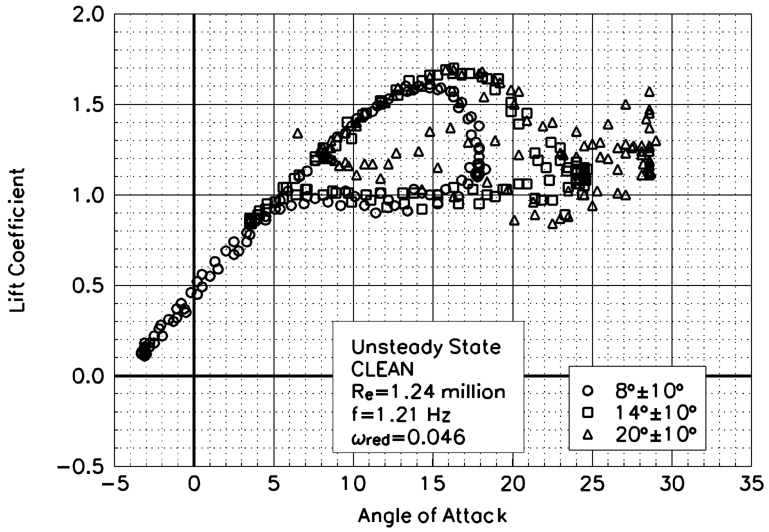

Figure C112. Lift coefficient vs α.

NACA 4415
Clean
Re=1.24 million
$\omega_{reduced}$=0.046

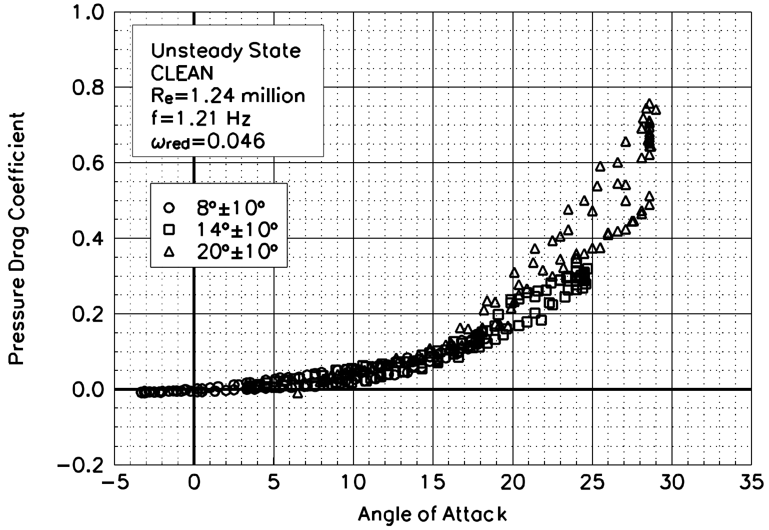

Figure C113. Pressure drag coefficient vs α.

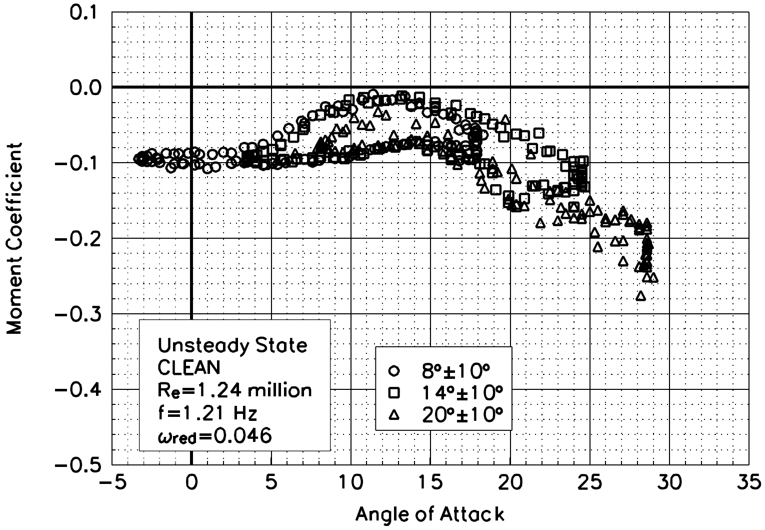

Figure C114. Moment coefficient vs α.

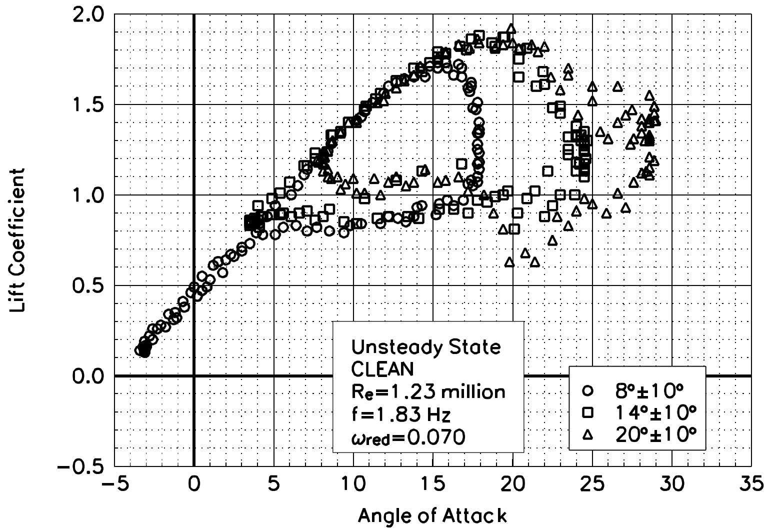

Figure C115. Lift coefficient vs α.

NACA 4415
Clean
Re=1.23 million
$\omega_{reduced}$=0.070

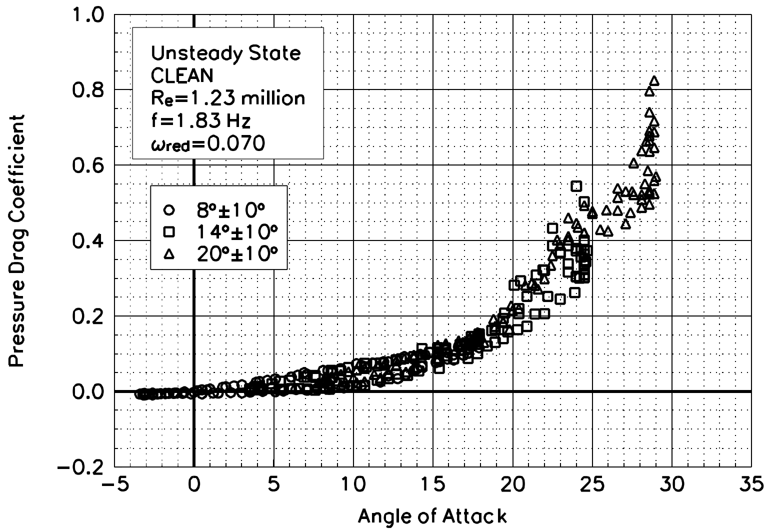

Figure C116. Pressure drag coefficient vs α.

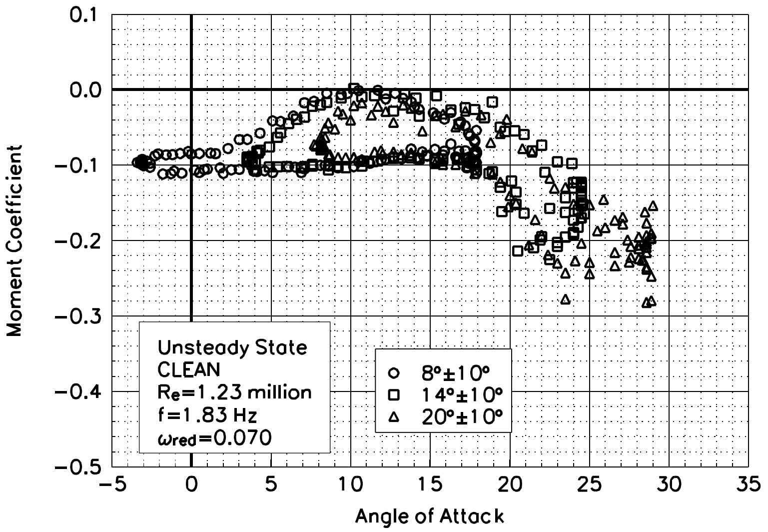

Figure C117. Moment coefficient vs α.

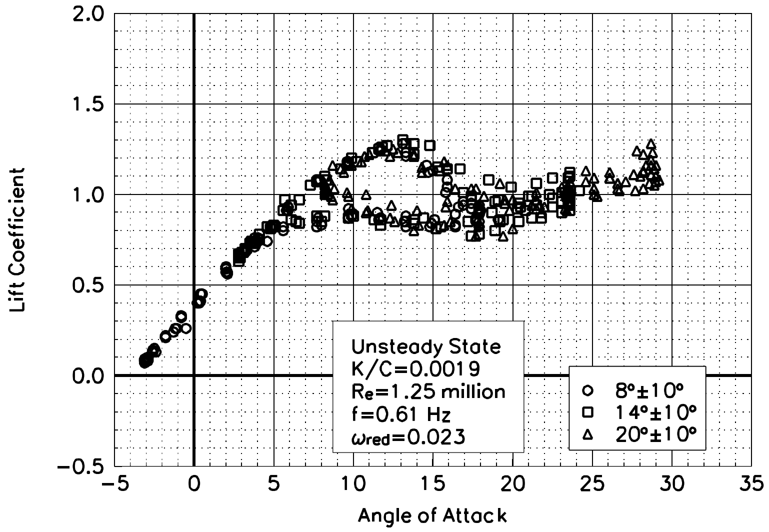

Figure C118. Lift coefficient vs α.

NACA 4415
LEGR
Re=1.25 million
$\omega_{reduced}$=0.023

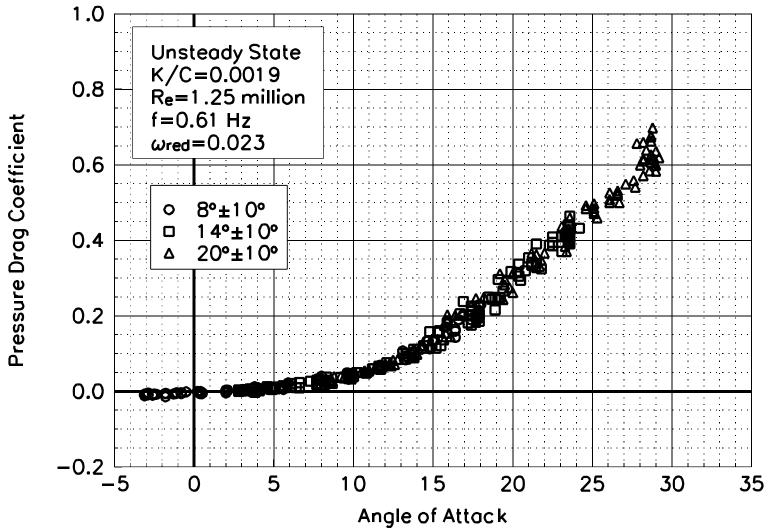

Figure C119. Pressure drag coefficient vs α.

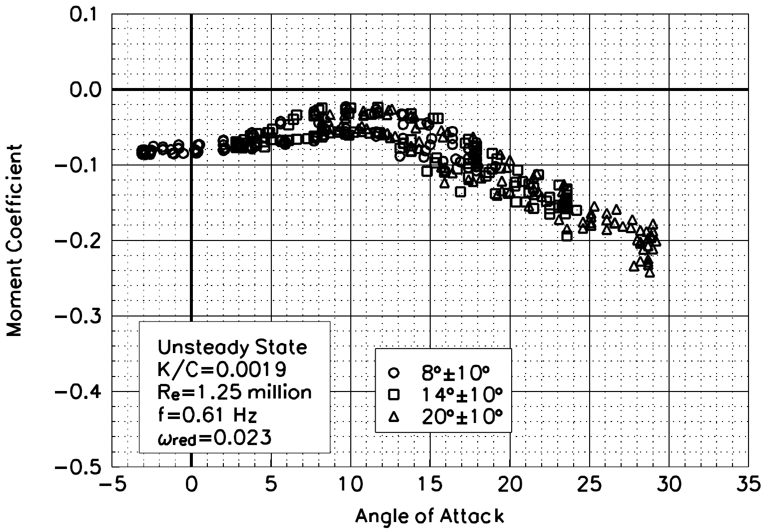

Figure C120. Moment coefficient vs α.

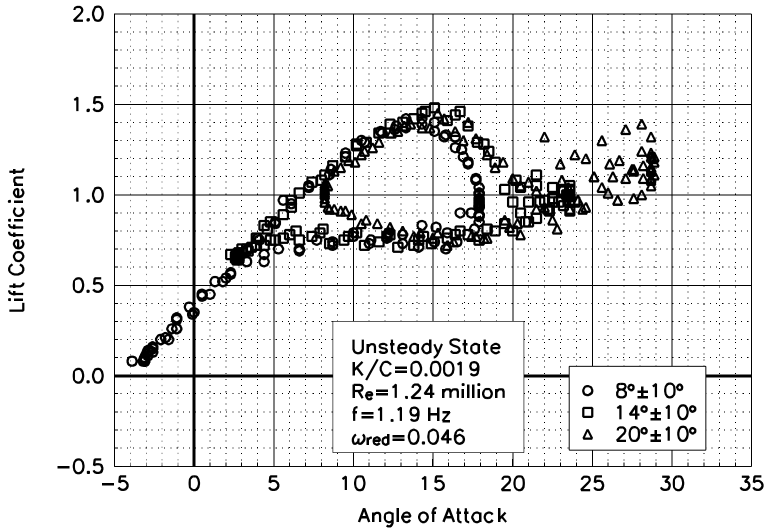

Figure C121. Lift coefficient vs α.

NACA 4415
LEGR
Re=1.24 million
$\omega_{reduced}$=0.046

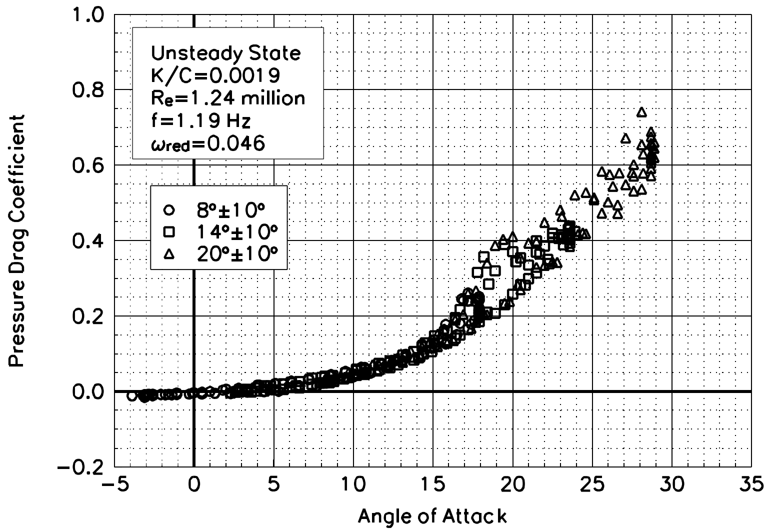

Figure C122. Pressure drag coefficient vs α.

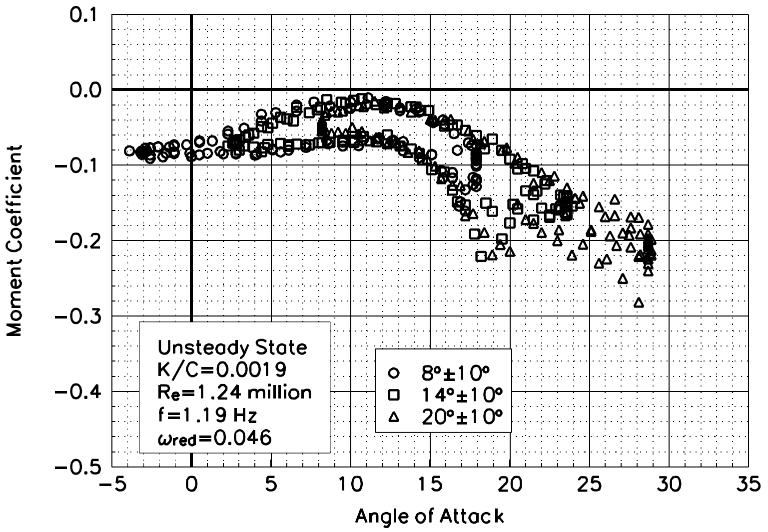

Figure C123. Moment coefficient vs α.

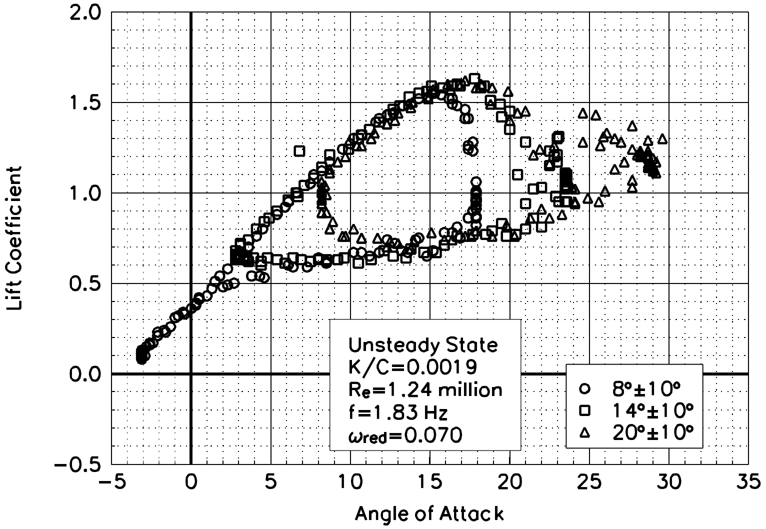

Figure C124. Lift coefficient vs α.

NACA 4415
LEGR
Re=1.24 million
$\omega_{reduced}$=0.070

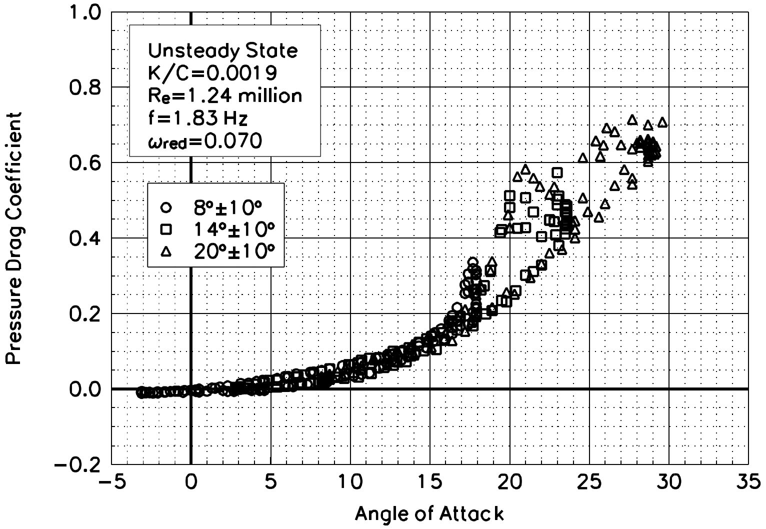

Figure C125. Pressure drag coefficient vs α.

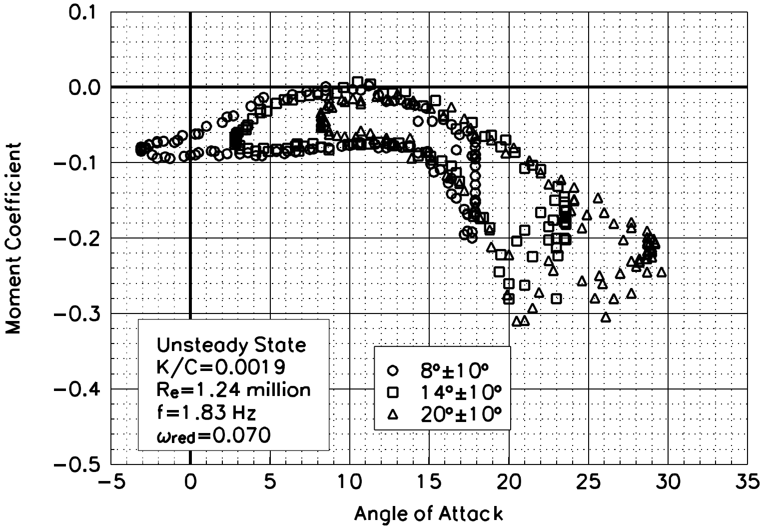

Figure C126. Moment coefficient vs α.

Unsteady Airfoil Characteristics

±10° Sine, Re = 1.5 million

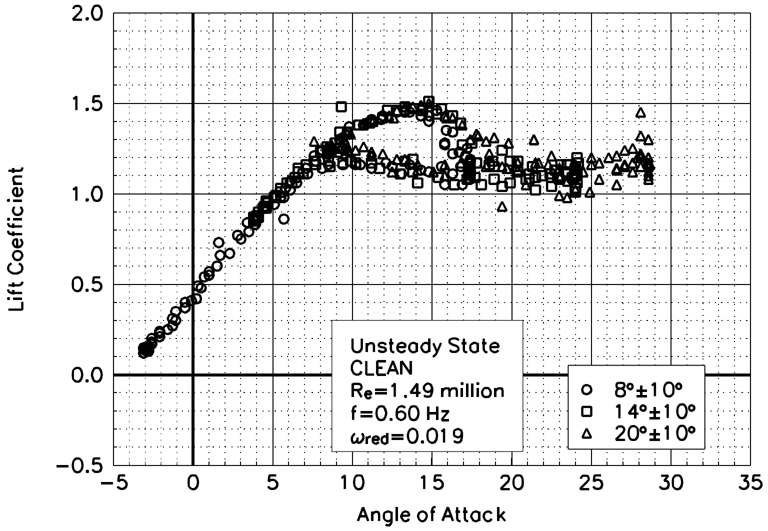

Figure C127. Lift coefficient vs α.

NACA 4415
Clean
Re=1.49 million
$\omega_{reduced}$=0.019

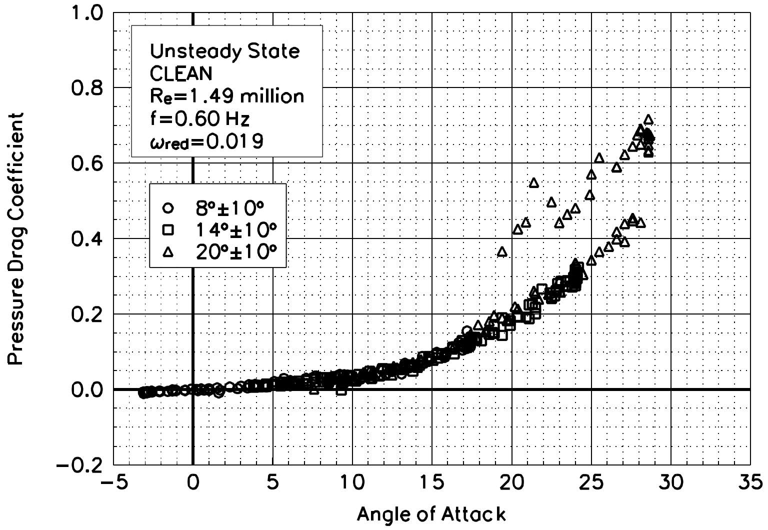

Figure C128. Pressure drag coefficient vs α.

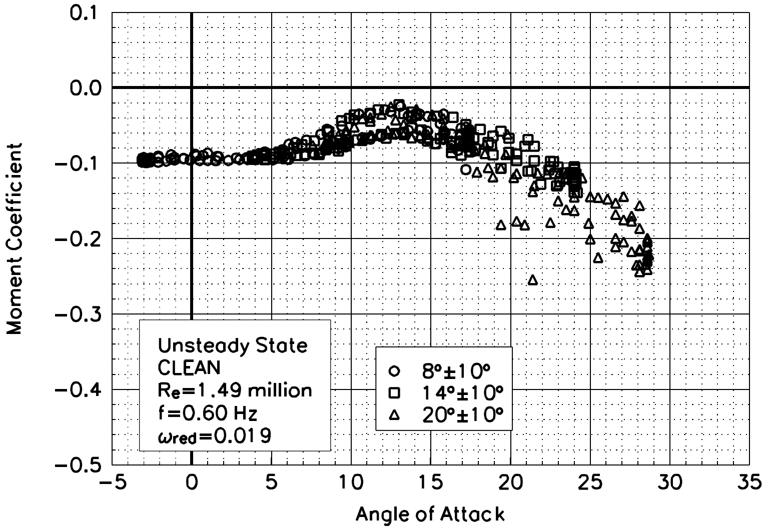

Figure C129. Moment coefficient vs α.

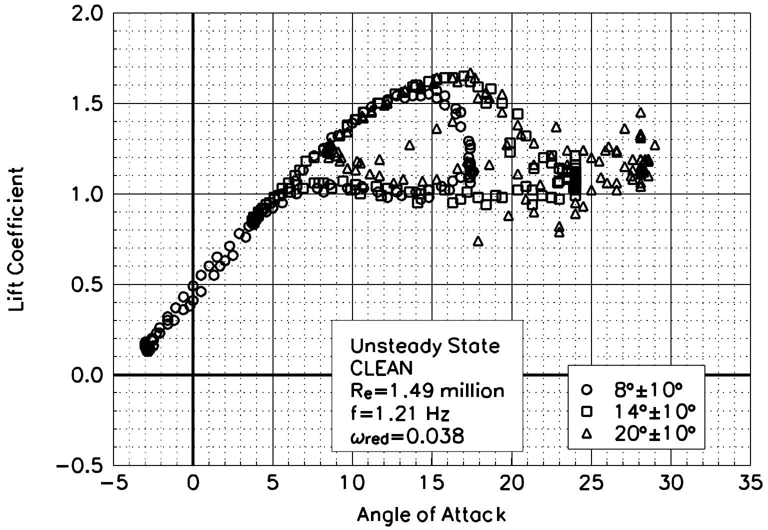

Figure C130. Lift coefficient vs α.

NACA 4415
Clean
Re=1.49 million
$\omega_{reduced}$=0.038

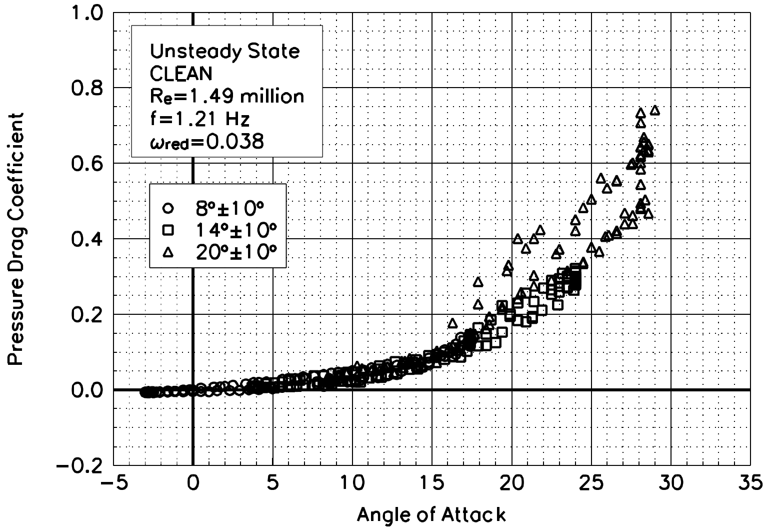

Figure C131. Pressure drag coefficient vs α.

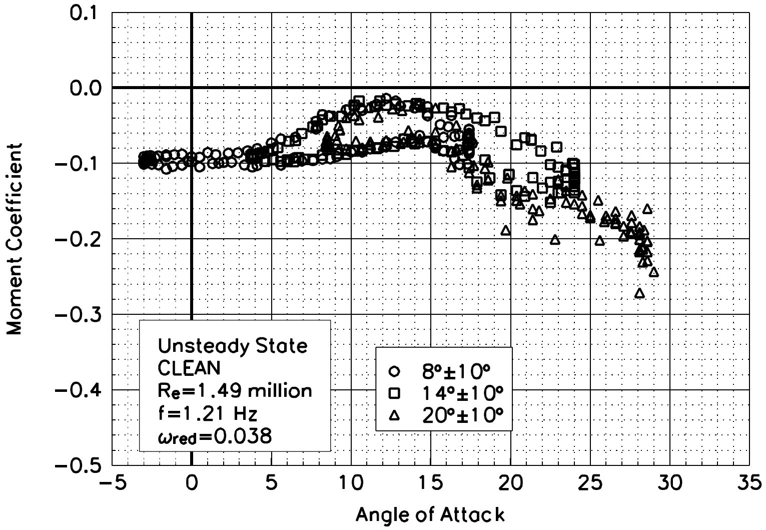

Figure C132. Moment coefficient vs α.

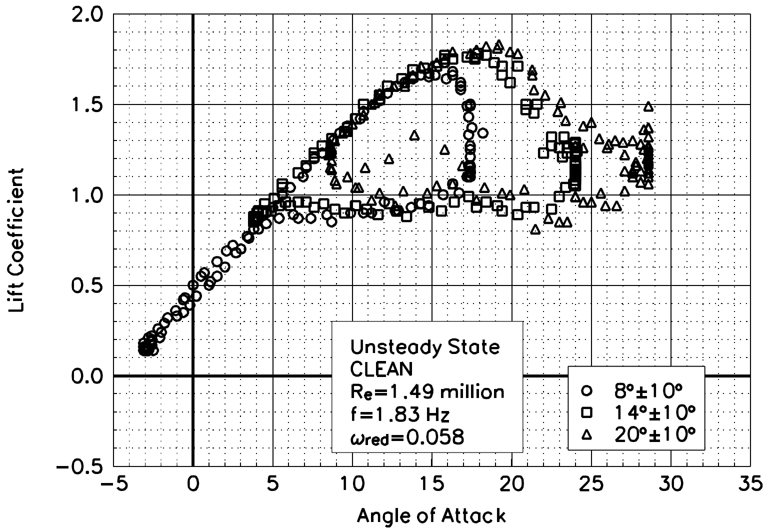

Figure C133. Lift coefficient vs α.

NACA 4415
Clean
Re=1.49 million
$\omega_{reduced}$=0.058

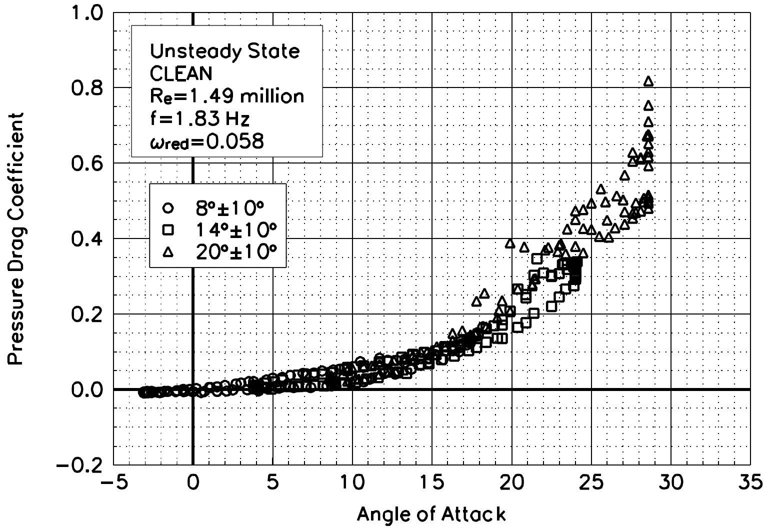

Figure C134. Pressure drag coefficient vs α.

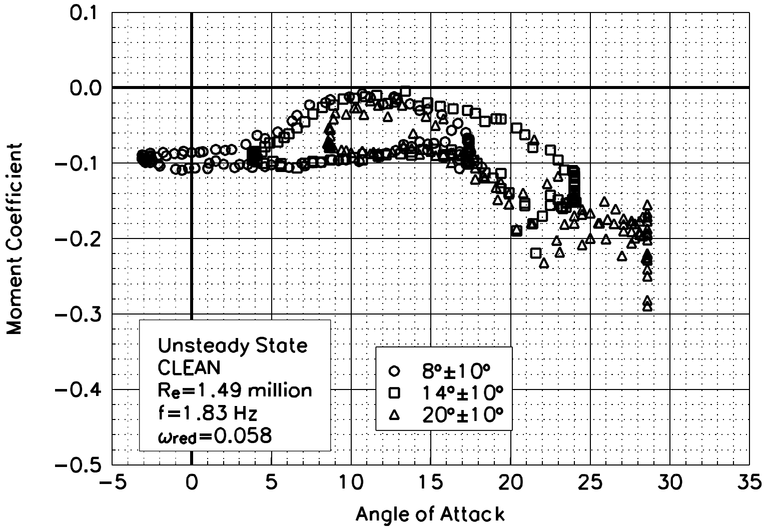

Figure C135. Moment coefficient vs α.

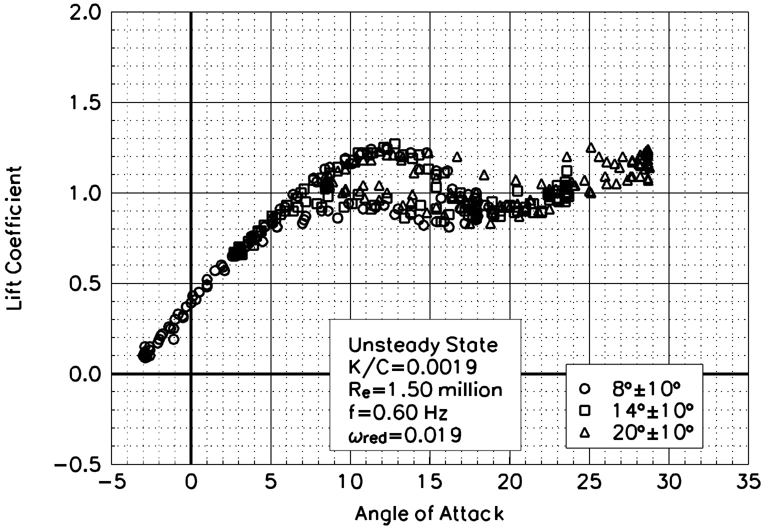

Figure C136. Lift coefficient vs α.

NACA 4415
LEGR
Re=1.50 million
$\omega_{reduced}$=0.019

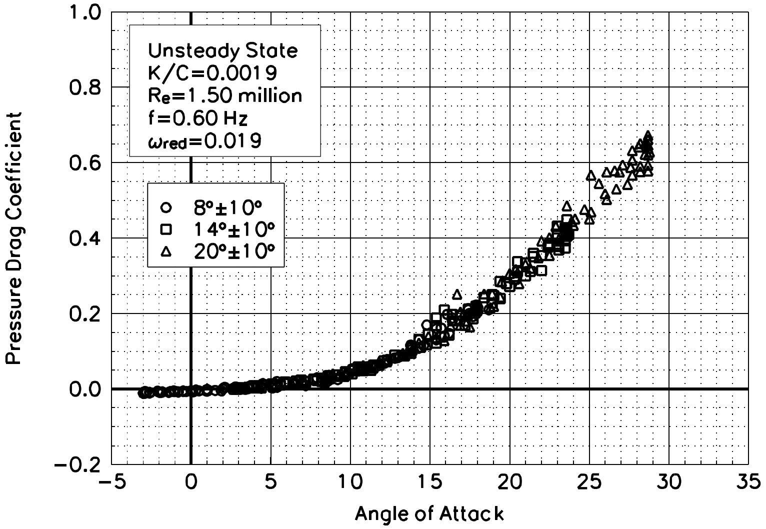

Figure C137. Pressure drag coefficient vs α.

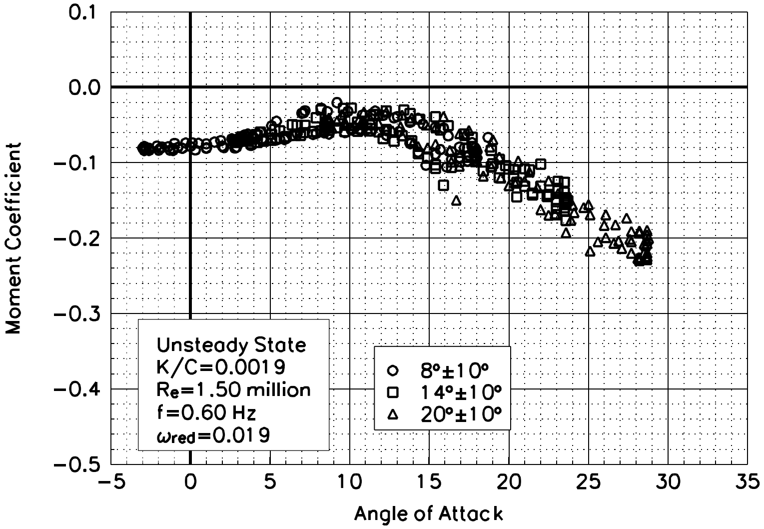

Figure C138. Moment coefficient vs α.

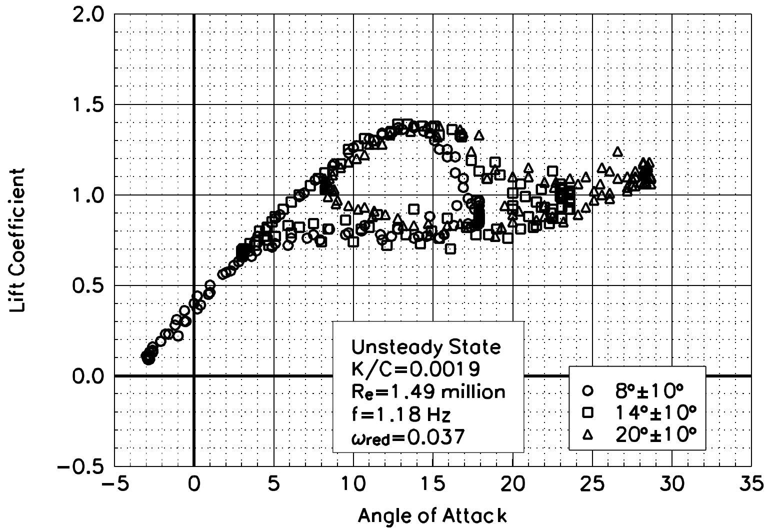

Figure C139. Lift coefficient vs α.

NACA 4415
LEGR
Re=1.49 million
$\omega_{reduced}$=0.037

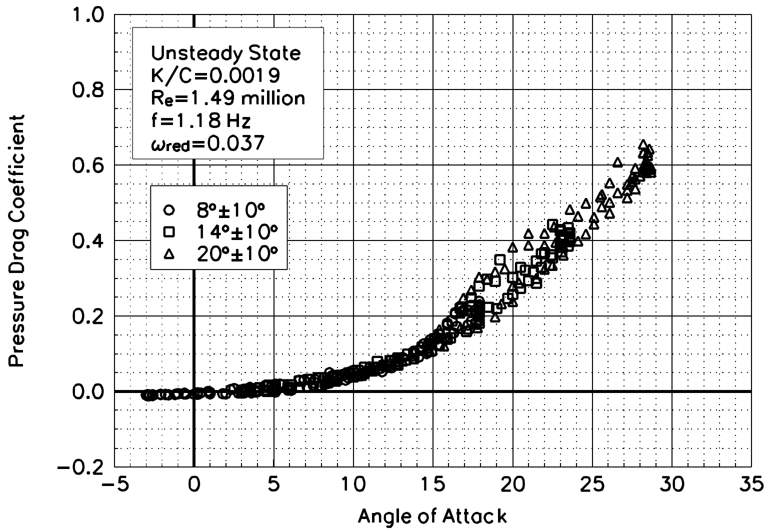

Figure C140. Pressure drag coefficient vs α.

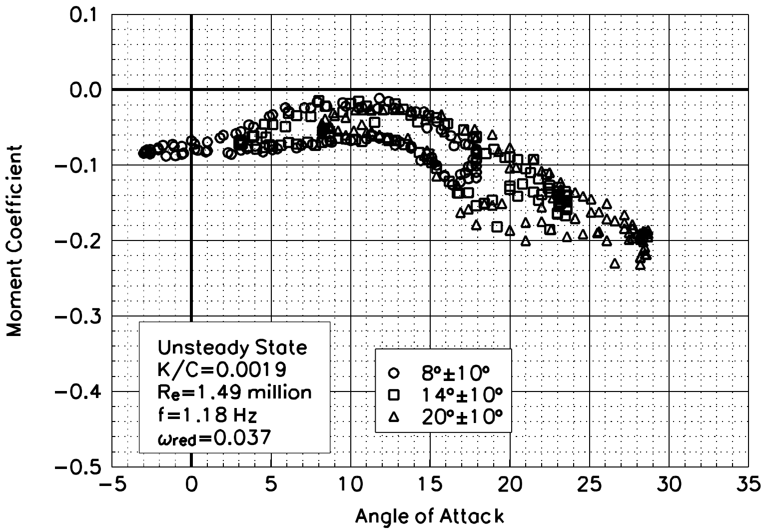

Figure C141. Moment coefficient vs α.

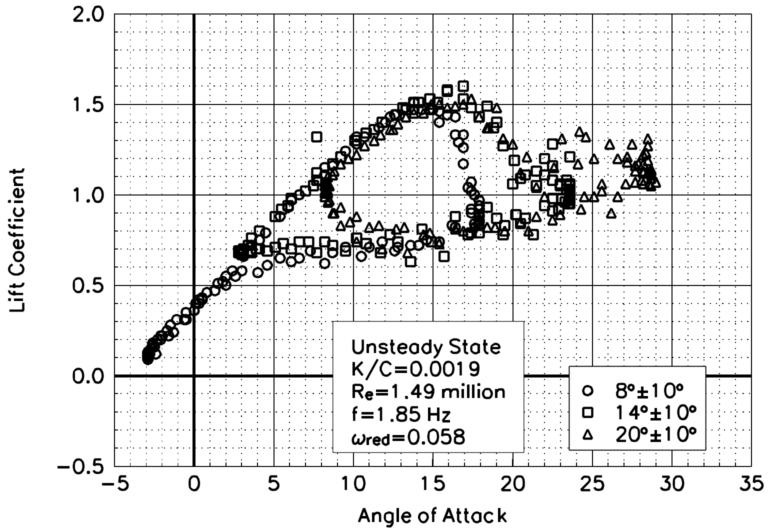

Figure C142. Lift coefficient vs α.

NACA 4415
LEGR
Re=1.49 million
$\omega_{reduced}$=0.058

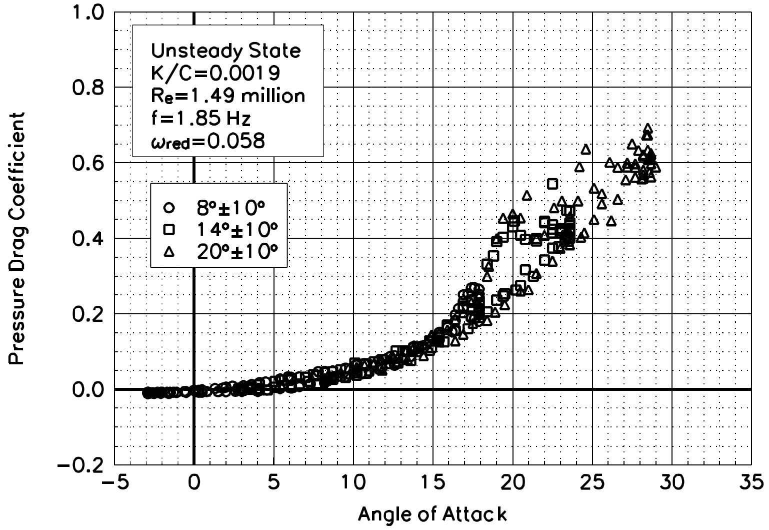

Figure C143. Pressure drag coefficient vs α.

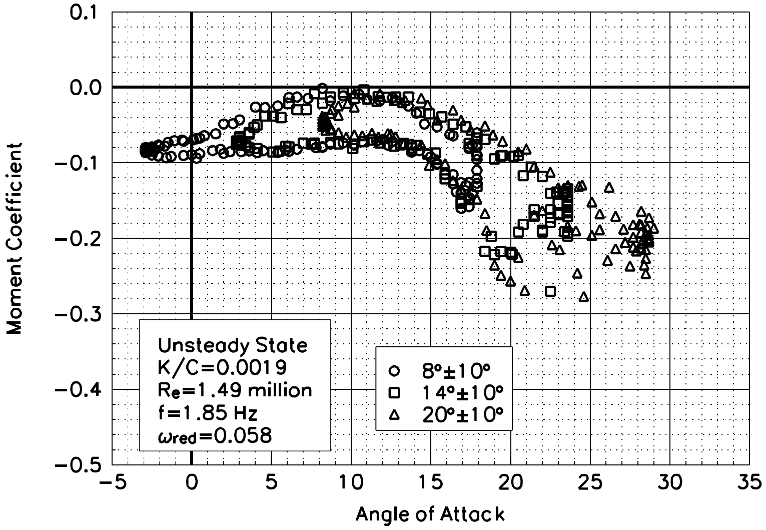

Figure C144. Moment coefficient vs α.